Magnetic reconnection in the solar wind: Modelling and analysis of *Solar Orbiter* observations in the inner heliosphere.

Gabriel Ho Hin Suen

PhD Thesis

Mullard Space Science Laboratory
Department of Space and Climate Physics
University College London

September 16, 2025

I, Gabriel Ho Hin Suen, confirm that the work presented in this thesis is my own. Where information has been derived from other sources, I confirm that this has been indicated in the work.

Abstract

I use a combination of magnetic field and particle data from the *Solar Orbiter* mission, as well as mathematical modelling tools, to study the role magnetic reconnection in the solar wind plays in the inner heliosphere.

Our current understanding of the structure of reconnection outflows in the solar wind is based on the bifurcated reconnection current sheet model, where the reconnection outflow region is bounded by a pair of current sheets. For the first part of this thesis, I adapt existing current sheet stress balance models for reconnection in the Earth's magnetotail to develop a novel theoretical framework to describe the structure of reconnection outflows in the solar wind. I apply my new stress balance framework to a simple model of a symmetric bifurcated reconnection outflow, using it to interpret some of the key observed properties of counterstreaming proton beams in solar wind reconnection outflows.

I then test my model on five examples of bifurcated reconnection outflows observed by *Solar Orbiter* with properties that closely satisfy the symmetry assumptions of our model. I determine the properties of the reconnection inflow and outflow beams and reconstruct the distribution function that characterises the beam population in both the inflow and outflow regions. I then validate my model by comparing the reconstructed distribution functions with the observations.

Finally, I investigate the role reconnection plays in the erosion of magnetic switchbacks. Using *Solar Orbiter* in-situ data, I identify three examples of reconnecting switchbacks in the solar wind and perform a timing analysis to estimate the timescales over which these structures are fully eroded by reconnection. My results show that this process occurs over timescales ranging from a few minutes to a few hours, suggesting that reconnection is a fast and efficient process mechanism for eroding individual switchbacks.

Impact Statement

Plasmas are the most abundant form of matter in the observable universe. While we often think of space as being a vacuum, the Solar System is in fact filled with a tenuous plasma of solar origin, known as the solar wind. The solar wind provides an ideal environment in which to study a wide range of plasma processes. In this thesis, I focus specifically on magnetic reconnection, a fundamental plasma process that converts magnetic energy into kinetic and thermal energy.

The overarching goal of my research is to understand how reconnection transfers energy from the heliospheric magnetic field to the solar wind plasma. I develop a new theoretical framework based on existing current sheet stress balance models to describe the structure and proton population in solar wind reconnection outflows. Using magnetic field and solar wind particle data from the European Space Agency's *Solar Orbiter* spacecraft, I then tested and validated my framework against in-situ observations of reconnection in the solar wind. Additionally, I also investigate the viability of magnetic reconnection as an erosion mechanism for magnetic switchbacks in the solar wind. The results of this latter project were published in the Astronomy & Astrophysics journal and were featured in a series of literature review papers on magnetic switchbacks, to which I contributed a detailed review of reconnection at switchback boundaries. My work directly addresses one of the key science questions that the *Solar Orbiter* mission aims to answer – 'what mechanisms heat and accelerate the solar wind?' – a question that remains one of the outstanding challenges in heliophysics.

Besides its immediate application to the solar wind, my research also has implications for other aspects of space physics, particularly in the context of space weather. Magnetic reconnection plays a central role in driving space weather events on Earth, both as a likely generation mechanism for solar flares and coronal mass ejections, and as an important coupling mechanism that governs the solar wind-magnetosphere interaction. These space weather events have the potential to inflict significant damage to our space and ground-based infrastructure, including GPS navigation, satellite communication, and the electrical grid, all of which underpin the technology we rely on in our everyday lives. Understanding how magnetic reconnection drives space weather is essential for enhancing our ability to forecast space weather events and mitigate its effects.

Finally, space plasma physics research offers valuable insights that are directly applicable to laboratory plasma physics research. My research is part of a cross-disciplinary project between the Royal Society and the National Research Council of Italy to explore connections between space and laboratory plasma physics. As part of this collaboration, I presented the work in this thesis to nuclear fusion researchers working on the RFX experiment in Italy. Magnetic reconnection in nuclear fusion reactors is a major obstacle to achieving the sustained nuclear fusion needed for clean energy production. Insights gained from studying reconnection in space plasmas therefore provide pathways that will help overcome this challenge.

Acknowledgements

'It's been a long way, but we're here'

Alan Shepard Commander, *Apollo 14*

First and foremost, I would like to offer my utmost thanks to my supervisors, Professor Christopher Owen and Dr. Daniel Verscharen for all the support and guidance they have given me over the past 4.5 years. It's been a privilege to work with both of you on *Solar Orbiter*, and I am truly fortunate to have been given this opportunity to fulfil my childhood dream of space exploration. This PhD has been a challenging, yet rewarding experience, and you have taught me so much — not only about space physics and the solar wind, but also about thinking like a scientist and effectively communicating my ideas. Your insightful questions and detailed discussions have been especially helpful in this regard.

I would also like to extend my thanks to all the academics, staff, and engineers at MSSL. To all the academics, for taking the time to answer my questions about life in academia and offering helpful career advice. To the staff, Philippa, Sam, Sarah, and the others in the general office who work behind the scenes, for ensuring everything runs smoothly at the lab. You truly are the unsung heroes! To the engineers, for organising all sorts of fun social activities like lab football and the Social Club quiz.

A big shout-out to my cohort: Jun, Jenny, Teia, Sam, and the rest of the Ariel House crew, who made the pandemic months of the PhD so much more bearable. Camille, my ever-reliable conference buddy and TA partner. Mattijs, for all the board games and Formula 1 watchalongs. Catherine, for all the mad house parties. Sachin and Priya, for the lunchtime banter.

Thank you to the Plasma Group students: Abid, Christian, Harry, Chiara, Jingting for all the good vibes and putting up with my wild tangents. To all my office mates: Simon, Saeeda, Gianpaolo, Ruth, Jess, Alice, Bhagyashri, and Wiktoria. Thank you for making every day at the lab an enjoyable one and for making 101 the best office in the lab! To the other Hong Kongers: Andy, Cynthia, Paul, and Kay, thank you for bringing a piece of home to MSSL. To the other students: Ahlam

and Aisha, for the tea and long conversations about all things anime. Nawin, for all the football and making conference travel more fun. Cristi, for our interesting discussions about all things historical and political.

Finally, I would like to express my deepest gratitude to my family for their unwavering support and belief in me, without which none of this would have been possible. Thank you for all your encouragement, your words of advice, and the countless home-cooked meals that helped me push through to the completion of this thesis and my PhD.

I dedicate this thesis and my PhD to my grandfather, who sadly passed away in October 2021. Granddad, this one's for you.

UCL Research Paper Declaration Form

Referencing the doctoral candidate's own published work(s)

- 1. **1. For a research manuscript that has already been published** (if not yet published, please skip to section 2):
 - (a) What is the title of the manuscript? Magnetic reconnection as an erosion mechanism for magnetic switchbacks
 - (b) **Please include a link to or doi for the work:** https://doi.org/10.1051/0004-6361/202345922
 - (c) Where was the work published? Astronomy & Astrophysics
 - (d) Who published the work? EDP Sciences
 - (e) When was the work published? July 2023
 - (f) List the manuscript's authors in the order they appear on the publication: Gabriel H.H. Suen, Christopher J. Owen, Daniel Verscharen, Timothy S. Horbury, Philippe Louarn, Rossana de Marco.
 - (g) Was the work peer reviewed? Yes
 - (h) Have you retained the copyright? Yes
 - (i) Was an earlier form of the manuscript uploaded to a preprint server (e.g. medRxiv)? If 'Yes', please give a link or doi: https://arxiv.org/abs/2305.06035
 - If 'No', please seek permission from the relevant publisher and check the box next to the below statement:
 - ☐ I acknowledge permission of the publisher named under 1d to include in this thesis portions of the publication named as included in 1c.
- 2. For a research manuscript prepared for publication but that has not yet been published (if already published, please skip to section 3):
 - (a) What is the current title of the manuscript?

(b) Has the manuscript been uploaded to a preprint server 'e.g. medRxiv'?

If 'Yes', please please give a link or doi:

- (c) Where is the work intended to be published?
- (d) List the manuscript's authors in the intended authorship order:
- (e) Stage of publication:
- 3. For multi-authored work, please give a statement of contribution covering all authors (if single-author, please skip to section 4):
 - G.H.H. Suen performed the majority of the analysis of the MAG and SWA data, identified all three examples of reconnecting switchbacks highlighted in the paper, and performed the timing analysis used to estimate the erosion timescale. C.J. Owen and D. Verscharen provided valuable scientific discussion, detailed advice, and guidance throughout the project. In addition, C.J. Owen also assisted with the analysis of SWA electron data and provided the electron strahl pitch angle distribution data used in the analysis of Event 1. T.S. Horbury provided help with the MAG instrument and magnetic field data. P. Louarn provided help with the SWA instrument and proton data. R. de Marco assisted with the analysis of the SWA alpha particle data and provided the alpha particle data used in the analysis of Events 2 and 3. G.H.H. Suen produced all the figures and wrote the manuscript text, with significant feedback provided by C.J. Owen and D. Verscharen during the drafting phase. All co-authors reviewed the manuscript and provided useful comments prior to publication.
- 4. In which chapter(s) of your thesis can this material be found? Chapter 5

e-Signatures confirming that the information above is accurate (this form should be co-signed by the supervisor/ senior author unless this is not appropriate, e.g. if the paper was a single-author work):

Candidate:

Gabriel H.H. Suen **Date:** 27 March 2025

Supervisor/Senior Author signature (where appropriate):

Professor Christopher J. Owen

Date: 27 March 2025

Contents

A	Acknowledgments				
1	Intr	oductio	on	23	
	1.1	Funda	mentals of plasma physics	23	
		1.1.1	What is a plasma?		
		1.1.2	Single particle motion and drift motion	. 24	
		1.1.3	Kinetic theory	. 28	
		1.1.4	Magnetohydrodynamics	. 29	
		1.1.5	Ideal MHD and the frozen-in theorem	31	
	1.2	Magne	etic reconnection	33	
		1.2.1	Sweet-Parker model	33	
		1.2.2	Petschek model	36	
	1.3	The he	eliosphere	. 37	
		1.3.1	The Sun	. 37	
		1.3.2	The solar wind	41	
		1.3.3	The heliospheric magnetic field	. 44	
		1.3.4	In-situ observations of reconnection in the solar wind	47	
	1.4	Magno	etic switchbacks	49	
		1.4.1	General characteristics	49	
		1.4.2	Formation mechanisms	. 52	
	1.5	Curre	nt sheet stress balance models	53	
		1.5.1	Symmetric cold inflows	. 54	
		1.5.2	Cold asymmetric inflows	. 58	
		1.5.3	Potential effects of reconnection heating	60	
2	Inst	rument	tation and Methods	61	
	2.1	Solar	Orbiter	61	
	2.2	Fluxga	ate magnetometers	63	
		2.2.1	Magnetometer (MAG)	64	
	2.3	Electr	ostatic analysers	64	
		2.3.1	Solar Wind Analyser (SWA)	66	
	2.4	Coord	linate systems and frame transformation techniques	67	

Contents	1	1	
Contents	1	1	

		2.4.1 2.4.2	Current sheet-aligned coordinate system deHoffmann-Teller analysis	68 69
3	Deve	elopmen	at of bifurcated current sheet stress balance models for re-	
	conn	ection i	n the solar wind	72
	3.1	Introdu	action	72
	3.2	Stress l	balance for a single current sheet	73
	3.3	Stress l	balance for a bifurcated reconnection current sheet	77
		3.3.1	Speed of the inflow and outflow beams	82
	3.4	Applica	ation to a simple bifurcated reconnection current sheet model	83
	3.5	Discus	sion	88
	3.6	Conclu	sions	91
4	App	lication	of bifurcated current stress balance models on Solar Orbiter	
	obse	rvations	s of reconnection outflows in the solar wind	94
	4.1	Introdu	ection	94
	4.2		nd methods	95
		4.2.1	Reconnection outflow identification algorithm	95
		4.2.2	VDF resampling program	
	4.3		8	
		4.3.1	Event selection	
		4.3.2	Event 4 — 9 July 2023 06:46:31 – 06:48:27 UT	
		4.3.3	Event 1 — 9 January 2023 18:34:20 – 18:38:40 UT	
	4.4		balance analysis	
		4.4.1	Outflow region opening angle	
		4.4.2	Outflow beam temperature and velocity	
	4.5	-	rison of VDFs	
		4.5.1	Event 4	
	1.0	4.5.2	Event 1	
	4.6		sion	
	4.7	Conciu	sions	121
5	_		econnection as an erosion mechanism for magnetic switch-	
	back			123
	5.1		ection	
	5.2		nd methods	
		5.2.1	Instrumentation and event selection	
		5.2.2	Testing for rotational discontinuities	
	5.3		3	
		5.3.1	Event 1 – 10 August 2021 07:45:50 - 07:48:45 UT	
		5.3.2	Event 2 - 30 August 2021 10:19:05 - 10:21:28 UT	
		5.3.3	Event 3 - 30 August 2021 10:03:46 - 10:12:15 UT	130

Contents	12
----------	----

Re	eferen	ices		147
6	Con	clusion	s and future work	143
	5.5	Concl	usions	. 141
			heliosphere	. 139
		5.4.4	Implications on switchback formation and evolution in the	
		5.4.3	Estimating the timescales for switchback erosion	. 137
		5.4.2	Switchback and reconnection geometry	. 135
		5.4.1	Evidence for reconnection at switchback boundaries	. 133
	5.4	Discus	ssion	. 133

List of Figures

1.1	Direction of the drift velocity of a positively charged particle due	
	to the a) $\mathbf{E} \times \mathbf{B}$ drift and magnetic field gradient drift, and b) the curvature drift	26
1.2	Diamagnetic current in an isothermal plasma. In this configuration, positive ions gyrate in the clockwise direction. Due to the density gradient, there is a net flow of ions downwards generating a diamagnetic current J_{DM} (red arrow). Figure adapted from Chen (2015).	28
1.3	Magnetic flux tube formed by surfaces S_1 , S_2 , and ΔS . The latter surface is parallel to the magnetic field B linking S_1 and S_2 at all points. In the ideal MHD limit, the magnetic flux passing through this tube is time-invariant leading to the frozen-in theorem	32
1.4	Sweet-Parker reconnection model. Black lines represent the separatrices separating the inflow and outflow regions, the blue box represents the diffusion region, and $\mathbf{E_R}$ is the reconnection electric field. The reconnection inflow $\mathbf{u_i}$ from each side carries opposing magnetic flux together, which are separated by a current sheet. If R_M is sufficiently small, a diffusion region is formed inside the current sheet and the magnetic field 'reconnects' across it. Magnetic tension in the reconnected field lines accelerates the reconnection outflow $\mathbf{u_0}$, which re-freezes into the reconnected magnetic field and carries it out of the diffusion region	34
1.5	Petschek reconnection model. The thick black lines, labelled SS1 and SS2, represent the standing slow mode shocks bounding the reconnection outflow. Figure adapted from Petschek (1964)	37
1.6	Structure of the solar interior and atmosphere. Figure reproduced from Priest (1995)	38
1.7	Structure of the Sun's magnetic field during solar minimum (top) and maximum (bottom). Figure reproduced from Meyer-Vernet (2007)	39
1.8	Graph of the four solutions to Equation 1.56. Figure adapted from Parker (1965).	43

1.9	Variation in the solar wind speed with heliographic latitude during solar minimum (left) and solar maximum (right). The polar plots overlaid on top of the images of the solar disk are solar wind speed measurements from the <i>Ulysses</i> spacecraft. Regions with sunward and anti-sunward magnetic polarity are coloured in blue and red, respectively. The bottom panel shows the variation in sunspot number over the solar cycle. Figure adapted from McComas et al. (2003).		44
1.10	Diagram of the heliospheric magnetic field up to 1 AU in the ecliptic plane, showing the Parker spiral and sector structure. The sector with positive, anti-sunward magnetic polarity (red) is separated from the sector with negative, sunward polarity (blue) by the heliospheric current sheet (dashed green line). Figure reproduced from Owens & Forsyth (2013)	•	45
1.11	Variation in the suprathermal electron strahl pitch angle distribution (right) depending on the magnetic field topology (left). The black arrows show the magnetic field lines and the red arrows show the direction of the strahl beam. Region A contains sunward open magnetic flux, Region B contains closed magnetic flux, Region C contains anti-sunward open magnetic flux, and Region D contains magnetic flux completely disconnected from the Sun. Figure reproduced from Owens & Forsyth (2013).		47
1.12	Gosling reconnection model. The dashed arrows CS1 and CS2 represent the bifurcated current sheet bounding the outflow region. Figure adapted from Gosling et al. (2005a).		48
1.13	1D proton VDF measurements in the reconnection inflow region (top left and bottom right) and outflow region (top right and bottom left). In this event, a pair of counterstreaming beams are clearly resolvable in the outflow region. Figure reproduced from Gosling et al. (2005a)	•	48
1.14	Vector diagram showing the evolution of \mathbf{B} in an Alfvénic structure and the correlation between the magnetic field and velocity fluctuations, $\delta \mathbf{u}$ and $\delta \mathbf{b}$, respectively. θ_0 is the angle between the radial direction, $\hat{\mathbf{R}}$, and the background magnetic field \mathbf{B}_0 . θ_{BR} is the angle between $\hat{\mathbf{R}}$, and the deflected magnetic field \mathbf{B} . Figure reproduced from Matteini et al. (2014)	•	50
1.15	Simplified diagram of the magnetic field geometry of a switchback. Figure reproduced from Kasper et al. (2019).	•	51
1.16	Formation of magnetic switchbacks through interchange reconnection in the corona. Figure reproduced from Fisk & Kasper (2020).		52

1.17	Diagram of the a) magnetic and electric field configuration of a 1-D RCS, with associated inflows and outflows in the b) field line rest frame, and c) neutral line rest frame. Figure reproduced from Owen & Cowley (1987a)	54
1.18	Structure of the reconnected field wedge earthward and tailward of the neutral line at X_N . The RCS is represented by the solid black line at the centre of the figure and \mathbf{B} is represented by the blue arrows. The red arrows represent the tailward inflows from the magnetotail lobes with velocity $\mathbf{v_I}$ in the neutral line rest frame. The reconnection outflow region is shown by the red hatched region and the region occupied by high-energy particles is shown by the green hatched region. Figure adapted from Owen & Cowley (1987a)	577
1.19	Magnetic reconnection configuration with asymmetric inflows in the a) NLRF and b) FLRF. The magnetic and electric field geometry is the same as in the symmetric inflow case. Figure reproduced from Owen & Cowley (1987b)	58
2.1	Solar latitude (top) and heliocentric distance (bottom) of <i>Solar Orbiter</i> during the NMP and EMP. The vertical blue lines mark times where <i>Solar Orbiter</i> performs gravity assist manoeuvers at Venus and Earth. Figure reproduced from Müller et al. (2020)	62
2.2	Location of instruments onboard <i>Solar Orbiter</i> . EPD, MAG, RPW, and SWA are in-situ instruments. EUI, Metis, PHI, SoloHI, SPICE, and STIX are remote sensing instruments. Reproduced from Müller et al. (2020)	62
2.3	Cross-sectional diagram of the PAS EA. The blue line shows the trajectory of a particle through the instrument: 1) The EDS steers particles into the entrance of the EA. 2) The EA filters the incident particles based on their energy per charge. 3) Those with the correct range of energies per charge, determined by the potential difference applied to the EA, can pass through and strike the CEMs in the detector array. Top right: Arrangement of the CEMs in the detector array and their corresponding azimuthal range. Figure reproduced from Owen et al. (2020).	65

3.1	Left: Inflow and outflow beam configuration for a single 1-D current sheet in steady state in the FLRF. The dotted black line represents the current sheet and the blue arrows represent the magnetic field.	
	The red arrows show the inflow beam \mathbf{u}'_{1A} before and after it passes	
	through the current sheet to become beam \mathbf{u}'_{1B} . Similarly, the green	
	arrows show the inflow beam \mathbf{u}_{2B}' before and after it passes through	
	the current sheet to become beam \mathbf{u}'_{2A} . Top right: Proton distri-	
	bution function in Region A, consisting of the isothermal counter-	
	streaming beams \mathbf{u}'_{1A} (red) and \mathbf{u}'_{2A} (green). The black cross repre-	
	sents the net proton bulk velocity and the dashed blue line denote	
	the <i>l</i> and <i>n</i> -components of the beam velocities that result in field-	
	aligned propagation. <i>Bottom right</i> : Proton distribution function in	
	Region B, consisting of the isothermal counterstreaming beams \mathbf{u}'_{1B} (red) and \mathbf{u}'_{2B} (green)	74
3.2	Reconnection geometry for a symmetric outflow region bound by a	
	bifurcated reconnection current sheet in a) real space and b) velocity	
	space, based on the Gosling reconnection model (Gosling et al.,	
	2005a)	78
3.3	a) Overview of the assumed inflow and outflow beam configuration	
	in velocity space for the reconnection geometry shown in Figure	
	3.2. b) Velocity of the inflow Beam 1 before (\mathbf{u}_{1A}^{IT}) and after (\mathbf{u}_{1B}^{IT})	
	passing through current sheet IT, shown in the rest frame of the	
	magnetic field discontinuity at this current sheet. c) Velocity of the inflow Beam 2 before (\mathbf{u}_{2C}^{IB}) and after (\mathbf{u}_{2B}^{IB}) passing through current	
	sheet IB, shown in the rest frame of the magnetic field discontinuity	
	at this current sheet	79
3.4	Graph of the normal component of the outflow beam velocity $u_{1B,n}^{IT}$.,
	(black) and $u_{2B,n}^{IB}$ (blue) against temperature. The dotted, horizon-	
	tal purple lines denote the expected value of $u_{1B,n}^{IT}$ and $u_{2B,n}^{IB}$. The	
	dashed, vertical line denotes the corresponding beam temperature.	86
3.5	Distribution function of the proton beam population in Regions A	
	(top left), B (middle), and C (top right) shown in the field-aligned	
	NLRF. The teal square denotes the velocity of Beam 1, \mathbf{u}'_{1A} in Re-	
	gion A and \mathbf{u}'_{1B} in Region B. The grey circle denotes the velocity of	
	Beam 2, \mathbf{u}'_{2C} in Region C and \mathbf{u}'_{2B} in Region B	87
3.6	1-D cut through the distribution function of the beam population in	
	Region B along the v_{\parallel} axis at $v_{\perp} = \mathbf{u}_{\mathbf{B}}' $. The teal curve is the dis-	
	tribution function of Beam 1 f_{1B} , the grey curve is the distribution	
	function of Beam 2 f_{2B} , and the black curve is the total distribution	
	function $f_B = f_{1B} + f_{2B}$. The vertical, dotted purple lines show the	07
	field-aligned speed of the individual outflow beams, $u'_{1B,\parallel}$ and $u'_{2B,\parallel}$.	87

3.7	Illustration of how the current sheet bifurcation assumptions in the stress balance model can produce an unphysical build-up of plasma at the current sheets IT and IB. Circles <i>a</i> , <i>b</i> , <i>c</i> represent parcels of beam 1 (red) and beam 2 (green). As each parcel enters the outflow region, it catches up with the opposing current sheet without passing through, leading to a build-up of material	. 91
4.1	Diagram showing idealised magnetic field (blue) and bulk velocity (red) time series measurements for each permutation of model θ . a) θ_1 , correlation between B and v on both sides of the window. b) θ_2 , anti-correlation between B and v on both sides of the window. c) θ_3 , correlation when $t \leq t_0$ and anti-correlation when $t > t_0$. d) θ_4 ,	
4.2	anti-correlation when $t \le t_0$ and correlation when $t > t_0$ Location of SWA-PAS on <i>Solar Orbiter</i> and its field of view. The axis in black, green, and blue represent the RTN, PAS, and space-craft (SC) coordinate systems, respectively. In the RTN coordinate system, X_{RTN} corresponds to the R -direction, Y_{RTN} corresponds to the T -direction, and T_{RTN} corresponds to the T -direction (see	. 96
4.3	Section 2.3). Figure reproduced from Fedorov (2020) Selection of the nearest neighbouring sampling points for a grid point X at position (ϕ_X, θ_X, E_X) in the sampling space. Each neighbour 1–8 is assigned a weighting coefficient based on its distance to	. 98
4.4	X in the (ϕ, θ, E) sampling space as a fraction of the total distance between neighbours.	. 99
4.4	Comparison of an artificial dataset consisting of a pair of Maxwellian distribution functions, M1 and M2 (left), and the same distribution functions as observed by PAS after application of the VDF resampling program (right) in the RT (top) and RN-planes (bottom) through $v_N = 0 \text{ km s}^{-1}$ and $v_T = 0 \text{ km s}^{-1}$, respectively.	101
4.5	Combined magnetic field and ground-calculated proton moments for Event 4 in the <i>lmn</i> coordinate system. a) Magnetic field strength with the magnetic field strength in black. b) Proton bulk velocity in the NLRF, with the proton bulk speed in black. In both panels, the $\hat{\bf l}$ -component is red, the $\hat{\bf m}$ is in green, and the $\hat{\bf n}$ -component is in blue. c) Proton bulk density. d) Proton bulk temperature. e) Magnetic pressure P_{mag} , plasma pressure P_{th} , and their sum, the total pressure P_{tot} . The reconnection outflow region is shaded in purple, and the vertical dashed purple lines mark the location of the bifurcated RCS	
4.6	pair, IT and IB	. 104
	same as in Figure 4.5	. 106

4.7	Graph of $u_{1B,n}^{IT}$ (black) and $u_{2B,n}^{IB}$ (blue) as a function of temperature T for Event 4. The dashed purple line denotes the value of $u_{1B,n}^{IT}$, derived in Section 4.4.1, and its corresponding temperature T_{1B} . The dotted purple line denotes the value of $u_{2B,n}^{IB}$, also derived in Section 4.4.1, and its corresponding temperature T_{2B}
4.8	Selected PAS ion VDF measurements at different times during Event 4, presented in the NLRF using the field-aligned coordinate system. Distribution I is the VDF observed in Region A at 06:45:52 UT. Distributions II and III are the VDFs observed in Region B at 06:47:00 and 06:48:00, respectively. Distribution IV is the VDF observed in Region C at 06:49:48 UT. The left column shows the 2-D cut of the VDF in the $\mathbf{v}_{\parallel} - \mathbf{v}_{\perp 1}$ plane, the middle column shows the 2-D cut of the VDF in the $\mathbf{v}_{\parallel} - \mathbf{v}_{\perp 2}$ plane, and the right column shows the 2-D cut of the VDF in the $\mathbf{v}_{\parallel} - \mathbf{v}_{\perp 2}$ plane
4.9	1-D cuts through the reconstructed and observed VDFs shown in Figure 4.8. The solid black curves represent the observed VDF, while the dotted curves represent the reconstructed VDFs describing the reconnection inflow and outflow beam population. The vertical dashed purple lines mark the predicted field-aligned speed of the beams
4.10	Selected PAS ion VDF measurements at different times during Event 1. The figure layout is identical to Figure 4.8. Distribution I is the VDF observed in Region A at 18:30:28 UT. Distributions II and III are the VDFs observed in Region B at 18:35:56 UT and 18:37:44 UT, respectively. Distribution IV and V are observed in Region C at 18:38:48 UT and 18:41:44 UT, respectively
4.11	1-D cuts through the reconstructed and observed VDFs shown in Figure 4.10. The figure layout is identical to Figure 4.9
5.1	Combined magnetic field, proton, and electron strahl PAD time series data for Event 1 in the hybrid MVAB lmn -frame. a) Magnetic field vector with the magnetic field strength in black. b) Proton bulk velocity with the proton bulk speed in black. The average proton bulk velocity $\langle \mathbf{v_p} \rangle$ over this interval has been removed. In both panels, the l -component is in red, the m -component is in green, and the n -component is in blue. c) Proton temperature (left scale, purple) and number density (right scale, gold). d) Alfvén speed. e) 1D proton energy spectrogram. f) Electron strahl PAD for energies > 70 eV. The dashed lines mark the region boundaries identified in the text and numbered at the top of the figure

5.2	Magnetic hodographs and Walén plots for CS0 (07:45:50 – 07:46:20 UT), CS1 (07:46:35 – 07:46:43 UT), and CS2 (07:48:15	
	- 07:48:45 UT) in Event 1. Time progression in the hodographs	
	is represented by the colour of the dots, with earlier times in blue	
	and later times in red. The red, green, and blue dots in the Walén	
	plots represent the R , T , and N -components of the Alfvén velocity	
	${f v_A}$ and the HT frame bulk plasma velocity ${f v_p}-{f v_{HT}}.$ a) ${\it lm}$ -plane	
	hodograph for CS0. b) <i>ln</i> -plane hodograph for CS0. c) <i>lm</i> -plane	
	hodograph for CS1 and CS2. d) <i>ln</i> -plane hodograph for CS1 and	
	CS2. e) Walén plot for CS0. f) Walén plot for CS1. g) Walén plot	
	for CS2	127
5.3	Combined magnetic field and proton time series data for Event 2 in	
	the hybrid MVAB <i>lmn</i> -frame. The figure layout is the same as in	
	Figure 5.1 except for the absence of electron strahl PAD data, which	
	are unavailable for this interval. Panel f) instead shows the signed	100
	magnitude of the alpha-proton velocity difference vector, $v_{\alpha p}$	129
5.4	Magnetic hodographs and Walén plots for CS0 (10:19:05 –	
	10:19:11 UT), CS1 (10:20:50 – 10:21:07 UT), and CS2 (10:21:24 –	
	10:21:28 UT) in Event 2. The figure layout is the same as in Figure	101
	5.2	131
5.5	Combined magnetic field and proton time series data for Event 3	
	in the hybrid MVAB <i>lmn</i> -frame. The figure layout is the same as	100
		132
5.6	Magnetic hodographs and Walén plots for CS0 (10:03:35 –	
	10:03:46 UT), CS1 (10:11:05 – 10:11:10 UT), and CS2 (10:11:41 –	
	10:12:15 UT) in Event 3. The figure layout is the same as in Figure	122
		133
5.7	Feather plot of the B (blue/light green) and $\mathbf{v'_p}$ vectors measured in	
	Event 1 in the ln -plane with the spacecraft trajectory marked by the	
	dark green arrow. The B_m component of B is represented by the colour bar on the right. Overlaid on top is a possible interpretation	
	of the magnetic field configuration of the switchback, shown here	
	by the black arrows. The purple lines mark the assumed configu-	
	ration of the current sheets CS0, CS1, and CS2. The purple stars	
	show the locations where <i>Solar Orbiter</i> crosses the current sheets	135
5.8	Diagram showing possible mechanism by which switchback bound-	100
3.0	ary reconnection can generate a flux rope embedded within a	
	switchback. For visualisation purposes, the figure is not to scale	
	and has been compressed along the Î -axis to show the switchback	
	structure on both sides of the reconnection site. Arrow colours are	
	defined as in Figure 5.7	137

5.9	Simplified diagram of the switchback and reconnection geometry in	
	Event 1, with quantities relevant to the calculation of τ	138

List of Tables

2.1	Measurement ranges of the <i>Solar Orbiter</i> MAG instrument. Table reproduced from Horbury et al. (2020a)	64
3.1	Summary of the properties of the inflow and outflow proton beams in Regions A, B, and C. Velocities and speeds are given in the DRF at IT for beams 1A and 1B, and in the DRF at IB for beams 2B and 2C	85
4.1	Breakdown of algorithm-identified reconnection outflows, sorted by duration	103
4.2	Summary of the properties of the 5 reconnection events shortlisted for stress balance analysis. Γ : magnetic shear angle across the outflow region, R : heliocentric distance from the Sun, $ \mathbf{v}_{SW} $: mean background solar wind speed, $\Delta_{ \mathbf{B} }$: percentage change in magnetic field strength, Δ_n percentage change in proton number density, Δ_T : percentage change in proton temperature, $\Delta_{ \mathbf{u}' }$: percentage change	
	in the NLRF proton bulk speed	103
4.3	Summary of the average magnetic field and solar wind proton bulk properties for Event 4. B : magnetic field in lmn coordinates, $ \mathbf{B} $: magnetic field strength, \mathbf{u}'_p : proton bulk velocity in lmn coordinates,	105
4.4	$ \mathbf{u}'_p $: proton bulk speed, n_p : proton density, T_p : proton temperature. Summary of the average magnetic field and solar wind proton bulk properties for Event 1. Table layout is the same as in Table 4.3	105
4.5	Estimates for the outflow region opening angle γ , outflow region width W , and distance D of <i>Solar Orbiter</i> from the neutral line	
4.6	Summary of the velocity, speed, pitch angle, density, and temperature of Beams 1 and 2 in Regions A, B, and C for all five reconnection events in the dataset	111
5.1	Event 1 <i>lmn</i> -frame basis vectors for CS0 and CS1 + CS2 expressed in RTN coordinates	126
5.2	Event 2 <i>lmn</i> -frame basis vectors for CS0 and CS1 + CS2 expressed in RTN coordinates	129

5.3	Event 3 <i>lmn</i> -frame basis vectors for CS0 and CS1 + CS2 expressed
	in RTN coordinates
5.4	Estimates for the remaining lifetime, τ , of the three switchbacks
	discussed in this paper, and the convection distance, D, travelled by
	the switchbacks before they fully erode away. Λ: switchback width,
	B_{SB} : magnetic field strength in the switchback, B_{out} : magnetic field
	strength in the outflow region, v_{out} : exhaust outflow bulk speed,
	$\langle v_{SW} \rangle$: average solar wind speed

Chapter 1

Introduction

1.1 Fundamentals of plasma physics

Although we do not encounter plasmas commonly in our everyday lives, they are in fact the most common state of matter in the observable universe. On Earth, we often think of plasmas as a man-made occurrence, typically associated with laboratory experiments or nuclear fusion reactors. However, they can also occur in natural phenomenon such as lightning and aurorae. In the astrophysical context, plasmas are ubiquitous. For instance, stars — such as our Sun — are massive spheres of plasma. The Sun also drives flows of plasmas in the form of the solar wind, which permeates the whole of the Solar System.

In this section, I start by defining a plasma and the key parameters that characterise it. I then discuss the various mathematical descriptions of plasmas, focusing on single particle motion, kinetic theory, and magnetohydrodynamic (MHD) theory. Finally, using these ideas, I explain ideal MHD and derive the frozen-in theorem, both key concepts that underpin the large-scale behaviour of the solar wind.

1.1.1 What is a plasma?

A plasma is a state of matter in which the atoms have been ionised, but the plasma remains quasi-neutral at large scales. It consists of negatively-charged electrons, positively-charged ions, and some neutrals (e.g., Chen 2015). The charged particles exhibit collective behaviour and interact with each other through long-range electromagnetic forces. Over large scales, quasi-neutrality is maintained in a plasma because the overall number of positive and negative charges is equal. The thermal motion of the particles induces local charge imbalances, which free electrons move to screen on the scale of the Debye length:

$$\lambda_D = \sqrt{\frac{\varepsilon_0 k_B T_e}{n_e e^2}} \tag{1.1}$$

where ε_0 is the permittivity of free space, k_B is the Boltzmann constant, T_e is the electron temperature, n_e is the electron density, and e is the elementary charge. On length scales $L \gg \lambda_D$, the quasi-neutrality condition is therefore satisfied.

The plasma parameter N_D is defined as the number of electrons within a sphere of radius λ_D , known as the Debye sphere:

$$N_D = \frac{4\pi}{3} n_e \lambda_D^3 \tag{1.2}$$

When $N_D \gg 1$, the number of electrons within the sphere is large and Debye screening is effective in maintaining quasi-neutrality in the plasma. This condition also implies the kinetic energy of the electrons is greater than the electrostatic potential energy between them and the ions, preventing recombination and thus ensuring the plasma remains well-ionised.

If a layer of electrons in a quasi-neutral plasma is displaced relative to the ions, the resulting charge separation induces an electric field in the plasma. As the ions are much heavier than the electrons, they remain stationary with respect to the electrons, which undergo oscillatory motion due to the restoring force exerted by the electric field. The characteristic frequency of this oscillation is the plasma frequency ω_p , defined as:

$$\omega_p = \sqrt{\frac{n_e e^2}{m_e \varepsilon_0}} \tag{1.3}$$

where m_e is the electron mass. If $\omega_p \tau_{coll} \gg 1$, where τ_{coll} is the average time between electron-neutral collisions, then collective behaviour due to electromagnetic forces dominate over collisional effects and the plasma can be considered collisionless.

The Debye length λ_D , the plasma parameter N_D , and the plasma frequency ω_p , thus combine to give a pair of conditions for an ideal plasma:

$$L \gg \lambda_D \gg n_e^{-1/3} \tag{1.4}$$

$$\omega_p \tau_{coll} \gg 1$$
 (1.5)

which state that an ideal plasma is defined as one that is quasi-neutral, well-ionised, and collisionless.

1.1.2 Single particle motion and drift motion

In an ideal plasma, the most significant force acting on the particles is the Lorentz force:

$$\mathbf{F_L} = m\frac{d\mathbf{v}}{dt} = q(\mathbf{E} + \mathbf{v} \times \mathbf{B}) \tag{1.6}$$

where m is the particle mass, q is the particle charge, \mathbf{v} is the particle velocity, \mathbf{E} is the electric field, and \mathbf{B} is the magnetic field. The single particle motion description of plasmas characterises the trajectories of each individual charged particle in these electromagnetic fields by solving their equations of motion.

Gyromotion in a uniform magnetic field

In the simplest case of $\mathbf{E} = 0$ and uniform \mathbf{B} , the force exerted on the particle is perpendicular to both \mathbf{v} and \mathbf{B} . This causes the particle to execute circular motion (gyromotion) in the plane perpendicular to \mathbf{B} about a guiding centre. The angular frequency of the circular motion (gyrofrequency) is:

$$\omega_c = \frac{qB}{m} \tag{1.7}$$

and the radius of the orbit (gyroradius) is:

$$r_c = \frac{v_\perp}{|\omega_c|} = \frac{mv_\perp}{|q|B} \tag{1.8}$$

where v_{\perp} is the component of the particle's velocity perpendicular to the magnetic field and B is the magnetic field strength. As the force exerted on the particle is perpendicular to its direction of motion, the magnetic field does no work on the particle and its kinetic energy remains constant. Furthermore, the field-aligned component of the particle velocity, v_{\parallel} , does not change. If $v_{\parallel}=0$ initially, the particle will continue to execute gyromotion about a stationary guiding centre. Conversely, if $v_{\parallel} \neq 0$, the guiding centre moves along the magnetic field line with constant velocity v_{\parallel} , and the particle will follow a helical trajectory along the field line. The direction of gyration depends on the charge of the particle: positively-charged ions will gyrate in the opposite direction to negatively-charged electrons.

Drift motion in a uniform electric field

When a uniform ${\bf E}$ is introduced to the system, an additional electric field force ${\bf F}_{\bf E}=q{\bf E}$ acts on the particle. The component of this force parallel to the magnetic field accelerates the particle (and its guiding centre) along the field line, but otherwise does not alter the gyromotion. However, the perpendicular component of this force causes the guiding centre to drift across field lines with velocity:

$$\mathbf{v_E} = \frac{\mathbf{E} \times \mathbf{B}}{B^2} \tag{1.9}$$

in the direction perpendicular to \mathbf{E} and \mathbf{B} , as shown in Figure 1.1. This $\mathbf{E} \times \mathbf{B}$ drift is independent of both the particle mass and charge. Therefore, ions and electrons drift together with the same speed v_E , preventing the generation of drift currents and charge separation through this mechanism.

Drift motion due to external forces and non-uniform fields

Equation 1.9 can be generalised for any uniform and constant force \mathbf{F} by substituting in $\mathbf{E} = \mathbf{F}/q$:

$$\mathbf{v_D} = \frac{\mathbf{F} \times \mathbf{B}}{qB^2} \tag{1.10}$$

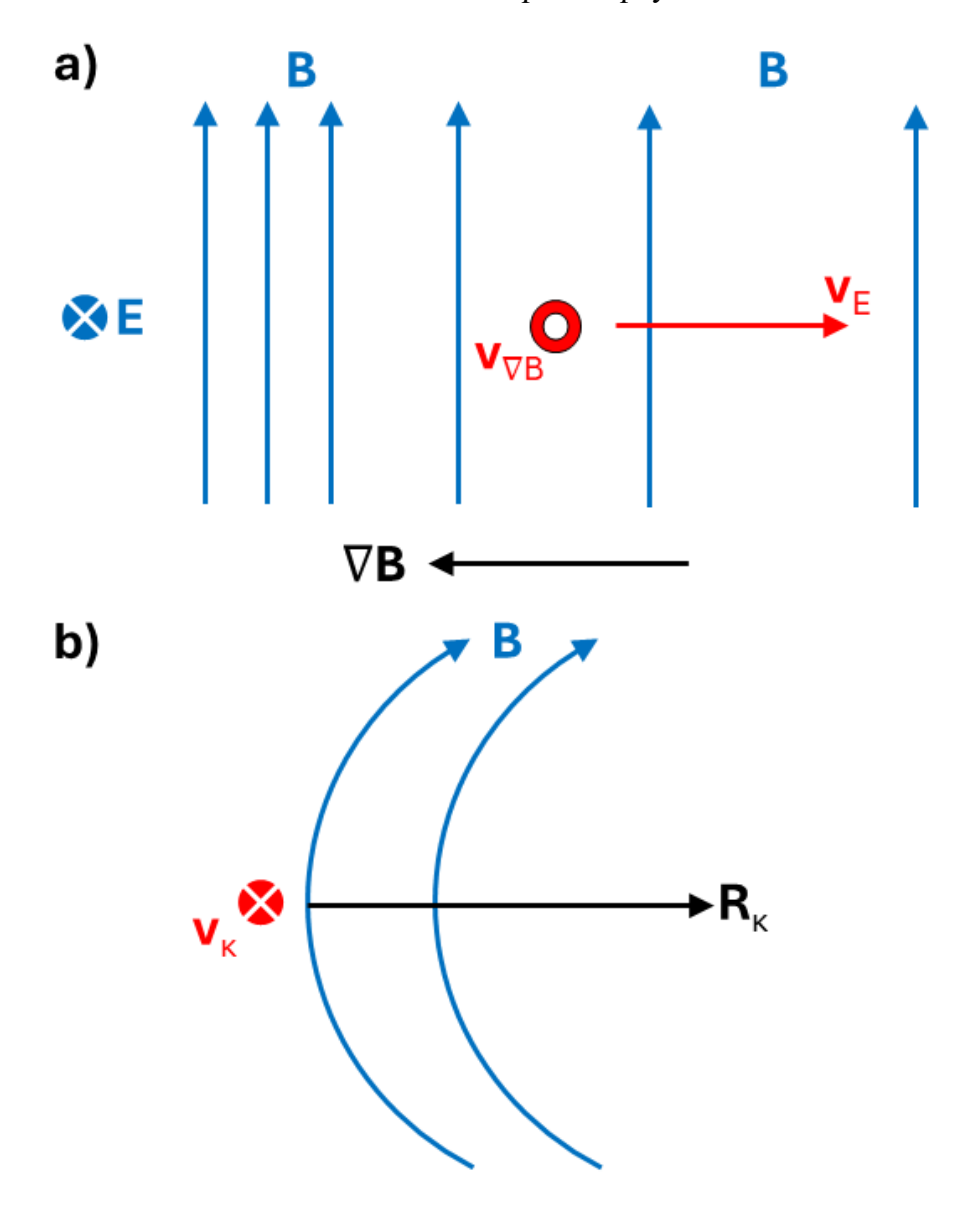


Figure 1.1: Direction of the drift velocity of a positively charged particle due to the a) $\mathbf{E} \times \mathbf{B}$ drift and magnetic field gradient drift, and b) the curvature drift.

If \mathbf{F} is charge-independent, $\mathbf{v_D}$ becomes charge-dependent and will induce drift currents and charge separation within the plasma. For completeness, it is noted that a non-uniform \mathbf{B} can also induce drift motion associated with the curvature of the magnetic field and gradients in the magnetic field strength. The curvature drift velocity is given by:

$$\mathbf{v}_{\kappa} = -\frac{mv_{\parallel}^2}{qR_{\kappa}^2} \frac{\mathbf{R}_{\kappa} \times \mathbf{B}}{B^2}$$
 (1.11)

and the gradient drift velocity is given by:

$$\mathbf{v}_{\nabla \mathbf{B}} = \frac{1}{2} \frac{m v_{\perp}^2}{q B^3} (\mathbf{B} \times \nabla \mathbf{B})$$
 (1.12)

where v_{\parallel} is the component of the particle's velocity parallel to ${\bf B}$, ${\bf R}_{\kappa}$ is the radius of curvature, and $\nabla {\bf B}$ is the magnetic field gradient. Unlike the ${\bf E} \times {\bf B}$ drift, both the direction of ${\bf v}_{\kappa}$ and ${\bf v}_{\nabla {\bf B}}$ are dependent on the sign of q. Figure 1.1 shows the drift direction of an ion under the effects of the curvature and gradient drifts. In this configuration, the curvature drift is directed into the plane, while the gradient drift is directed out of the plane. For negatively charged particles, both drift directions are reversed. As a result, positively charged and negatively charged particles drift in opposite directions, which leads to charge separation and the generation of an associated drift current.

Diamagnetic drift motion

Another important drift mechanism is the diamagnetic drift, which arises from pressure gradients ∇P in the plasma, where $P = nk_BT$ (e.g., Chen 2015). Figure 1.2 shows an isothermal plasma with $\mathbf{E} = 0$, uniform \mathbf{B} , and a positive density gradient ∇n to the left. In the absence of an electric field, the positive ions gyrate in the clockwise direction about their guiding centres without experiencing an $\mathbf{E} \times \mathbf{B}$ drift. Within any fluid parcel, there are more downward-moving ions than there are upward-moving ones due to the density gradient, resulting in a downward net flow of ions with a diamagnetic drift velocity:

$$\mathbf{v_{DM}} = -\frac{\nabla P \times \mathbf{B}}{qnB^2} \tag{1.13}$$

The charge dependence of v_{DM} means electrons drift in the opposite direction to the ions, thus generating a diamagnetic current:

$$\mathbf{J}_{\mathbf{DM}} = -\frac{\nabla P \times \mathbf{B}}{R^2} \tag{1.14}$$

This current, in turn, induces a magnetic field that opposes the external magnetic field ${\bf B}$ and decreases the magnetic field strength in the plasma. Unlike the ${\bf E}\times{\bf B}$ drift, the diamagnetic drift is not caused by the motion of the guiding centres of the individual particles, but is instead a consequence of the macroscopic fluid-like behaviour of the plasma.

Overall, the motion of individual particles within an external magnetic and electric field can be treated as a superposition of gyromotion and drift motion. In order to obtain a complete and self-consistent description of the plasma using the single particle motion approach, the coupled set of equations of motion for each particle in the plasma must be solved. However, an exact, analytical solution to such a system is not possible for an arbitrary **E** and **B**. Instead, the state of a plasma can be described using kinetic or magnetohydrodynamic (MHD) theory, which I briefly describe in the following two sections.

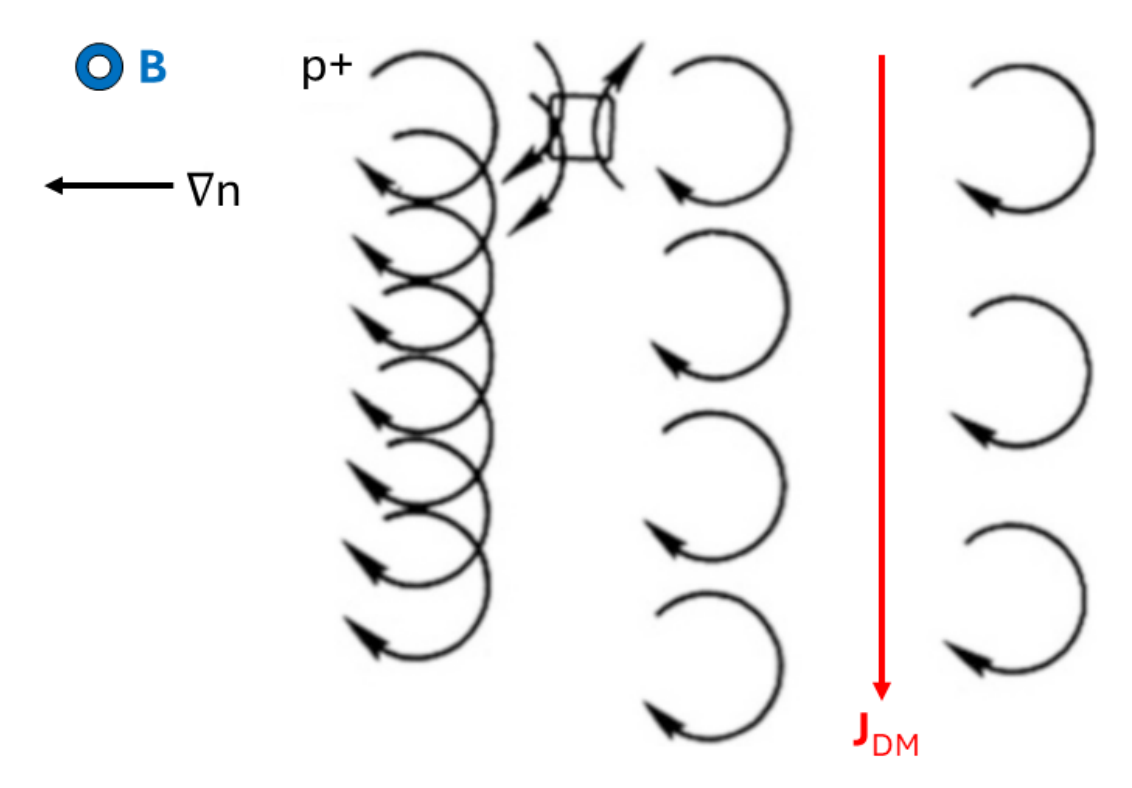


Figure 1.2: Diamagnetic current in an isothermal plasma. In this configuration, positive ions gyrate in the clockwise direction. Due to the density gradient, there is a net flow of ions downwards generating a diamagnetic current J_{DM} (red arrow). Figure adapted from Chen (2015).

1.1.3 Kinetic theory

Kinetic theory is a statistical description of the collective behaviour of particles in plasmas (e.g., Boyd & Sanderson 2003; Chen 2015). At its heart are the particle distribution functions $f_s(\mathbf{r}, \mathbf{v}, t)$, where s is the particle species label, \mathbf{r} is the position vector, \mathbf{v} is the velocity vector, and t is time. The number of particles of species s in a 6-D phase space volume element $d^3\mathbf{r}d^3\mathbf{v}$ centred around the phase space coordinates (\mathbf{r}, \mathbf{v}) at time t is $\delta N(\mathbf{r}, \mathbf{v}, t) = f_s(\mathbf{r}, \mathbf{v}, t)d^3\mathbf{r}d^3\mathbf{v}$.

The evolution of $f_s(\mathbf{r}, \mathbf{v}, t)$ is governed by the Boltzmann equation:

$$\frac{\partial f_s}{\partial t} + \mathbf{v} \cdot \frac{\partial f_s}{\partial \mathbf{r}} + \mathbf{a} \cdot \frac{\partial f_s}{\partial \mathbf{v}} = \left(\frac{\partial f_s}{\partial t}\right)_{coll}$$
(1.15)

where \mathbf{a} is the acceleration due to macroscopic forces and the term on the right-hand side of this equation describes the change in $f_s(\mathbf{r}, \mathbf{v}, t)$ due to collisions. In many space plasmas, which are often assumed to be collisionless, the collisional term is neglected. Under this assumption, substituting Equation 1.6 for \mathbf{a} in Equation 1.15 leads to:

$$\frac{\partial f_s}{\partial t} + \mathbf{v} \cdot \frac{\partial f_s}{\partial \mathbf{r}} + \frac{q_s}{m_s} (\mathbf{E} + \mathbf{v} \times \mathbf{B}) \cdot \frac{\partial f_s}{\partial \mathbf{v}} = 0 \tag{1.16}$$

This special case of the Boltzmann equation is known as the Vlasov equation. To obtain a complete and self-consistent description of the plasma, the evolution of $f_s(\mathbf{r}, \mathbf{v}, t)$ must be linked to the macroscopic magnetic and electric fields through Maxwell's equations:

$$\nabla \cdot \mathbf{E} = \frac{\rho_q}{\varepsilon_0} \tag{1.17}$$

$$\nabla \cdot \mathbf{B} = 0 \tag{1.18}$$

$$\nabla \times \mathbf{E} = -\frac{\partial \mathbf{B}}{\partial t} \tag{1.19}$$

$$\nabla \times \mathbf{B} = \mu_0 \left(\mathbf{J} + \varepsilon_0 \frac{\partial \mathbf{E}}{\partial t} \right) \tag{1.20}$$

where ρ_q is the total charge density, μ_0 is the permeability of free space, and ${\bf J}$ is the total current density. If the plasma is non-relativistic and high frequency fluctuations are neglected, as will be true for the cases discussed in this thesis, the displacement current term $\varepsilon_0 \frac{\partial {\bf E}}{\partial t}$ term in Ampére's Law (Equation 1.20) can be neglected.

Single particle motion (see Section 1.1.2) and kinetic theory are both microscopic descriptions of plasmas, with the former focusing on the individual behaviour and the latter on the collective behaviour of the constituent particles. In the next section, I introduce MHD theory which is instead a macroscopic description of plasmas that focuses on its fluid properties.

1.1.4 Magnetohydrodynamics

In MHD theory, plasmas are treated as a single, continuous fluid with no distinction made between the particle species (e.g., Boyd & Sanderson 2003; Chen 2015). Their fluid bulk parameters are derived by taking the velocity moments of $f_s(\mathbf{r}, \mathbf{v}, t)$. The zeroth order moment is associated with the number density n_s :

$$n_s = \int f_s(\mathbf{r}, \mathbf{v}, t) d^3 \mathbf{v}$$
 (1.21)

the first order moment is associated with the bulk velocity \mathbf{u}_s :

$$\mathbf{u_s} = \frac{1}{n_s} \int \mathbf{v} f_s(\mathbf{r}, \mathbf{v}, t) d^3 \mathbf{v}$$
 (1.22)

and the second order moment is associated with the pressure tensor P_s :

$$\mathbf{P_s} = m_s \int (\mathbf{v} - \mathbf{u_s})(\mathbf{v} - \mathbf{u_s}) f_s(\mathbf{r}, \mathbf{v}, t) d^3 \mathbf{v}$$
 (1.23)

Similarly, the MHD fluid equations are also derived by taking moments, this time of the Vlasov equation (Equation 1.16). The zeroth and first moments lead to the mass continuity equation:

$$\frac{\partial \rho}{\partial t} + \nabla \cdot (\rho \mathbf{u}) = 0, \tag{1.24}$$

and the momentum conservation equation, respectively:

$$\rho\left(\frac{\partial \mathbf{u}}{\partial t} + (\mathbf{u} \cdot \nabla)\mathbf{u}\right) = -\nabla \cdot \mathbf{P} + \mathbf{J} \times \mathbf{B},\tag{1.25}$$

where ρ is the mass density. If the plasma pressure is isotropic, it can be treated as a scalar quantity P and $\nabla \cdot \mathbf{P}$ simplifies to ∇P . Additionally, an equation of state describing the conservation of energy is needed to close out the MHD fluid equations. For an adiabatic plasma, this is:

$$\frac{P}{\rho^{\gamma}} = const. \tag{1.26}$$

where $\gamma = 5/3$ is the ratio of specific heats.

The plasma is treated as a quasi-neutral fluid where $n_i \simeq n_e$. Consequently, Gauss' Law (Equation 1.17) reduces to $\nabla \cdot \mathbf{E} = 0$ and hence, cannot be used to calculate \mathbf{E} . Instead, the electric field is calculated using the generalised Ohm's law, which is derived from the electron momentum equation:

$$\mathbf{E} = -\mathbf{u} \times \mathbf{B} + \frac{1}{en_e} (\mathbf{J} \times \mathbf{B}) + \frac{1}{en_e} \nabla P_e + \frac{m_e}{e} \left(\frac{\partial \mathbf{J}}{\partial t} \right) + \frac{\mathbf{J}}{\sigma}$$
(1.27)

where σ is the electrical conductivity. The first term on the right-hand side is the convection electric field due to the bulk plasma flow, the second term is the Hall field due to differential flow between ions and electrons, the third term is the ambipolar electric field due to electron pressure gradients, the fourth term is the electron inertia term, and the fifth term is the resistive term. Under steady-state conditions, and on spatial and temporal scales larger than the ion gyroradius and gyroperiod, the generalised Ohm's law simplifies to:

$$\mathbf{E} = -\mathbf{u} \times \mathbf{B} + \frac{\mathbf{J}}{\sigma} \tag{1.28}$$

Equation 1.28 can be substituted into Faraday's Law (Equation 1.19) to get:

$$\frac{\partial \mathbf{B}}{\partial t} = \nabla \times (\mathbf{u} \times \mathbf{B}) - \frac{1}{\sigma} (\nabla \times \mathbf{J}) \tag{1.29}$$

Further substitution of Equation 1.20 into this equation yields the magnetic induction equation, which describes the time evolution of a magnetic field in a plasma:

$$\frac{\partial \mathbf{B}}{\partial t} = \nabla \times (\mathbf{u} \times \mathbf{B}) + \eta \nabla^2 \mathbf{B} \tag{1.30}$$

where $\eta = 1/\mu_0 \sigma$ is the magnetic diffusivity. The $\nabla \times (\mathbf{u} \times \mathbf{B})$ term represents the convection of the magnetic field with the bulk plasma flow, while the $\eta \nabla^2 \mathbf{B}$ term

represents the diffusion of the magnetic field through the plasma.

The behaviour of the plasma and the magnetic field depends on the relative size of the convection and diffusion terms in Equation 1.30. Using simple scale analysis arguments on variations over length scale L with characteristic velocity U, the convection and diffusion terms can be re-written as:

$$\nabla \times (\mathbf{u} \times \mathbf{B}) \to \frac{UB}{L} \tag{1.31}$$

$$\eta \nabla^2 \mathbf{B} \to \eta \frac{B}{L^2} \tag{1.32}$$

The magnetic Reynolds number R_M is defined as the ratio between Equations 1.31 and 1.32:

$$R_M = \frac{UL}{\eta} = \mu_0 \sigma UL \tag{1.33}$$

If $R_M \gg 1$, the convection term dominates, whereas if $R_M \ll 1$, the diffusion term dominates. Another useful parameter used to characterise a plasma is the plasma β , defined as the ratio between the plasma thermal pressure $P = nk_BT$ and the magnetic pressure $P_{mag} = B^2/2\mu_0$:

$$\beta = \frac{P}{P_{mag}} = \frac{2\mu_0 n k_B T}{B^2} \tag{1.34}$$

This parameter determines whether the behaviour of the plasma and magnetic field is dominated by plasma pressure or magnetic forces. If $\beta \gg 1$, the plasma pressure forces dominate and the magnetic field is convected by the plasma flow. If $\beta \ll 1$, the magnetic forces dominate and the plasma flow is controlled by the magnetic field.

1.1.5 Ideal MHD and the frozen-in theorem

In plasmas where the conductivity, characteristic velocity, or length scale are large, $R_M \gg 1$ and Equation 1.30 reduces to just the convection term:

$$\frac{\partial \mathbf{B}}{\partial t} = \nabla \times (\mathbf{u} \times \mathbf{B}) \tag{1.35}$$

which is known as the ideal MHD limit. This limit applies for most space plasmas, including the solar wind, on length scales greater than the ion gyroradius and timescales longer than the ion gyroperiod (e.g., Baumjohann & Treumann 2022). One of the most important consequences of ideal MHD is the frozen-in theorem (e.g., Boyd & Sanderson 2003).

In order to better understand its implications, consider a magnetic flux tube with the geometry shown in Figure 1.3. A surface S_1 in the plasma is bound by the closed loop l_1 at time t. As the plasma moves with bulk velocity \mathbf{u} , the surface elements making up S_1 will move along with the plasma to form a new surface S_2 bound by the loop l_2 , at time $t + \Delta t$. The line elements $d\mathbf{l}$ of both loops are oriented

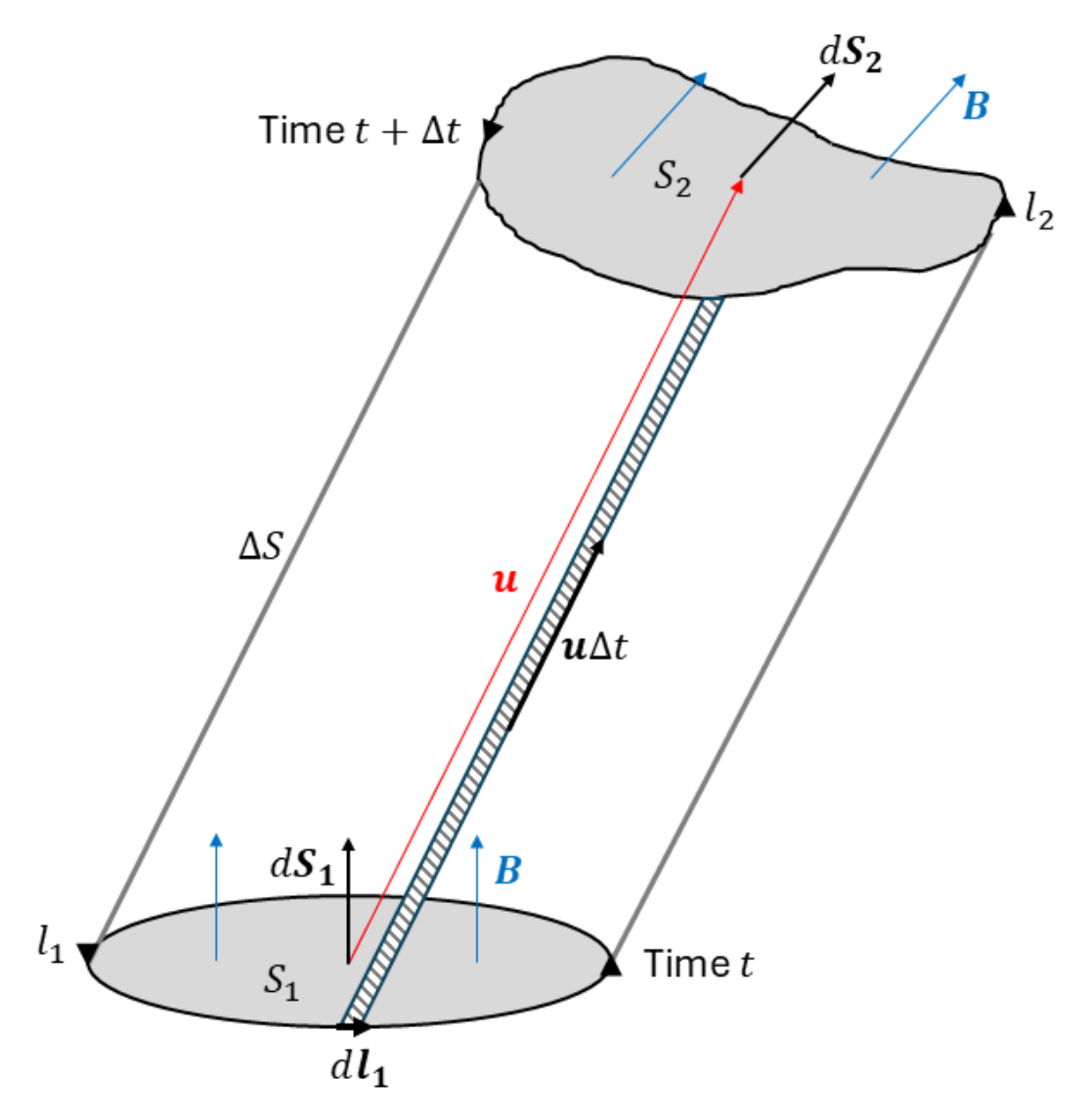


Figure 1.3: Magnetic flux tube formed by surfaces S_1 , S_2 , and ΔS . The latter surface is parallel to the magnetic field **B** linking S_1 and S_2 at all points. In the ideal MHD limit, the magnetic flux passing through this tube is time-invariant leading to the frozen-in theorem.

such that they are not parallel to the magnetic field **B** linking these two surfaces at any point, i.e., $\mathbf{B} \times d\mathbf{l} \neq 0$. The connecting surface ΔS between S_1 and S_2 is parallel to **B** within the flux tube at all points.

The $\nabla \cdot \mathbf{B} = 0$ condition states that the change in magnetic flux through the flux tube is zero. Since ΔS is parallel to \mathbf{B} everywhere, no magnetic flux passes through the walls of the flux tube. As a result, the flux entering the flux tube through S_1 must be equal to the flux exiting through S_2 . By applying the divergence theorem and taking the time derivative of ϕ , it can be shown that:

$$\frac{d\phi}{dt} = \int_{S_1} \left(\frac{\partial \mathbf{B}(t)}{\partial t} - \nabla \times (\mathbf{u} \times \mathbf{B}) \right) \cdot d\mathbf{S_1} = 0, \tag{1.36}$$

This equation shows that in the ideal MHD limit, the magnetic flux through a closed loop co-moving with a perfectly conducting plasma is time-invariant. Consequently, the flux through S_1 and S_2 remains constant as the flux tube evolves with the plasma. Furthermore, to ensure $\nabla \cdot \mathbf{B} = 0$ is always satisfied, the flux through the flux tube walls must be zero at all times. Consequently, the magnetic field topology inside the flux tube does not change, regardless of any variations in the plasma flow or flux tube geometry.

This result is known as the frozen-in theorem, which states that in a perfectly conducting plasma where $R_M \to \infty$ (if $\sigma \to \infty$ or equivalently, $\eta \to 0$), the magnetic field lines are embedded into the bulk plasma flow. Since $R_M \gg 1$ in the solar wind, both ideal MHD and the frozen-in theorem apply. A key implication of the frozen-in theorem is that plasmas bound to different magnetic fields cannot mix and are instead separated by a current sheet. However, if the current sheet thickness becomes comparable to the ion gyroradius, the frozen-in theorem breaks down and allows non-ideal MHD processes such as magnetic reconnection to occur.

1.2 Magnetic reconnection

Magnetic reconnection is a fundamental energy conversion process in plasmas, converting magnetic energy into kinetic and thermal energy through a change in magnetic field topology across a thin current sheet. In the context of the heliosphere, it is a key driver of solar wind heating and acceleration, and also plays an important role in the formation of CMEs and solar flares. I begin this section by introducing the physics behind magnetic reconnection with the Sweet-Parker model (Parker, 1957; Sweet, 1958), before discussing the Petschek reconnection model (Petschek, 1964).

1.2.1 Sweet-Parker model

In the ideal MHD limit, $R_M \gg 1$ and the frozen-in theorem holds (see Section 1.1.5). As a consequence of the frozen-in theorem, a current sheet forms at the boundary between two regions of opposing magnetic flux, where $\nabla \times \mathbf{B} \neq 0$. When a plasma inflow with bulk velocity \mathbf{u}_i is introduced that advects magnetic flux towards the current sheet from both sides, the plasma and magnetic field in the immediate vicinity of the current sheet is compressed. This leads to a reduction in the current sheet thickness. When the current sheet thickness approaches the ion gyroradius, the previously neglected terms in the generalised Ohm's law (Equation 1.27) become relevant and contribute to an increase in the magnetic diffusivity η (e.g., Boyd & Sanderson 2003; Baumjohann & Treumann 2022). Given the small length scale L of the current sheet and increase in η , Equation 1.33 suggests that R_M is locally small near the current sheet. In plasmas where $R_M \ll 1$, the diffusion term of the magnetic induction equation (Equation 1.30) dominates. In this limit, a diffusion region forms in the current sheet where ideal MHD and the frozen-in theorem break down. Here, plasmas can decouple from the magnetic field and mix, thereby setting up the prerequisite conditions for magnetic reconnection to occur.

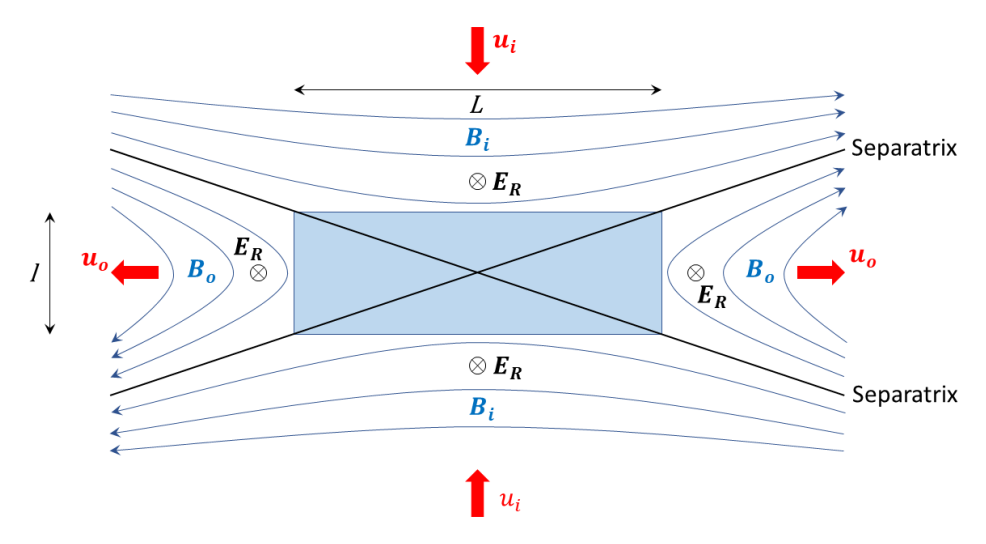


Figure 1.4: Sweet-Parker reconnection model. Black lines represent the separatrices separating the inflow and outflow regions, the blue box represents the diffusion region, and $\mathbf{E_R}$ is the reconnection electric field. The reconnection inflow $\mathbf{u_i}$ from each side carries opposing magnetic flux together, which are separated by a current sheet. If R_M is sufficiently small, a diffusion region is formed inside the current sheet and the magnetic field 'reconnects' across it. Magnetic tension in the reconnected field lines accelerates the reconnection outflow $\mathbf{u_o}$, which re-freezes into the reconnected magnetic field and carries it out of the diffusion region.

Inside the diffusion region, the magnetic field lines 'break' and 'reconnect' across the reconnection current sheet (RCS) to form the newly reconnected magnetic field. Although it is more intuitive to think of the field lines as 'breaking' in the diffusion region, this is not strictly true as it would violate the $\nabla \cdot \mathbf{B} = 0$ condition and imply the formation of magnetic monopoles. Material cannot flow indefinitely into the diffusion region, and plasma is eventually ejected out along the RCS as reconnection outflows. As the reconnected field and outflows emerge from the diffusion region, ideal MHD conditions are restored and the magnetic field re-freezes into the plasma. Magnetic tension in the highly kinked reconnected field lines then accelerate the outflow jet and act to straighten the field line.

Figure 1.4 shows the configuration of a reconnecting current sheet (RCS) in the Sweet-Parker model (Parker, 1957; Sweet, 1958). The diffusion region, represented by the blue box, has length L and width l. The inflow and outflow regions are separated by a pair of separatrices that intersect at the magnetic X-point. Assuming the diffusion region is in steady-state, contains no sources or sinks of plasma, and that the plasma flows are incompressible, the mass continuity condition (Equation 1.24) reduces to $\nabla \cdot \mathbf{u} = 0$. From the divergence theorem, the volume integral over a diffusion region with volume V_d and surface area A_d is:

$$\int_{V_d} (\nabla \cdot \mathbf{u}) dV = \oint_{A_d} \mathbf{u} \cdot d\mathbf{S} = 0$$
 (1.37)

which leads to the following expression when the surface integral is expanded out:

$$u_i L = u_o l \tag{1.38}$$

where u_o is the reconnection outflow speed. By the same reasoning, since $\nabla \cdot \mathbf{B} = 0$,

$$B_i l = B_o L \tag{1.39}$$

where B_i and B_o are the magnetic field strength in the inflow and outflow region, respectively. In the Sweet-Parker model, the aspect ratio of the diffusion region is assumed to be large such that $L \gg l$. Hence, Equations 1.38 and 1.39 imply that $u_o \gg u_i$ and $B_o \ll B_i$. Since ideal MHD applies outside the diffusion region, the conductivity of the plasma is large $(\sigma \to \infty)$, so the simplified Ohm's Law (Equation 1.28) reduces to $\mathbf{E} = -\mathbf{u} \times \mathbf{B}$. Under steady-state conditions, the reconnection electric field, $\mathbf{E_R}$, is assumed to be uniform (e.g., Hughes 1995; Priest & Forbes 2007):

$$|\mathbf{E}_{\mathbf{R}}| = u_i B_i = u_o B_o \tag{1.40}$$

The electromagnetic energy flux S, given by the Poynting vector, and the kinetic energy flux K transported into the diffusion region are:

$$S_i = \frac{u_i B_i^2}{\mu_0} \tag{1.41}$$

$$K_i = \frac{1}{2}\rho u_i^3 \tag{1.42}$$

The equations for the outgoing energy fluxes have similar form, except with subscripts o replacing i. By energy conservation, the total energy inflow \mathcal{E}_i along L must be equal to the total energy outflow \mathcal{E}_o along l:

$$\mathcal{E}_i = 2Ldu_i \left(\frac{B_i^2}{\mu_0} + \frac{1}{2}\rho u_i^2\right) \tag{1.43}$$

$$\mathscr{E}_0 = 2ldu_o \left(\frac{B_o^2}{\mu_0} + \frac{1}{2}\rho u_o^2 \right) \tag{1.44}$$

where d is the diffusion region depth. Equating these two expressions results in the following equation for u_0 :

$$u_o = \sqrt{\frac{2B_i^2}{\rho \mu_0}} = \sqrt{2}V_{A,i} \tag{1.45}$$

which states that the reconnection outflow speed is on the same order of magnitude as the Alfvén speed in the inflow region $V_{A,i}$.

If $R_M = 1$ defines the scale length at which the plasma transition from the ideal

MHD to diffusive regime, Equation 1.33 leads to this expression for the upper limit of l:

$$l = \frac{1}{u_i \mu_0 \sigma} \tag{1.46}$$

Substituting this equation and Equation 1.45 into Equation 1.38 yields:

$$u_i = 2^{\frac{1}{4}} \sqrt{\frac{V_{A,i}}{L\mu_0 \sigma}} = \frac{2^{1/4}}{\sqrt{S}} V_{A,i}$$
 (1.47)

where $S = \mu_0 \sigma V_{A,i} L$ is the Lundquist number. The Sweet-Parker reconnection rate r_{SP} is given by normalising u_i to $V_{A,i}$:

$$r_{SP} = \frac{u_i}{V_{A,i}} = \sqrt{\frac{\sqrt{2}}{S}} = \frac{2^{1/4}}{\sqrt{S}}$$
 (1.48)

For typical conditions in the solar corona: $L \sim 10^4$ km, $u_i \sim 10^{-2}$ km s⁻¹, and $V_{A,i} \sim 10^2$ km s⁻¹, the reconnection rate is $r_{SP} \sim 10^{-4}$ and the characteristic reconnection timescale $\tau_{SP} = L/u_i$ is approximately 10^6 s, or about 11 days. This rate is too slow to account for solar flare generation in the corona, which is observed to occur over timescales of a few minutes.

1.2.2 Petschek model

Equations 1.47 and 1.48 show that the inflow speed — and hence the reconnection rate — depends on the Lundquist number, which in turn depends on the geometry of the diffusion region. Since the Sweet-Parker model assumes a high aspect ratio $(L\gg l)$ for the diffusion region, S is large resulting in a low inflow velocity and reconnection rate. Additionally, this model requires that all plasma undergoing reconnection pass through the diffusion region, further restricting the reconnection rate.

Figure 1.5 shows the Petschek reconnection model, an extension of the Sweet-Parker model that addresses the problem of slow reconnection rates (Petschek, 1964). In this model, *L* is much reduced and the diffusion region is smaller, which enables an increased inflow speed and reconnection rate. The reconnection outflow is bounded by a pair of standing slow mode shocks, SS1 and SS2, that heat and accelerate the plasma inflow as it crosses into the outflow region. In contrast to the Sweet-Parker model, the majority of the plasma energisation in the Petschek model occurs at these shocks rather than the diffusion region (e.g., Priest & Forbes 2007). As a result, Petschek reconnection can process a greater amount of plasma and sustain higher reconnection rates than Sweet-Parker reconnection, despite having a smaller diffusion region.

Heating of the plasma at the shocks increases the plasma pressure inside the outflow region and sets up a pressure gradient across its boundary. This generates

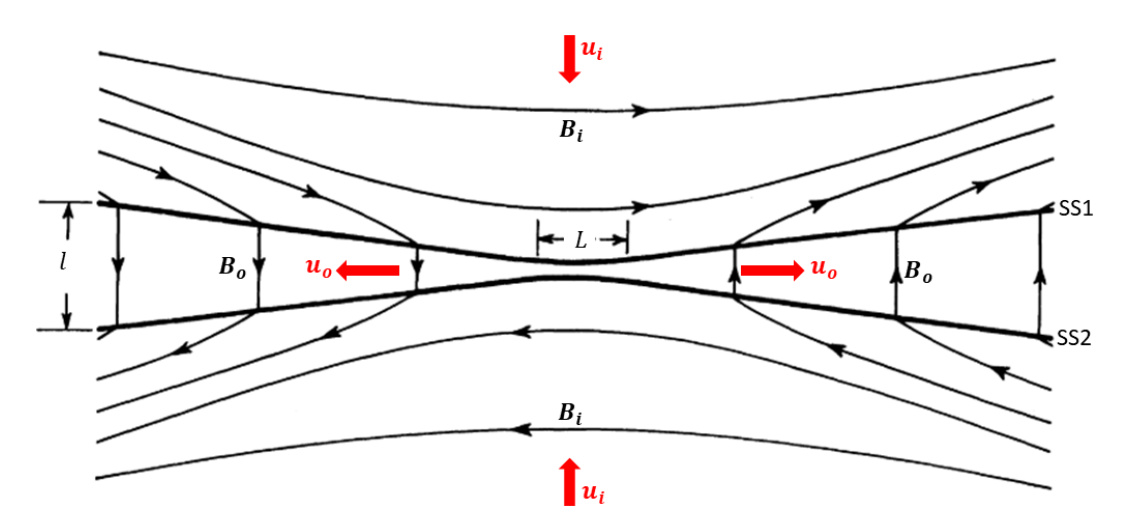


Figure 1.5: Petschek reconnection model. The thick black lines, labelled SS1 and SS2, represent the standing slow mode shocks bounding the reconnection outflow. Figure adapted from Petschek (1964).

a diamagnetic current (Equation 1.14), which induces a magnetic field that reduces the magnetic field strength within the outflow region. This reduction in magnetic pressure counteracts the increase in plasma pressure, ensuring the reconnection outflow structure remains in pressure balance. Since the component of the magnetic field normal to the shock must remain constant to satisfy the $\nabla \cdot \mathbf{B} = 0$ condition, the tangential component of \mathbf{B} has to decrease. Consequently, the RCS bifurcates into a pair of current sheets that may be present alongside slow mode shocks in the reconnection outflow region. Although reconnection outflows with bifurcated RCS are frequently observed in the solar wind (Gosling et al., 2005a; Gosling & Szabo, 2008; Mistry et al., 2015), relatively few examples exhibit signatures of slow mode shocks (Zhou et al., 2018; Duan et al., 2023).

1.3 The heliosphere

The heliosphere is the region of space influenced by the Sun and the solar wind, which encompasses the entire solar system. It also contains a large-scale magnetic field system that couples the Sun and the solar wind to the various bodies within the solar system. In this section, I provide an overview of the key components of the heliosphere, namely the Sun, solar wind, and heliospheric magnetic field (HMF).

1.3.1 The Sun

The Sun is the host star of the solar system and the main source of plasma and magnetic fields in the heliosphere. It is a main sequence star, approximately 4.6 billion years old, with radius $R_{\odot} = 7.0 \times 10^8$ m and mass $M_{\odot} = 2.0 \times 10^{30}$ kg. Figure 1.6 shows the structure of the solar interior, consisting of the core, radiative zone, and convective zone; as well as the solar atmosphere, consisting of the photosphere, chromosphere, and corona (e.g., Priest 1995).

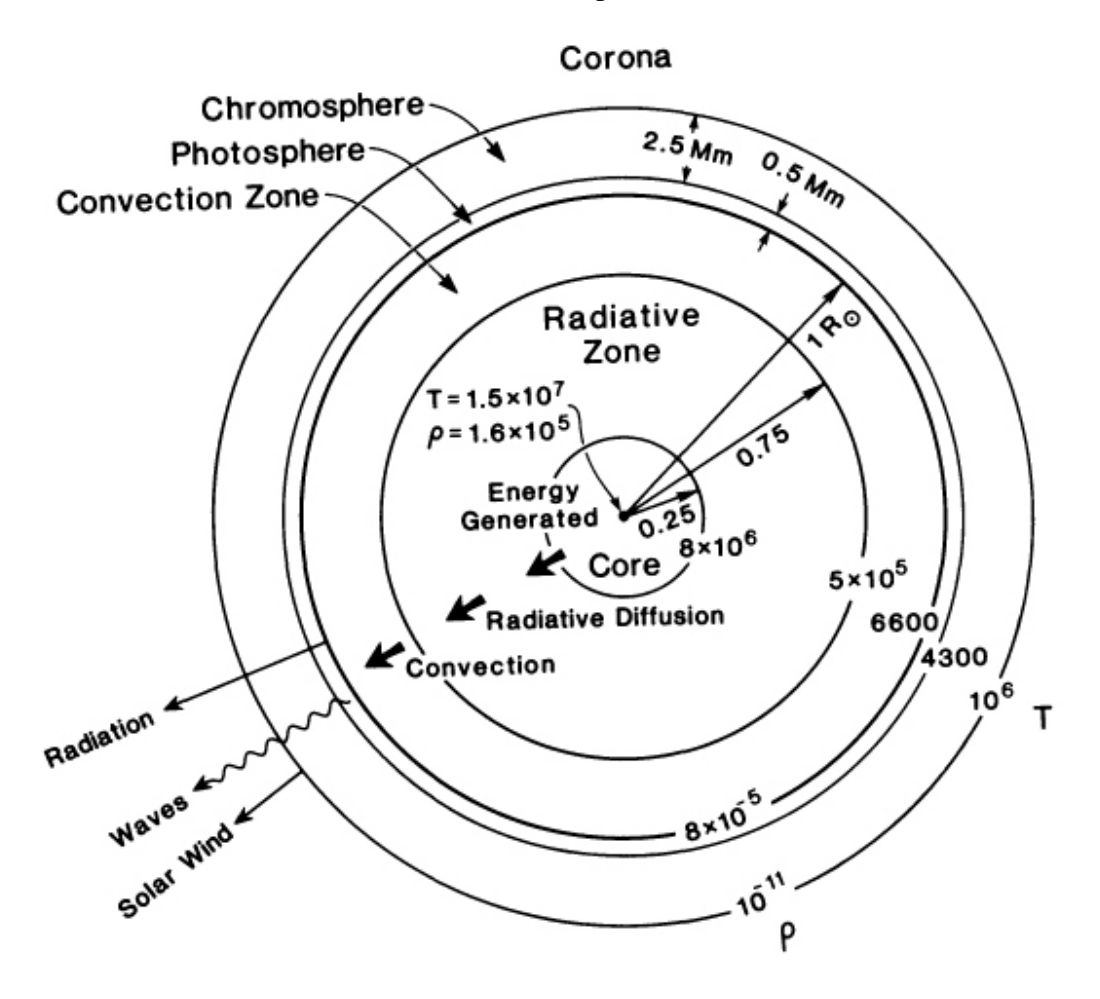


Figure 1.6: Structure of the solar interior and atmosphere. Figure reproduced from Priest (1995).

The main energy generation mechanism in the Sun is the proton-proton chain, a sequence of three nuclear fusion reactions that converts four protons into a single helium nucleus (Bethe, 1939). This takes place in the core, which has a radius of $0.25~R_{\odot}$. Surrounding the core is the radiative zone, where the energy released by nuclear fusion is transmitted by photons out to a distance of $0.75~R_{\odot}$. Beyond this region is the convective zone, located between $0.75-1.0~R_{\odot}$, where temperature gradients drive convective instabilities that transfer energy out to the Sun's photosphere (e.g., Priest 1995). These convective flows also drive the Sun's internal dynamo, which generates the solar magnetic field (e.g., Meyer-Vernet 2007).

The photosphere is the visible 'surface' of the Sun and has a temperature of ~ 5800 K. Magnetic field loops rising through this layer give rise to one of its most striking features in visible light: sunspots. These are dark regions on the photosphere consisting of a central umbra $\sim 2.0 \times 10^4$ km in diameter with strong radial magnetic fields, and a penumbra $\sim 4.0 \times 10^4$ km in diameter with weaker transverse fields (see review by Solanki 2003). Sunspots form in pairs, with opposing magnetic polarities at the footpoints of the magnetic loops (Hale, 1908; Hale et al.,

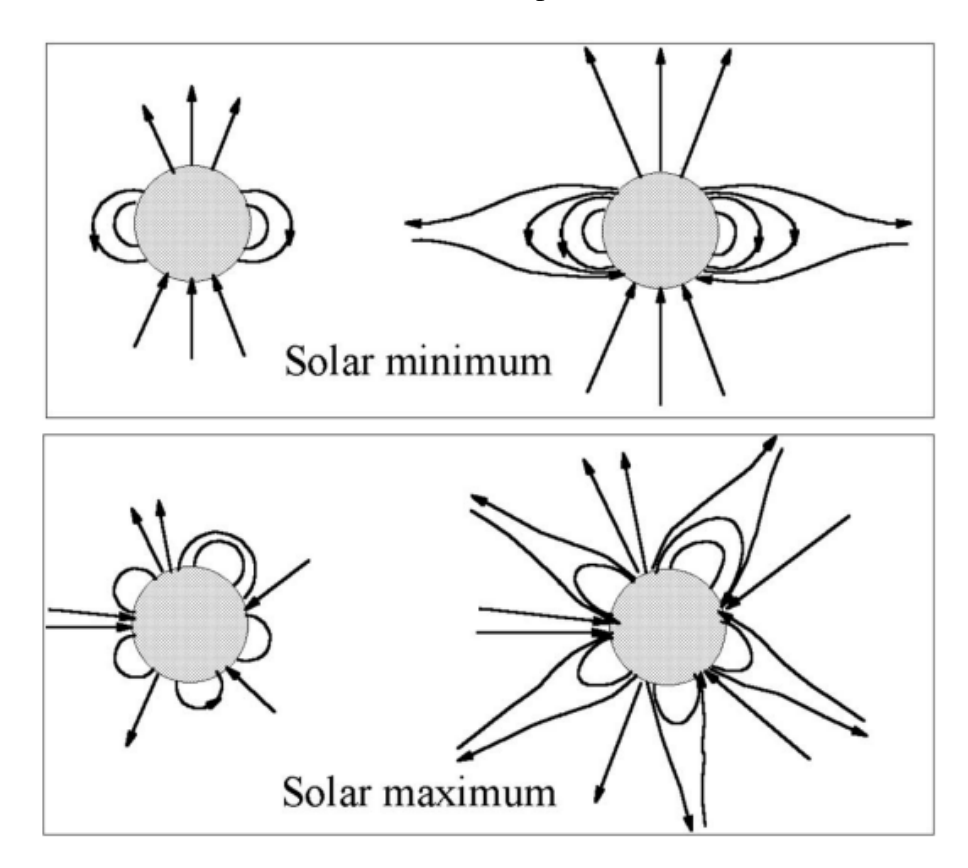


Figure 1.7: Structure of the Sun's magnetic field during solar minimum (top) and maximum (bottom). Figure reproduced from Meyer-Vernet (2007).

1919). They are cooler compared to the surrounding photosphere, with temperatures of \sim 3300 K. This is due to the suppression of convection in the solar interior by the enhanced magnetic fields within the sunspots, which reduces energy transport from the convection zone to the photosphere.

The Sun exhibits cyclical behaviour where the solar activity varies over an 11-year period. Sunspot numbers are a useful indicator for solar activity (e.g., Priest 1995); there are fewer sunspots during periods of low solar activity (solar minimum) and more sunspots during periods of high solar activity (solar maximum). The structure of the Sun's magnetic field is closely linked to solar activity, and its evolution over the solar activity cycle is described by the Babcock model (Babcock, 1961; Leighton, 1969). Figure 1.7 illustrates the magnetic field structure during solar minimum and solar maximum. During solar minimum, the Sun's magnetic field is approximately dipolar with the dipole axis aligned with the rotation axis of the Sun. As solar activity increases, more magnetic field loops emerge from the photosphere, perturbing the dipole field and forming new sunspot pairs (e.g., Meyer-Vernet 2007). The Sun exhibits latitude-dependent differential rotation with a period of 26 days at the equator and 37 days near the polar regions (e.g., Priest 1995). Because the magnetic field lines are frozen into the solar plasma, this motion causes the Sun's magnetic field to become increasingly distorted. At solar maxi-

mum, the Sun is in a magnetically disorganised state and the dipole component of the field no longer dominates. When the Sun returns to solar minimum, the dipole field configuration is restored but with reversed polarity. A full solar magnetic cycle therefore takes 22 years to complete, twice as long as the solar activity cycle (see review by Owens & Forsyth 2013).

The solar atmosphere is divided into the chromosphere, the layer directly above the photosphere with a thickness of ~ 2500 km, and the corona, which extends several R_{\odot} away from the Sun. Separating these two layers is a thin transition region a few hundred km thick, where the temperature increases sharply from 10^4 K in the chromosphere to 10^6 K in the corona (e.g., Priest 1995). The coronal plasma is rarefied and fully ionised, with $\beta \ll 1$, indicating that its behaviour is magnetic field-dominated. The mechanisms responsible for heating the corona are unknown, and the coronal heating problem is one of the key unresolved questions in solar physics. Based on energy budget considerations, the most likely energy source for coronal heating is the Sun's magnetic field (see reviews by Klimchuk 2006; Van Doorsselaere et al. 2020). Various theories invoking wave dissipation and magnetic reconnection (e.g., Parker 1988; Schrijver et al. 1998) have also been put forward to explain coronal heating.

The corona is a highly dynamic environment that supports a variety of structures (e.g., Priest 1995). Coronal holes are regions of open magnetic flux containing cooler, less dense plasma. By contrast, coronal loops are formed by closed magnetic field lines and contain the hottest and densest material in the corona. They are associated with active regions, which are areas of increased magnetic activity commonly found over sunspots. Helmet streamers are formed by the network of closed magnetic loops linking the sunspots in active regions together. Much like the Sun's magnetic field, the global structure of the corona varies across the solar cycle. During solar minimum, coronal holes concentrate around the polar regions while the helmet streamers form a continuous belt around the equator (see review by Cranmer 2009). Conversely, during solar maximum, helmet streamers and coronal holes appear across the Sun at all latitudes and active regions become more common.

Coronal loops are pressure-balanced structures and can remain in stable equilibrium for up to several days. However, the motion of their footpoints introduces shear into the loop magnetic field, thus increasing the stored magnetic energy (see review by Priest 1978). Eventually, the coronal loops become unstable and erupt, rapidly releasing the stored energy through magnetic reconnection of the loop magnetic field (Mikic et al., 1988). This process often generates solar flares (Hagyard et al., 1984; Somov et al., 2002), which are short-lived, energetic bursts of electromagnetic radiation, or coronal mass ejections (CMEs), which expel large quantities of magnetised coronal plasma into interplanetary space (e.g. Antiochos et al. 1999; Gopalswamy 2003). Both types of events occur more frequently during solar maximum, when the Sun's magnetic activity is at its greatest.

1.3.2 The solar wind

The solar wind is the continuous outflow of plasma from the Sun's corona, primarily composed of protons, electrons, and alpha particles, as well as trace amounts of heavier ions. It forms because the thermal pressure exerted by the corona exceeds the solar gravitational force, causing the coronal plasma to expand into the interplanetary medium (Parker, 1958, 1960).

The existence of the solar wind was already suspected by scientists as early as the early twentieth century. Kristian Birkeland's observations of quasi-permanent auroral activity during this period pointed towards a constant flow of charged particles from the Sun impinging on the Earth's magnetosphere (e.g., Meyer-Vernet 2007). This idea of the 'solar corpuscular radiation' as it was called at the time was further elaborated upon by Ludwig Biermann's work on cometary tails (Biermann, 1952). It was known that the ion tail is always oriented radially away from the Sun, but the observed acceleration of ions within the tail could not be fully accounted for by solar radiation pressure alone. However, both of these properties could be readily explained if interactions between cometary ions and the surrounding plasma streams — later identified as the solar wind — were factored in (Biermann, 1952; Parker, 1959). Based on these observations of comets, the bulk speed of the plasma streams were constrained to a few hundred km s⁻¹. This culminated in the development of the first theoretical model of the solar wind by Eugene Parker (Parker, 1958), which was then observationally confirmed by the Mariner 2 spacecraft (Neugebauer & Snyder, 1962).

In the Parker model, the expansion of the corona is assumed to be isothermal and spherically symmetric, resulting in purely radial outflow. In such a system, all variables are dependent only on the heliocentric distance r. Additionally it is also assumed that the outflow is steady-state, and the effects of magnetic forces are neglected. Under these assumptions, the MHD equations for mass continuity (Equation 1.24) and momentum conservation (Equation 1.25) in spherical coordinates are:

$$\frac{d}{dr}(r^2\rho(r)u(r)) = 0 \tag{1.49}$$

$$\rho(r)u(r)\frac{du(r)}{dr} = -\frac{dP(r)}{dr} - \rho(r)\frac{GM_{\odot}}{r^2}$$
 (1.50)

where u(r) is the outflow speed and G is the gravitational constant. The last term in Equation 1.50 replaces the $\mathbf{J} \times \mathbf{B}$ in Equation 1.25 and describes the Sun's gravitational force.

First, consider the case when the corona is static, i.e. u(r) = 0. Equation 1.49 is trivially satisfied and Equation 1.50 reduces to the hydrostatic equilibrium equation:

$$\frac{dP(r)}{dr} + \rho(r)\frac{GM_{\odot}}{r^2} = 0 \tag{1.51}$$

The coronal plasma can be treated as an ideal gas composed of protons and electrons with number densities n_i and n_e , respectively, and uniform temperature T_{\odot} . The ideal gas law then states that $P(r) = n_i k_B T_{\odot} + n_e k_B T_{\odot} = 2n(r) k_B T_{\odot}$, where the quasi-neutrality condition stipulates that $n_i = n_e = n(r)$. Substituting this into Equation 1.51 yields the following differential equation:

$$\frac{1}{P(r)}dP(r) = -\frac{GM_{\odot}m_i}{2k_BT_{\odot}}\frac{1}{r^2}dr,$$
(1.52)

with a solution as $r \to \infty$:

$$P(r \to \infty) = P_{\odot} e^{-\frac{GM_{\odot}m_i}{2k_B T_{\odot}R_{\odot}}},\tag{1.53}$$

where P_{\odot} is the plasma pressure at r=1 R_{\odot} . For typical values of P_{\odot} and T_{\odot} in the corona, $P(r \to \infty) \sim 10^{-7}$ Pa. Since this is approximately 10^6 times larger than the pressure of the interstellar medium, the static corona solution is not valid as no pressure balance exists at the heliopause.

Next, consider the case when the corona is expanding hydrodynamically with $u(r) \neq 0$. Equation 1.49 can be re-written as:

$$\frac{dn(r)}{dr} = -n(r)\left(\frac{1}{u(r)}\frac{du(r)}{dr} + \frac{2}{r}\right). \tag{1.54}$$

The derivative of the ideal gas law with respect to r can therefore be expressed as:

$$\frac{dP(r)}{dr} = 2k_B T_{\odot} \frac{dn(r)}{dr} = -2n(r)k_B T_{\odot} \left(\frac{1}{u(r)} \frac{du(r)}{dr} + \frac{2}{r}\right),\tag{1.55}$$

which, when substituted into Equation 1.50, gives an equation describing the hydrodynamic expansion of the corona:

$$\frac{1}{u(r)} \frac{du(r)}{dr} \left(u(r)^2 - \frac{2k_B T_{\odot}}{m_i} \right) = \frac{4k_B T_{\odot}}{m_i r} - \frac{GM_{\odot}}{r^2}.$$
 (1.56)

The critical radius $r_c = GM_{\odot}m_i/4k_BT_{\odot}$ is defined as the value of r at which the right-hand side of this equation is equal to zero. This is true if:

$$\left. \frac{du(r)}{dr} \right|_{r=r_c} = 0,\tag{1.57}$$

or:

$$\left. \left(u(r)^2 - \frac{2k_B T_{\odot}}{m_i} \right) \right|_{r=r_{\odot}} = 0 \tag{1.58}$$

Equation 1.57 suggests that there is a local maximum or minimum in u(r) at $r = r_c$, whereas Equation 1.58 suggests that $u(r) = \sqrt{2k_BT_{\odot}/m_i}$ at $r = r_c$, which corre-

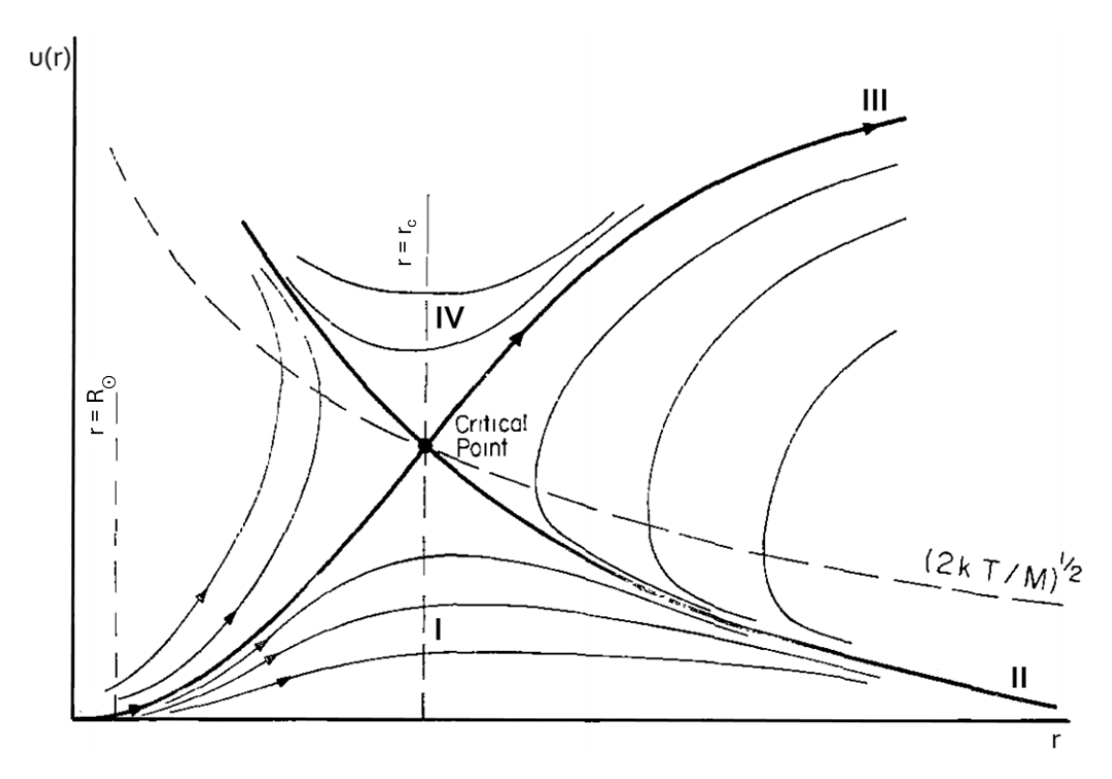


Figure 1.8: Graph of the four solutions to Equation 1.56. Figure adapted from Parker (1965).

sponds to the isothermal sound speed. In addition to these, the following boundary conditions must also be satisfied: 1) $u(r) \to 0$ as $r \to 0$, and 2) the corona must be in pressure balance with the interstellar medium at the heliopause as $r \to \infty$.

Figure 1.8 shows the four classes of solution to Equation 1.56, denoted as I, II, III, and IV. The class II and IV solutions can be immediately ruled out as they do not satisfy the $r \to 0$ boundary condition by suggesting $u(r) \to \infty$ as $r \to 0$. The class I solution is known as the 'solar breeze' and satisfies the $r \to 0$ boundary condition. However, this solution approximates to the static corona solution when $r \to \infty$ which has been shown to be unphysical. This leaves the class III, or Parker solar wind solution where u(r) increases monotonically, becomes supersonic when $r > r_c$, and asymptotically approaches a constant terminal value u_{SW} beyond the critical radius. Since the solar wind speed $u(r) = u_{SW}$ and the mass flux $r^2 \rho(r) u(r)$ are constant (Equation 1.49), the density of the solar wind follows the inverse square law, $\rho(r) \propto r^{-2}$.

The observed solar wind can be broadly separated into two categories, slow and fast (see review by Verscharen et al. 2019). The slow solar wind is more variable than the fast solar wind, with speeds of 350–400 km s⁻¹ and helium abundance $A_{He} = n_{He}/n_p$ ranging between 1% during solar minimum and 4% during solar maximum (Aellig et al., 2001). The source of the slow solar wind is not well-understood. It is commonly associated with helmet streamers, although recent observations indicate pseudostreamers and small coronal holes may also be possible

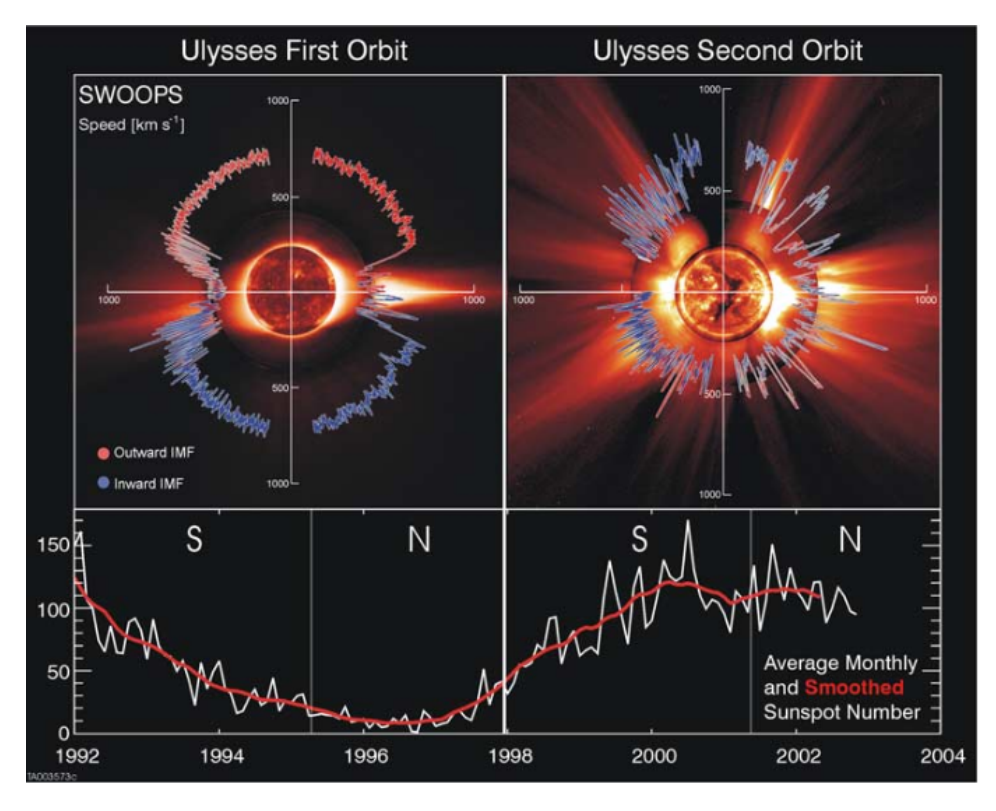


Figure 1.9: Variation in the solar wind speed with heliographic latitude during solar minimum (left) and solar maximum (right). The polar plots overlaid on top of the images of the solar disk are solar wind speed measurements from the *Ulysses* spacecraft. Regions with sunward and anti-sunward magnetic polarity are coloured in blue and red, respectively. The bottom panel shows the variation in sunspot number over the solar cycle. Figure adapted from McComas et al. (2003).

source regions (Bale et al., 2019; D'Amicis et al., 2021). Conversely, the fast solar wind is quasi-steady and reaches speeds of up to ~ 750 km s⁻¹, with a constant helium abundance $A_{He} = n_{He}/n_p$ of 5% (Kasper et al., 2012). It originates from coronal holes and is thus cooler and less dense than the slow solar wind. Figure 1.9 shows the variation in solar wind speed with heliographic latitude and the solar cycle. It is immediately clear that the structure of the solar wind reflects the structure of the corona (McComas et al., 2003). During solar minimum, the solar wind structure is bimodal — fast solar wind streams originate from coronal holes around the Sun's poles and slow solar wind streams originate from the equatorial streamer belt. By contrast, this bimodal structure breaks down during solar maximum, with fast and slow solar wind streams appearing at all latitudes.

1.3.3 The heliospheric magnetic field

The Sun's magnetic field is frozen into the outflowing solar wind, which carries it into interplanetary space to form the heliospheric magnetic field (HMF). As the magnetic field lines remain anchored to the photosphere, the combination

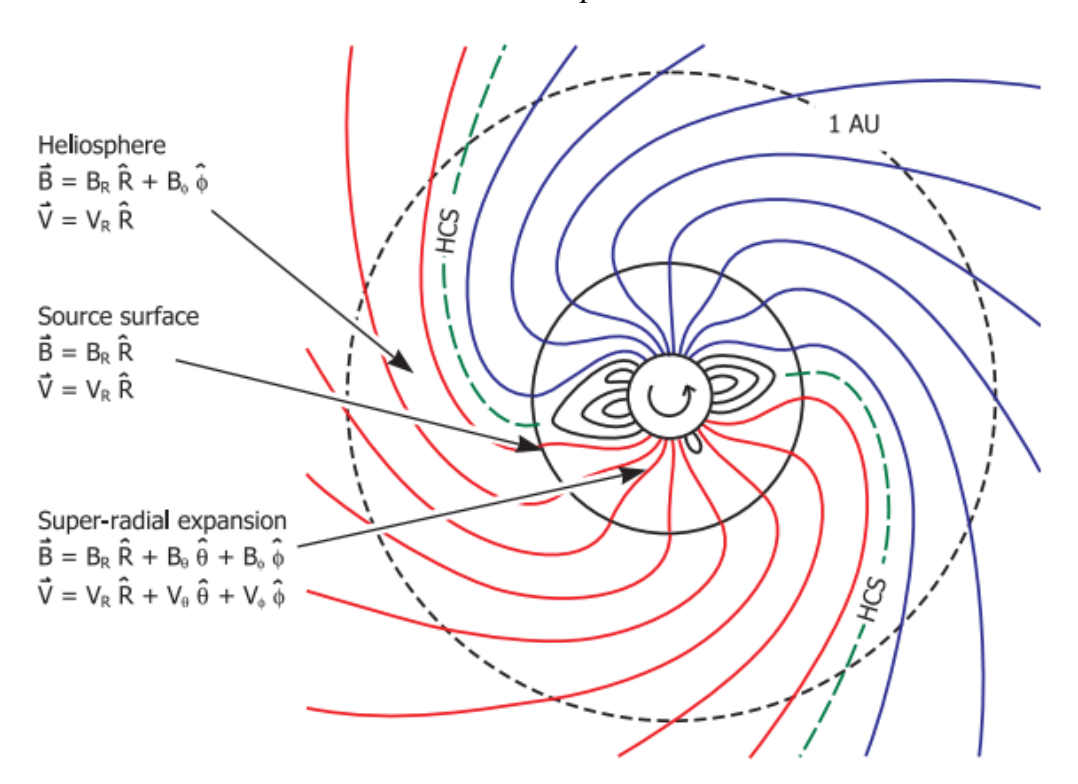


Figure 1.10: Diagram of the heliospheric magnetic field up to 1 AU in the ecliptic plane, showing the Parker spiral and sector structure. The sector with positive, antisunward magnetic polarity (red) is separated from the sector with negative, sunward polarity (blue) by the heliospheric current sheet (dashed green line). Figure reproduced from Owens & Forsyth (2013).

of the Sun's rotation and the radial solar wind outflow warps the HMF into an Archimedean spiral configuration known as the Parker spiral (Parker, 1959; Wilcox & Ness, 1965). Neglecting the motion of the magnetic field footpoints and the differential rotation of the Sun, the HMF spiral angle α is:

$$\tan \alpha = \frac{B_{\phi}}{B_R} = -\frac{r\Omega_{\odot}\sin\theta}{u_{SW}} \tag{1.59}$$

where B_R is the radial component of the HMF, B_{ϕ} is the azimuthal component, Ω_{\odot} is the average angular frequency of the Sun's rotation and θ is the co-latitude. For typical solar wind conditions, α is approximately 45° at 1 AU in the ecliptic plane.

Figure 1.10 shows the configuration of the HMF, which is divided into sectors with sunward (negative) or anti-sunward (positive) magnetic polarity separated by the heliospheric current sheet (HCS). As the Sun's rotation axis is not aligned with its magnetic axis, the HCS is wavy rather than planar. An observer in the ecliptic plane will therefore observe periodic flips in the HMF polarity corresponding to the sector structure. The offset of the axes also means slow and fast solar wind streams can originate from the same latitude, and due to the Sun's rotation, successively emerge into interplanetary space at the same longitude (see review by Owens &

Forsyth 2013). Equation 1.59 shows that the spiral angle α is proportional to $1/u_{SW}$ at a given r and θ . Hence, the Parker spiral is less tightly wound for fast streams compared to slow streams. Compression occurs where the fast solar wind catches up with the slow solar wind ahead of it, forming co-rotating interaction regions, while rarefaction occurs where the fast solar wind 'runs away' from the slow solar wind behind it (Gosling & Pizzo, 1999).

As a consequence of the $\nabla \cdot \mathbf{B} = 0$ condition, the radial component of the magnetic field B_R follows an inverse square law in r, similar to the solar wind density:

$$B_R(r) = B_0 \left(\frac{r_0}{r}\right)^2 \tag{1.60}$$

where B_0 is the magnetic field strength at a reference heliocentric distance r_0 . Combining this with Equation 1.59, the magnetic field strength of the HMF is:

$$B(r) = \sqrt{B_R^2 + B_\phi^2} = B_0 \left(\frac{r_0}{r}\right)^2 \sqrt{1 + \left(\frac{r\Omega_{\odot}\sin\theta}{u_{SW}}\right)^2}$$
 (1.61)

In the case of purely radial solar wind outflow, the polar component of the HMF is $B_{\theta} = 0$. At small r, the $(\frac{r_0}{r})^2$ term dominates and $B \propto r^{-2}$, while at large r, the square root term dominates and $B \propto r^{-1}$ for constant θ :

$$B(r) \simeq \frac{B_0 r_0^2 \Omega_{\odot}}{u_{SW}} \frac{\sin \theta}{r}$$
 (1.62)

From Equation 1.34, the variation in β with r depends on the relative scaling of the plasma pressure and the magnetic pressure. Given the assumption of isothermal solar wind, the plasma pressure is proportional to the density and hence decreases as $P \propto r^{-2}$. Near the Sun, the magnetic pressure scales as $P_{mag} \propto r^{-4}$ due to its dependence on B^2 . Therefore, in this region, $\beta \propto r^2$ and the effects of the magnetic field on the solar wind flow diminishes rapidly with increasing heliocentric distance. Further away from the Sun, where $B \propto r^{-1}$, the magnetic pressure instead scales as $P_{mag} \propto r^{-2}$ and β becomes constant in r. This result justifies one of the starting assumptions of the Parker model: that the effects of magnetic forces on the coronal expansion can be neglected.

A useful indicator of the connectivity of the HMF to the Sun is provided by the pitch angle distribution of the population of suprathermal electrons in the solar wind. These electrons form a field-aligned beam, known as the strahl, which streams away from the Sun along the HMF (see review by Owens & Forsyth 2013). Figure 1.11 illustrates how the strahl pitch angle distribution varies depending on the topology of the HMF. Regions A and C correspond to areas of open magnetic flux with a single connection to the Sun. In these regions, a single strahl is observed which is anti-parallel to the field when its polarity is sunward (A), or parallel

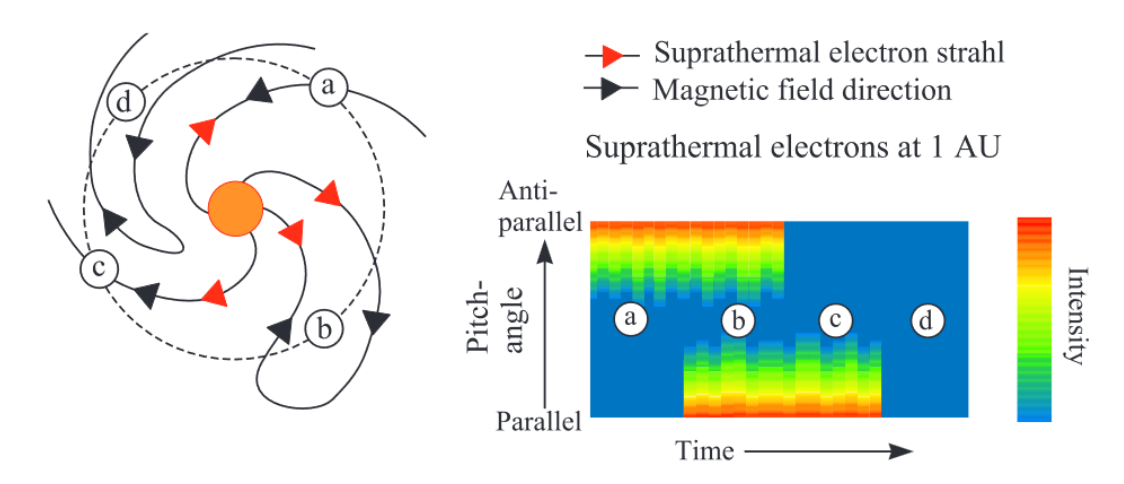


Figure 1.11: Variation in the suprathermal electron strahl pitch angle distribution (right) depending on the magnetic field topology (left). The black arrows show the magnetic field lines and the red arrows show the direction of the strahl beam. Region A contains sunward open magnetic flux, Region B contains closed magnetic flux, Region C contains anti-sunward open magnetic flux, and Region D contains magnetic flux completely disconnected from the Sun. Figure reproduced from Owens & Forsyth (2013).

when the polarity is anti-sunward (C). Region B corresponds to an area of closed magnetic flux with two points of connection to the Sun. Here, a parallel and anti-parallel strahl are observed simultaneously; this is known as a bi-directional strahl signature. In Region D, the magnetic field is completely disconnected from the Sun and no strahl is observed.

1.3.4 In-situ observations of reconnection in the solar wind

Direct observations of reconnection outflows in the Earth's magnetosphere were reported in the 1970s (Paschmann et al., 1979; Sonnerup et al., 1981), but similar observations in the solar wind were not identified as such until the mid-2000s (Gosling et al., 2005a, 2006a; Gosling, 2012).

Figure 1.12 shows the Gosling reconnection model (Gosling et al., 2005a), which is commonly used to interpret the spatial structure of observed reconnection outflows in the solar wind. The reconnected field line is kinked at the edge of the outflow region, and these kinks propagate along the field line as Alfvén waves. Outside the diffusion region, the magnetic field is frozen into the inflowing plasma and is advected towards the outflow region by the $\mathbf{E} \times \mathbf{B}$ drift. Therefore, as the field line recoils away from the neutral line, the net motion of the kinks is a superposition of their field-aligned Alfvénic propagation and the $\mathbf{E} \times \mathbf{B}$ drift of the surrounding plasma. The resulting trajectories are marked by the dashed arrows CS1 and CS2. This sets up a pair of standing Alfvénic rotational discontinuities (RDs) at the outflow region boundaries. When plasma from the inflow regions encounters the discontinuities, it is heated and accelerated away from the neutral line

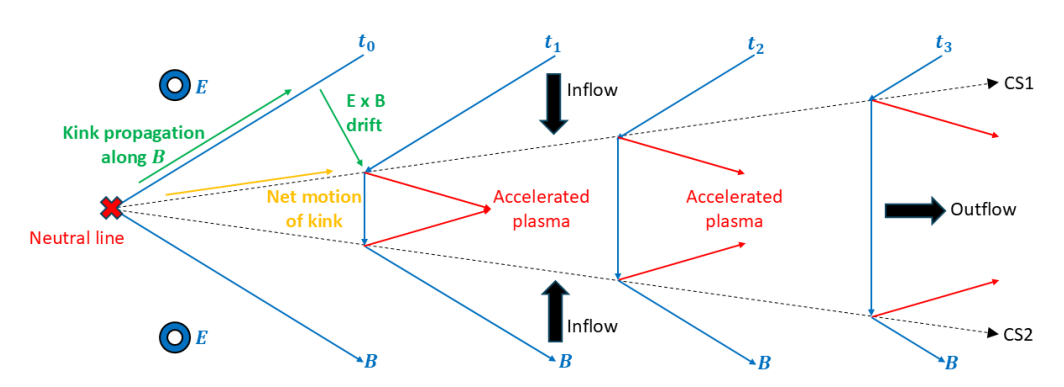


Figure 1.12: Gosling reconnection model. The dashed arrows CS1 and CS2 represent the bifurcated current sheet bounding the outflow region. Figure adapted from Gosling et al. (2005a).

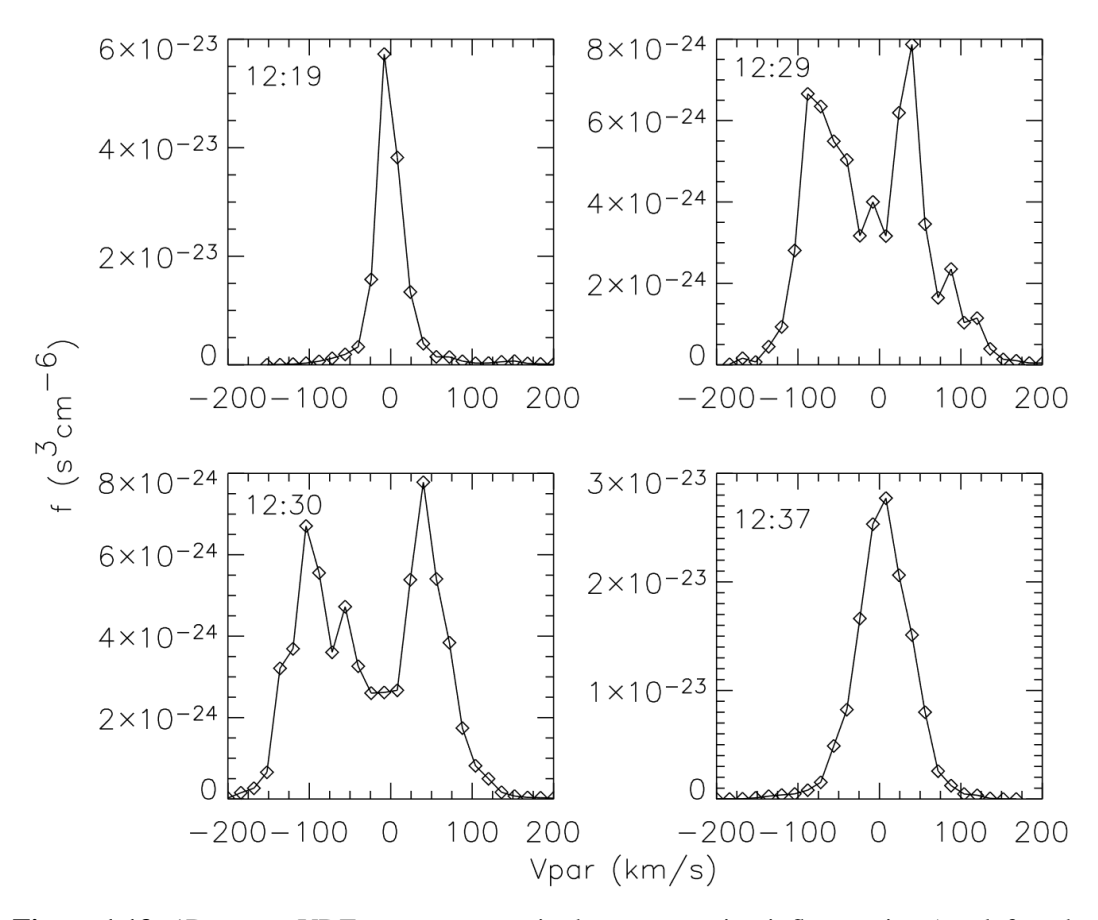


Figure 1.13: 1D proton VDF measurements in the reconnection inflow region (top left and bottom right) and outflow region (top right and bottom left). In this event, a pair of counterstreaming beams are clearly resolvable in the outflow region. Figure reproduced from Gosling et al. (2005a).

to form the reconnection outflow jet. Similar to the Petschek reconnection model (Petschek 1964, see Section 1.2.2), the Gosling model also features a bifurcated RCS. However, in this model, the outflow region is bound by a pair of rotational discontinuities rather than slow mode shocks.

A spacecraft traversing the reconnection outflow will observe a jet in the outflow region bound by a pair of step-like rotations in the magnetic field. On the side of the outflow region where the kink propagates parallel to the magnetic field, the fluctuations in **u** and **B** are anti-correlated. Conversely, on the side where the kink propagates anti-parallel to the magnetic field, the fluctuations in **u** and **B** are correlated. The inflow entering the outflow region along the reconnected field lines from both sides produces a population of counterstreaming beams that may be resolvable in proton VDF measurements, provided the beams are well-separated in velocity space (Gosling et al., 2005a). Figure 1.13 shows an example of clearly resolved counterstreaming beams within the reconnection outflow region.

Magnetic reconnection is commonly observed in the regular solar wind (Gosling et al., 2007; Phan et al., 2020), around interplanetary coronal mass ejections (McComas et al., 1994; Gosling et al., 2005a), and at the HCS (Gosling et al., 2005b, 2006b; Phan et al., 2021). Reconnection is also sometimes observed at switchback boundaries (Froment et al., 2021; Suen et al., 2023), though less frequently than in the regions previously listed. How the occurrence rate of reconnection varies with heliocentric distance differs across these locales. At the HCS, reconnection is more frequent between 0.1–0.5 AU than at 1 AU (Phan et al., 2021). By contrast, the occurrence rate of reconnection in the regular solar wind decreases with heliocentric distance, especially in the slow Alfvénic wind where switchbacks are prevalent (Phan et al., 2020). Finally, reconnection outflows in the solar wind appear to cluster regardless of solar wind speed (Fargette et al., 2023).

1.4 Magnetic switchbacks

The Parker spiral model provides a good description of the HMF and its associated sector structure over large scales. However, localised deviations from the Parker spiral occur when the magnetic field polarity is reversed relative to the dominant polarity of the sector. These structures, known as magnetic switchbacks, are present throughout the heliosphere (Balogh et al., 1999; Owens et al., 2013) but recent observations from the *Parker Solar Probe* mission (Fox et al., 2016) show that they are particularly prevalent in the near-Sun solar wind (Bale et al., 2019; Kasper et al., 2019). In this section, I examine the key physical properties of magnetic switchbacks and briefly discuss some of their proposed formation mechanisms.

1.4.1 General characteristics

Although the name 'switchback' implies a full polarity reversal is required for a structure to be classified as such, this type of switchback constitutes only a subset of observed events. More generally, switchbacks are defined as local deflections of the magnetic field away from the background HMF orientation. They exhibit a continuum of deflection angles, and while switchbacks with larger deflections are more common further from the Sun, most do not result in a full polarity reversal (Dudok de Wit et al., 2020; Mozer et al., 2020). Those with small deflection angles

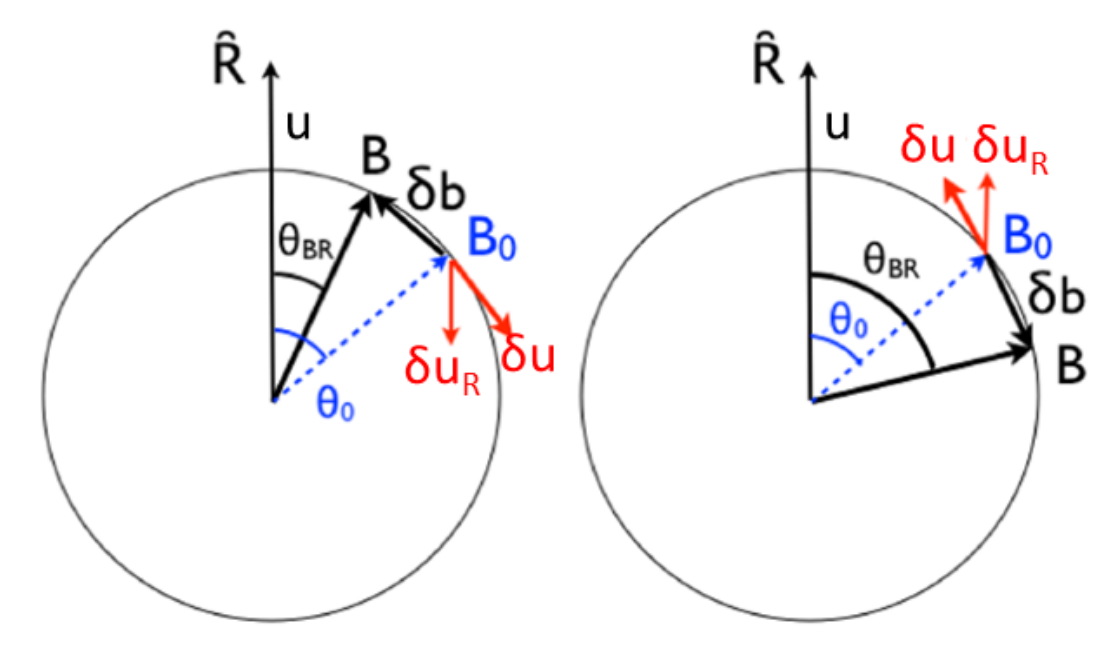


Figure 1.14: Vector diagram showing the evolution of **B** in an Alfvénic structure and the correlation between the magnetic field and velocity fluctuations, $\delta \mathbf{u}$ and $\delta \mathbf{b}$, respectively. θ_0 is the angle between the radial direction, $\hat{\mathbf{R}}$, and the background magnetic field \mathbf{B}_0 . θ_{BR} is the angle between $\hat{\mathbf{R}}$, and the deflected magnetic field **B**. Figure reproduced from Matteini et al. (2014).

are difficult to distinguish from random fluctuations in the HMF, making it challenging to define a threshold angle above which a magnetic field deflection can be classified as a switchback. Additionally, these structures also preferentially deflect in the azimuthal $(\pm \hat{\phi})$ direction within the plane of the Parker spiral, rather than the polar $(\pm \hat{\theta})$ direction normal to this plane. Switchbacks cluster into patches that last for several hours and were present 75% of the time during PSP's first encounter with the Sun (Bale et al., 2019; Dudok de Wit et al., 2020; Horbury et al., 2020b). Within these patches, individual switchbacks tend to deflect in the same direction (Fargette et al., 2022; Laker et al., 2022).

Switchbacks are highly Alfvénic, arc-polarised structures with correlated variations in $\bf u$ and $\bf B$, while maintaining constant magnetic field strength B (Bale et al., 2019; Kasper et al., 2019). Figure 1.14 shows that in such structures, the deflection in $\bf B$ away from and back to the background field $\bf B_0$ traces the same arc on the surface of a sphere with radius B (Matteini et al., 2014). The radial component of the Alfvén wave polarisation equation is:

$$-\frac{\delta u_R}{\pm V_A} = \frac{\delta b_R}{B} \tag{1.63}$$

where δb_R is the change in the radial component of the magnetic field, δu_R is the change in the radial component of the velocity, and $V_A = B/\sqrt{\rho \mu_0}$ is the Alfvén speed. Here, the Alfvén wave is propagating away from the Sun along a magnetic

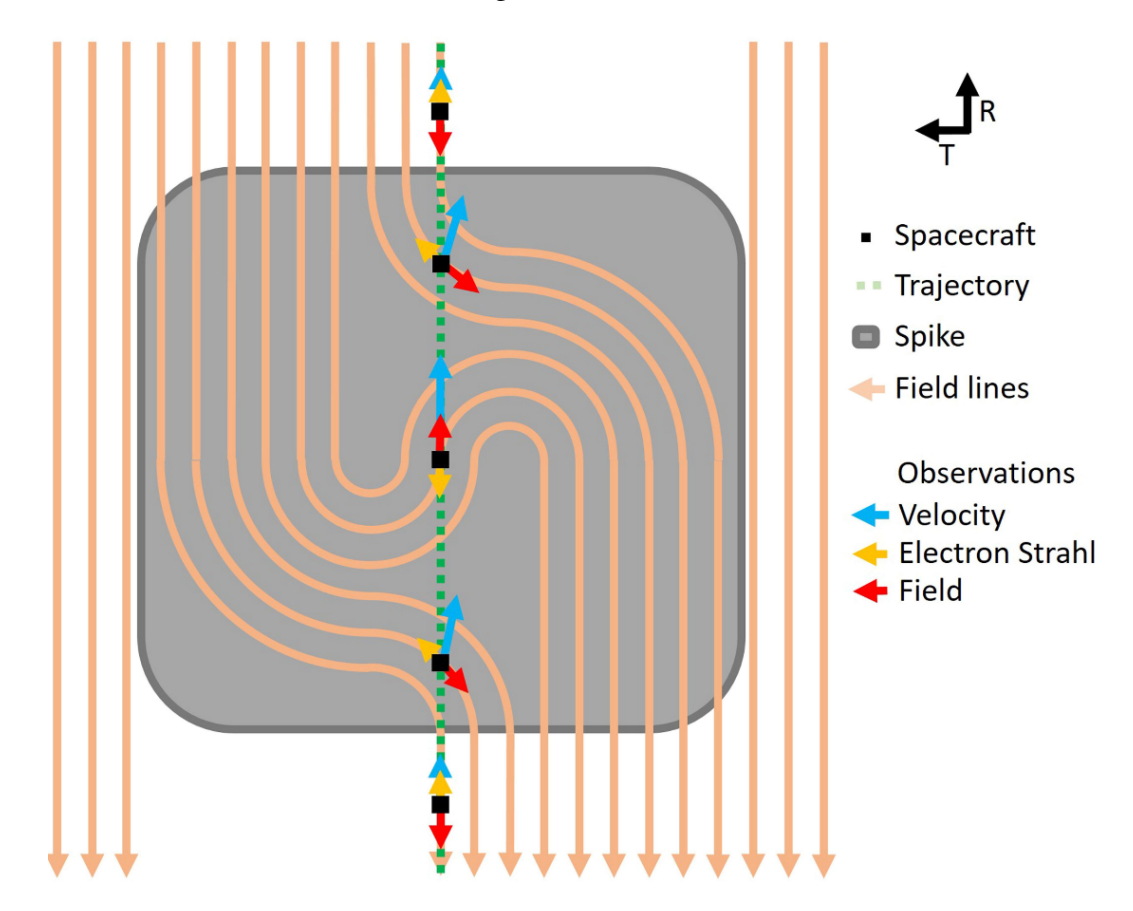


Figure 1.15: Simplified diagram of the magnetic field geometry of a switchback. Figure reproduced from Kasper et al. (2019).

field line with anti-sunward (+R) polarity. As a result, the sign of V_A is positive and δu_R and δb_R are anti-correlated. If **B** deflects towards the radial direction, δb_R is positive and δu_R is negative; conversely, if **B** deflects away from the radial direction, δb_R is negative and δu_R is positive. However, if the same Alfvén wave is now propagating along a magnetic field line with sunward (-R) polarity, the sign of V_A is negative and δu_R and δb_R becomes correlated. If **B** deflects towards the radial direction, both δb_R and δu_R are negative. On the other hand, if **B** deflects away from the radial direction, both δb_R and δu_R are positive. Regardless of the polarity of **B**₀, a deflection in **B** away from the radial direction — as expected in a switchback — leads to positive δu_R and an increase in the magnitude of **u** (Matteini et al., 2014). This result explains the velocity spikes observed in switchbacks and why they are always enhancements rather than reductions (Horbury et al., 2018, 2020b). While most switchbacks are Alfvénic, some examples do exhibit simultaneous changes in *B* and particle density, suggesting compressive behaviour (Krasnoselskikh et al., 2020; Larosa et al., 2021).

Switchbacks may therefore be treated as folds in the HMF that propagate away from the Sun along the magnetic field line as Alfvén waves (Balogh et al., 1999; Kasper et al., 2019). Figure 1.15 shows the magnetic field geometry of an idealised

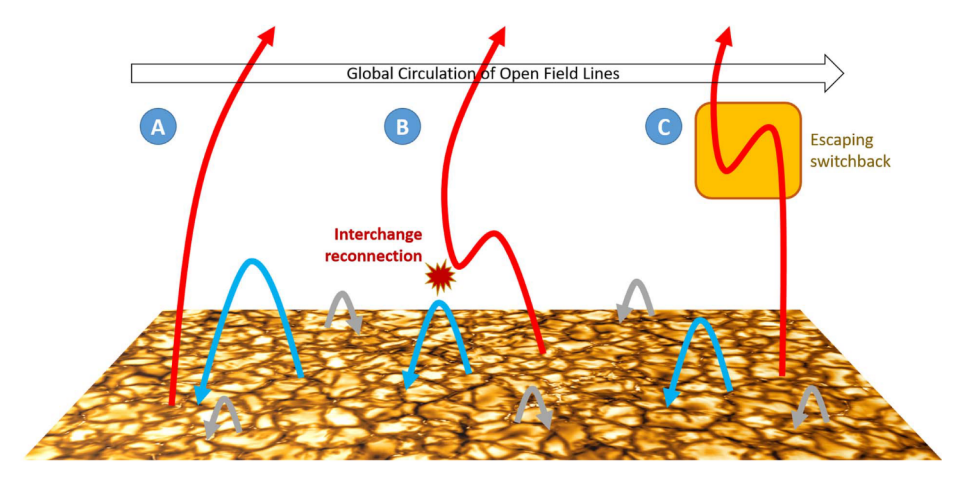


Figure 1.16: Formation of magnetic switchbacks through interchange reconnection in the corona. Figure reproduced from Fisk & Kasper (2020).

switchback with full polarity reversal. The electron strahl follows the field line as it reverses, becoming sunward-directed inside the switchback. As a result, the strahl pitch angle distribution inside and outside the switchback is the same. This property distinguishes local polarity reversals due to switchbacks from global polarity changes in the HMF due to HCS crossings, where the strahl pitch angle switches direction (see Section 1.3.3, Kasper et al. 2019). The field-aligned proton-alpha particle relative streaming velocity $\mathbf{v}_{\alpha \mathbf{p}} = \mathbf{v}_{\alpha} - \mathbf{v}_{\mathbf{p}}$, defined in the solar wind rest frame, is another useful diagnostic to check if a polarity reversal is due to local deflections in the HMF. In the regular solar wind, the alpha particles stream away from the Sun along the HMF faster than the protons so $\mathbf{v}_{\alpha \mathbf{p}} > 0$. However, $\mathbf{v}_{\alpha \mathbf{p}} < 0$ inside switchbacks because $|\mathbf{v}_{\mathbf{p}}| > |\mathbf{v}_{\alpha}|$ (Steinberg et al., 1996; Yamauchi et al., 2004).

1.4.2 Formation mechanisms

Various mechanisms have been proposed to explain how magnetic switchbacks are formed, but their origins remain poorly understood. These mechanisms can be grouped into two categories based on where switchbacks are formed: in the solar corona or in-situ in the solar wind.

Theories of switchback formation in the corona invoke interchange reconnection between areas of open and closed magnetic flux, often at the interfaces separating active regions and small coronal holes (Fisk & Kasper, 2020). Figure 1.16 shows the proposed mechanism behind this process. The corona and photosphere rotate at different rates, with open magnetic flux in the corona moving to maintain overall magnetic pressure balance while the magnetic footpoints remain anchored in the photosphere. The movement of magnetic flux in the corona drags open magnetic field lines against coronal loops (A), which then reconnect with each other (B) and release a propagating switchback along the newly opened field line (C). In this model, the differential rotation of the corona favours magnetic field deflections in the azimuthal direction of the Parker spiral. Repeated reconnection at the same

location will also launch multiple switchbacks in quick succession, thus forming the switchback patches observed in the solar wind (Laker et al., 2022). A key issue with this model is that magnetic tension at the folds in the magnetic field line will quickly act to unwind the switchback. Variations of this model suggest interchange reconnection instead produces flux ropes (Drake et al., 2021; Agapitov et al., 2022), which are more resistant to erosion and are therefore more likely to survive propagation into the solar wind. These structures do exhibit some, but not all, of the properties associated with switchbacks, namely the strong correlation between **u** and **B** expected of Alfvénic structures (Kasper et al., 2019; Horbury et al., 2020b; Drake et al., 2021).

Switchback formation in the solar wind is attributed to multiple in-situ processes. Outward-propagating, small-amplitude Alfvén waves generated in the corona may evolve into full magnetic reversals due to the radial expansion of the solar wind. The Parker spiral enhances the growth of these waves compared to a purely radial HMF and introduces preferential deflection of the magnetic field within the plane of the Parker spiral (Squire et al., 2020, 2022). Magnetic field footpoint motion from regions of slow to fast solar wind flow may also introduce velocity shears along the magnetic field line. The section of the magnetic field line frozen into the fast stream overtakes the section embedded within the slow stream, creating folds in the field line that are observed as switchbacks (Schwadron & McComas, 2021).

There is compelling evidence that points to the formation of switchbacks in the corona, but does not rule out in-situ formation. The spatial scales of switchback patches are comparable to supergranulation structures on the solar surface (Bale et al., 2021; Fargette et al., 2021), and coronagraph images from *Solar Orbiter* show what appear to be nascent switchbacks in the corona, directly above active region-coronal hole boundaries (Telloni et al., 2022). It is possible that a combination of coronal and in-situ processes are responsible for the formation of switchbacks. MHD simulations show that interchange reconnection releases non-switchback Alfvénic fluctuations onto open field lines. These structures may then evolve into fully-developed switchbacks through in-situ processes, such as the aforementioned Alfvén wave growth mechanism (Wyper et al., 2022).

1.5 Current sheet stress balance models

RCS bifurcation in the Gosling reconnection models arises as a consequence of maintaining pressure balance between the reconnection inflow and outflow regions. In a similar vein, the forces acting on the reconnected field line and plasma at the RCS must be balanced in order for the whole outflow structure to remain in equilibrium. This balance of forces can be described by current sheet stress balance models. In this section, I introduce these models in the simpler context for which they were first developed — magnetic reconnection in the Earth's magnetotail (see Owen & Cowley 1987a,b, and references therein).

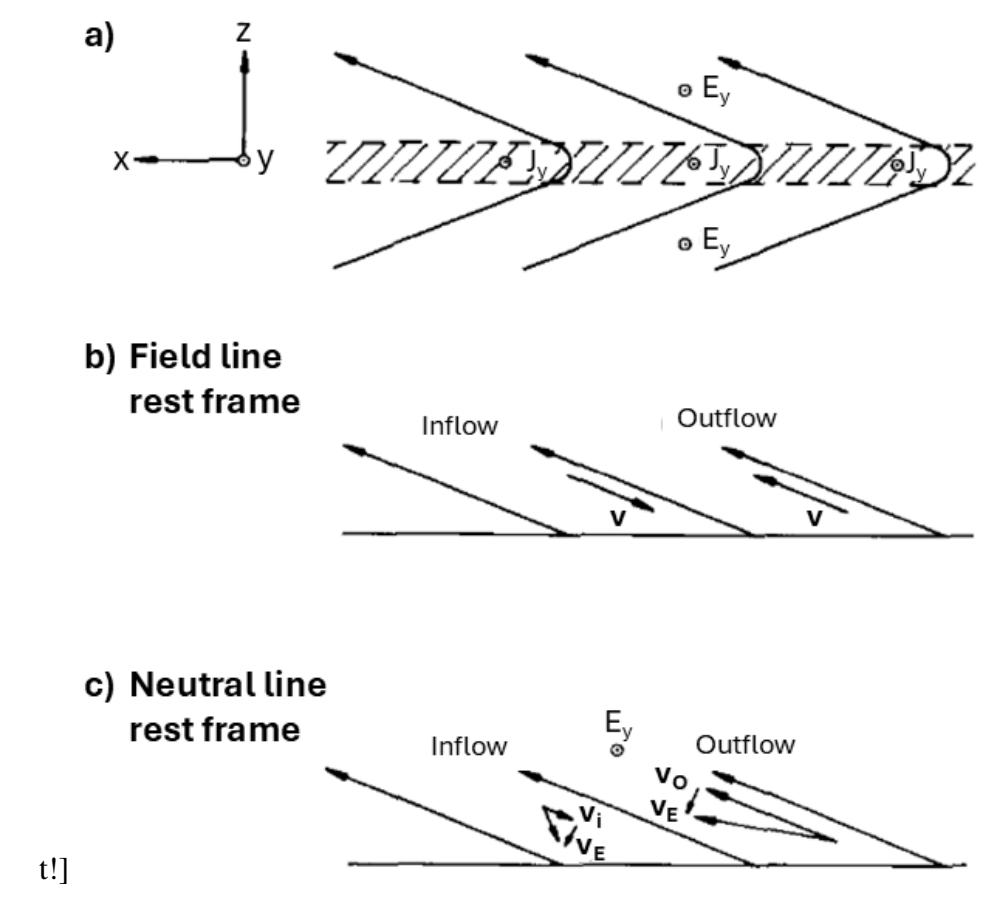


Figure 1.17: Diagram of the a) magnetic and electric field configuration of a 1-D RCS, with associated inflows and outflows in the b) field line rest frame, and c) neutral line rest frame. Figure reproduced from Owen & Cowley (1987a).

1.5.1 Symmetric cold inflows

The magnetotail lobe is a low plasma β regime, so the plasma thermal pressure may be neglected. The reconnection inflows and outflows can be treated as a cold plasma, and so to maintain total pressure balance, the magnetic field strength on both sides of the RCS must be equal. Variations in the plasma and magnetic field along the RCS can be neglected, provided they occur on spatial scales greater than the thickness of the RCS (Cowley & Southwood, 1980; Owen & Cowley, 1987a,b).

Figure 1.17 shows a symmetric 1-D steady-state reconnection configuration with magnetic field and electric fields:

$$\mathbf{B} = (B_x(z), 0, B_z) \tag{1.64}$$

$$\mathbf{E} = (0, E_y, 0) \tag{1.65}$$

where B_z and E_y are constants. The Geocentric Solar Ecliptic coordinate system is used in this figure, where **x** points along the Earth-Sun line, **y** points towards dusk, and **z** points northward. The magnetic field varies only in z, the direction

normal to the RCS, with B_x reversing sign across the RCS while $|B_x| \gg |B_z|$ in the magnetotail lobes that form the reconnection inflow region. Under these conditions, the current sheet stress balance conditions, as derived from the MHD momentum equation (Equation 1.25), are given by (Owen & Cowley, 1987b):

$$M_{\parallel} - P_{\perp} = \frac{B^2}{\mu_0} \tag{1.66}$$

$$P_{\perp} + \frac{B^2}{2\mu_0} = Const. \tag{1.67}$$

where M_{\parallel} is the field-parallel momentum flux and P_{\perp} is the field-perpendicular component of the pressure tensor in the plasma surrounding the RCS. The M_{\parallel} term accounts for both the parallel plasma pressure and the field-aligned flow pressure (Owen & Cowley, 1987b; Owen & Mist, 2001).

The reconnection inflow from the lobes on both sides of the RCS is symmetric and directed tailward along $-\hat{\mathbf{x}}$ in the neutral line rest frame (NLRF) with velocity \mathbf{v}_I . The field line rest frame (FLRF) moves away from the neutral line along the $\pm \hat{\mathbf{x}}$ -direction at the $\mathbf{E} \times \mathbf{B}$ drift speed at the RCS centreline:

$$v_F = \frac{E_y}{B_z} \tag{1.68}$$

In this frame, the electric field vanishes, so the particles entering and leaving the RCS do not experience an $\mathbf{E} \times \mathbf{B}$ drift. Furthermore, with no forces due to the electric field, magnetic pressure, or plasma pressure doing work on them, the particles' speed remains constant as they cross the RCS. The out-of-plane component of the particle motion due to the magnetic field curvature and gradient drifts (see Section 1.1.2) is neglected throughout this analysis. For symmetric lobe inflows, the inflow and outflow beams can therefore be treated as a pair of cold, field-aligned beams with density n and speed v'.

Under the cold plasma approximation, $P_{\perp}=0$ and the only contribution to M_{\parallel} comes from the field-aligned flow pressure of the counterstreaming beams. Hence, Equation 1.66 becomes:

$$2nm_i v'^2 = \frac{B^2}{\mu_0} \tag{1.69}$$

which states that magnetic tension in the reconnected field line is balanced by the change in momentum of the beams as they reverse across the RCS. Re-arranging this equation gives the field-aligned beam speed in the FLRF, v':

$$v' = \frac{B}{\sqrt{2nm_i\mu_0}} = \frac{V'_{A,in}}{\sqrt{2}} = V'_A \tag{1.70}$$

where $V'_{A,in}$ is the Alfvén speed in the inflow region and V'_A is the Alfvén speed in

the vicinity of the RCS. In the latter region, the total mass density $\rho = 2nm_i$ is the sum of the inflow and outflow beam densities. Additionally, if $P_{\perp} = 0$, Equation 1.67 shows that the magnetic field strength B must be equal on both sides of the RCS, as expected.

On the Earthward side of the neutral line, the reconnection inflow in the FLRF is directed along $-\mathbf{x}$, the outflow is directed along $+\mathbf{x}$, and the reconnected field line recoils in the $+\mathbf{x}$ direction. The velocity transformation from the NLRF to the FLRF is $\mathbf{v}' = \mathbf{v} - \mathbf{v_F}$, where primed and unprimed quantities denote velocities in the FLRF and NLRF, respectively. Using this transformation, the field line recoil speed and outflow speed v_O in the NLRF are:

$$v_{FE} = V_A' - v_I \tag{1.71}$$

$$v_{OE} = 2V_A' - v_I \tag{1.72}$$

where the subscript E denotes quantities on the Earthward side of the neutral line. On the tailward side of the neutral line, the reconnection inflow in the FLRF is instead directed along $+\mathbf{x}$ and the outflow is directed along $-\mathbf{x}$. Additionally, the reconnected field line now recoils in the $-\mathbf{x}$ direction. Using the same approach, the tailward field line recoil speed and outflow speed in the NLRF are:

$$v_{FT} = V_A' + v_I \tag{1.73}$$

$$v_{OT} = 2V_A' + v_I \tag{1.74}$$

where the subscript T denotes quantities on the tailward side of the neutral line.

Figure 1.18 shows the reconnected field wedge on the Earthward and tailward sides of the neutral line. It is bound by a separatrix, defined as the field line that directly connects back to the neutral line. At a point X along the RCS at distance $|X - X_N|$ from the neutral line, the half-width of the wedge is W(X). By magnetic flux conservation, the flux threading through the RCS between X and the neutral line must equal to the flux convected into the wedge by the inflow. This leads to the following equation for the half-width of the reconnected field wedge (Owen & Cowley, 1987a):

$$W(X) = \frac{E_y}{B} \frac{|X - X_N|}{v_F}$$
 (1.75)

If $|B_x| \gg |B_z|$, W(X) scales linearly with $|X - X_N|$ and the opening angle of the wedge is proportional to E_y . Particles within the reconnected field wedge occupy a region bounded by the particle trajectory that maps back to the neutral line. The portion of the wedge between this boundary and the separatrix contains the magnetic flux reconnected in the time taken for a particle with speed v_p to reach X. Using similar flux conservation arguments, the half-width of the particle region S(X) is

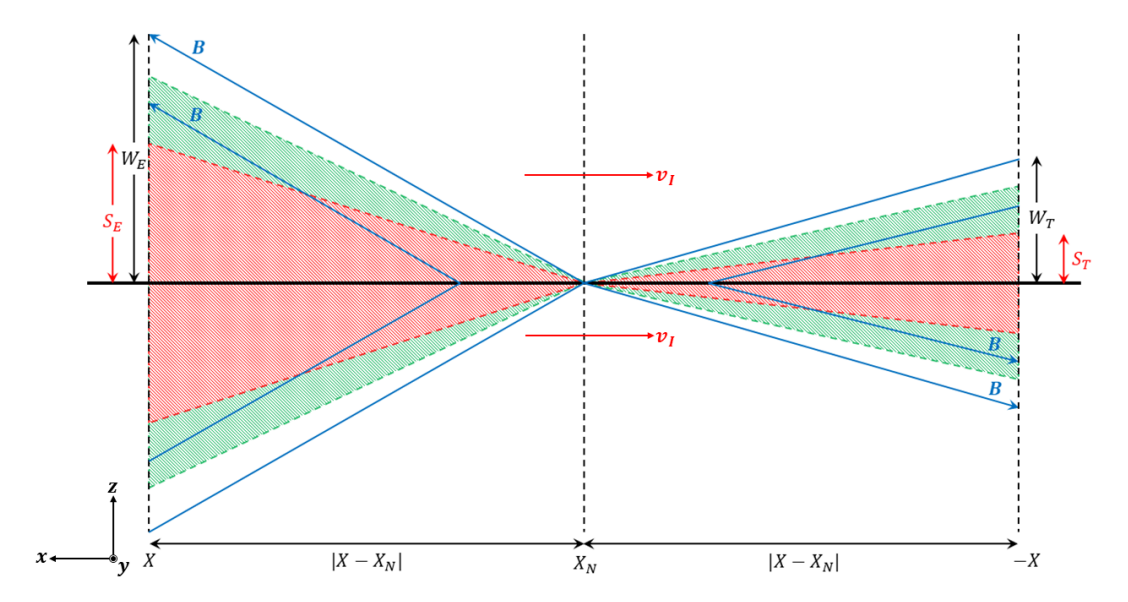


Figure 1.18: Structure of the reconnected field wedge earthward and tailward of the neutral line at X_N . The RCS is represented by the solid black line at the centre of the figure and **B** is represented by the blue arrows. The red arrows represent the tailward inflows from the magnetotail lobes with velocity $\mathbf{v_I}$ in the neutral line rest frame. The reconnection outflow region is shown by the red hatched region and the region occupied by high-energy particles is shown by the green hatched region. Figure adapted from Owen & Cowley (1987a).

(Owen & Cowley, 1987a):

$$S(X) = \frac{E_y}{B}|X - X_N| \left(\frac{1}{\nu_F} - \frac{1}{\nu_p}\right)$$
 (1.76)

Substituting in Equations 1.71–1.74 for the field line recoil speed and outflow speeds yields expressions for the outflow region half-width on both the earthward and tailward sides of the neutral line:

$$S_E = W_E \left(\frac{V_A'}{2V_A' - v_I} \right) \tag{1.77}$$

$$S_T = W_T \left(\frac{V_A'}{2V_A' + v_I} \right) \tag{1.78}$$

If the reconnection inflow is downtail ($v_i > 0$), Equations 1.71–1.74 show that $v_{FE} < v_{FT}$ and $v_{OE} < v_{OT}$. Given this, Equation 1.75 suggests that $W_E < W_T$. Additionally, since E_y is constant for steady-state reconnection, Equation 1.68 implies that $|B_{zE}| > |B_{zT}|$. This supports the assertion that the reconnected field wedge is wider on the Earthward side of the neutral line than on the tailward side. From Equations 1.77 and 1.78, the outflow region occupies more than half the width of the wedge on the Earthward side and less than half the width on the tailward side. High-energy particles with speeds $v_p > v_0$ travel further down the field line during

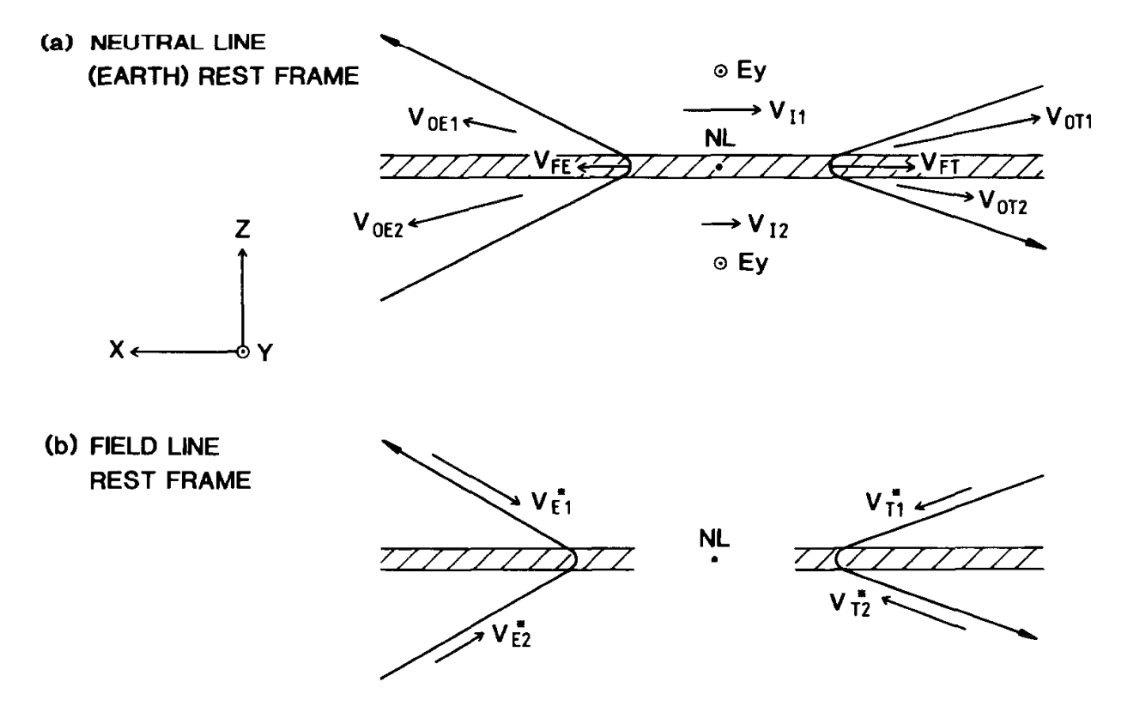


Figure 1.19: Magnetic reconnection configuration with asymmetric inflows in the a) NLRF and b) FLRF. The magnetic and electric field geometry is the same as in the symmetric inflow case. Figure reproduced from Owen & Cowley (1987b).

time t, and thus occupy a greater portion of the reconnected field wedge than the outflow ions (Equation 1.76). In the limit $v_p \to \infty$, the boundary of the high energy particle layer approaches the separatrix. The reconnected field wedge thus consists of a central outflow region containing field-aligned beams with speed v_{OE} and v_{OT} on the Earthward and tailward side of the neutral line, respectively. This region is surrounded by layers of energetic particles with speeds $v_p > v_O$ that extend to the separatrix (Owen & Cowley, 1987a; Owen et al., 2021).

1.5.2 Cold asymmetric inflows

Figure 1.19 shows a reconnecting current sheet with the same magnetic and electric field configuration as in the symmetric inflow case. However, unlike the previous scenario, the reconnection inflow is now assumed to be cold and asymmetric with different densities $n_1 > n_2$ and speeds $v_{I1} > v_{I2}$ in the NLRF. The subscripts 1 and 2 denote quantities above and below of the RCS, respectively. For brevity, I will only discuss the stress balance for the tailward side of the neutral line here. The stress balance analysis for the Earthward side follows similar reasoning and is detailed in Owen & Cowley (1987b).

Assuming full transmission of the inflow through the RCS with no reflection or scattering, the speed and density of the inflow beams remain constant as they cross the RCS. By summing the inflow and outflow beam distributions on each side of the RCS, Equation 1.66 yields the following current sheet stress balance condition on

the tailward side of the neutral line (Owen & Cowley, 1987b):

$$m_i(n_1 v_{IT1}^{\prime 2} + n_2 v_{IT2}^{\prime 2}) = \frac{B^2}{\mu_0}$$
 (1.79)

Setting $n_1 = n_2$ and $v'_1 = v'_2$ recovers the stress balance condition for the symmetric inflow case (Equation 1.69). Recalling the relationship between velocities in the NLRF and FLRF, the inflow beam speeds in the FLRF are:

$$v'_{IT1} = v_{FT} - v_{I1} \tag{1.80}$$

$$v'_{IT2} = v_{FT} - v_{I2} \tag{1.81}$$

Substituting Equations 1.80 and 1.81 into Equation 1.79 gives the following expression for the tailward field line recoil speed:

$$v_{FT} = R + v_{IM} \tag{1.82}$$

where $v_{IM} = (n_1v_{I1} + n_2v_{I2})/(n_1 + n_2)$ is the density-weighted mean of the inflow speeds and R is:

$$R = \sqrt{\frac{B^2}{\mu_0 m_i (n_1 + n_2)} - \frac{n_1 n_2 (v_{I1} - v_{I2})^2}{(n_1 + n_2)^2}}$$
(1.83)

This equation shows that real solutions to the stress balance conditions only exist if the inflow shear $\Delta v_I = v_{I1} - v_{I2}$ satisfies the inequality $|\Delta v_I| < \sqrt{V_{A1}^2 + V_{A2}^2}$, where V_{A1} and V_{A2} are the Alfvén speeds in the inflow region north and south of the RCS, respectively. If this condition is not met, no frame exists where the RCS stress balance conditions are satisfied. Therefore, reconnection is suppressed if the inflow shear across the RCS is sufficiently large (Owen & Cowley, 1987b).

Using similar reasoning to the symmetric inflow case, the outflow beam speeds in the NLRF are:

$$v_{OT1} = 2R + v_{IM} + \frac{n_1}{n_1 + n_2} \Delta v_I \tag{1.84}$$

$$v_{OT2} = 2R + v_{IM} - \frac{n_2}{n_1 + n_2} \Delta v_I \tag{1.85}$$

For the reconnection configuration specified in Figure 1.19 where $n_1 > n_2$ and $\Delta v_I >$ 0, these equations show that $v_{OT1} > v_{OT2}$. Therefore, the asymmetry in the outflow speed on the tailward side of the neutral line has the same sense as the inflow speed asymmetry. In the $|B_x| \gg |B_z|$ approximation, the angle ϕ between the RCS and the outflow region boundary is given by (Owen & Cowley, 1987b):

$$\phi = \left(1 - \frac{v_F}{v_O}\right)\theta\tag{1.86}$$

where $\theta = |B_z|/B$ is the opening angle of the reconnected field wedge. As expected, ϕ increases with v_O , ranging from a minimum of $\phi = 0$ when $v_O = v_F$ up to a maximum of $\phi = \theta$ as $v_O \to \infty$. As a result, outflow particles with greater field-aligned speeds will occupy a larger portion of the wedge.

1.5.3 Potential effects of reconnection heating

In both the symmetric (Section 1.5.1) and asymmetric (Section 1.5.2) inflow cases, the Owen & Cowley (1987a,b) current sheet stress balance models predict the existence of multi-layered reconnection outflow regions. Slower, less energetic particles are confined to layers near the central RCS, while faster, more energetic particles can extend to layers near the separatrix (see Figure 1.18). A key assumption in these models is that the reconnection inflow and outflow plasmas are treated as cold, with no heating as they cross the RCS.

However, this assumption breaks down if the inflow plasma is heated by reconnection as it crosses the RCS. When the outflow plasma is warm, density gradients develop between the inflow and outflow plasmas. This can induce diamagnetic current sheets at the boundary of the outflow region (Owen & Cowley, 1987a), consistent with observations of bifurcated RCS in solar wind reconnection outflows (Gosling et al., 2005a, 2006a; Gosling & Szabo, 2008). Additionally, similar density gradients between the particle layers inside the outflow region may also result in more complex reconnection outflow structures containing multiple current sheets (Owen et al., 2021).

Chapter 2

Instrumentation and Methods

2.1 Solar Orbiter

Solar Orbiter is an M-class mission under the European Space Agency's (ESA) Cosmic Vision programme jointly built and operated by ESA and NASA. It was launched on 10 February 2020, and after a 21-month cruise and commissioning phase, commenced full science operations on 26 November 2021 (Müller et al., 2020). The nominal mission phase (NMP) is projected to last 5 years, ending on 24 December 2026. During this phase, Solar Orbiter performed a series of gravity assist manoeuvers around Venus to gradually lower its perihelion to 0.284 AU and raise its orbital inclination out of the ecliptic plane. Subject to approval in early 2026, the three-year extended mission phase (EMP) will begin immediately following the end of the NMP and run until the end of mission, currently planned for July 2030 (García Marirrodriga et al., 2021). Additional Venus gravity assist manoeuvers during this phase will further raise the spacecraft's orbital inclination to 33°, allowing images of the Sun's polar regions to be taken for the first time. Figure 2.1 shows the trajectory of Solar Orbiter over the full duration of the NMP and EMP.

Solar Orbiter carries a comprehensive suite of instruments that enable it to make high-resolution remote sensing observations of the Sun and in-situ measurements of the solar wind in the inner heliosphere, both within and outside the ecliptic plane. Its scientific payload consists of six remote sensing instruments and four insitu instruments; their locations on the spacecraft are shown in Figure 2.2. The data collected by these instruments are publicly available on the *Solar Orbiter* Archive (SOAR, European Space Agency 2021). These combined observations are essential for answering the four top-level scientific questions of this mission:

- 1. What drives the solar wind and where does the coronal magnetic field originate?
- 2. How do solar transients drive heliospheric variability?
- 3. How do solar eruptions produce energetic particle radiation that fills the heliosphere?

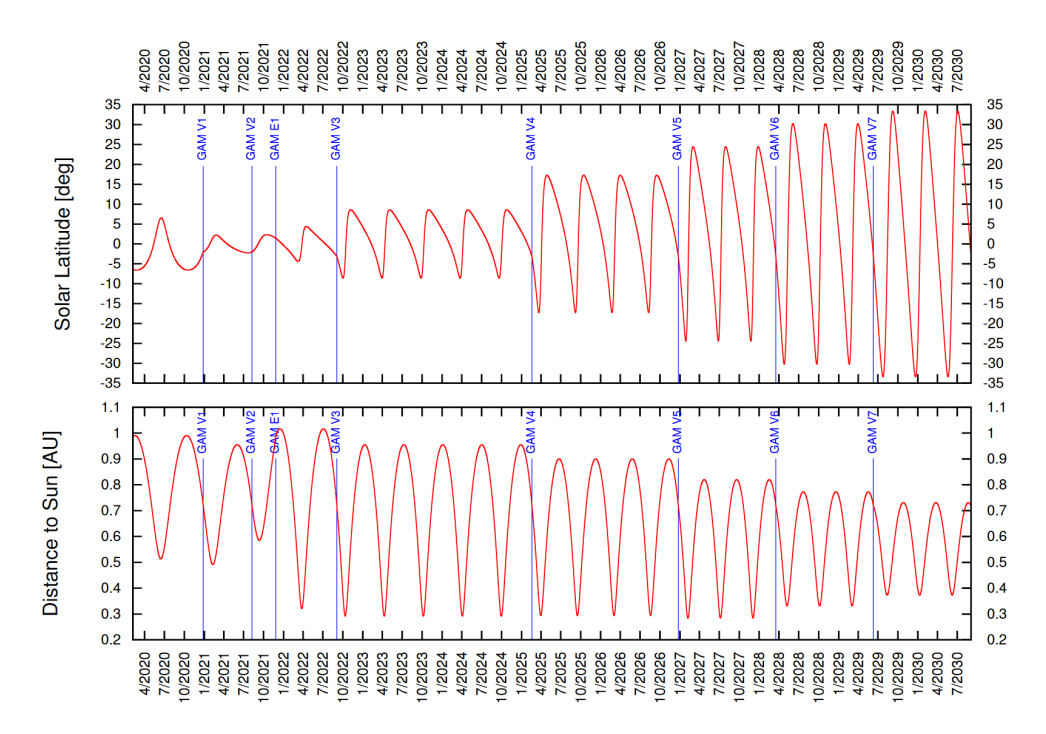


Figure 2.1: Solar latitude (top) and heliocentric distance (bottom) of *Solar Orbiter* during the NMP and EMP. The vertical blue lines mark times where *Solar Orbiter* performs gravity assist manoeuvers at Venus and Earth. Figure reproduced from Müller et al. (2020).

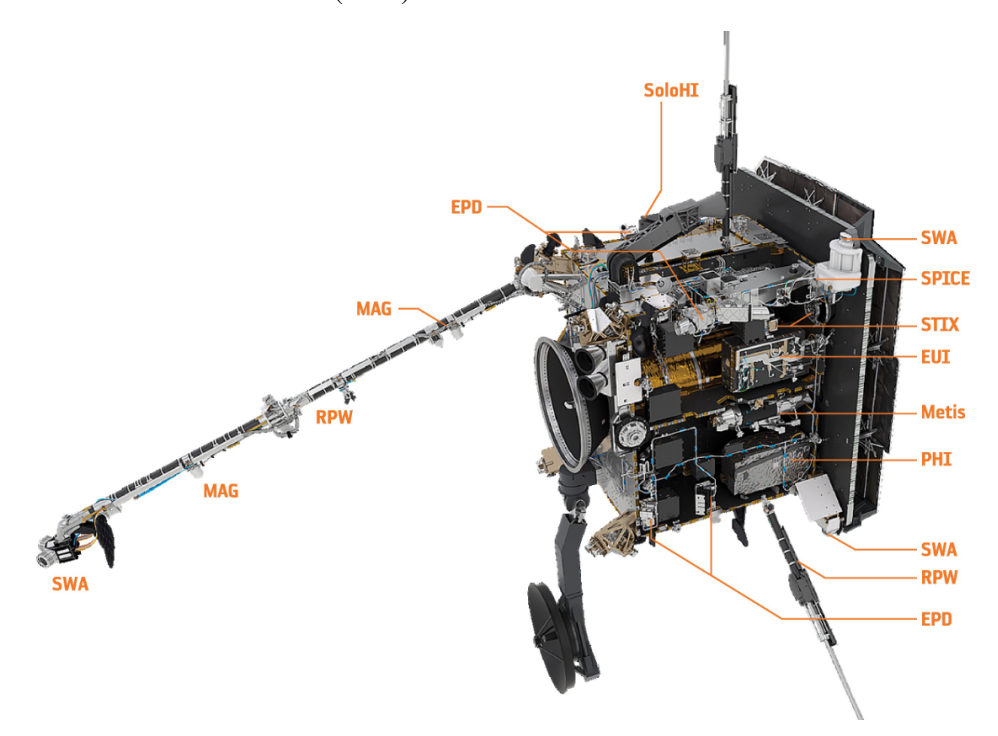


Figure 2.2: Location of instruments onboard *Solar Orbiter*. EPD, MAG, RPW, and SWA are in-situ instruments. EUI, Metis, PHI, SoloHI, SPICE, and STIX are remote sensing instruments. Reproduced from Müller et al. (2020).

4. How does the solar dynamo work and drive connections between the Sun and the heliosphere?

The work in this thesis on solar wind reconnection physics addresses a key subobjective of science question 1 – "What mechanisms heat and accelerate the solar wind?" (Müller et al., 2013; Zouganelis et al., 2020).

My analysis of reconnection outflows in the solar wind require local magnetic field and particle measurements. The discussion in Section 2.2 will briefly introduce the operating principles and capabilities of the Magnetometer (MAG) instrument, while Section 2.3 will cover the Electron Analyser System (EAS) and Proton Alpha Sensor (PAS) of the Solar Wind Analyser (SWA) instrument suite.

2.2 Fluxgate magnetometers

A fluxgate sensor comprises two coils — the driving coil and the sensing coil — wrapped around a ferromagnetic core (Ness, 1970). An alternating current is applied to the driving coil to induce a time-varying magnetic field B(t) in the sensor core. Through magnetic hysteresis, a sufficiently strong current will saturate the core at a constant $B = \pm B_{sat}$. In the absence of an external magnetic field, the core will spend an equal amount of time in positive and negative saturation. However, where there is an external field, the core will spend longer in saturation if the induced field is aligned with the external field than when it is anti-aligned.

This time-varying field produces an alternating voltage in the sensing coil, described by Faraday's Law:

$$\varepsilon(t) = N_{s} A \frac{dB(t)}{dt} \tag{2.1}$$

where N_s is the number of turns in the sensing coil and A is the cross-sectional area of the core. $\frac{dB(t)}{dt} = 0$ when the core is saturated, at which point $\varepsilon(t) = 0$. The waveform of $\varepsilon(t)$ thus depends on how much time the core spends in positive or negative saturation. Its second harmonic is a direct measure of the external field strength and can be isolated through use of a bandpass filter to attenuate higher order harmonics (Ness, 1970). A single fluxgate sensor can only measure one component of the magnetic field: the component aligned with the core axis. To measure all three, fluxgate magnetometers typically contain three orthogonally arranged sensors to provide 3-D magnetic field measurements.

Fluxgate magnetometers are ideal for space exploration as they have large measurements ranges, low power requirements, good reliability, and are well-suited for continuous operation during long missions (Acuña, 2002). For these reasons, they are the most common type of magnetometer used on spacecraft. This type of magnetometer is optimised for measuring background magnetic fields and low-frequency field fluctuations; the upper limit is set by the frequency of the driving coil. For measuring high-frequency field fluctuations, search coil magnetometer are preferred. *Solar Orbiter* is equipped with a pair of 3-axis fluxgate magnetometers

Mode	Range (nT)	Nominal resolution (pT)
3	±128	4
2	± 512	16
1	± 2048	64
0	± 58000	1800

Table 2.1: Measurement ranges of the *Solar Orbiter* MAG instrument. Table reproduced from Horbury et al. (2020a).

as part of its Magnetometer (MAG) instrument (Horbury et al., 2020a), and a single search coil magnetometer as part of its Radio and Plasma Waves (RPW) instrument suite (Maksimovic et al., 2020).

2.2.1 Magnetometer (MAG)

The *Solar Orbiter* magnetometer measures the local vector magnetic field at the spacecraft (Horbury et al., 2020a). The instrument consists of a pair of fluxgate magnetometers mounted on the instrument boom (see Figure 2.2): the outboard sensor (MAG-OBS) is located 3 m away from the spacecraft bus, and the inboard sensor (MAG-IBS) is located 1 m away. This configuration provides redundancy and enables in-flight measurement of the spacecraft's intrinsic magnetic field through gradiometry. By default, MAG-OBS is the primary sensor and operates at a higher cadence and resolution than MAG-IBS.

MAG has four measurement ranges, listed in Table 2.1, that it can switch between autonomously or on command. For typical conditions in the solar wind, MAG functions in the ± 128 nT range with a nominal resolution of 4 pT. Continuous measurements of the magnetic field are available at a cadence of 8 vectors/s in normal mode, and at a higher cadence of 64 or 128 vectors/s in burst mode.

2.3 Electrostatic analysers

The electrostatic analysers (EA) employed on *Solar Orbiter* are made up of three components: the entrance deflection system (EDS), the electrostatic analyser itself, and a detector array. Figure 2.3 shows a cross-section of the EA design used for the Proton Alpha Sensor (PAS) onboard *Solar Orbiter* (Owen et al., 2020). Incoming solar wind particles are guided into the entrance of the EA by the EDS. This consists of a pair of deflector plates above and below the entrance aperture; the potential difference between them can be adjusted to direct incident particles from a particular elevation angle into the EA.

The particles enter the EA, which has a 'top-hat' design, consisting of two concentrically nested hemispherical shells separated by a narrow channel (Carlson et al., 1982). A potential difference is applied across them, generating an electric field that determines the trajectory of the incident particles through the EA. For a given potential difference, only particles with a specific range of energy-to-charge

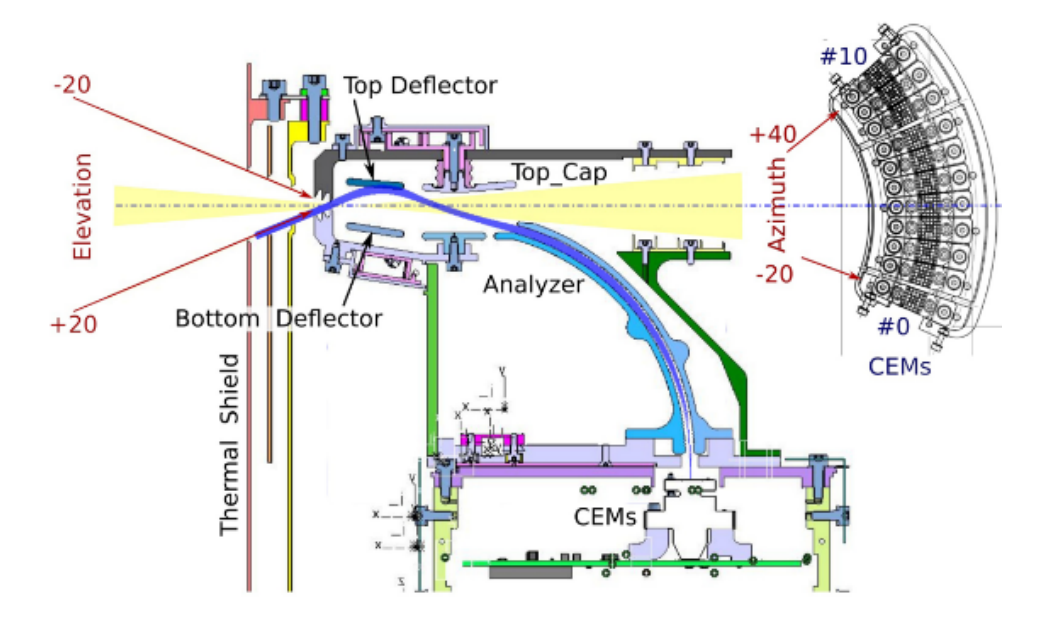


Figure 2.3: Cross-sectional diagram of the PAS EA. The blue line shows the trajectory of a particle through the instrument: 1) The EDS steers particles into the entrance of the EA. 2) The EA filters the incident particles based on their energy per charge. 3) Those with the correct range of energies per charge, determined by the potential difference applied to the EA, can pass through and strike the CEMs in the detector array. Top right: Arrangement of the CEMs in the detector array and their corresponding azimuthal range. Figure reproduced from Owen et al. (2020).

ratios can pass through the EA to reach the detector array at the bottom of the hemispheres, while those that do not strike the walls of the EA. Varying the potential difference allows particles with different energies to pass through. The energy per charge resolution is determined by the geometry of the hemisphere and width of the channel between them.

The EA also serves to focus the incident particles onto the detector array. On *Solar Orbiter*, this array is comprised of a series of channeltron electron multipliers (CEMs), divided into sectors covering the azimuthal range of the instrument. The azimuthal direction of the particles is determined by the azimuthal sector where the focal point is located, and the azimuthal resolution depends on the width of each individual sector. At each CEM, the count rate is a function of the incident particle flux for a given azimuth ϕ , elevation θ , and energy E. The relationship between the total number of counts C in time Δt with the distribution function f at a point (ϕ, θ, E) in phase space is:

$$C(\phi, \theta, E) \simeq \frac{2E^2}{m^2} Gf(\phi, \theta, E)$$
 (2.2)

where *G* is the geometric factor:

$$G = A_0 \Delta t \Delta \phi \Delta \theta \frac{\Delta E}{E} \tag{2.3}$$

This parameter is an inherent property of the EA, determined by its geometry and detection efficiency. Here, A_0 is the collecting area of the detector, $\Delta \phi$ is the azimuthal resolution, $\Delta \theta$ is the elevation resolution, and ΔE is the energy resolution. Although EAs are designed to keep G roughly constant, in practice it varies with (ϕ, θ, E) as well as time, due to degradation of the CEMs (Nicolaou et al., 2020). Therefore, the raw counts data from the instrument must be carefully calibrated on the ground in order to obtain valid distribution functions that describe the plasma.

2.3.1 Solar Wind Analyser (SWA)

The *Solar Orbiter* Solar Wind Analyser instrument suite measures various properties of the in-situ solar wind plasma population, including the 3-D VDFs of the protons, electrons, and alpha populations, as well as the VDFs and composition of the heavy ion population (Owen et al., 2020). It consists of three subsystems: EAS, PAS, and the Heavy Ion Sensor (HIS), along with a Data Processing Unit (DPU). As I do not use HIS data in this thesis, this section will only cover the details of EAS and PAS.

Electron Analyser System (EAS)

EAS measures 3-D VDFs of the electron population in the solar wind. It consists of a pair of identical, orthogonally arranged EA sensor heads mounted at the end of the instrument boom (see Figure 2.2). Each head has a field of view covering an azimuthal range of 360° , split into 32 equally sized bins; an elevation range $-45^{\circ} \le \theta \le +45^{\circ}$, split into 16 bins; and an energy range from 1 eV to 5 keV, split into 64 logarithmic bins. Together, the two sensor heads provide EAS with a full-sky field of view.

A single 3-D electron VDF measurement combines the $32 \times 16 \times 64$ sampling space in azimuth, elevation, and energy of each sensor head. EAS measures the incident particle counts across all azimuthal bins simultaneously, whereas measurements across the elevation and energy bins are performed sequentially — for each elevation bin, EAS sweeps across all energy bins before proceeding to the next elevation bin. The entire sampling process takes 1 s to complete.

Due to telemetry restriction, full 3-D electron VDFs can not be transmitted to the ground at 1 s cadence. Instead, they are stored by the DPU in a 5 minute rolling buffer, with the cadence and type of the data transmitted to the ground dependent on the operational mode of EAS. In normal mode, EAS delivers 1 full 3-D electron VDF every 10 or 100 seconds and partial moments every 4 seconds. In burst mode, EAS measures 8 2-D pitch angle distributions (PAD) per second. Finally, if trigger mode is enacted, EAS delivers all 3-D electron VDFs stored in the buffer at a cadence of 1 second covering a period of 5 minutes. EAS operates in normal mode by default, while the higher cadence modes are activated by command or in the case of trigger mode, upon the detection of a shock by the RPW Data Processing Unit.

Proton Alpha Sensor (PAS)

PAS measures 3-D VDFs of the proton and alpha populations in the solar wind. It consists of a single Sun-facing EA mounted behind a cutout in the spacecraft heat shield (see Figure 2.2). The instrument has a field of view covering an azimuthal range $-24^{\circ} \le \phi \le +42^{\circ}$, split into 11 bins; an elevation range $-22.5^{\circ} \le \theta \le +22.5^{\circ}$, split into 9 bins; and an energy-per-charge range from 200 eV to 20 keV, split into 96 logarithmic bins.

A single 3-D ion VDF measurement may cover the full $11 \times 9 \times 96$ sampling space in azimuth, elevation, and energy. As with EAS, PAS measures the incident particle counts across all azimuthal bins simultaneously, and across the elevation and energy bins sequentially. Unlike EAS, however, PAS instead sweeps across all elevation bins for each energy bin before proceeding to the next. The entire sampling process takes 1 s to complete. PAS has known sensitivity problems at the lower end of its energy range, leading to undercounting in the low energy bins. While these lost counts are often recoverable through careful calibration of the instrument, at energies below 300 eV, there are too few counts in these bins for them to be recovered by statistical methods. Consequently, when the solar wind velocity is less than $\sim 300 \text{ km s}^{-1}$, the VDFs and all PAS data products derived from them are unreliable (Fedorov, 2022; Lewis et al., 2023).

In normal mode, the cadence of PAS is 1 full 3-D VDF every 4 seconds with 3 seconds of downtime between measurements. These VDFs are then processed on the ground to produce a set of moments data at the same cadence, describing the bulk properties of the solar wind protons: density, bulk velocity, and pressure tensor. The size of the sampling space can be reduced to decrease the sampling time and increase the measurement cadence. To achieve this without losing information, PAS automatically centres the reduced sampling space about the peak of the ion VDF. In burst mode, PAS measures 4 reduced VDFs per second. This high-cadence mode is activated either by command or during pre-programmed 'snapshot' windows that occur once every 5 minutes.

2.4 Coordinate systems and frame transformation techniques

MAG and SWA data from the *Solar Orbiter* Archive are provided in the RTN coordinate system. This is a spacecraft-centred coordinate system commonly used in heliophysics where R is the Sun-spacecraft radial vector, T is the cross product between the Sun's rotation axis and R, and N completes the triad. However, reconnection current sheets and outflows usually do not align with the basis vectors of this coordinate system. Additionally, these structures are convected past the spacecraft by the solar wind flow at speeds of several 10^2 km s^{-1} . To facilitate the analysis of solar wind reconnection, an RCS-aligned coordinate system and a reference frame

that is co-moving with the entire reconnection outflow structure must therefore be defined.

2.4.1 Current sheet-aligned coordinate system

The current sheet-aligned coordinate system, or lmn coordinate system, is determined using the minimum variance analysis (MVAB) method (Sonnerup & Cahill, 1967) on measurements of the magnetic field vector \mathbf{B} . To understand how MVAB works, an idealised planar current sheet is first considered. If this current sheet is infinitely thin, the normal component B_n of \mathbf{B} across it must be constant, in order to satisfy the $\nabla \cdot \mathbf{B} = 0$ condition for magnetic fields. For current sheets of finite thickness, this is also approximately true provided that its radius of curvature and length scale for lateral changes are much greater than its thickness. Therefore:

$$\mathbf{B}_{IJ} \cdot \hat{\mathbf{n}} = \mathbf{B}_{I} \cdot \hat{\mathbf{n}} = \mathbf{B}_{D} \cdot \hat{\mathbf{n}}, \tag{2.4}$$

where $\hat{\mathbf{n}}$ is the unit vector normal to the current sheet, and \mathbf{B}_U , \mathbf{B}_I , \mathbf{B}_D are the magnetic field vectors upstream, within, and downstream of the current sheet, respectively. As a direct consequence of Equation 2.4, the vectors $\mathbf{B}_U - \mathbf{B}_D$ and $\mathbf{B}_U - \mathbf{B}_I$ must be both co-planar and tangential to the current sheet. Hence, $\hat{\mathbf{n}}$ can be defined as:

$$\hat{\mathbf{n}} = \frac{(\mathbf{B}_U - \mathbf{B}_D) \times (\mathbf{B}_U - \mathbf{B}_I)}{|(\mathbf{B}_U - \mathbf{B}_D) \times (\mathbf{B}_U - \mathbf{B}_I)|}.$$
(2.5)

Only three magnetic field measurements upstream, within, and downstream of the current sheet are needed to determine $\hat{\mathbf{n}}$, provided that they are either simultaneous or taken over a time period that is shorter than the timescales over which the current sheet evolves.

In practice, it is easier to choose $\hat{\mathbf{n}}$ such that the variance σ^2 of $\mathbf{B}_i \cdot \hat{\mathbf{n}}$ about a mean $\langle \mathbf{B} \rangle \cdot \hat{\mathbf{n}}$ is minimised for N measurements:

$$\sigma^2 = \frac{1}{N} \sum_{i=1}^{N} (\mathbf{B}_i \cdot \hat{\mathbf{n}} - \langle \mathbf{B} \rangle \cdot \hat{\mathbf{n}})^2$$
 (2.6)

where the subscript i denotes an individual measurement of **B** and $\langle \rangle$ denotes the average of any given quantity over N measurements. The minimisation of Equation 2.6 is the equivalent of finding the smallest eigenvalue λ_3 of the co-variant matrix **M**:

$$\mathbf{M} = \begin{pmatrix} \langle B_R B_R \rangle - \langle B_R \rangle \langle B_R \rangle & \langle B_R B_T \rangle - \langle B_R \rangle \langle B_T \rangle & \langle B_R B_N \rangle - \langle B_R \rangle \langle B_N \rangle \\ \langle B_R B_T \rangle - \langle B_R \rangle \langle B_T \rangle & \langle B_T B_T \rangle - \langle B_T \rangle \langle B_T \rangle & \langle B_T B_N \rangle - \langle B_T \rangle \langle B_N \rangle \\ \langle B_R B_N \rangle - \langle B_R \rangle \langle B_N \rangle & \langle B_T B_N \rangle - \langle B_T \rangle \langle B_N \rangle & \langle B_N B_N \rangle - \langle B_N \rangle \langle B_N \rangle \end{pmatrix} (2.7)$$

The eigenvector corresponding to λ_3 is therefore the minimum variance direction of **B**. Similarly, the eigenvectors corresponding to the intermediate eigenvalue λ_2

and the largest eigenvalue λ_1 point in the intermediate and maximum variance directions, respectively. It is commonly assumed that if the eigenvalue ratios λ_1/λ_2 and λ_2/λ_3 are greater than ~ 10 (Sonnerup & Scheible, 1998; Knetter et al., 2004), these eigenvectors are well-defined and well-separated. In this case, the maximum, intermediate, and minimum variance directions can be used to define the *lmn* coordinate system basis vectors $\hat{\bf l}$, $\hat{\bf m}$, $\hat{\bf n}$, respectively.

The MVAB method thus works on the basis of finding the direction in which B_n varies the least, in order to approximately satisfy Equation 2.4. If this equation is exactly satisfied, the smallest eigenvalue of \mathbf{M} is zero and the MVAB method produces the same results as Equation 2.5. It should be noted that Equation 2.5 breaks down if $(\mathbf{B}_U - \mathbf{B}_D)$ and $(\mathbf{B}_U - \mathbf{B}_I)$ are parallel to each other, corresponding to the case where \mathbf{M} has degenerate eigenvalues. This results in a situation where neither method can be used to determine $\hat{\mathbf{n}}$. Similarly, if any of the eigenvalues of \mathbf{B} are degenerate, the basis vectors $\hat{\mathbf{l}}$, $\hat{\mathbf{m}}$, $\hat{\mathbf{n}}$ derived using the MVAB method are not well-defined. Furthermore, the dependence of Equation 2.6 and \mathbf{M} on $\langle \mathbf{B} \rangle$ means that MVAB estimate of $\hat{\mathbf{n}}$ is sensitive to the choice of start and end times of the averaging window used to calculate $\langle \mathbf{B} \rangle$.

In this thesis, I employ a modified version of the minimum variance analysis method known as hybrid MVAB (Gosling & Phan, 2013). The majority of RCS in the solar wind are characterised by magnetic shear angles $< 60^{\circ}$ (Gosling et al., 2007; Phan et al., 2010; Gosling & Phan, 2013), for which MVAB estimates of $\hat{\mathbf{n}}$ are inaccurate (Knetter et al., 2004). Compared to traditional MVAB, hybrid MVAB produces more reliable estimates of $\hat{\mathbf{n}}$ for RCS with modest shear angles below 60° , while producing similar estimates to traditional MVAB at larger shear angles (Wang et al., 2024). Using this method, $\hat{\mathbf{n}}$ is defined as the cross product between the magnetic field vector $\mathbf{B_1}$ and $\mathbf{B_2}$ at the leading and trailing edges of the current sheet, respectively:

$$\hat{\mathbf{n}} = \frac{\mathbf{B}_1 \times \mathbf{B}_2}{|\mathbf{B}_1 \times \mathbf{B}_2|} \tag{2.8}$$

and $\hat{\mathbf{m}} = \hat{\mathbf{l}}' \times \hat{\mathbf{n}}$, where $\hat{\mathbf{l}}'$ is the maximum variance direction determined from traditional MVAB. For most reconnection events, $\hat{\mathbf{l}}'$ has the largest eigenvalue ratio λ_1/λ_2 and hence, is the most well-defined direction (Denton et al., 2018). To complete the triad, $\hat{\mathbf{l}} = \hat{\mathbf{m}} \times \hat{\mathbf{n}}$. For an idealised planar RCS, $\hat{\mathbf{l}}$, $\hat{\mathbf{m}}$, and $\hat{\mathbf{n}}$ are approximately aligned with the reconnection outflow, neutral line, and RCS normal, respectively (Gosling & Phan, 2013; Phan et al., 2020, 2024).

2.4.2 deHoffmann-Teller analysis

In the ideal MHD limit, Ohm's Law implies that the convection electric field $\mathbf{E} = -\mathbf{u} \times \mathbf{B}$ is perpendicular to both the magnetic field and bulk flow (i.e., $\mathbf{E}_{\parallel} = 0$), where \mathbf{u} is the bulk velocity in the frame of the observing spacecraft. Charged particles in these fields will execute helical gyromotion along the magnetic field with

parallel velocity \mathbf{u}_{\parallel} and experience an $\mathbf{E} \times \mathbf{B}$ drift across the magnetic field lines (Section 1.1.2). Substituting \mathbf{E} into Equation 1.9 shows that the $\mathbf{E} \times \mathbf{B}$ drift velocity $\mathbf{v}_E = \mathbf{u}_{\perp}$, the perpendicular component of the bulk velocity.

A new reference frame, where $\mathbf{u}_{\perp}'=0$, can then be defined, using the transformation $\mathbf{u}'=\mathbf{u}-\mathbf{V}_{HT}$. In this frame, the perpendicular component of the electric field $\mathbf{E}_{\perp}'=0$. If $\mathbf{E}_{\parallel}=0$, as is the case in ideal MHD, then the total electric field \mathbf{E}' in the transformed frame is zero:

$$\mathbf{E}' = \mathbf{E} + \mathbf{V}_{HT} \times \mathbf{B} = 0 \tag{2.9}$$

This frame, known as the deHoffmann-Teller (HT) frame (de Hoffmann & Teller, 1950), moves with velocity \mathbf{V}_{HT} relative to the spacecraft frame. If a structure in the magnetic field is time stationary and frozen into the bulk flow, then \mathbf{u} is equal across the structure. In this case, a single HT frame can be defined where $\mathbf{E}'=0$ everywhere; this HT frame thus corresponds to the rest frame of the structure. It is important to note that while a transformation into the HT frame removes the perpendicular component of the bulk flow (i.e., $\mathbf{u}'_{\perp}=0$), it does not necessarily remove the \mathbf{u}_{\parallel} component of the bulk flow. Therefore, the flow on both sides of the structure is field-aligned in the absence of the $\mathbf{E} \times \mathbf{B}$ drift. Furthermore, if $\mathbf{E}'=0$ in the HT frame, Faraday's Law:

$$\nabla \times \mathbf{E}' = -\left(\frac{\partial \mathbf{B}'}{\partial t}\right) = 0 \tag{2.10}$$

implies that the magnetic field structure is time-stationary in this frame.

In the real solar wind, non-ideal MHD effects may introduce a non-zero \mathbf{E}_{\parallel} component into the electric field that can not be transformed away. As a result, the deHoffmann-Teller analysis method is used to determine \mathbf{V}_{HT} for a set of observations by minimising \mathbf{E}' in Equation 2.9, which is done by solving the following linear matrix equation (Khrabrov & Sonnerup, 1998; Paschmann & Sonnerup, 2008):

$$\begin{pmatrix} \langle B_T^2 + B_N^2 \rangle & \langle -B_R B_T \rangle & \langle -B_R B_N \rangle \\ \langle -B_R B_T \rangle & \langle B_R^2 + B_N^2 \rangle & \langle -B_T B_N \rangle \\ \langle -B_R B_N \rangle & \langle -B_T B_N \rangle & \langle B_R^2 + B_T^2 \rangle \end{pmatrix} \begin{pmatrix} V_{HT,R} \\ V_{HT,T} \\ V_{HT,N} \end{pmatrix} = \begin{pmatrix} \langle E_T B_N - E_N B_T \rangle \\ \langle E_N B_R - E_R B_N \rangle \\ \langle E_R B_T - E_T B_R \rangle \end{pmatrix} (2.11)$$

As the solar wind can be approximated in the ideal MHD regime over large scales, the spacecraft frame electric field is calculated using $\mathbf{E} = -\mathbf{u} \times \mathbf{B}$. I chose to do this instead of using direct measurements from RPW (Maksimovic et al., 2020), which can only measure two components of \mathbf{E} . It has been shown that estimates of \mathbf{V}_{HT} derived using measurements of \mathbf{E} from RPW do not differ significantly from those obtained using \mathbf{E} calculated from Ohm's Law (Steinvall et al., 2021).

In a single RCS configuration (i.e., magnetotail reconnection; see Section 1.5),

the current sheet stress balance conditions are evaluated in the FLRF, which corresponds to a single HT frame with a frame speed equal to the $\mathbf{E} \times \mathbf{B}$ drift speed at the RCS centreline (Owen & Cowley, 1987a,b). However, in a bifurcated RCS configuration (i.e., solar wind reconnection; see Section 1.3.4), the system is no longer characterised by a single global HT frame. Although a FLRF can still be defined, the magnetic field discontinuities across each current sheet are not stationary in this frame. Instead, they move apart as the bifurcated RCS diverges with increasing distance from the neutral line (see Figure 1.11). The stress balance conditions at each current sheet must therefore be evaluated in the corresponding discontinuity rest frame (DRF), which is determined by performing the HT analysis locally at each discontinuity (Gosling et al., 2005a).

Chapter 3

Development of bifurcated current sheet stress balance models for reconnection in the solar wind

3.1 Introduction

In Section 1.5, I introduced the current sheet stress balance models in the context of magnetic reconnection in the Earth's magnetotail (Owen & Cowley, 1987a,b). As plasma β is small in this regime, the plasma pressure can be neglected and the magnetic pressure on both sides of the reconnection current sheet (RCS) must be equal to maintain overall pressure balance. The reconnection inflows and outflows are treated as cold plasmas that do not experience heating as they cross the single central RCS. Under these conditions, magnetic tension in the reconnected field lines is balanced by the change in momentum of the plasma as it flows across the RCS. In this chapter, I extend the mathematical framework of these existing current sheet stress balance models to describe reconnection outflows in the solar wind.

There are some key differences between the magnetotail and the solar wind that must be accounted for. Firstly, plasma β is comparable to 1 in the solar wind, so the plasma pressure can no longer be neglected. Secondly, RCS in the solar wind are bifurcated (Gosling et al., 2005a, 2006a; Gosling & Szabo, 2008), with the reversal in the magnetic field occurring across two current sheets rather than just one. If reconnection heats the outflow plasma, a plasma pressure gradient will exist across the RCS that must be balanced in steady state by a change in the magnetic pressure and hence, magnetic field strength. It is postulated (Owen et al., 2021) that this mechanism may be responsible for the bifurcation of the RCS in the Gosling reconnection model (Gosling et al. 2005a, see Section 1.3.4), and means the magnetic field strength on either side of the bifurcated RCS are not equal.

Since the outflow from one current sheet contributes to the stress balance at the other current sheet in this configuration, the bifurcated current sheet pair form a coupled system and the solutions to the stress balance conditions at both must be self-consistent. In the magnetotail stress balance models, it is assumed that $|B_x| \gg |B_z|$ on both sides of the current sheet (Owen & Cowley, 1987a,b), where B_x is the component of the magnetic field tangential to the current sheet and B_z is the component normal to it. In a bifurcated RCS, the decrease in the magnetic field strength in the outflow region leads to a decrease in $|B_x|$ while $|B_z|$ remains constant. As a result, the $|B_x| \gg |B_z|$ assumption does not necessarily apply on the side of the current sheet containing the outflow region.

In Section 3.2, I re-work the stress balance conditions for a single current sheet, taking into account the differences between conditions in the Earth's magnetotail and the solar wind. In Section 3.3, I extend the modified single current sheet stress balance conditions to a bifurcated RCS configuration, typical of those found in the solar wind. In Section 3.4, I test the bifurcated RCS stress balance conditions using a simple model of a reconnection outflow in the solar wind. Using these conditions, I make predictions of the reconnection geometry and the nature of the beam population within the outflow region. Finally, I discuss the results of my model and compare its predictions with the observed properties of reconnection outflows in the solar wind in Section 3.5.

3.2 Stress balance for a single current sheet

I first consider the stress balance for a single, thin, 1-D current sheet in steady-state, with isothermal proton inflow beams incident upon it from Region A above (Beam 1) and Region B below (Beam 2). Throughout this work, I use the convention that the subscripts 1 and 2 refer to properties pertaining to Beams 1 and 2, respectively. Similarly, the subscripts A and B denote the properties of the beams and magnetic field in Regions A and B, respectively. In the field line rest frame (FLRF), Beam 1 has velocity \mathbf{u}'_{1A} , density n_{1A} , and temperature T_{1A} in Region A, while Beam 2 has velocity \mathbf{u}'_{2B} , density n_{2B} , and temperature T_{2B} in Region B.

Figure 3.1 shows the current sheet configuration in the FLRF using the lmn coordinate system, where $\hat{\bf n}$ is the current sheet normal vector, and the $\hat{\bf l}$ and $\hat{\bf m}$ vectors lie in the plane of the current sheet. The FLRF corresponds to its deHoffmann-Teller (HT) frame (Section 2.4.2), which means the electric field in this frame is transformed away (Khrabrov & Sonnerup, 1998; Paschmann & Sonnerup, 2008). In the absence of the $\bf E \times \bf B$ drift, the beams passing through the current sheet propagate along the field-aligned direction on both sides. The proton population in Regions A and B consists of a pair of counterstreaming beams. In Region A, the inflow Beam 1 is co-located with Beam 2 after the latter has passed through the current sheet. Here, Beam 2 has velocity $\bf u'_{2A}$, density n_{2A} , and temperature T_{2A} . Likewise, in Region B, the inflow Beam 2 is co-located with Beam 1 after the latter has passed through the current sheet. Here, Beam 1 has velocity $\bf u'_{1B}$, density n_{1B} , and temperature T_{1B} . Therefore, the total distribution function describing the proton population in both

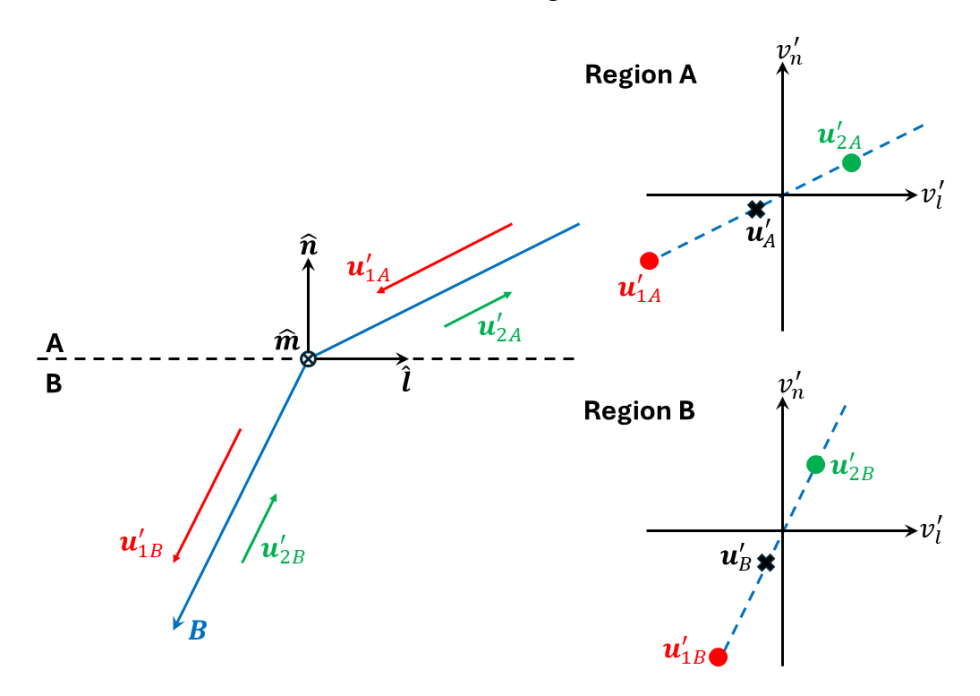


Figure 3.1: Left: Inflow and outflow beam configuration for a single 1-D current sheet in steady state in the FLRF. The dotted black line represents the current sheet and the blue arrows represent the magnetic field. The red arrows show the inflow beam \mathbf{u}'_{1A} before and after it passes through the current sheet to become beam \mathbf{u}'_{1B} . Similarly, the green arrows show the inflow beam \mathbf{u}'_{2B} before and after it passes through the current sheet to become beam \mathbf{u}'_{2A} . Top right: Proton distribution function in Region A, consisting of the isothermal counterstreaming beams \mathbf{u}'_{1A} (red) and \mathbf{u}'_{2A} (green). The black cross represents the net proton bulk velocity and the dashed blue line denote the l and n-components of the beam velocities that result in field-aligned propagation. Bottom right: Proton distribution function in Region B, consisting of the isothermal counterstreaming beams \mathbf{u}'_{1B} (red) and \mathbf{u}'_{2B} (green).

regions is the sum of the distribution of the individual counterstreaming beams:

$$f_A = f_{1A} + f_{2A} \tag{3.1}$$

$$f_B = f_{1B} + f_{2B} (3.2)$$

Furthermore, since $|\mathbf{u}'_{1A}| \neq |\mathbf{u}'_{2A}|$ and $|\mathbf{u}'_{1B}| \neq |\mathbf{u}'_{2B}|$, there is a non-zero bulk flow $\mathbf{u}'_{\mathbf{A}}$ and $\mathbf{u}'_{\mathbf{B}}$ in Regions A and B, respectively.

As a net field-aligned bulk flow exists across the current sheet (Owen & Cowley 1987b, see Section 1.5.2), the steady-state MHD momentum conservation equation (Equation 1.25) for this system is:

$$\rho(\mathbf{u}' \cdot \nabla)\mathbf{u}' = -\nabla \cdot \mathbf{P} - \nabla \left(\frac{B^2}{2\mu_0}\right) + \frac{1}{\mu_0} (\mathbf{B} \cdot \nabla)\mathbf{B}$$
 (3.3)

where $\rho = nm_i$ is the mass density. Here, I have expanded the $\mathbf{J} \times \mathbf{B}$ term into

a magnetic pressure gradient and magnetic tension component, corresponding to the second and third terms on the right-hand side, respectively. In a 1-D system, quantities vary only in the $\hat{\bf n}$ -direction so $\partial/\partial l = \partial/\partial m = 0$. Thus, Equation 3.3 simplifies to:

$$\rho u_n' \frac{\partial}{\partial n} \mathbf{u}' = -\nabla \cdot \mathbf{P} - \frac{\partial}{\partial n} \left(\frac{B^2}{2\mu_0} \right) \hat{\mathbf{n}} + \frac{1}{\mu_0} B_n \frac{\partial}{\partial n} \mathbf{B}$$
 (3.4)

Additionally, the steady-state mass continuity condition $\nabla \cdot (\rho \mathbf{u}') = 0$ (Equation 1.24) and divergence-free magnetic field condition $\nabla \cdot \mathbf{B} = 0$ for a 1-D system imply that $\rho u'_n$ and B_n are both constants. I then expand $\nabla \cdot \mathbf{P}$ term in Equation 3.4 that describes the divergence of the pressure tensor:

$$\nabla \cdot \mathbf{P} = \frac{\partial P_{nl}}{\partial n} \hat{\mathbf{i}} + \frac{\partial P_{nm}}{\partial n} \hat{\mathbf{m}} + \frac{\partial P_{nn}}{\partial n} \hat{\mathbf{n}}$$
(3.5)

Substituting this into Equation 3.4, the MHD momentum equation can be decomposed into its $\hat{\mathbf{l}}$, $\hat{\mathbf{m}}$, and $\hat{\mathbf{n}}$ components:

$$\rho u_n' u_l' + P_{nl} - \frac{B_n B_l}{\mu_0} = C_1. \tag{3.6}$$

$$\rho u_n' u_m' + P_{nm} - \frac{B_n B_m}{\mu_0} = C_2. \tag{3.7}$$

$$\rho u_n^{'2} + P_{nn} + \frac{B^2}{2\mu_0} = C_3. \tag{3.8}$$

where C_1 , C_2 , and C_3 are constants.

In the next step, I derive equations for the P_{nl} , P_{nm} , and P_{nn} terms of Equations 3.6–3.8 in Regions A and B. For brevity, only the derivation of these terms for Region A is shown here, as the derivation for Region B is identical. Starting with the pressure tensor (Equation 1.23) in Region A:

$$P_{A,ij} = m \left(\int (v_i - u'_{A,i})(v_j - u'_{A,j}) f_{1A} d^3 \mathbf{v} + \int (v_i - u'_{A,i})(v_j - u'_{A,j}) f_{2A} d^3 \mathbf{v} \right)$$
(3.9)

By expanding both integrals on the right-hand side of this equation, I obtain:

$$P_{A,ij} = n_{1A}k_BT_{1A,ij} + \rho_{1A}(u'_{1A,i} - u'_{A,i})(u'_{1A,j} - u'_{A,j}) + n_{2A}k_BT_{2A,ij} + \rho_{2A}(u'_{2A,i} - u'_{A,i})(u'_{2A,j} - u'_{A,j})$$
(3.10)

Since the inflow and outflow beams are assumed isotropic, $T_{ij} = 0$ if $i \neq j$ and $T_{ij} = T$ if i = j, therefore:

$$P_{A,nl} = \rho_{1A}(u'_{1A,l} - u'_{A,l})(u'_{1A,n} - u'_{A,n}) + \rho_{2A}(u'_{2A,l} - u'_{A,l})(u'_{2A,n} - u'_{A,n})$$
(3.11)

$$P_{A,nm} = \rho_{1A}(u'_{1A,m} - u'_{A,m})(u'_{1A,n} - u'_{A,n}) + \rho_{2A}(u'_{2A,m} - u'_{A,m})(u'_{2A,n} - u'_{A,n})$$
(3.12)

$$P_{A,nn} = P_{1A} + P_{2A} + \rho_{1A}(u'_{1A,n} - u'_{A,n})^2 + \rho_{2A}(u'_{2A,n} - u'_{A,n})^2$$
(3.13)

where $P_{1A} = n_{1A}k_BT_{1A}$ and $P_{2A} = n_{2A}k_BT_{2A}$. Substituting these expressions for $P_{A,nl}$, $P_{A,nm}$, and $P_{A,nn}$ into Equations 3.6–3.8 yields:

$$\rho_{A}u'_{A,n}u'_{A,l} + P_{A,nl} - \frac{B_{n}B_{A,l}}{\mu_{0}} = \rho_{1A}u'_{1A,l}u'_{1A,n} + \rho_{2A}u'_{2A,l}u'_{2A,n} - \frac{B_{n}B_{A,l}}{\mu_{0}}$$
(3.14)

$$\rho_{A}u'_{A,n}u'_{A,m} + P_{A,nm} - \frac{B_{n}B_{A,m}}{\mu_{0}} = \rho_{1A}u'_{1A,m}u'_{1A,n} + \rho_{2A}u'_{2A,m}u'_{2A,n} - \frac{B_{n}B_{A,m}}{\mu_{0}} \quad (3.15)$$

$$\rho_{A}u_{A,n}^{'2} + P_{A,nn} + \frac{B_{A}^{2}}{2\mu_{0}} = P_{1A} + P_{2A} + \rho_{1A}u_{1A,n}^{'2} + \rho_{2A}u_{2A,n}^{'2} + \frac{B_{A}^{2}}{2\mu_{0}}$$
(3.16)

Applying the same procedure for Region B, the corresponding equations in this region are:

$$\rho_B u_{B,n} u'_{B,l} + P_{B,nl} - \frac{B_n B_{B,l}}{\mu_0} = \rho_{1B} u'_{1B,l} u'_{1B,n} + \rho_{2B} u'_{2B,l} u'_{2B,n} - \frac{B_n B_{B,l}}{\mu_0}$$
(3.17)

$$\rho_B u'_{B,n} u'_{B,m} + P_{B,nm} - \frac{B_n B_{B,m}}{\mu_0} = \rho_{1B} u'_{1B,m} u'_{1B,n} + \rho_{2B} u'_{2B,m} u'_{2B,n} - \frac{B_n B_{B,m}}{\mu_0} \quad (3.18)$$

$$\rho_B u_{B,n}^{'2} + P_{B,nn} + \frac{B_B^2}{2\mu_0} = P_{1B} + P_{2B} + \rho_{1B} u_{1B,n}^{'2} + \rho_{2B} u_{2B,n}^{'2} + \frac{B_B^2}{2\mu_0}$$
(3.19)

Equating Equations 3.14, 3.15, and 3.16 with Equations 3.17, 3.18, and 3.19, respectively yields the stress balance conditions for a single current sheet in the FLRF in the $\hat{\mathbf{l}}$, $\hat{\mathbf{m}}$, and $\hat{\mathbf{n}}$ directions:

$$\rho_{1B}u'_{1B,l}u'_{1B,n} + \rho_{2B}u'_{2B,l}u'_{2B,n} - \rho_{1A}u'_{1A,l}u'_{1A,n} - \rho_{2A}u'_{2A,l}u'_{2A,n} = \frac{B_n}{\mu_0}(B_{B,l} - B_{A,l})$$

$$\rho_{1B}u'_{1B,m}u'_{1B,n} + \rho_{2B}u'_{2B,m}u'_{2B,n} - \rho_{1A}u'_{1A,m}u'_{1A,n} - \rho_{2A}u'_{2A,m}u'_{2A,n} = \frac{B_n}{\mu_0}(B_{B,m} - B_{A,m})$$

$$(3.20)$$

$$P_{1A} + P_{2A} - P_{1B} - P_{2B} + \rho_{1A}u'_{1A,n}^2 + \rho_{2A}u'_{2A,n}^2 - \rho_{1B}u'_{1B,n}^2 - \rho_{2B}u'_{2B,n}^2 = \frac{1}{2\mu_0}(B_B^2 - B_A^2)$$

$$(3.22)$$

Equations 3.20 and 3.21 shows that the magnetic tension force in the $\hat{\mathbf{l}}$ and $\hat{\mathbf{m}}$ directions, respectively, is balanced by the combined change in momentum of the beams in the corresponding directions as they cross the current sheet. This result is in agreement with the stress balance conditions derived for current sheets in the Earth's magnetotail (Owen & Cowley, 1987a,b).

Equation 3.22 shows that in the $\hat{\mathbf{n}}$ direction, the change in magnetic pressure is balanced by the change in the plasma thermal pressure of the individual beams and their flow pressure across the current sheet. This differs from the magnetotail case,

where the beams are assumed to be cold (i.e., P = 0), and there is no change in the magnetic pressure across the current sheet (Owen & Cowley, 1987b).

Focusing on the flow pressure terms $\rho u'^2$ on the left-hand side of Equation 3.22, the mass continuity condition requires $\rho_{1A}u'_{1A,n} = \rho_{1B}u'_{1B,n}$ and $\rho_{2A}u'_{2A,n} = \rho_{2B}u'_{2B,n}$. One of the underlying assumptions of the magnetotail stress balance conditions is that the beam densities do not vary across the current sheet, i.e., $\rho_{1A} = \rho_{1B}$ and $\rho_{2A} = \rho_{2B}$ (Owen & Cowley 1987b, see Section 1.5.2). Hence, from the mass continuity condition, it follows that $u'_{1A,n} = u'_{1B,n}$ and $u'_{2A,n} = u'_{2B,n}$, so the sum of the flow pressure terms becomes:

$$\rho_{1A}u_{1A,n}^{'2} + \rho_{2A}u_{2A,n}^{'2} - \rho_{1B}u_{1B,n}^{'2} - \rho_{2B}u_{2B,n}^{'2} = 0$$
(3.23)

Equation 3.22 thus simplifies to:

$$P_{1A} + P_{2A} + \frac{B_A^2}{2\mu_0} = P_{1B} + P_{2B} + \frac{B_B^2}{2\mu_0}$$
 (3.24)

which is identical to the magnetotail stress balance condition described by Equation 1.67. Under this assumption, Equations 3.23 and 3.24 suggest that there is no change in the normal momentum flux, and the normal pressure balance is solely due to the magnetic and plasma pressure. Additionally, under the further assumption that P = 0 for a cold plasma, $B_A = B_B$ and the magnetic pressure on both sides of the current sheet is equal. Therefore, by applying the same set of assumptions used to characterise the magnetotail plasma regime on Equation 3.22, I recover the stress balance conditions for a 1-D current sheet in the magnetotail (Owen & Cowley, 1987b) from those for a 1-D current sheet in the solar wind.

3.3 Stress balance for a bifurcated reconnection current sheet

Having modified the stress balance conditions for a single 1-D current sheet to account for fundamental differences between the properties of the magnetotail and solar wind plasma, I now apply them to a bifurcated RCS structure typical of reconnection in the solar wind (Gosling et al., 2005a, 2006a; Gosling & Szabo, 2008).

Figure 3.2a shows a model of a symmetric reconnection outflow region in steady-state with opening angle γ , bound by a bifurcated pair of thin current sheets IT and IB, with the neutral line located at the origin. Observations of bifurcated RCS outflow structures in the solar wind suggest that γ is usually small, typically around $\sim 10^\circ$ (Mistry et al., 2015; Lavraud et al., 2021). It is therefore assumed that current sheets IT and IB are quasi-parallel and can be characterised using a common *lmn*-coordinate system, denoted by the large axes. Regions A and C correspond to the inflow regions, and Region B corresponds to the outflow region.

In Figure 3.2b, I present this reconnection configuration in velocity space,

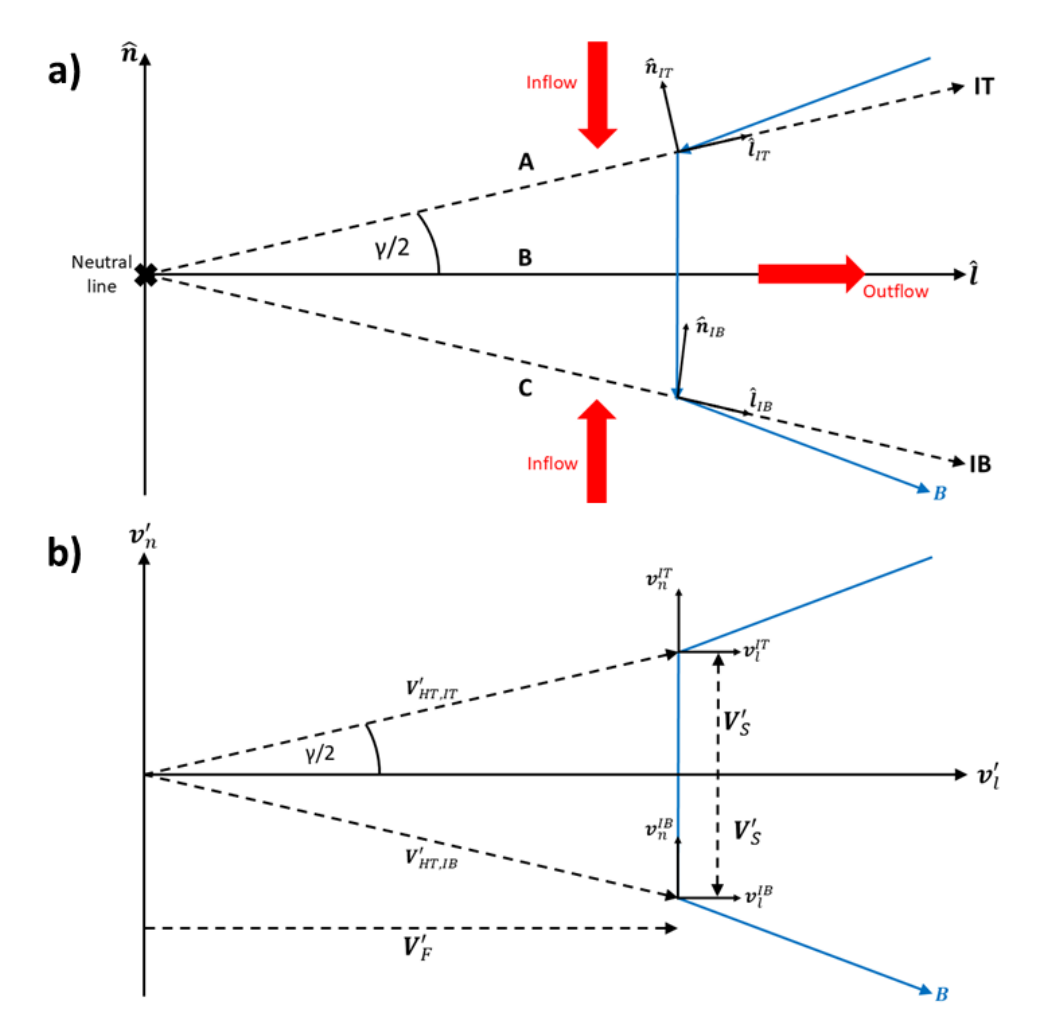


Figure 3.2: Reconnection geometry for a symmetric outflow region bound by a bifurcated reconnection current sheet in a) real space and b) velocity space, based on the Gosling reconnection model (Gosling et al., 2005a).

where the large, primed axes v_l' and v_n' represent the neutral line rest frame (NLRF). In this frame, the reconnected field line recoils away from the neutral line with speed V_F' in the $\hat{\bf l}$ -direction. Unlike the single current sheet case, the individual magnetic field discontinuities at at IT and IB are not stationary in the FLRF. Instead, they move apart from each other with speed V_S' in the $\pm \hat{\bf n}$ -direction as the bifurcated RCS diverges. Each discontinuity has a locally defined rest frame, which is referred to as the discontinuity rest frame (DRF), that is characterised by the HT velocities ${\bf V}'_{HT,IT}$ at IT and ${\bf V}'_{HT,IB}$ at IB in the NLRF (Gosling et al. 2005a, see Section 2.4.2). These HT velocities can be decomposed into the two components: V_F' , directed in the $\hat{\bf l}$ -direction, and V_S' , directed in the $\pm \hat{\bf n}$ -direction.

Similar to the analysis for the single current sheet case, I now consider a pair of isothermal proton inflow beams entering the outflow region from Regions A and C, labelled Beam 1 and Beam 2, respectively. The two inflow beams are assumed to be identical, with equal density $n_{1A} = n_{2C}$, temperature $T_{1A} = T_{2C}$, and field-aligned

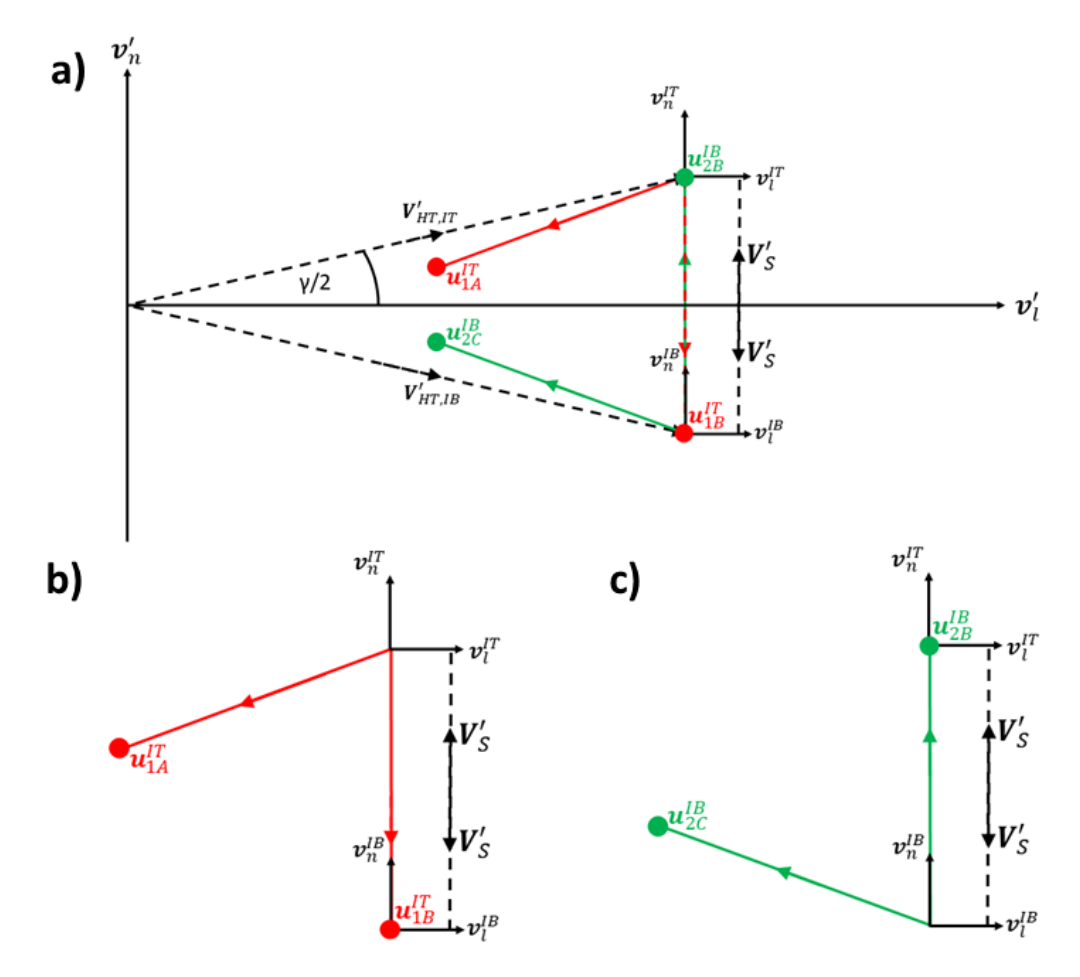


Figure 3.3: a) Overview of the assumed inflow and outflow beam configuration in velocity space for the reconnection geometry shown in Figure 3.2. b) Velocity of the inflow Beam 1 before (\mathbf{u}_{1A}^{IT}) and after (\mathbf{u}_{1B}^{IT}) passing through current sheet IT, shown in the rest frame of the magnetic field discontinuity at this current sheet. c) Velocity of the inflow Beam 2 before (\mathbf{u}_{2C}^{IB}) and after (\mathbf{u}_{2B}^{IB}) passing through current sheet IB, shown in the rest frame of the magnetic field discontinuity at this current sheet.

speed $|\mathbf{u}_{1A}^{IT}| = |\mathbf{u}_{2C}^{IB}|$. Throughout this thesis, I use the convention that quantities defined in the DRF of IT and IB are denoted by the superscript IT and IB, respectively. Figure 3.3 shows the assumed beam configuration for the symmetric bifurcated RCS described above. In the DRF at current sheets IT and IB, the inflow and outflow beams are field-aligned (Figure 3.3b, c). Beam 1 enters IT with velocity \mathbf{u}_{1A}^{IT} , then follows the reconnected field line across the current sheet to enter the outflow region with velocity \mathbf{u}_{1B}^{IT} . Likewise, Beam 2 enters IB with velocity \mathbf{u}_{2C}^{IB} and exits into the outflow region with velocity \mathbf{u}_{2B}^{IB} . Therefore, I expect to observe single inflow beams in Regions A and C, and a pair of counterstreaming outflow beams in Region B.

In order for there to be a bifurcated RCS, I make the assumption that the outflow beam from IT (IB) will have sufficient speed to catch up with IB (IT), but not to overtake and pass through it. This condition implies that $u_{1B,n}^{IT} = u_{2B,n}^{IB} = 2V_S'$, which leads to the following equation linking the $\hat{\bf n}$ -component of the outflow beam velocity with the opening angle γ of the outflow region:

$$\sin\frac{\gamma}{2} = \frac{|V_S'|}{|\mathbf{V}_{HT}'|} = \frac{|u_{1B,n}^{IT}|}{2|\mathbf{V}_{HT}'|} = \frac{|u_{2B,n}^{IB}|}{2|\mathbf{V}_{HT}'|}$$
(3.25)

Here, I highlight an important difference between the stress balance analysis for reconnection with a single RCS and reconnection with a bifurcated RCS. In a bifurcated RCS, the outgoing beam from one current sheet contributes to the stress balance at the other. As a result, the current sheets IT and IB form a coupled system and their stress balance conditions must be evaluated simultaneously. Hence, the solutions to these conditions at one current sheet must also satisfy the conditions at the other.

Starting with Equations 3.20–3.22, I evaluate the stress balance conditions at IT to derive a set of equations for the velocity \mathbf{u}_{1B}^{IT} of the outflow beam from IT in Region B. Based on the properties of the hypothesised reconnection configuration outlined above, a few simplifying assumptions are made. Since the outflow beam from IB is assumed to catch up with the magnetic field discontinuity at IT but not pass through it, I set $\mathbf{u}_{2B}^{IT} = 0$ in the DRF of IT (see Figure 3.3c). Additionally, $\rho_{2A} = 0$ and $P_{2A} = 0$ because this beam does not enter Region A. In this frame, the $\hat{\mathbf{l}}$ -component stress balance condition (Equation 3.20) thus simplifies to:

$$\rho_{1B}u_{1B,l}^{IT}u_{1B,n}^{IT} - \rho_{1A}u_{1A,l}^{IT}u_{1A,n}^{IT} = \frac{B_n}{\mu_0}(B_{B,l} - B_{A,l})$$
(3.26)

This shows that in the $\hat{\bf l}$ -component, only Beam 1 contributes to the stress balance at IT. Using the mass continuity condition $\rho_{1A}u_{1A,n}^{IT}=\rho_{1B}u_{1B,n}^{IT}$, this equation can be re-arranged to give:

$$u_{1B,l}^{IT} = u_{1A,l}^{IT} + \frac{V_{A,A}^2}{u_{1A,n}^{IT}} \frac{B_n \Delta B_l^{IT}}{B_A^2}$$
 (3.27)

where $V_{A,A}$ is the Alfvén speed in Region A and $\Delta B_l^{IT} = B_{B,l} - B_{A,l}$ is the difference in the $\hat{\bf l}$ -component of the magnetic field across IT. The $\hat{\bf m}$ -component stress balance condition (Equation 3.21) has the same form as Equation 3.20 so:

$$u_{1B,m}^{IT} = u_{1A,m}^{IT} + \frac{V_{A,A}^2}{u_{1A,n}^{IT}} \frac{B_n \Delta B_m^{IT}}{B_A^2}$$
 (3.28)

where $\Delta B_m^{IT} = B_{B,m} - B_{A,m}$. The $\hat{\mathbf{n}}$ -component stress balance condition (Equation 3.22) simplifies to:

$$P_{1A} - (P_{1B} + P_{2B}) + \rho_{1A} u_{1A,n}^{IT} (u_{1A,n}^{IT} - u_{1A,n}^{IB}) = \frac{1}{2\mu_0} (B_B^2 - B_A^2)$$
 (3.29)

which re-arranges to give:

$$u_{1B,n}^{IT} = u_{1A,n}^{IT} - \frac{1}{\rho_{1A}u_{1A,n}^{IT}} (\Delta P_{th}^{IT} + \Delta P_{mag}^{IT})$$
 (3.30)

where $\Delta P_{th}^{IT} = (P_{1B} + P_{2B}) - P_{1A}$ is the difference between the sum of the individual beam plasma pressures in Region A and Region B, and $\Delta P_{mag}^{IT} = (B_B^2 - B_A^2)/2\mu_0$ is the change in magnetic pressure across IT. Under the assumptions made, these equations imply that P_{2B} , the plasma pressure of Beam 2, contributes to the overall stress balance at IT, whereas the change in its momentum flux across IT does not. Writing out the plasma pressure terms of each beam in Equation 3.30 in full as $P = nk_BT$ and by symmetry, assuming $n_{1B} = n_{2B}$ and $T_{1B} = T_{2B}$, the ΔP_{th}^{IT} term can be re-written as:

$$\Delta P_{th}^{IT} = 2 \frac{u_{1A,n}^{IT}}{u_{1B,n}^{IT}} n_{1A} k_B T_{1B} - n_{1A} k_B T_{1A}$$
(3.31)

Substituting this equation into Equation 3.30 yields a quadratic equation in $u_{1B,n}^{IT}$:

$$u_{1B,n}^{IT^{2}} - \left(u_{1A,n}^{IT} - \frac{1}{\rho_{1A}u_{1A,n}^{IT}} (\Delta P_{mag}^{IT} - n_{1A}k_{B}T_{1A})\right) u_{1B,n}^{IT} + \frac{2k_{B}}{m_{i}}T_{1B} = 0$$
 (3.32)

Repeating the same procedure for the stress balance conditions at current sheet IB, the corresponding equations for the velocity of the outflow beam from IB \mathbf{u}_{2B}^{IB} in Region B are:

$$u_{2B,l}^{IB} = u_{2C,l}^{IB} - \frac{V_{A,C}^2}{u_{2C,n}^{IB}} \frac{B_n \Delta B_l^{IB}}{B_C^2}$$
 (3.33)

$$u_{2B,m}^{IB} = u_{2C,m}^{IB} + \frac{V_{A,C}^2}{u_{2C,n}^{IB}} \frac{B_n \Delta B_m^{IB}}{B_C^2}$$
 (3.34)

$$u_{2B,n}^{IB^{2}} - \left(u_{2C,n}^{IB} + \frac{1}{\rho_{2C}u_{2C,n}^{IB}} (\Delta P_{mag}^{IB} + n_{2C}k_{B}T_{2C})\right) u_{2B,n}^{IB} + \frac{2k_{B}}{m_{i}}T_{2B} = 0$$
 (3.35)

where $V_{A,C}$ is the Alfvén speed in Region C; $\Delta B_l^{IB} = B_{C,l} - B_{B,l}$ and $\Delta B_m^{IB} = B_{C,m} - B_{B,m}$ is the difference in the $\hat{\bf l}$ and $\hat{\bf m}$ -components of the magnetic field across IB, respectively; $\Delta P_{mag}^{IB} = (B_C^2 - B_B^2)/2\mu_0$ is the change in magnetic pressure across IB, and $\Delta P_{th}^{IB} = P_{2C} - (P_{1B} + P_{2B})$ is the difference between the sum of the individual beam plasma pressures in Region B and Region C.

For a specified reconnected magnetic field geometry in Regions A, B, and C, as well as a given set of inflow beam conditions, I use this set of stress balance conditions for a bifurcated RCS to predict the velocity, density, and temperature of the outflow beams in Region B. Using these predictions, I can then estimate the opening angle γ of the outflow region, and reconstruct the distribution function describing the beam population within it.

3.3.1 Speed of the inflow and outflow beams

In the current sheet stress balance models of magnetotail reconnection (Section 1.5), it is assumed that the speed of the inflow and outflow beams is constant in the FLRF as there is no electric field or pressure forces doing work on the beam particles as they cross the current sheet (Owen & Cowley, 1987a,b). Using the stress balance conditions derived in the previous section, I check whether this assumption also holds true in the solar wind where forces due to magnetic and plasma pressure gradients must be accounted for, even in the DRF where the electric field is transformed away.

Taking Beam 1 as it crosses current sheet IT as an example, if the speed of the inflow and outflow beams are equal, then:

$$|\mathbf{u}_{1A}^{IT}| = |\mathbf{u}_{1B}^{IT}| = \sqrt{u_{1B,l}^{IT^2} + u_{1B,m}^{IT^2} + u_{1B,n}^{IT^2}}$$
(3.36)

For simplicity, I neglect the $\hat{\mathbf{n}}$ -component in this analysis and set $u_{1B,m}^{IT} = 0$. Substituting in Equations 3.27 and 3.30 gives:

$$\frac{V_{A,A}^{2}}{u_{1A,n}^{IT}} \frac{B_{n}}{B_{A}^{2}} \Delta B_{l}^{IT} \left(2u_{1A,l}^{IT} + \frac{V_{A,A}^{2}}{u_{1A,n}^{IT}} \frac{B_{n} \Delta B_{l}^{IT}}{B_{A}^{2}} \right) = \frac{\Delta P_{mag}^{IT} + \Delta P_{th}^{IT}}{\rho_{1A}} \left(2 - \frac{\Delta P_{mag}^{IT} + \Delta P_{th}^{IT}}{\rho_{1A} u_{1A,n}^{IT^{2}}} \right)$$
(3.37)

For the the $|\mathbf{u}_{1A}^{IT}| = |\mathbf{u}_{1B}^{IT}|$ assumption to hold, the plasma pressure difference ΔP_{th}^{IT} and magnetic pressure difference ΔP_{mag}^{IT} across the current sheet must satisfy this equation. As this is generally not true in the solar wind, it cannot always be assumed that $|\mathbf{u}_{1A}^{IT}| = |\mathbf{u}_{1B}^{IT}|$ when considering the current sheet stress balance in the solar wind, unlike in the magnetotail.

However, specific cases can be derived from the stress balance conditions where $|\mathbf{u}_{1A}^{IT}| = |\mathbf{u}_{1B}^{IT}|$. If the change in magnetic pressure exactly balances the change in plasma pressure across the current sheet (i.e., $\Delta P_{mag}^{IT} + \Delta P_{th}^{IT} = 0$), the right-hand side of Equation 3.37 is zero, which leads to the following solutions:

$$\frac{V_{A,A}^2}{u_{1A,n}^{IT}} \frac{B_n}{B_A^2} \Delta B_l^{IT} = 0 {(3.38)}$$

$$2u_{1A,l}^{IT} + \frac{V_{A,A}^2}{u_{1A,n}^{IT}} \frac{B_n \Delta B_l^{IT}}{B_A^2} = 0$$
 (3.39)

The solution to Equation 3.38 is trivial: $\Delta B_l^{IT} = 0$ as the other terms must be non-zero. This implies that $B_{A,l} = B_{B,l}$, in which case there is no change in the magnetic field (since B_n is constant), and hence, no current sheet. Equation 3.39 can be rewritten as:

$$-2\rho_{1A}u_{1A,l}^{IT}u_{1A,n}^{IT} = \frac{B_n}{\mu_0}(B_{B,l} - B_{A,l})$$
 (3.40)

which, when equated to Equation 3.26, gives $\rho_{1B}u_{1B,l}^{IT}u_{1B,n}^{IT} = -\rho_{1A}u_{1A,l}^{IT}u_{1A,n}^{IT}$. By once again applying the mass continuity condition, this equation reduces to $u_{1B,l}^{IT} = -u_{1A,l}^{IT}$. Additionally, Equation 3.30 implies that $u_{1B,n}^{IT} = u_{1A,n}^{IT}$ if $\Delta P_{mag}^{IT} + \Delta P_{th}^{IT} = 0$. This result suggests that the speed of the inflow and outflow beams is constant, but only if the $\hat{\bf l}$ -component of the inflow beam velocity reverses as it crosses IT. In the DRF, this reversal is also associated with a similar reversal in the $\hat{\bf l}$ -component of the magnetic field as the beams are assumed to be field-aligned. This magnetic field configuration is inconsistent with the symmetric bifurcated RCS configuration shown in Figure 3.2, further reinforcing the earlier point that the $|{\bf u}_{1A}^{IT}| = |{\bf u}_{1B}^{IT}|$ assumption does not always hold in the solar wind. Another situation where $\Delta P_{mag}^{IT} + \Delta P_{th}^{IT} = 0$ is if $\Delta P_{th}^{IT} = 0$ and $\Delta P_{mag}^{IT} = 0$, which is assumed for cold plasmas in the magnetotail. In this case, the reversal of the beam direction and magnetic field is consistent with the expected behaviour described in current sheet stress balance models for magnetotail reconnection (Owen & Cowley 1987a,b, see Section 1.5).

3.4 Application to a simple bifurcated reconnection current sheet model

I test the stress balance conditions derived in Section 3.3 by applying them to a simple model of a reconnection outflow with a bifurcated RCS. The model is set up on the basis of the reconnection geometry shown in Figures 3.2 and 3.3, with a symmetric outflow region in steady-state and identical inflow beams from Regions A and C. For simplicity, this reconnection structure is assumed to be 2-D and the magnetic field and flow components in the $\hat{\mathbf{m}}$ -direction are neglected. I define the reconnected magnetic field and inflow conditions based on typical values from observed reconnection events in the solar wind. In *lmn*-coordinates, the reconnected magnetic field in Regions A, B, and C is:

$$\mathbf{B_A} = (-5.0, 0.0, -0.5) \text{ nT} \tag{3.41}$$

$$\mathbf{B_B} = (0.0, 0.0, -0.5) \text{ nT}$$
 (3.42)

$$\mathbf{B_C} = (5.0, 0.0, -0.5) \text{ nT}$$
 (3.43)

The inflow plasma in Regions A and C has equal bulk density $n_A = n_C = 7.5 \text{ cm}^{-3}$ and temperature $T_A = T_C = 7.0 \text{ eV}$, and is assumed to be at rest in the NLRF such that $\mathbf{u}_A' = \mathbf{u}_C' = 0 \text{ km s}^{-1}$. Using the stress balance conditions, the set of unknowns in this model that I solve for are the velocity, density, and temperature of the outflow beams in Region B, the bulk velocity of the reconnection outflow, and the outflow region opening angle γ .

I start the analysis of this model by evaluating the stress balance conditions in the **Î**-direction to determine the bulk outflow velocity. Recall that in the DRF, the inflow and outflow beams of the current sheet must be field-aligned (Owen &

Cowley, 1987a,b). If this is the case, then the assumed magnetic field geometry of the model requires that $u_{1B,l}^{IT} = 0$ and $u_{2B,l}^{IB} = 0$ (Figure 3.3b,c). Additionally, if the inflow beams are field-aligned, then the properties $u_{1A,n}^{IT}/u_{1A,l}^{IT} = B_n/B_{A,l}$ and $u_{2C,n}^{IB}/u_{2C,l}^{IB} = B_n/B_{C,l}$ can be used to re-write Equations 3.27 and 3.33 as:

$$u_{1A,l}^{IT} = \sqrt{V_{A,A}^2 \frac{B_{A,l}}{B_A^2} (B_{A,l} - B_{B,l})}$$
 (3.44)

$$u_{2C,l}^{IB} = \sqrt{V_{A,C}^2 \frac{B_{C,l}}{B_C^2} (B_{C,l} - B_{B,l})}$$
 (3.45)

The solutions to these equations have positive and negative roots, but it can be deduced from the model geometry that $u_{1A,l}^{IT}$ and $u_{2C,l}^{IT}$ must be negative. Given the specified magnetic field and densities in Regions A and C, $V_{A,A} = V_{A,C} = 40.1 \,\mathrm{km \, s^{-1}}$. Using these values, I determine that $u_{1A,l}^{IT} = u_{2C,l}^{IB} = -39.9 \,\mathrm{km \, s^{-1}}$.

Because the inflow plasma in Regions A and C is static in the NLRF, the inflow of plasma into the outflow region is solely due to the motion of the reconnected field lines as they recoil away from the neutral line. Velocities in the NLRF are linked to velocities in the DRF by the transformations:

$$\mathbf{u}^{IT} = \mathbf{u}' - \mathbf{V}'_{HT,IT} \tag{3.46}$$

$$\mathbf{u}^{IB} = \mathbf{u}' - \mathbf{V}'_{HT.IB} \tag{3.47}$$

at IT and IB, respectively. Substituting in the predicted values of $u_{1A,l}^{IT}$ and $u_{2C,l}^{IB}$ gives a field line recoil speed $V_F' = 39.9$ km s⁻¹ in the $+\hat{\bf l}$ -direction. Since the reconnected magnetic field is frozen into the reconnection outflow, V_F' also corresponds to the $\hat{\bf l}$ -component of the bulk outflow velocity in Region B. Moreover, the outflow beams have equal and opposite velocity components in the $\hat{\bf n}$ -direction so there is no net bulk flow in this direction. Therefore, the bulk outflow velocity in the NLRF is ${\bf u}_B' = (39.9, 0.0, 0.0)$ km s⁻¹.

Having obtained the bulk velocities in Regions A, B, and C, I use HT analysis (Khrabrov & Sonnerup, 1998; Paschmann & Sonnerup, 2008) to determine $\mathbf{V}'_{HT,IT}=(39.9,0.0,4.0)~\mathrm{km~s^{-1}}$ and $\mathbf{V}'_{HT,IB}=(39.9,0.0,-4.0)~\mathrm{km~s^{-1}}$. As the inflow beam from Region A is at rest in the NLRF, i.e. $\mathbf{u}'_{1A}=0$, Equation 3.46 implies that $\mathbf{u}^{IT}_{1A}=(-39.9,0.0,-4.0)~\mathrm{km~s^{-1}}$. Similarly, Equation 3.47 implies the velocity of the inflow beam in Region C is $\mathbf{u}^{IB}_{2C}=(-39.9,0.0,4.0)~\mathrm{km~s^{-1}}$ in the DRF at IB. The speed $|\mathbf{u}^{IT}_{1A}|$ and $|\mathbf{u}^{IB}_{2C}|$ of both inflow beams is equal to the Alfvén speed in the inflow region. In Region B, the assumption for current sheet bifurcation implies $|u^{IT}_{1B,n}|=|u^{IB}_{2B,n}|=2|V'_{S}|$. From the HT velocities, I deduce that $V'_{S}=4.0~\mathrm{km~s^{-1}}$ which leads to $u^{IT}_{1B,n}=-8.0~\mathrm{km~s^{-1}}$ and $u^{IB}_{2B,n}=8.0~\mathrm{km~s^{-1}}$. Since it has already been stated that $u^{IT}_{1B,l}=u^{IB}_{2B,l}=0$, the velocities of Beam 1 in Region

Table 3.1: Summary of the properties of the inflow and outflow proton beams in Regions A, B, and C. Velocities and speeds are given in the DRF at IT

	Inflow beam, 1A	Outflow beam, 1B Outflow beam, 2B	Outflow beam, 2B	Inflow beam, 2C
Velocity (km s ⁻¹) $\mathbf{u}_{1A}^{IT} = ($	$\mathbf{u}_{1A}^{IT} = (-39.9, 0.0, -4.0)$	$(-39.9, 0.0, -4.0)$ $\mathbf{u}_{1B}^{IT} = (0.0, 0.0, -8.0)$ $\mathbf{u}_{2B}^{IB} = (0.0, 0.0, 8.0)$ $\mathbf{u}_{2C}^{IB} = (-39.9, 0.0, 4.0)$	$\mathbf{u}_{2B}^{IB} = (0.0, 0.0, 8.0)$	$\mathbf{u}_{2C}^{IB} = (-39.9, 0.0, 4.0)$
Speed (km s^{-1})	$ {f u}_{1A}^{IT} =40.1$	$ \mathbf{u}_{1B}^{IT} =8.0$	$ \mathbf{u}_{2B}^{IB} =8.0$	$ \mathbf{u}_{2C}^{IB} =40.1$
Density (cm^{-3})	7.5	3.75	3.75	7.5
Temperature (eV)	7.0	15.1	15.1	7.0

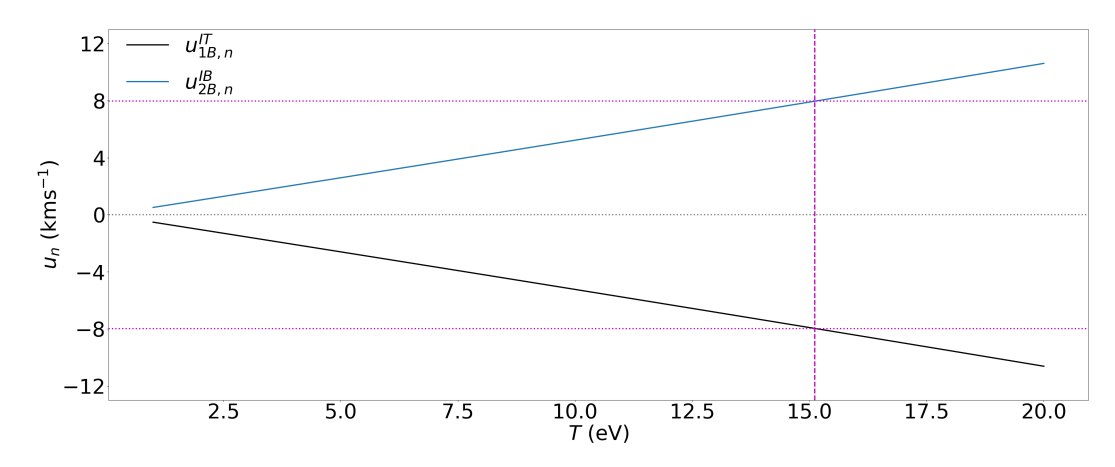


Figure 3.4: Graph of the normal component of the outflow beam velocity $u_{1B,n}^{IT}$ (black) and $u_{2B,n}^{IB}$ (blue) against temperature. The dotted, horizontal purple lines denote the expected value of $u_{1B,n}^{IT}$ and $u_{2B,n}^{IB}$. The dashed, vertical line denotes the corresponding beam temperature.

B (given in the DRF at IT) and Beam 2 in Region B (given in the DRF at IB) are $\mathbf{u}_{1B}^{IT} = (0.0, 0.0, -8.0) \text{ km s}^{-1}$. and $\mathbf{u}_{2B}^{IB} = (0.0, 0.0, 8.0) \text{ km s}^{-1}$, respectively. Furthermore, substituting V_S' into Equation 3.25 gives an outflow region opening angle of $\gamma = 10.4^{\circ}$.

As the proton beam population in Regions A and C each consists of a single inflow beam, the inflow beam density is equal to the bulk density in these regions, so $n_{1A} = n_{2A} = 7.5 \text{ cm}^{-3}$. Applying the mass continuity conditions $n_{1A}u_{1A,n}^{IT} = n_{1B}u_{1B,n}^{IT}$ and $n_{2C}u_{2C,n}^{IB} = n_{2B}u_{2B,n}^{IB}$ gives the density of the outflow beams $n_{1B} = n_{2B} = 3.75 \text{ cm}^{-3}$. If the total density in Region B is the sum of the densities of the individual outflow beams, then $n_B = n_{1B} + n_{2B} = 7.5 \text{ cm}^{-3}$. Given this, the Alfvén speed in Region B is $V_{A,B} = 4.0 \text{ km s}^{-1}$, which shows that the outflow beam speed $|\mathbf{u}_{1B}^{IT}| = |\mathbf{u}_{2B}^{IB}| = 8.0 \text{ km s}^{-1}$ is twice that of $V_{A,B}$.

Figure 3.4 shows the relationship between $u_{1B,n}^{IT}$ and T_{1B} , and $u_{2B,n}^{IB}$ and T_{2B} , derived from Equations 3.32 and 3.35, respectively. For the predicted values of $u_{1B,n}^{IT}$ and $u_{2B,n}^{IB}$, the temperature of the individual outflow beams required for normal pressure balance is $T_{1B} = T_{2B} = 15.1$ eV. I have therefore demonstrated using the stress balance conditions, that the bulk outflow velocity, the opening angle of the outflow region, and the properties of the outflow beams for a bifurcated RCS can be determined. Table 3.1 provides a summary of the properties of the inflow and outflow beams in each region of the reconnection outflow structure.

With these results, I then reconstruct the distribution function describing the proton beam population in each region. As the inflow and outflow beams are assumed to be isothermal, they are treated as Maxwellians:

$$f_M = n \left(\frac{m_i}{2\pi k_B T}\right)^{3/2} e^{-\frac{m_i}{2k_B T} \left((v'_{\parallel} - u'_{\parallel})^2 + (v'_{\perp} - u'_{\perp})^2\right)}$$
(3.48)

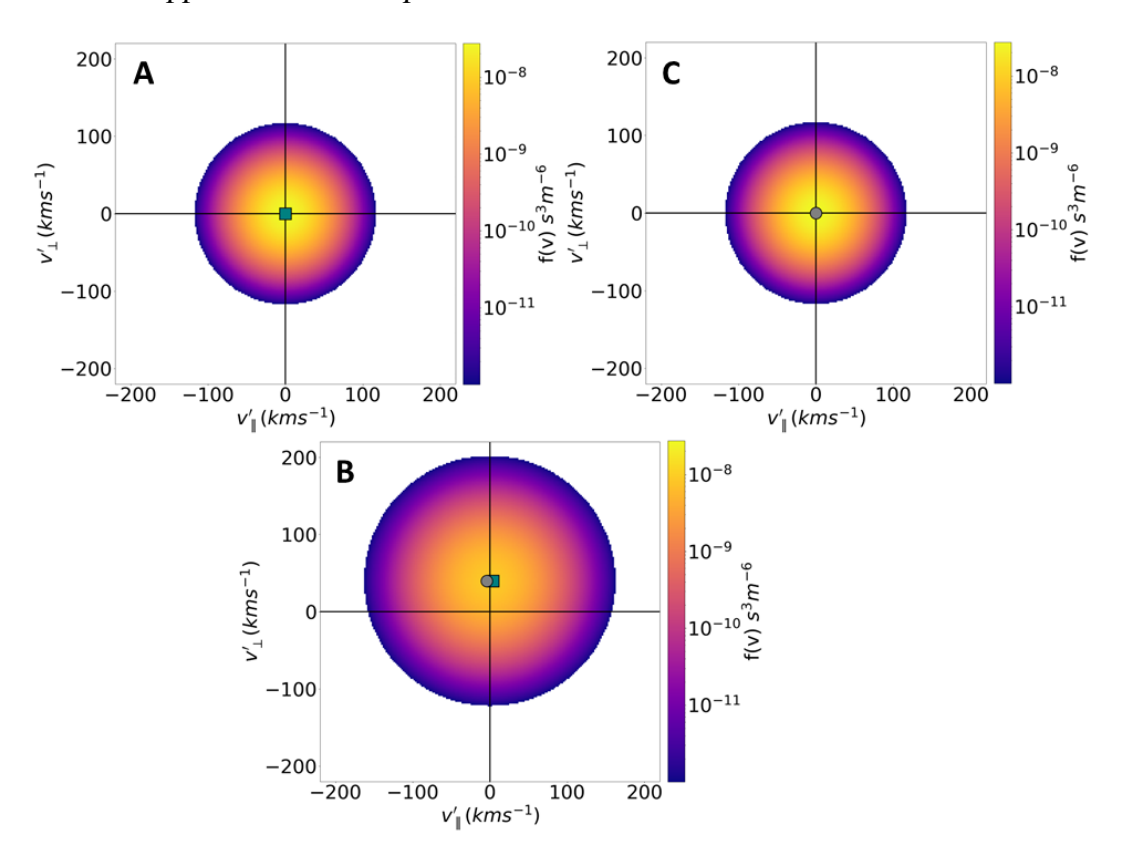


Figure 3.5: Distribution function of the proton beam population in Regions A (top left), B (middle), and C (top right) shown in the field-aligned NLRF. The teal square denotes the velocity of Beam 1, \mathbf{u}'_{1A} in Region A and \mathbf{u}'_{1B} in Region B. The grey circle denotes the velocity of Beam 2, \mathbf{u}'_{2C} in Region C and \mathbf{u}'_{2B} in Region B.

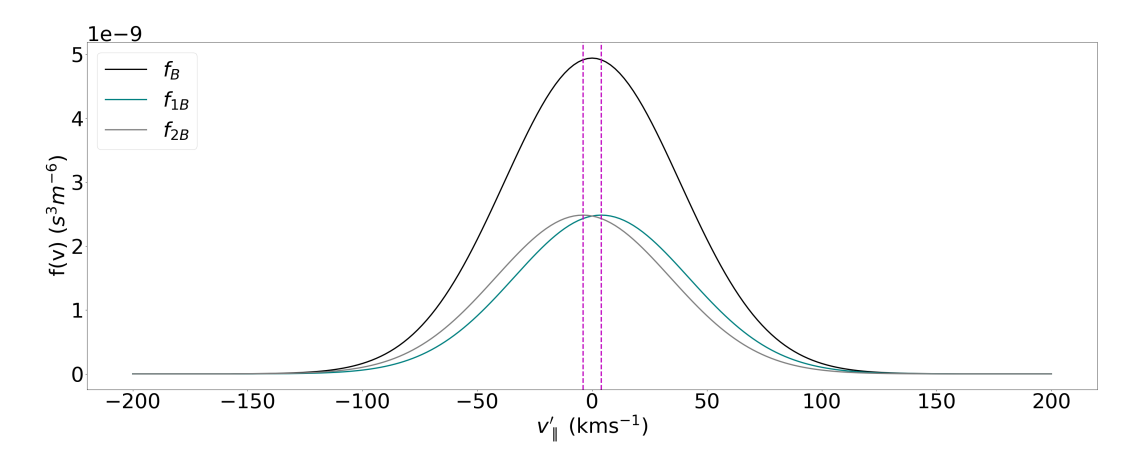


Figure 3.6: 1-D cut through the distribution function of the beam population in Region B along the v_{\parallel} axis at $v_{\perp} = |\mathbf{u_B'}|$. The teal curve is the distribution function of Beam 1 f_{1B} , the grey curve is the distribution function of Beam 2 f_{2B} , and the black curve is the total distribution function $f_B = f_{1B} + f_{2B}$. The vertical, dotted purple lines show the field-aligned speed of the individual outflow beams, $u'_{1B,\parallel}$ and $u'_{2B,\parallel}$.

where v'_{\parallel} and u'_{\parallel} are the velocity components parallel to the magnetic field, and v'_{\perp} and u'_{\perp} are the perpendicular components, both in the NLRF. Figure 3.5 shows the distribution functions in Regions A, B, and C in the field-aligned NLRF. In Regions A and C, the plasma is static so the distribution function of the inflow beam in both is centred about the origin. For the symmetric reconnection configuration considered in this model, the bulk outflow is perpendicular to the magnetic field in Region B. As a result, the distribution in this region is offset in the v_{\perp} direction by the outflow speed $|\mathbf{u}'_{\mathbf{B}}| = 39.9 \, \mathrm{km \, s^{-1}}$. Additionally, the outflow beams have equal and opposite field-aligned speeds so there is no bulk flow in the v_{\parallel} direction. Figure 3.6 shows the 1-D cut through the peak of the distribution function in Region B along the v_{\parallel} axis at $v_{\perp} = |\mathbf{u}'_{\mathbf{B}}|$. There is significant overlap between the individual distribution functions f_{1B} and f_{2B} of the outflow beams. Consequently, a well-separated pair of counterstreaming proton beams in the total distribution function in Region B, $f_B = f_{1B} + f_{2B}$ is not observed.

3.5 Discussion

The bulk outflow speed of $|\mathbf{u}_B'| = 39.9 \text{ km s}^{-1}$ is equal to the Alfvén speed in the inflow regions, $V_{A,A}$ and $V_{A,C}$. This is consistent with observations of reconnection outflows reported in the solar wind, which typically have outflow speeds of a few tens of km s⁻¹, comparable to the Alfvén speed in the surrounding solar wind (Enžl et al., 2014; Phan et al., 2020). The predicted opening angle of $\gamma = 10.4^{\circ}$ is also in line with previous results (Mistry et al., 2015). These results show that at least in the symmetric, steady-state case, my current sheet stress balance model can successfully reproduce some of the observed properties of reconnection outflows with bifurcated RCS in the solar wind.

The stress balance conditions Equation 3.44 and 3.45 determine the $\hat{\bf l}$ -component of the inflow beam velocity in the DRF. $u_{1A,l}^{IT}$ and $u_{2C,l}^{IB}$ are both fixed by their respective densities n_{1A} and n_{2C} , as well as the geometry of the reconnected magnetic field. If a symmetric non-zero bulk inflow velocity in Regions A and C is introduced, while keeping all other parameters of the model unchanged, Equations 3.46 and 3.47 suggest that ${\bf V}'_{HT}$ must change in order to keep $u_{1A,l}^{IT}$ and $u_{2C,l}^{IB}$ the same in the DRF and thus, satisfy the stress balance conditions at the bifurcated current sheet. As a result, the field line recoil speed V'_F and discontinuity separation speed V'_S will also change in response.

To better illustrate this point, consider the case where the bulk inflow in Regions A and C is now directed away from the neutral line in the $+\hat{\bf l}$ -direction, such that ${\bf u}_A'={\bf u}_C'=(20,0,0)$ km s⁻¹. The stress balance conditions at IT and IB do not change, so $u_{1A,l}^{IT}$ and $u_{2C,l}^{IB}$ remain the same. Therefore, in order to compensate for the increase in $u_{A,l}'$ and $u_{C,l}'$, the $\hat{\bf l}$ -component of ${\bf V}_{HT,IT}'$ and ${\bf V}_{HT,IB}'$ must increase by the same amount. This gives a faster field line recoil speed (and bulk outflow speed) of $V_F'=59.9$ km s⁻¹. Repeating the HT analysis for this new value of V_F' , I find

that $\mathbf{V}'_{HT,IT} = (59.9, 0.0, 4.0) \, \mathrm{km \, s^{-1}}$ and $\mathbf{V}'_{HT,IB} = (59.9, 0.0, -4.0) \, \mathrm{km \, s^{-1}}$. Here, V'_S has not changed as a result of this non-zero inflow and still has the same value as the static inflow case. As a result, the outflow region is now elongated in $\hat{\mathbf{l}}$ and Equation 3.25 implies that the outflow region opening angle decreases to $\gamma = 7.6^{\circ}$. Conversely, introducing a bulk inflow in the $-\hat{\mathbf{l}}$ -direction towards the neutral line decreases V'_F , leading to the contraction of outflow region in $\hat{\mathbf{l}}$ and an increase in γ . This is analogous to the situation described in Section 1.5.1 for stress balance models of magnetotail reconnection (Owen & Cowley, 1987a) who show for a tailward inflow, the opening angle of the tailward reconnected field wedge is less than the Earthward reconnected field wedge (Figure 1.17).

I show that for the initial conditions of the model, which reflect conditions in the regular solar wind, it is difficult to clearly resolve the pair of counterstreaming proton beams in the outflow region. The difficulty arises because the relative field-aligned speed $|\mathbf{u}'_{1B} - \mathbf{u}'_{2B}|$ of the two beams is small compared to their thermal speeds. In the case presented here, $|\mathbf{u}'_{1B} - \mathbf{u}'_{2B}| = 8.0 \text{ km s}^{-1}$ which is equal to $2V_{A,B}$. By comparison, the thermal speed of the outflow beams is $v_{th} = \sqrt{2k_BT/m_i} = 53.8 \text{ km s}^{-1}$ for T = 15.1 eV. Similar difficulties in resolving multiple beam populations in reconnection outflows have been encountered in previous studies (Lavraud et al., 2021).

Most reports of counterstreaming reconnection outflow beams in the solar wind are from reconnection events associated with interplanetary coronal mass ejections (ICMEs) (Gosling et al., 2005a). These are structures in the solar wind associated with strong magnetic fields and cooler plasma (Gosling, 1990; Neugebauer & Goldstein, 1997). The speed of the inflow and outflow beams are dependent on the Alfvén speed. When B is large, the Alfvén speed increases and as a result, the outflow beam speed and the relative field-aligned speed will also increase. For reconnection outflow observed at ICMEs, V_A is typically $\sim 100 \text{ km s}^{-1}$ (Gosling et al., 2005a). The combination of greater relative field-aligned speed and cooler temperatures thus produces conditions that are conducive to the observation of well-separated counterstreaming beams in the reconnection outflow regions.

In previous analyses (Owen & Cowley, 1987a,b), the inflow and outflow beams are assumed to have equal field-aligned speed in the DRF, provided the inflow beams are not heated as they enter the outflow region (Gosling et al., 2005a; Lavraud et al., 2021). Using my stress balance model, I demonstrate that the constant beam speed assumption is not generally true in the solar wind (see Section 3.3.1). Under this assumption, if the speed of the inflow beam in the DRF is equal to the inflow region Alfvén speed, the expected relative beam speed is the sum of the Alfvén speed in Regions A and C, $V_{A,A} + V_{A,C} = 80.2 \text{ km s}^{-1}$. This is much larger than the actual relative beam speed of 8.0 km s⁻¹ obtained from the model. A similar deficit in the relative beam speed is also seen in observed examples of reconnection outflows with counterstreaming outflow beams (Gosling et al., 2005a; Lavraud et al., 2021).

This was explained as a consequence of the electromagnetic ion beam instability, which places a maximum limit on the relative beam speed of $\sim 1.5V_{A,A}$ (Goldstein et al., 2000).

In this model, the inflow beams are strongly decelerated as they enter the outflow region, with their speed decreasing from 40.1 km s^{-1} to 8.0 km s^{-1} . At the same time, they are also heated, with their temperature increasing from 7.0 eV to 15.1 eV. This suggests that the discrepancy between the expected and actual relative field-aligned speed is a natural consequence of stress balance at the bifurcated RCS. As the inflow beams pass through the RCS, their kinetic energy is converted into thermal energy and they slow down as they enter the outflow region. The heating of the outflow beams is required to maintain normal pressure balance and satisfy the stress balance conditions, although the model does not identify a specific mechanism responsible for the beam heating. For simplicity, I have assumed isotropic heating of the outflow beams in my analysis, although this is not expected to be representative of real conditions in the solar wind. There are several potential heating mechanisms that could explain this behaviour, including the aforementioned ion beam instability (Goldstein et al., 2000). Additionally, strong perpendicular heating of the outflow beams may lead to a reduction in their flow speeds (Cowley & Shull, 1983; Owen & Mist, 2001), consistent with my results.

One caveat of this stress balance model for solar wind reconnection is noted in relation to the outflow region opening angle. A key assumption is that if γ is small, the bifurcated RCS can be treated as a pair of quasi-parallel current sheets and characterised by the same lmn-coordinate system. This assumption is usually satisfied in observed reconnection events in the solar wind, where $\gamma \leq 10^\circ$ (Mistry et al., 2015). However, if γ were instead a few tens of degrees, then the quasi-parallel current sheet assumption breaks down. In this case, the stress balance conditions at IT and IB would have to be evaluated in their respective lmn-coordinate system, and the angular difference between the current sheets accounted for when coupling the stress balance conditions at IT and IB.

Another important aspect of the model is the assumption regarding current sheet bifurcation, in which the outflow beam exiting IT (IB) catches up with IB (IT) without passing through it, leading to the condition $u_{1B,n}^{IT} = u_{2B,n}^{IB} = 2V_S'$ (see Section 3.3). This assumption is justified by empirical evidence, as real observations of reconnection outflows show a single beam in the inflow region and a counterstreaming beam pair in the outflow region. However, if the outflow beam exits IT (IB) with speed $2V_S'$, it would never catch up with IB (IT). Therefore, the beams must exit the current sheet with a speed greater than $2V_S'$, implying that some mechanism must slow them down during propagation across the outflow region. Consequently, the value $2|\mathbf{V}_S'| = 8.0 \text{ km s}^{-1}$ underestimates the true speeds of $|\mathbf{u}_{1B}^{IT}|$ and $|\mathbf{u}_{2B}^{IB}|$. This in turn implies the estimate of $T_{1B} = T_{2B} = 15.1 \text{ eV}$ derived from these speeds using Equations 3.32 and 3.35 is also an underestimate (see Figure 3.4). Conversely, be-

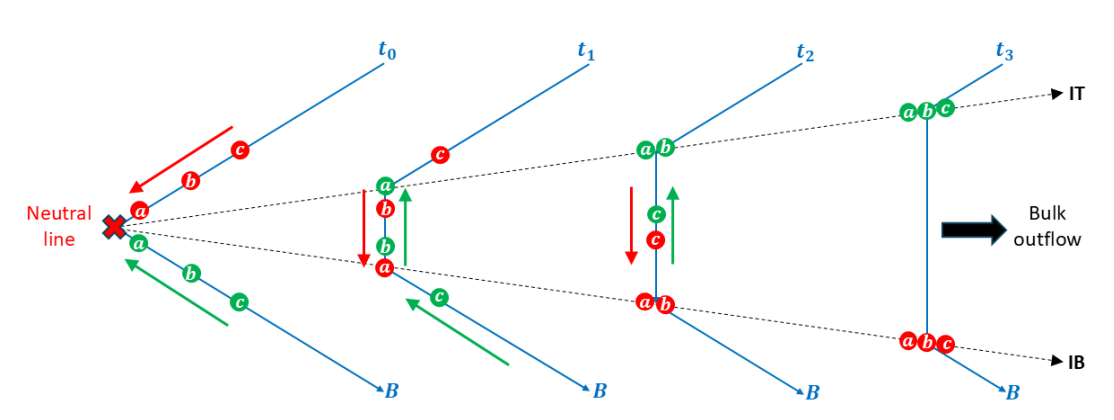


Figure 3.7: Illustration of how the current sheet bifurcation assumptions in the stress balance model can produce an unphysical build-up of plasma at the current sheets IT and IB. Circles *a*, *b*, *c* represent parcels of beam 1 (red) and beam 2 (green). As each parcel enters the outflow region, it catches up with the opposing current sheet without passing through, leading to a build-up of material.

cause V'_S has been directly derived from the HT analysis independent of $|\mathbf{u}_{1B}^{IT}|$ and $|\mathbf{u}_{2B}^{IB}|$, the estimate for the outflow region opening angle should be robust.

Finally, if the outflow beams were to 'stop' at IT or IB, a pile-up of plasma would occur at both current sheets, as shown in Figure 3.7. The circles labelled a, b, c represent plasma parcels belonging to beams 1 (red) and 2 (green). At time t_0 , all parcels are in the inflow region and have not yet entered the outflow region. At time t_1 , parcel a for both beams enters the outflow region, with beam 1 reaching IB and beam 2 reaching IT. Consistent with the model assumptions, these parcels move along the current sheets as the reconnected field lines recoil, without passing through. Subsequently, parcels b and c enter the outflow region and catch up to the opposing current sheet at times t_2 and t_3 , respectively. This leads to an unphysical scenario in which material infinitely accumulates at the current sheets. The present stress balance model presented here does not provide an explanation as to how this material is dissipated; identifying the mechanism responsible is left to future work.

3.6 Conclusions

In this chapter, I develop a new model describing current sheet stress balance for magnetic reconnection in the solar wind, based on previous work done in the context of magnetotail reconnection (Owen & Cowley, 1987a,b). I begin by deriving the stress balance conditions for a single current sheet, before adapting them to a bifurcated current sheet structure of the type commonly associated with magnetic reconnection in the solar wind (Gosling et al., 2005a, 2006b; Gosling & Szabo, 2008).

I show that there are several key differences between stress balance models in the magnetotail and the solar wind. In contrast to the magnetotail, where forces due to magnetic and plasma pressure gradients across the current sheet are neglected, these forces contribute to the stress balance in the solar wind and must be accounted for in the analysis. As a result, the assumption that the speed of the inflow and outflow beams remains unchanged as they cross the current sheet no longer holds, even in the frame where the electric field is transformed away.

I then set up a model of a symmetric, 2-D, steady-state reconnection outflow bound by a bifurcated RCS and use the stress balance conditions to determine the bulk outflow speed, the outflow region opening angle, and the properties of the inflow and outflow beams. My model yields a bulk outflow speed of 39.9 km s $^{-1}$ and an opening angle of 10° , both of which are consistent with the observed properties of reconnection outflows in the solar wind (Enžl et al., 2014; Mistry et al., 2015; Phan et al., 2020). The beam population in the reconnection inflow regions consists of a single inflow beam in each region, which cross the bifurcated RCS to form a pair of counterstreaming beams in the outflow region. Compared to the inflow beams, which have a speed of 40 km s $^{-1}$ and a temperature of 7 eV, the outflow beams are slower and hotter, with a speed of 8 km s $^{-1}$ and a temperature of 15.1 eV.

Using the model-derived properties of the inflow and outflow beams, I reconstruct the distribution function of the proton beam population in the reconnection inflow and outflow regions. I show that for typical conditions in the solar wind, it is difficult to clearly resolve counterstreaming beams in the outflow region. This is because the thermal speed of the individual outflow beams is greater than their relative speed. The speed of the inflow and outflow beams, and hence the relative speed of the counterstreaming beams, is related to the local Alfvén speed. Therefore, counterstreaming beams are more likely to be clearly resolved if the Alfvén speed in the surrounding plasma is large, and if the outflow beams are cool. This may explain why reconnection outflows with well-defined counterstreaming beams are typically associated with ICMEs (Gosling et al., 2005a), which have stronger magnetic fields and cooler temperatures than the regular solar wind (Gosling, 1990; Neugebauer & Goldstein, 1997).

In previous studies, the estimates of the expected relative speed of the counter-streaming beams were consistently greater than the observed values (Gosling et al., 2005a; Lavraud et al., 2021). This discrepancy was attributed to the electromagnetic ion beam instability, which limits the relative speed to $\sim 1.5V_A$ (Goldstein et al., 2000). It is noted that these studies assume the speed of the inflow and outflow beams remains unchanged as they cross the RCS, an assumption shown here to be false in the solar wind. My analysis instead shows that the inflow beams slow down and heat up as they enter the outflow region, trading kinetic energy for thermal energy. This suggests that the discrepancy between the expected and observed relative speed of the counterstreaming outflow beams is a natural consequence of current sheet stress balance. Although my stress balance model shows that beam heating in the outflow region is required to maintain normal pressure balance, it

does not explain how the beams are heated. It is suggested that heating mechanisms such as the aforementioned ion beam instability and anisotropic heating of the outflow beams (Cowley & Shull, 1983; Owen & Mist, 2001) may play a role in this process.

Chapter 4

Application of bifurcated current stress balance models on *Solar Orbiter* observations of reconnection outflows in the solar wind

4.1 Introduction

In Chapter 3, I develop a current sheet stress balance model for magnetic reconnection in the solar wind. As a test case, I then apply it to a simulated example of a reconnection outflow region bound by a bifurcated RCS which is assumed to be 2-D, symmetric, and in steady-state, using typical solar wind values. With this model, I obtain values for the bulk outflow speed and outflow region opening angle that are in general agreement with the observed properties of reconnection outflows in the solar wind (Enžl et al., 2014; Mistry et al., 2015; Phan et al., 2020). Additionally, the model provides an explanation for some of the known characteristics of counterstreaming proton beams in the outflow region (Gosling et al., 2005a; Lavraud et al., 2021).

The work in this chapter builds upon the results from the simple test case presented in the previous chapter. I apply my stress balance model to real examples of reconnection outflows in the solar wind observed by *Solar Orbiter* and use it to calculate the outflow region opening angle, as well as the properties of the reconnection inflow and outflow beams. I then use these results to reconstruct the velocity distribution function (VDF) describing the proton beam population in the inflow and outflow regions and compare them with the *Solar Orbiter* VDF measurements to validate my model. In Section 4.2, I describe the data products and analysis methods used in this study, as well as detail how I identify reconnection outflows in the solar wind. In Section 4.3, I introduce the set of five reconnection outflows to which the stress balance analysis is applied and showcase two representative examples. In Section 4.4, I present the results of my stress balance analysis and then compare the

reconstructed and observed VDFs in Section 4.5, before discussing the implications of my findings in Section 4.6.

4.2 Data and methods

In this study, I use in-situ magnetic field and solar wind proton data from *Solar Orbiter*. Magnetic field measurements are provided by MAG (Horbury et al. 2020a, see Section 2.2.1) at a cadence of 8 vectors/s, while proton VDF measurements are provided by SWA-PAS (Owen et al. 2020, see Section 2.3.1) once every 4 seconds when both instruments are operating in normal mode. The VDF data undergo further processing on the ground to derive the proton moments data, which describes the bulk properties of the solar wind protons including density, velocity, temperature, and pressure. I search for reconnection events in the solar wind throughout the entire year of 2023, during which *Solar Orbiter* was at a heliocentric distance between 0.29–0.95 AU from the Sun.

4.2.1 Reconnection outflow identification algorithm

The identification of reconnection outflows in the solar wind is typically performed by visual inspection of the magnetic field and proton moments time series data. I look for the following signatures consistent with the Gosling model (Gosling et al. 2005a, see Section 1.3.4) of reconnection outflow structures in the solar wind: (1) an increase in the proton bulk speed, signifying an outflow jet, (2) bound by a bifurcated RCS marked by a pair of Alfvénic rotational discontinuities (RDs) in the magnetic field at the edges of the outflow region; and (3) changes in **B** and **v** that are correlated on one side of the outflow region and anti-correlated on the other. This process is often time-consuming, especially when looking for events in large datasets, as has been done in this study. Various methods have been employed in recent statistical studies (Enžl et al., 2014; Tilquin et al., 2020; Eriksson et al., 2022) to automate the identification of reconnection events in the solar wind. In this section, I briefly summarise the operating principles of the identification algorithm developed by Fargette et al. (2023) used in this study.

The first identification criterion for this algorithm is a check on whether there is a change in the **B**–**v** correlation, consistent with paired Alfvénic RDs at the outflow region boundaries. A sampling window centred on time t_0 is set up, containing N measurements each separated by a constant time dt. The vector change in velocity between t_0 and a time t_i within the window is $\Delta \mathbf{v}(t_i) = \mathbf{v}(t_i) - \mathbf{v}(t_0)$. For an Alfvénic RD, $\Delta \mathbf{v}$ across the discontinuity is expected to be given by the Walén relation (Hudson, 1970):

$$\Delta \mathbf{v} = \pm \Delta \mathbf{V_A} \tag{4.1}$$

$$\mathbf{V_A} = \frac{\mathbf{B}}{\sqrt{\mu_0 \rho}} \sqrt{1 - \frac{\mu_0}{B^2} (P_{\parallel} - P_{\perp})}$$
 (4.2)

where $\mathbf{V_A}$ is the local Alfvén velocity, P_{\parallel} is the pressure parallel to the magnetic

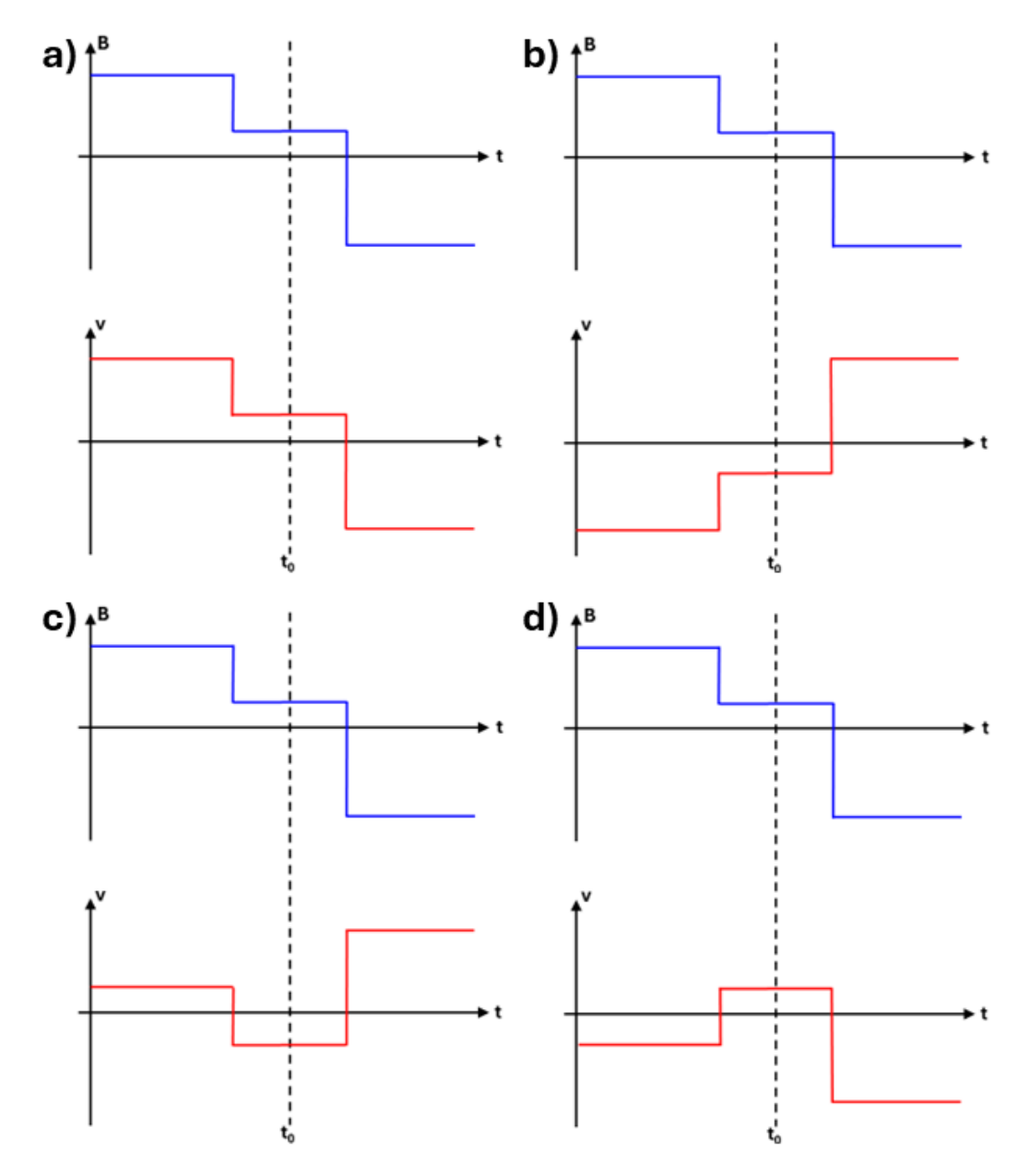


Figure 4.1: Diagram showing idealised magnetic field (blue) and bulk velocity (red) time series measurements for each permutation of model θ . a) θ_1 , correlation between **B** and **v** on both sides of the window. b) θ_2 , anti-correlation between **B** and **v** on both sides of the window. c) θ_3 , correlation when $t \le t_0$ and anti-correlation when $t > t_0$. d) θ_4 , anti-correlation when $t \le t_0$ and correlation when $t > t_0$.

field, and P_{\perp} is the pressure perpendicular to the magnetic field. To evaluate the correlation, $\Delta \mathbf{v}$ is compared against a modelled change in velocity $\Delta \mathbf{V_M}(t_i, \theta)$ defined on the basis of the Walén relation:

$$\Delta \mathbf{V_M}(t_i, \theta) = \begin{cases} \theta_a \Delta \mathbf{V_A}(t_i), & \text{if } t_i \le t_0 \\ \theta_b \Delta \mathbf{V_A}(t_i), & \text{if } t_i > t_0 \end{cases}$$
(4.3)

where $\Delta \mathbf{V_A}(t_i) = \mathbf{V_A}(t_i) - \mathbf{V_A}(t_0)$ is the vector change in $\mathbf{V_A}$ between t_0 and t_i . $\theta = [\theta_a, \theta_b]$ is a two-component parameter describing the sense of the correlation between $\Delta \mathbf{v}$ and $\Delta \mathbf{V_A}$, where each component θ_a and θ_b can take values of ± 1 . For Alfvénic solar wind, Figure 4.1 shows the four permutations of θ each corresponding to a model for $\Delta \mathbf{V_M}(t, \theta)$:

- 1. $\theta_1 = [+1, +1]$, correlation on both sides of the window.
- 2. $\theta_2 = [-1, -1]$, anti-correlation on both sides of the window.
- 3. $\theta_3 = [+1, -1]$, correlation when $t \le t_0$ and anti-correlation when $t > t_0$.
- 4. $\theta_4 = [-1, +1]$, anti-correlation when $t \le t_0$ and correlation when $t > t_0$.

Models θ_3 and θ_4 describe reconnection outflows, where a change in correlation is expected to be observed; models θ_1 and θ_2 describe the regular Alfvénic solar wind, where no such change is expected.

Bayesian inference (e.g., Barlow 1989) is used to calculate the relative probability of observing a reconnection outflow to observing the regular solar wind, within a sampling window centred on t_0 (Fargette et al., 2023):

$$Q(t_0) \simeq p(\theta_J)^{1/N} \frac{\sum_{k=3,4} p(\Delta \mathbf{v} \mid \theta_k)^{1/N}}{\sum_{k=1,2} p(\Delta \mathbf{v} \mid \theta_k)^{1/N}}$$
(4.4)

where $p(\theta_J)$ is the prior probability of observing a reconnection outflow and $p(\Delta \mathbf{v} \mid \theta_k)$ is the probability of observing $\Delta \mathbf{v}$ given model θ_k . If $Q(t_0) > 1$, the probability of a data point at t_0 being part of a reconnection outflow is greater than the probability of being part of the regular solar wind. The centre of the sampling window is then shifted through each successive point in time and Q is calculated at each point. If Q > 1 for more than two consecutive points, the interval containing these points is flagged as a potential reconnection outflow.

The second identification criterion for the algorithm is a check on whether the following features are observed in the flagged intervals: (1) a reversal in the B_l component of the magnetic field in the lmn-coordinate system; (2) the presence of an outflow jet; and (3) an electric current density J greater than 0.04 nA m⁻² in the interval (Fargette et al., 2023), where:

$$J = \frac{\Delta B_l}{\mu_0 \nu_n \Delta t} \tag{4.5}$$

Here, ΔB_l is the difference in B_l across the interval, v_n is the normal component of the bulk velocity, and Δt is the interval length. An outflow jet is defined as a change in v_l , measured between the centre of the interval and both of its edges, that is greater than 30% of the maximum change in v_l and also exceeds the maximum

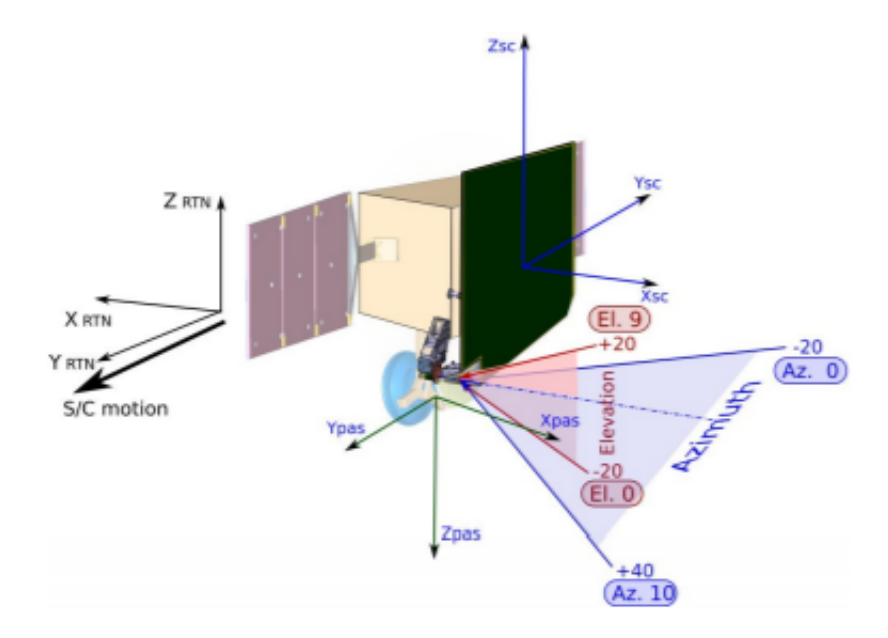


Figure 4.2: Location of SWA-PAS on *Solar Orbiter* and its field of view. The axis in black, green, and blue represent the RTN, PAS, and spacecraft (SC) coordinate systems, respectively. In the RTN coordinate system, X_{RTN} corresponds to the R-direction, Y_{RTN} corresponds to the T-direction, and Z_{RTN} A corresponds to the N-direction (see Section 2.3). Figure reproduced from Fedorov (2020).

changes in v_m and v_n . This requirement biases the algorithm by excluding asymmetric reconnection outflows (Fargette et al., 2023); however, this is not a problem as the aim is to identify reconnection outflows with a symmetric structure compatible with the stress balance model.

4.2.2 VDF resampling program

When comparing the VDFs reconstructed from my stress balance model with the observed VDFs, it is convenient to visualise 2-D slices of the 3-D VDF by taking cuts of the distribution function through planes of constant velocity components, rather than visualising the full VDF. I first define a 2-D grid of points in velocity space across the desired cut plane in the coordinate system under consideration. This grid is then transformed into the PAS coordinate system, Figure 4.2 shows how the RTN, PAS, and spacecraft (SC) coordinate systems are oriented relative to each other. The azimuth ϕ , elevation θ , and energy E values at each grid point are (Lewis et al., 2023):

$$E_i = \frac{1}{2}m_i v_i^2, (4.6)$$

$$\theta = \sin^{-1}(\hat{v_z}),\tag{4.7}$$

$$\phi = \sin^{-1}\left(\pm \frac{\hat{v_y}}{\cos \theta}\right),\tag{4.8}$$

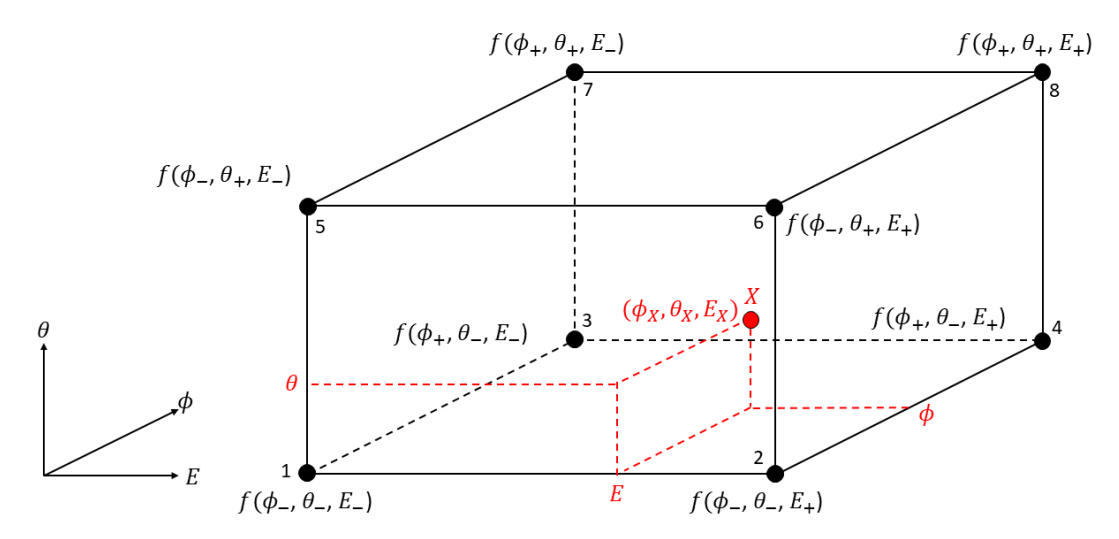


Figure 4.3: Selection of the nearest neighbouring sampling points for a grid point X at position (ϕ_X, θ_X, E_X) in the sampling space. Each neighbour 1–8 is assigned a weighting coefficient based on its distance to X in the (ϕ, θ, E) sampling space as a fraction of the total distance between neighbours.

where v_i is the proton bulk speed, and \hat{v}_y and \hat{v}_z are the y and z-components of the proton bulk velocity unit vectors in the PAS coordinate system respectively. Each point is then checked to see if they lie within the sensor field of view; those that are not are discarded.

PAS 3-D VDF measurements are arranged in an array with dimensions $11 \times 9 \times 96$, corresponding to the (ϕ, θ, E) bins of the instrument (see Section 2.3.1). The distribution function $f(\phi, \theta, E)$ is defined at each point in this sampling space. For a point X in the 2-D grid, characterised by its azimuth, elevation, and energy values (ϕ_X, θ_X, E_X) , the volume element bounding it is formed by the eight nearest neighbouring points in the 3-D sampling space. These are defined by the points labelled 1–8 in Figure 4.3, with (ϕ, θ, E) values that are immediately above and below (ϕ_X, θ_X, E_X) . The 3-D VDF is then resampled onto the 2-D grid by assigning to X the weighted average of $f(\phi, \theta, E)$ measured at the nearest neighbours:

$$\langle \log (f(\phi_X, \theta_X, E_X)) \rangle = \frac{\sum_{n=1}^8 W C_n \log (f_n(\phi_n, \theta_n, E_n))}{\sum_{n=1}^8 W C_n}, \tag{4.9}$$

where WC_n is the weighting coefficient, n = 1, 2, ..., 8 denotes the nearest neighbour, and f_n is the distribution function at n.

Each nearest neighbouring point n is assigned a weighting coefficient WC_n , based on the product of the normalised distance between X and the point diagonally opposite to n along the ϕ , θ , and E axes:

$$WC_{1} = \left(\frac{|\phi_{+} - \phi_{X}|}{\phi_{+} - \phi_{-}}\right) \left(\frac{|\theta_{+} - \theta_{X}|}{\theta_{+} - \theta_{-}}\right) \left(\frac{|E_{+} - E_{X}|}{E_{+} - E_{-}}\right) \tag{4.10}$$

$$WC_{2} = \left(\frac{|\phi_{+} - \phi_{X}|}{\phi_{+} - \phi_{-}}\right) \left(\frac{|\theta_{+} - \theta_{X}|}{\theta_{+} - \theta_{-}}\right) \left(\frac{|E_{-} - E_{X}|}{E_{+} - E_{-}}\right) \tag{4.11}$$

100

$$WC_{3} = \left(\frac{|\phi_{-} - \phi_{X}|}{\phi_{+} - \phi_{-}}\right) \left(\frac{|\theta_{+} - \theta_{X}|}{\theta_{+} - \theta_{-}}\right) \left(\frac{|E_{+} - E_{X}|}{E_{+} - E_{-}}\right) \tag{4.12}$$

$$WC_4 = \left(\frac{|\phi_{-} - \phi_{X}|}{\phi_{+} - \phi_{-}}\right) \left(\frac{|\theta_{+} - \theta_{X}|}{\theta_{+} - \theta_{-}}\right) \left(\frac{|E_{+} - E_{X}|}{E_{-} - E_{-}}\right)$$
(4.13)

$$WC_{5} = \left(\frac{|\phi_{+} - \phi_{X}|}{\phi_{+} - \phi_{-}}\right) \left(\frac{|\theta_{-} - \theta_{X}|}{\theta_{+} - \theta_{-}}\right) \left(\frac{|E_{+} - E_{X}|}{E_{-} - E_{-}}\right)$$
(4.14)

$$WC_{6} = \left(\frac{|\phi_{+} - \phi_{X}|}{\phi_{+} - \phi_{-}}\right) \left(\frac{|\theta_{-} - \theta_{X}|}{\theta_{+} - \theta_{-}}\right) \left(\frac{|E_{-} - E_{X}|}{E_{-} - E_{-}}\right) \tag{4.15}$$

$$WC_{7} = \left(\frac{|\phi_{-} - \phi_{X}|}{\phi_{+} - \phi_{-}}\right) \left(\frac{|\theta_{-} - \theta_{X}|}{\theta_{+} - \theta_{-}}\right) \left(\frac{|E_{+} - E_{X}|}{E_{-} - E_{-}}\right) \tag{4.16}$$

$$WC_8 = \left(\frac{|\phi_- - \phi_X|}{\phi_+ - \phi_-}\right) \left(\frac{|\theta_- - \theta_X|}{\theta_+ - \theta_-}\right) \left(\frac{|E_- - E_X|}{E_- - E_-}\right) \tag{4.17}$$

This approach ensures that the nearest neighbours closest to X are assigned the largest weights. By contrast, a simpler approach based on the distance between X and each neighbour would have assigned the smallest weights to the neighbours closest to X. Inverse distance weighting is also unsuitable because if X is co-located exactly with a neighbour n, the corresponding weighting coefficient WC_n becomes infinite, thus producing an unphysical value for $\langle f(\phi_X, \theta_X, E_X) \rangle$. The diagonally-opposite distance weighting method employed here avoids both of these issues.

The logarithm of the distribution function is used in Equation 4.9 to mitigate the effects of sharp gradients in the VDF on the resampling process. In cases where $f_n(\phi_n, \theta_n, E_n)$ varies by several orders of magnitude between nearest neighbours, directly evaluating Equation 4.9 with f_n introduces discontinuities in the resampled VDF because the weighted average $\langle f(\phi_X, \theta_X, E_X) \rangle$ becomes dominated by the neighbours with the largest values of f_n . Taking the logarithm of f_n dampens the magnitude differences in the VDF and gives the weighting coefficients more influence. However, this process requires all measurements where $f_n = 0$ be replaced by an arbitrary minimum value that must be small enough to not influence the calculation of $\langle \log(f(\phi_X, \theta_X, E_X)) \rangle$. For PAS data, this minimum is set at the one-count level of $f(\phi, \theta, E)$, which represents the theoretical minimum f that the instrument can measure. From Equation 2.2, this value is defined as:

$$f_{min} = \frac{2}{Gv_i^4}. (4.18)$$

where $G=5\times 10^{-6}~{\rm cm^2~sr~eV~eV^{-1}}$ is the geometrical factor of PAS (Owen et al., 2020). After computing Equation 4.9 for $\langle \log{(f)} \rangle$, the exponent is taken to recover $\langle f \rangle$ with zeros reinserted into the resampled VDF where $\langle f \rangle < f_{min}$. Finally, the

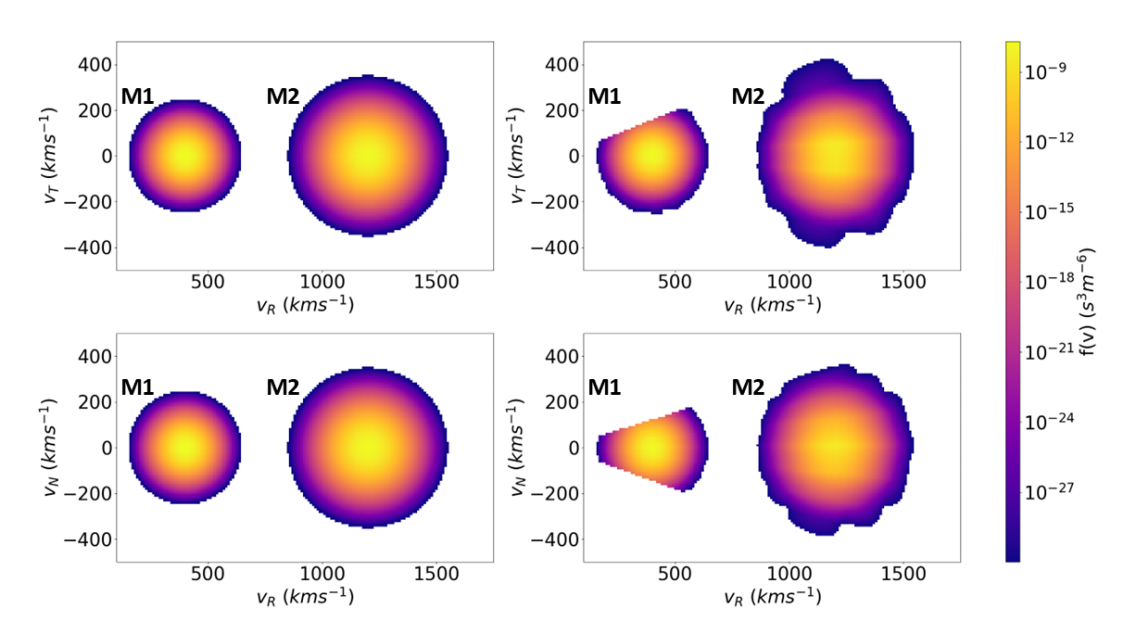


Figure 4.4: Comparison of an artificial dataset consisting of a pair of Maxwellian distribution functions, M1 and M2 (left), and the same distribution functions as observed by PAS after application of the VDF resampling program (right) in the RT (top) and RN-planes (bottom) through $v_N = 0$ km s⁻¹ and $v_T = 0$ km s⁻¹, respectively.

resampled VDFs are visualised in velocity using colour density plots with a logarithmic colour scale.

To test the performance of the VDF resampling program, I set up an artificial dataset consisting of a pair of Maxwellian distributions, M1 and M2, in RTN velocity space:

$$f_{DM} = n_1 \left(\frac{m_i}{2\pi k_b T_1} \right)^{\frac{3}{2}} e^{-\left(\frac{m_i (\mathbf{v} - \mathbf{v_1})^2}{2k_b T_1}\right)} + n_2 \left(\frac{m_i}{2\pi k_b T_2}\right)^{\frac{3}{2}} e^{-\left(\frac{m_i (\mathbf{v} - \mathbf{v_2})^2}{2k_b T_2}\right)}, \tag{4.19}$$

where the first and second terms correspond to the individual distribution function of M1 and M2, respectively. M1 is centred at $\mathbf{v_1} = (400,0,0)$ km s⁻¹, with number density $n_1 = 6$ cm⁻³ and temperature $T_1 = 6$ eV, while M2 is centred at $\mathbf{v_2} = (1200,0,0)$ km s⁻¹, with number density $n_2 = 12$ cm⁻³ and temperature T = 12 eV. Values of f_{DM} less than 10^{-31} s³ m⁻⁶ are omitted and replaced with zeros. I then apply the VDF resampling program to a simulated PAS observation of this artificial data, producing the VDFs shown in Figure 4.4. At all v_R ranges, the distributions M1 and M2 in the artificial data are very well-replicated in the resampled VDF. As expected, the circularly symmetric cross-section of the Maxwellian distribution is clearly visible in all four plots. The truncation of M1 in the resampled VDF is due to the removal of data points that fall outside the field of view of PAS.

4.3 Results

4.3.1 Event selection

I apply the automated algorithm (Fargette et al., 2023) described in Section 4.2.1 to normal mode magnetic field and proton moments data for the entire year of 2023 to identify potential reconnection outflows in the solar wind. Using this algorithm, I identify a total of 3163 potential reconnection events in the 2023 data and began the process of downselecting candidate reconnection outflows to study. Table 4.1 shows a breakdown of the number of events detected, sorted by their duration. Since a sufficient number of PAS VDF measurements inside the outflow region is required to properly resolve the outflow beam population, I first remove all events with durations < 1 minute from further consideration. At the PAS normal mode cadence of 4 seconds, this ensures that all remaining candidate events contain at least 15 VDF measurements in the outflow region. The lack of higher cadence PAS burst mode data in 2023 precludes the inclusion of shorter duration events in this study. Out of the full set of 3163 potential events, a total of 1800 satisfy this duration criterion.

To remove any false detections by the algorithm, I then performed a visual inspection of the remaining candidate events to confirm the presence of signatures consistent with a bifurcated RCS, as described in Section 1.3.4. In total, I find 517 confirmed examples of reconnection outflows with bifurcated RCS in the 2023 data. The false detection rate of 71% obtained in this study is higher than the 51% rate reported by Fargette et al. (2023), primarily because I remove all reconnection events with durations shorter than 1 minute, regardless of whether they were real events or false detections. These short-duration outflows account for the majority of events identified in that study.

Finally, I select events with symmetric inflow conditions, in order to satisfy the set of assumptions in the current sheet stress balance model (see Chapter 3). The percentage change Δ_A in a parameter A across the outflow region is defined relative to the average of the mean values of A in the one-hour periods before (A_{before}) and after (A_{after}) the outflow crossing interval:

$$\Delta_A = \frac{2(A_{after} - A_{before})}{A_{after} + A_{before}} \times 100 \tag{4.20}$$

The selected events must satisfy $\Delta_A < 10\%$ for the following inflow parameters: magnetic field strength $|\mathbf{B}|$, proton density n, proton temperature T, and proton bulk speed $|\mathbf{u'_p}|$. To account for the convection of the neutral line past the spacecraft by the solar wind, the spacecraft frame bulk proton velocity, $\mathbf{u_p}$, is transformed into the neutral line rest frame (NLRF) by $\mathbf{u'_p} = \mathbf{u_p} - \mathbf{v}_{SW}$. Here, \mathbf{v}_{SW} is the mean background solar wind velocity, defined as the mean of $\mathbf{u_p}$ in a two-hour window centred on the outflow region. Following the convention established in Chapter 3, velocities in the spacecraft frame are unprimed, while those in the NLRF are primed.

Table 4.1: Breakdown of algorithm-identified reconnection outflows, sorted by duration.

Number of events	1363	1208	330	119	62	64
Duration (min.)	< 1	1–3	3–5	5-7	7–10	> 10

Table 4.2: Summary of the properties of the 5 reconnection events shortlisted for stress balance analysis. T: magnetic shear angle across the outflow region, R: heliocentric distance from the Sun, $|\mathbf{v}_{SW}|$: mean background solar wind speed, $\Delta_{|\mathbf{B}|}$: percentage change in magnetic field strength, Δ_n percentage change in proton number density, Δ_T : percentage change in proton temperature, $\Delta_{|\mathbf{u}'|}$: percentage change in the NLRF proton

	Date and time	Duration (s)	Γ (°)	R(AU)	$ {\bf v}_{SW} ({\rm km \ s^{-1}})$	$\Delta_{ \mathbf{B} }$ (%)	Δ_n (%)	Δ_T (%)	$\Delta_{ \mathbf{u'_p} }$ (%)
50	09/01/23 18:34:20 - 18:38:40	260	102	0.95	377	1.0	4.5	1.9	6.1
0	$05/07/23 \ 09:54:08 - 09:58:53$	285	92	0.95	332	5.5	9.6	6.6	0.3
0	06/07/23 13:42:45 - 13:44:17	92	130	0.95	317	8.9	4.4	0.4	8.6
0	09/07/23 06:46:31 – 06:48:27	116	107	0.95	368	2.1	0.1	5.6	6.2
Ŏ	$06/12/23 \ 06:16:25 - 06:17:25$	09	35	0.87	498	4.3	2.4	9.4	0.3

4.3. Results 104

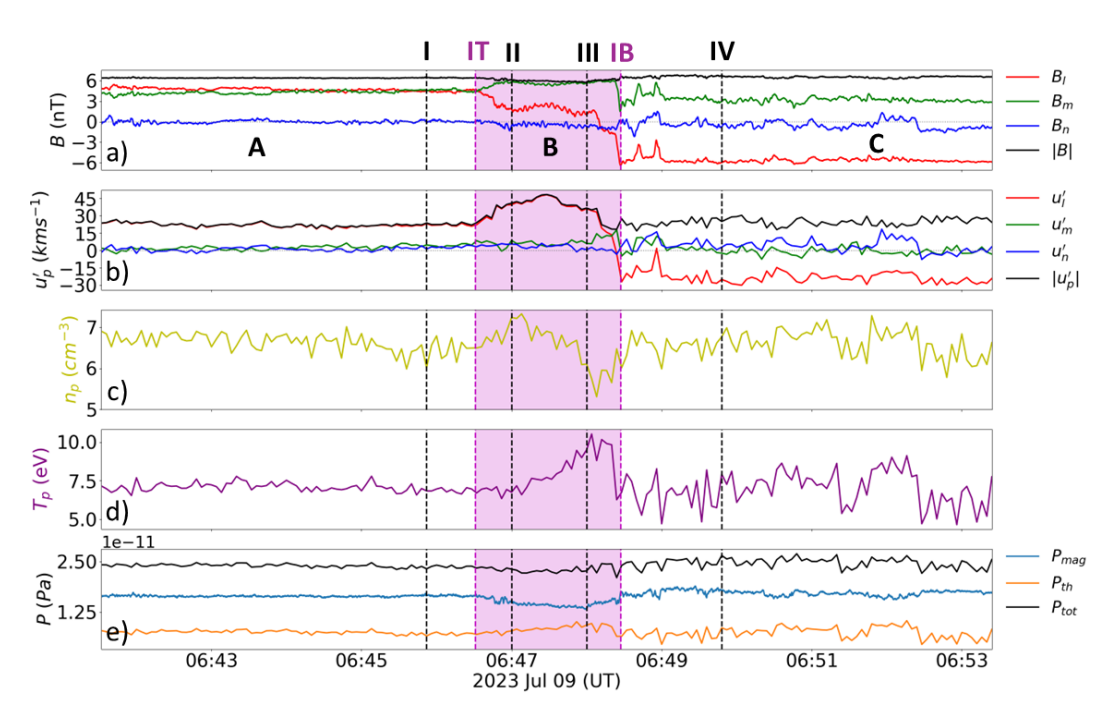


Figure 4.5: Combined magnetic field and ground-calculated proton moments for Event 4 in the *lmn* coordinate system. a) Magnetic field strength with the magnetic field strength in black. b) Proton bulk velocity in the NLRF, with the proton bulk speed in black. In both panels, the $\hat{\bf l}$ -component is red, the $\hat{\bf m}$ is in green, and the $\hat{\bf n}$ -component is in blue. c) Proton bulk density. d) Proton bulk temperature. e) Magnetic pressure P_{mag} , plasma pressure P_{th} , and their sum, the total pressure P_{tot} . The reconnection outflow region is shaded in purple, and the vertical dashed purple lines mark the location of the bifurcated RCS pair, IT and IB.

After this shortlisting process, 5 events are identified that satisfy all of the selection criteria. In producing this final shortlist, I also discard events with $\mathbf{v}_{SW} < 300 \text{ km s}^{-1}$ due to the unreliability of PAS measurements in this low energy range (Fedorov 2022; Lewis et al. 2023, see Section 2.3.1). Table 4.2 summarises the key properties of the shortlisted reconnection events. In this section, I describe two of these events which are representative of the complete dataset.

4.3.2 Event 4 — 9 July 2023 06:46:31 – 06:48:27 UT

Event 4 occurred on 9 July 2023 between 06:46:31 - 06:48:27 UT and has a duration of 116 seconds. During this period, *Solar Orbiter* was at a heliocentric distance of 0.95 AU from the Sun and the background solar wind velocity in RTN coordinates was $\mathbf{v}_{SW} = (367, -17, -20)_{RTN}$ km s⁻¹, which corresponds to a speed $|\mathbf{v}_{SW}| = 368$ km s⁻¹. Figure 4.5 shows the combined magnetic field vector and ground-calculated proton moments time series data for this event. Panel a) shows the magnetic field **B** and panel b) shows the proton bulk velocity \mathbf{u}_p' in the NLRF. The data in both panels are transformed into the *lmn* coordinate system, where the red line shows the *l*-component, the green line shows the *m*-component, and

Table 4.3: Summary of the average magnetic field and solar wind proton bulk properties for Event 4. **B**: magnetic field in *lmn* coordinates, $|\mathbf{B}|$: magnetic field strength, \mathbf{u}_p' : proton bulk velocity in *lmn* coordinates, $|\mathbf{u}_p'|$: proton bulk speed, n_p : proton density, T_p : proton temperature.

	Region A	Region B	Region C
B (nT)	(4.74, 4.34, 0.01)	(1.89, 5.64, -0.49)	(-5.62, 3.28, -0.43)
$ \mathbf{B} $ (nT)	6.42	6.27	6.52
\mathbf{u}_p' (km s ⁻¹)	(22.1, 2.7, 1.3)	(40.9, 5.8, 3.7)	(-23.1, 0.4, 4.4)
$ \mathbf{u}_p' (\mathrm{km} \mathrm{s}^{-1})$	22.3	41.5	23.5
$n_p (\text{cm}^{-3})$	6.6	6.7	6.6
T_p (eV)	7.1	7.9	7.1

blue line shows the *n*-component. The black line in panels a) and b) represent the magnetic field strength $|\mathbf{B}|$ and proton bulk speed $|\mathbf{u}'_p|$ in the NLRF, respectively. Panel c) shows the proton bulk number density n_p , and panel d) shows the proton bulk temperature T_p . Panel e) shows the magnetic pressure P_{mag} in light blue, plasma pressure P_{th} in orange, and the total pressure P_{tot} in black. This interval is divided into three regions: A, B, and C, with Region B (06:46:31 – 06:48:27 UT) marked by the purple box. To determine the *lmn* coordinate system associated with this event, I perform hybrid MVAB analysis (Gosling & Phan 2013, see Section 2.4.1) over Region B. This analysis yields eigenvalues $\lambda_1 = 3.23$, $\lambda_2 = 0.29$, and $\lambda_3 = 0.04$, with the corresponding *lmn* basis vectors in RTN coordinates given by $\hat{\mathbf{l}} = (0.32, -0.91, -0.26)_{RTN}$, $\hat{\mathbf{m}} = (-0.69, -0.03, -0.73)_{RTN}$, and $\hat{\mathbf{n}} = (0.65, 0.41, -0.63)_{RTN}$.

In Region A (06:41:31 – 06:46:31 UT), the average magnetic field is $\mathbf{B}_A = (4.74, 4.34, 0.01)$ nT, with a corresponding average field strength of $|\mathbf{B}_A| = 6.42$ nT. The average proton bulk speed is 22.3 km s⁻¹, with a density of 6.6 cm⁻³ and temperature of 7.1 eV. In Region C (06:48:27 – 06:53:27 UT), the average density and temperature is the same as in Region A but the average proton bulk speed of 23.5 km s⁻¹ is slightly higher. The average magnetic field is $\mathbf{B}_C = (-5.62, 3.28, -0.43)$ nT and is marginally stronger than in Region A, with a field strength of $|\mathbf{B}_C| = 6.52$ nT.

 B_l reverses sign across Region B, going from positive in Region A to negative in Region C. This reversal occurs in two steps at the boundaries of this region, which I interpret as a pair of current sheets and label IT and IB. Across IT, B_l decreases from +4.7 nT to +1.9 nT and then reverses sign across IB, decreasing further from +1.6 nT to -6.5 nT. The total magnetic shear angle Γ across Region B, defined as the angle between $\mathbf{B_A}$ and $\mathbf{B_C}$, is 107° . In between these two current sheets, the magnetic field is roughly constant, dwelling at an average of $\mathbf{B}_B = (1.89, 5.64, -0.49)$ nT. The magnetic field strength in Region B of $|\mathbf{B}_B| = 5.97$ nT is approximately the same as in Regions A and C. IT and IB also

4.3. Results 106

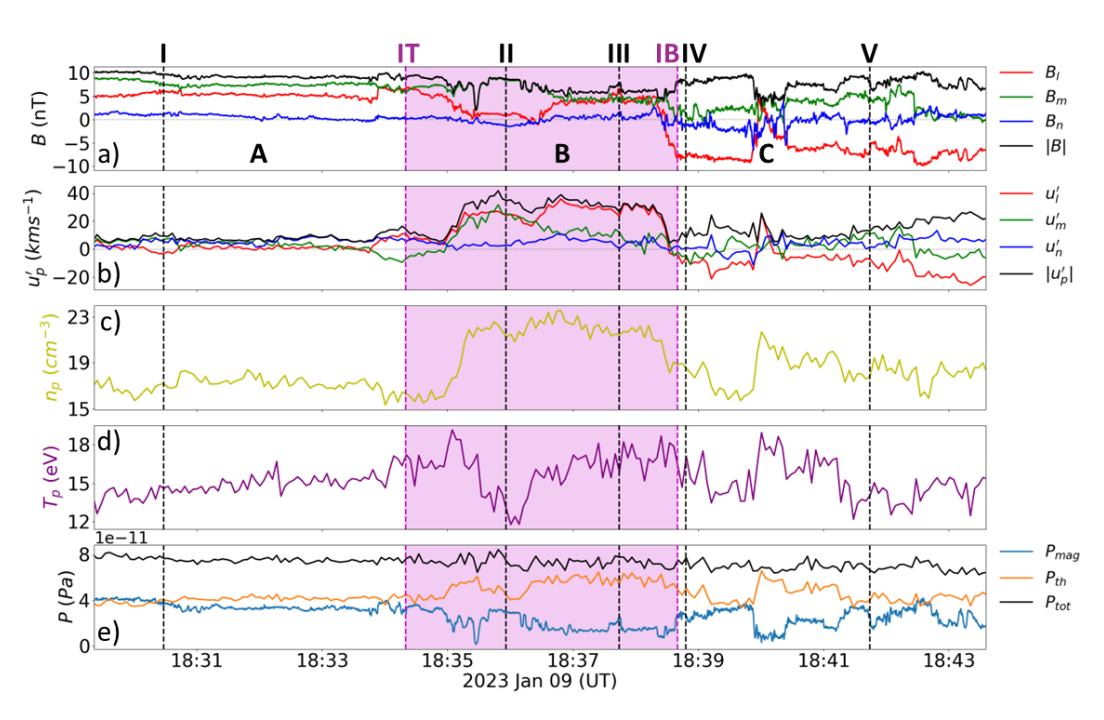


Figure 4.6: Combined magnetic field and ground-calculated proton moments for Event 1 in the *lmn* coordinate system. The figure layout is the same as in Figure 4.5.

bound an increase in the proton bulk speed, which increases from ~ 23 km s⁻¹ in Regions A and C to 42 km s-1 in Region B. The average density in Region B is $n_B = 6.7$ cm⁻³, although a decrease below this value to a minimum of 5.3 cm⁻³ is observed towards the end of Region B. This coincides with an increase in the temperature which reaches a maximum of 10.0 eV, above the average value of $T_B = 7.9$ eV in this region. Table 4.3 summarises the average magnetic field and solar wind proton bulk properties in Regions A, B, and C of Event 4.

4.3.3 Event 1 — 9 January 2023 18:34:20 – 18:38:40 UT

Event 1 occurred on 9 January 2023 between 18:34:20 - 18:38:40 UT and has a duration of 260 seconds. During this period, *Solar Orbiter* was at a heliocentric distance of 0.95 AU from the Sun and the background solar wind velocity in RTN coordinates was $\mathbf{v}_{SW} = (377, -9, -17)_{RTN}$ km s⁻¹, which corresponds to a speed $|\mathbf{v}_{SW}| = 377$ km s⁻¹. Figure 4.6 shows the observations for this event and follows the same layout as Figure 4.5. I again divide the interval shown in Figure 4.6 into Regions A, B, and C, then apply hybrid MVAB analysis over Region B to determine the basis vectors of the *lmn* coordinate system describing this event. This analysis yields eigenvalues $\lambda_1 = 6.71$, $\lambda_2 = 3.47$, and $\lambda_3 = 0.15$, with the corresponding *lmn* basis vectors $\hat{\mathbf{l}} = (-0.36, 0.75, 0.56)_{RTN}$, $\hat{\mathbf{m}} = (-0.80, 0.06, -0.60)_{RTN}$ and $\hat{\mathbf{n}} = (-0.48, -0.66, 0.58)_{RTN}$.

In Region A (18:29:56 – 18:34:20 UT), the B_l component of the magnetic field is positive. The average magnetic field in this region is $\mathbf{B}_A = (5.36, 7.59, 0.65) \,\mathrm{nT}$ with a corresponding average field strength $|\mathbf{B}_A|$ of 9.31 nT. The average u_l' compo-

for Eve	nt 1. Table layout is the	same as in Table 4.3.	
	Region A	Region B	Region C
B (nT)	(5.36, 7.59, 0.65)	(2.76, 5.63, 0.05)	(-6.63, 2.76, -0.31)

Table 4.4: Summary of the average magnetic field and solar wind proton bulk properties

	Region A	Region B	Region C
B (nT)	(5.36, 7.59, 0.65)	(2.76, 5.63, 0.05)	(-6.63, 2.76, -0.31)
$ \mathbf{B} $ (nT)	9.31	6.27	7.19
\mathbf{u}_p' (km s ⁻¹)	(1.5, 2.9, 5.4)	(27.4, 14.8, 5.4)	(-10.5, -1.5, 3.6)
$ \mathbf{u}_p' \text{ (km s}^{-1})$	6.4	31.6	11.2
$n_p (\mathrm{cm}^{-3})$	17.1	22.0	18.3
T_p (eV)	14.8	15.6	15.1

nent of the proton bulk velocity is $+1.5 \text{ km s}^{-1}$ and the average proton bulk speed is 6.4 km s⁻¹. Additionally, a density of 17.1 cm⁻³ and a temperature of 14.8 eV is measured. Throughout Region A, the magnetic field, bulk velocity, density, and temperature are fairly constant and do not exhibit large fluctuations.

Conversely, in Region C (18:38:40 – 18:43:40 UT), B_l is negative. The average magnetic field in this region is $\mathbf{B}_C = (-6.63, 2.76, -0.31)$ nT and is slightly weaker than in Region A, with $|\mathbf{B}_C| = 7.19$ nT. Here, the average u_I' is -10.5 km s⁻¹ and the average proton bulk speed of 11.2 km s⁻¹ is faster than in Region A. The solar wind plasma in Region C is denser and hotter than in Region A, with a density of 18.3 cm⁻³ and a temperature of 15.1 eV. In contrast to Region A, the magnetic field and plasma conditions show more variability in Region C. Although B_l and v_l are predominantly negative in this region, there is a brief interval around 18:40 where they both reverse sign and become positive, before their sign reverts to negative shortly afterwards.

In Region B (18:34:20 – 18:38:40 UT), the average magnetic field is \mathbf{B}_B = (2.76, 5.63, 0.05) nT and the magnetic field strength $|\mathbf{B}_B| = 6.27$ nT is weaker than in both Regions A and C. Across IT, B_l decreases from +6.5 nT to +1.3 nT and then reverses sign across IB, decreasing further from +4.6 nT to -8.1 nT. In between these current sheets, B_l is approximately constant, although there is a small jump from +1.3 nT to +4.0 nT near the midpoint of Region B. Similar trends are not observed in the other components of the magnetic field across Region B; B_m gradually decreases from +6.1 nT to +1.3 nT, while B_n is approximately constant at +0.1 nT. The magnetic shear angle across Region B is 103°. Compared to Regions A and C, there is a large increase in the u'_1 component of the proton bulk velocity to $+27 \,\mathrm{km}\,\mathrm{s}^{-1}$, accompanied by an increase in $|\mathbf{u}_p'|$ to 32 km s⁻¹. As is the case in Event 4, the changes in **B** and \mathbf{u}'_p are anti-correlated at IT and correlated at IB. The average density in this region of $n_B = 22.0 \text{ cm}^{-3}$ is much larger than in Regions A and C, while the average temperature of $T_B = 15.6$ eV is similar. Table 4.4 summarises the average magnetic field and solar wind proton bulk properties in Regions A, B, and C of Event 1.

4.4 Stress balance analysis

The two events presented in Section 4.3 exhibit features that are consistent with the Gosling model (Gosling et al., 2005a) of reconnection in the solar wind. This supports the interpretation that Region B corresponds to the reconnection outflow region, with the current sheets IT and IB forming a bifurcated RCS pair. In this framework, Regions A and C are the inflow regions immediately surrounding the reconnection outflow. Although not shown here, the remaining three events also display similar signatures of RCS bifurcation.

Having established that the five events in the dataset are indeed examples of reconnection outflow with bifurcated RCS structures, I apply my stress balance model on them. In this section, I use Event 4 as an example to demonstrate the procedure and results of the stress balance analysis. Tables 4.5 and 4.6 summarise the results of my analysis for all five events. I follow the labelling convention introduced in Chapter 3 to describe the relevant quantities associated with the stress balance. The inflow beam from Region A is Beam 1, while the inflow beam from Region C is Beam 2. Subscripts 1 and 2 indicate properties of Beams 1 and 2, while the subscripts A, B, and C refer to properties of the beams and magnetic field in the respective regions. The superscripts IT and IB denote velocities defined in the magnetic field discontinuity rest frame (DRF) at current sheets IT and IB.

4.4.1 Outflow region opening angle

I begin by calculating the opening angle of the reconnection outflow region. Since the stress balance model describes symmetric reconnection outflow regions, I make the following assumptions in the stress balance analysis. First, the beam population in both inflow regions is assumed to consist of a single proton beam in each region. Hence, the inflow beam velocity, density, and temperature are assumed to be the average of their bulk values in the corresponding inflow region. Second, the pair of beams in the outflow region are assumed to have equal density. If the total bulk density in the outflow region n_B is the sum of the density of the individual beams, then $n_{1B} = n_{2B} = n_B/2$. Third, RCS bifurcation requires the inflow beam passing through the current sheet on one side of the outflow region be fast enough to catch up with the current sheet on the opposing side (see Figure 3.3). The validity and limitations of this assumption are discussed in more detail in Section 3.5.

I evaluate the stress balance conditions in the DRF at IT and IB. The velocity at which this frame moves away from the neutral line is given by the deHoffmann-Teller (HT) velocity, which I derive by performing HT analysis (Khrabrov & Sonnerup 1998; Paschmann & Sonnerup 2008, see Section 2.4.2) at IT and IB. For Event 4, the HT velocity in *lmn* coordinates is $\mathbf{V}'_{HT,IT} = (46.7, 28.2, 2.6) \,\mathrm{km} \,\mathrm{s}^{-1}$ at IT and $\mathbf{V}'_{HT,IB} = (28.4, -29.6, 7.4) \,\mathrm{km} \,\mathrm{s}^{-1}$ at IB. Using the velocity transformations from the NLRF to the DRF given by Equations 3.46 and 3.47, the inflow beam velocities are $\mathbf{u}_{1A}^{IT} = (-24.6, -25.6, -1.3) \,\mathrm{km} \,\mathrm{s}^{-1}$ and

	Event 1	Event 2	Event 3	Event 4	Event 5
γ_1 (°)	2.9	2.6	3.0	3.4	1.6
γ_2 (°)	7.5	10.8	5.4	8.2	0.6
$W(d_i)$	985	1002	311	324	60
$D_1(d_i)$	19300	22900	6090	5305	2020
$D_2(d_i)$	7500	5300	3290	2270	5570

Table 4.5: Estimates for the outflow region opening angle γ , outflow region width W, and distance D of *Solar Orbiter* from the neutral line.

 $\mathbf{u}_{2C}^{IB} = (-51.5, 30.0, -3.0) \,\mathrm{km} \,\mathrm{s}^{-1}$. Given the observed proton densities in Regions A, B, and C (see Table 4.3), the density of the inflow beams are $n_{1A} = n_{2C} = 6.6 \,\mathrm{cm}^{-3}$, while the density of the outflow beams are $n_{1B} = n_{2B} = 3.4 \,\mathrm{cm}^{-3}$. With these density and velocity values, I apply the mass continuity condition across current sheets IT and IB to determine the $\hat{\mathbf{n}}$ -component of the outflow beam velocities. This yields $u_{1B,n}^{IT} = -2.5 \,\mathrm{km} \,\mathrm{s}^{-1}$ and $u_{2B,n}^{IB} = -5.9 \,\mathrm{km} \,\mathrm{s}^{-1}$.

Using Equation 3.25, I calculate two values for the outflow region opening angle: $\gamma_1 = 3.4^{\circ}$, based on the values of $u_{1B,n}^{IT}$ and $\mathbf{V}'_{HT,IT}$; and $\gamma_2 = 8.2^{\circ}$, based on the values of $u_{2B,n}^{IB}$ and $\mathbf{V}'_{HT,IB}$. From these predictions of γ , I then estimate the distance D between $Solar\ Orbiter$ and the neutral line. Assuming the spacecraft is stationary during the time taken for the solar wind to convect the reconnection outflow structure past it, the width of the outflow region is given by $W = v_{SW,n} \Delta t$, where $v_{SW,n} = \mathbf{v}_{SW} \cdot \hat{\mathbf{n}}$ is the $\hat{\mathbf{n}}$ -component of the background solar wind velocity and Δt is the duration of the outflow region crossing. This leads to the following equation for D:

$$D = \frac{W}{2\tan(\gamma/2)} \tag{4.21}$$

W and D are expressed in units of ion inertial length $d_i = c/\omega_p$, where $\omega_p = \sqrt{n_p e^2/m_i \varepsilon_0}$ is the ion plasma frequency. From Equation 4.21, the estimate of D derived from γ_1 is $D_1 = 5305 \ d_i$ (or $4.7 \times 10^5 \ \text{km}$), while the estimate of D derived from γ_2 is $D_2 = 2270 \ d_i$ (or $2.0 \times 10^5 \ \text{km}$). I repeat this analysis on the other four events in the dataset and summarise the results in Table 4.5.

4.4.2 Outflow beam temperature and velocity

Equations 3.32 and 3.35 relate $u_{1B,n}^{IT}$ and $u_{2B,n}^{IB}$ with the outflow beam temperatures T_{1B} and T_{2B} , respectively, taking the observed magnetic field and inflow beam properties in Regions A and C as inputs. Figure 4.7 shows these relationships for Event 4. For the values of $u_{1B,n}^{IT}$ and $u_{2B,n}^{IB}$ derived in the previous section, the corresponding outflow beam temperatures are $T_{1B} = 9.0$ eV and $T_{2B} = 9.3$ eV. This suggests that Beam 1 is heated as it crosses the current sheet IT, with its temperature increasing from 7.1 eV in Region A to 9.0 eV in Region B. Similarly, Beam 2 is also heated as it crosses the current sheet IB, with its temperature increasing from 7.0 eV

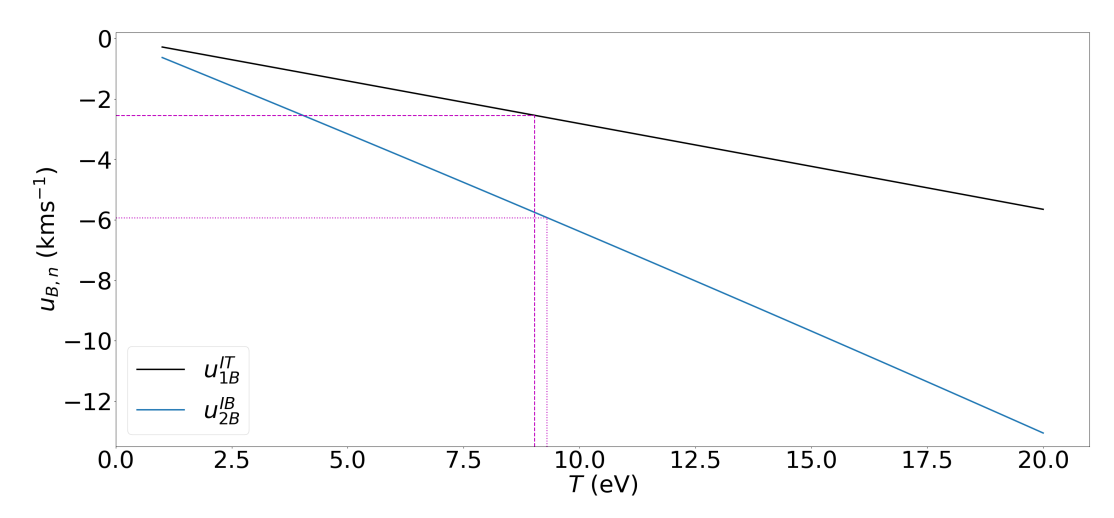


Figure 4.7: Graph of $u_{1B,n}^{IT}$ (black) and $u_{2B,n}^{IB}$ (blue) as a function of temperature T for Event 4. The dashed purple line denotes the value of $u_{1B,n}^{IT}$, derived in Section 4.4.1, and its corresponding temperature T_{1B} . The dotted purple line denotes the value of $u_{2B,n}^{IB}$, also derived in Section 4.4.1, and its corresponding temperature T_{2B} .

in Region C to 9.3 eV in Region B.

I then derive the $\hat{\bf l}$ and $\hat{\bf m}$ -components of the velocity of Beam 1 in Region B. From the observed magnetic field strength and density in Region A, the Alfvén speed in this region is $V_{A,A}=54.4~{\rm km~s^{-1}}$. Substituting this into Equations 3.27 and 3.28 yields $u_{1B,l}^{IT}=-24.0~{\rm km~s^{-1}}$ and $u_{1B,m}^{IT}=-25.9~{\rm km~s^{-1}}$. Therefore, the velocity of Beam 1 in Region B is $\mathbf{u}_{1B}^{IT}=(-24.0,-25.9,-2.5)~{\rm km~s^{-1}}$ with a speed of $|\mathbf{u}_{1B}^{IT}|=35.4~{\rm km~s^{-1}}$. This is similar to its speed in Region A of $|\mathbf{u}_{1A}^{IT}|=35.5~{\rm km~s^{-1}}$. As explained in the previous chapters, the inflow and outflow beams are expected to be field-aligned in the DRF. To check if this property is observed, I calculate the pitch angle of Beam 1, defined as the angle between its velocity and the magnetic field. The pitch angle of this beam is $\alpha_{1A}=176^{\circ}$ in Region A and $\alpha_{1B}=26^{\circ}$ in Region B.

Following a similar procedure, I determine the $\hat{\bf l}$ and $\hat{\bf m}$ -components of the velocity of Beam 2 in Region B using Equations 3.33 and 3.34, respectively. Given the Alfvén speed in Region C of $V_{A,C}=55.4~{\rm km~s^{-1}}$, I obtain $u_{2B,l}^{IB}=25.8~{\rm km~s^{-1}}$ and $u_{2B,m}^{IB}=54.3~{\rm km~s^{-1}}$. Therefore, the velocity of Beam 2 in Region B is ${\bf u}_{2B}^{IB}=(25.8,54.3,-5.9)~{\rm km~s^{-1}}$ and its speed is $|{\bf u}_{2B}^{IB}|=60.4~{\rm km~s^{-1}}$. This is similar to its speed in Region C of $|{\bf u}_{2C}^{IB}|=59.7~{\rm km~s^{-1}}$. The pitch angle of Beam 2 is $\alpha_{2C}=0^\circ$ in Region C and $\alpha_{2B}=7^\circ$ in Region B.

I repeat the analysis described in this section for the remaining four reconnection events in the dataset. Table 4.6 summarises the properties of Beams 1 and 2 derived from the stress balance analysis for these events.

Table 4.6: Summary of the velocity, speed, pitch angle, density, and temperature of Beams 1 and 2 in Regions A, B, and C for all five reconnection events in the dataset.

	Event 1	Event 2	Event 3	Event 4	Event 5
${\bf u}_{1A}^{IT} \ ({\rm km \ s^{-1}})$	(-15.5, -10.3, -0.6)	(-34.8, -18.9, -0.8)	(31.5, 21.2, 1.5)	(-24.6, -25.6, -1.3)	(-12.0, -40.8, -0.5)
$ \mathbf{u}_{1A}^{IT} \text{ (km s}^{-1})$	18.6	39.6	38.0	35.5	42.6
$lpha_{1A}$ $(^{\circ})$	159	1	7	176	7
$n_{1A} ({ m cm}^{-3})$	17.1	6.9	6.9	9.9	6.4
T_{1A} (eV)	14.8	3.2	4.4	7.1	9.3
$\mathbf{u}_{1B}^{IT} (\mathrm{km \ s}^{-1})$	(60.0, 46.4, -1.0)	(57.0, -59.7, -1.3)	(-129.1, 13.7, 2.2)	(-24.0, -25.9, -2.5)	(52.5, -52.1, -1.0)
$ \mathbf{u}_{1B}^{IT} \; (\mathrm{km \ s^{-1}})$	75.8	82.6	129.8	35.4	73.9
$lpha_{1B}\left(^{\circ} ight)$	26	43	09	154	42
$n_{1B} ({\rm cm}^{-3})$	11.0	4.4	4.5	3.4	3.2
T_{1B} (eV)	16.9	4.1	8.3	0.6	8.9
$\mathbf{u}_{2B}^{IB} (\mathrm{km \ s^{-1}})$	(22.9, 24.4, -2.5)	(10.1, 20.9, 5.5)	(-12.6, -34.7, -4.2)	(25.8, 54.3, -5.9)	(-179.5, -12.0, 0.4)
$ \mathbf{u}_{2B}^{IB} (\mathrm{km s^{-1}})$	33.6	23.8	37.2	60.4	179.9
$lpha_{2B}\left(^{\circ} ight)$	18	153	136	7	06
$n_{2B} (\mathrm{cm}^{-3})$	11.0	4.4	4.5	3.4	3.2
T_{2B} (eV)	13.9	5.0	9.0	9.3	8.9
$\mathbf{u}_{2C}^{IB} (\mathrm{km \ s}^{-1})$	(-27.3, 9.1, -1.5)	(-14.1, 20.0, 3.5)	(39.9, -3.8, -2.4)	(-51.5, 30.0, -3.0)	(-11.3, 24.1, 0.2)
$ \mathbf{u}_{2C}^{IB} (\mathrm{km \ s^{-1}})$	28.8	24.8	40.2	59.7	26.6
$lpha_{2C}$ (°)	4	175	177	0	175
$n_{2C} (\mathrm{cm}^{-3})$	18.3	7.0	8.0	9.9	6.4
T_{2C} (eV)	15.1	4.2	3.9	7.0	8.9

4.5 Comparison of VDFs

Using the values for the velocities, densities, and temperatures of Beams 1 and 2 derived from the stress balance analysis in Section 4.4, I reconstruct the distribution function describing the reconnection inflow and outflow beam population in Regions A, B, and C. The proton distribution function in the solar wind can often be divided into two components: a core population and a field-aligned beam population of faster protons (Feldman et al., 1973; Marsch et al., 1982b). In this analysis, the distinction between the proton core and fast beam populations is neglected, and the reconnection inflow and outflow beams are treated as Maxwellians.

4.5.1 Event 4

Figure 4.8 shows the ion VDFs measured by PAS at various times during Event 4; these times are indicated by the vertical dashed black lines in Figure 4.5. The VDFs are presented in the NLRF using the field-aligned coordinate system. In this coordinate system, the basis vectors are defined as follows: $\hat{\mathbf{v}}_{\parallel}$ points in the direction of the magnetic field; $\hat{\mathbf{v}}_{\perp 1} = (\hat{\mathbf{B}} \times \hat{\mathbf{u}}_p) \times \hat{\mathbf{B}}$; and $\hat{\mathbf{v}}_{\perp 2} = -(\hat{\mathbf{u}}_p \times \hat{\mathbf{B}})$, where $\hat{\mathbf{B}}$ and $\hat{\mathbf{u}}_p$ are the unit vectors of the magnetic field and proton bulk velocity, respectively. For each VDF, I take three 2-D cuts through the peak of the distribution in the $\mathbf{v}_{\parallel} - \mathbf{v}_{\perp 1}$ plane (left), $\mathbf{v}_{\parallel} - \mathbf{v}_{\perp 2}$ plane (middle), and the $\mathbf{v}_{\perp 1} - \mathbf{v}_{\perp 2}$ plane (right). The predicted velocity of the beams in each region is overlaid on the VDFs: the teal box marks the predicted velocity of Beam 1, while the gray circle marks the predicted velocity of Beam 2.

Distribution I shows the VDF measured at 06:45:52 UT in Region A. In the \mathbf{v}_{\parallel} – $\mathbf{v}_{\perp 1}$ and \mathbf{v}_{\parallel} – $\mathbf{v}_{\perp 2}$ planes, a strong core population with larger f(v) is observed near the origin, as well as a weaker shoulder with smaller f(v) at $v_{\parallel} < 0$, corresponding to the fast field-aligned beam protons. In the $\mathbf{v}_{\perp 1}$ – $\mathbf{v}_{\perp 2}$ plane, both the observed VDF and the predicted velocity of Beam 1 are centred on the origin, suggesting that the proton distribution and Beam 1 are gyrotropic. The predicted velocity of Beam 1 matches the location of the proton core population in velocity space. Distribution IV, the VDF measured in Region C at 06:49:48 UT, has very similar properties to distribution I apart from a more pronounced difference in the strength of the proton core and fast proton beam populations. The tail of the distributions, found in the upper left quadrant of the \mathbf{v}_{\parallel} – $\mathbf{v}_{\perp 1}$ plane VDFs, correspond to the solar wind alpha particle population (Marsch et al., 1982a; Lavraud et al., 2021; Duan et al., 2023). As the contribution of the alpha particles to the current sheet stress balance is not considered, the discussion in this section will focus on the solar wind proton population.

Distributions II and III show the VDFs measured in Region B at 06:47:00 and 06:48:00, respectively. The distributions are comprised of two proton beams of similar strength along the field-aligned direction, rather than the core and fast beam-type distribution seen in Regions A and C. The predicted velocities of Beams

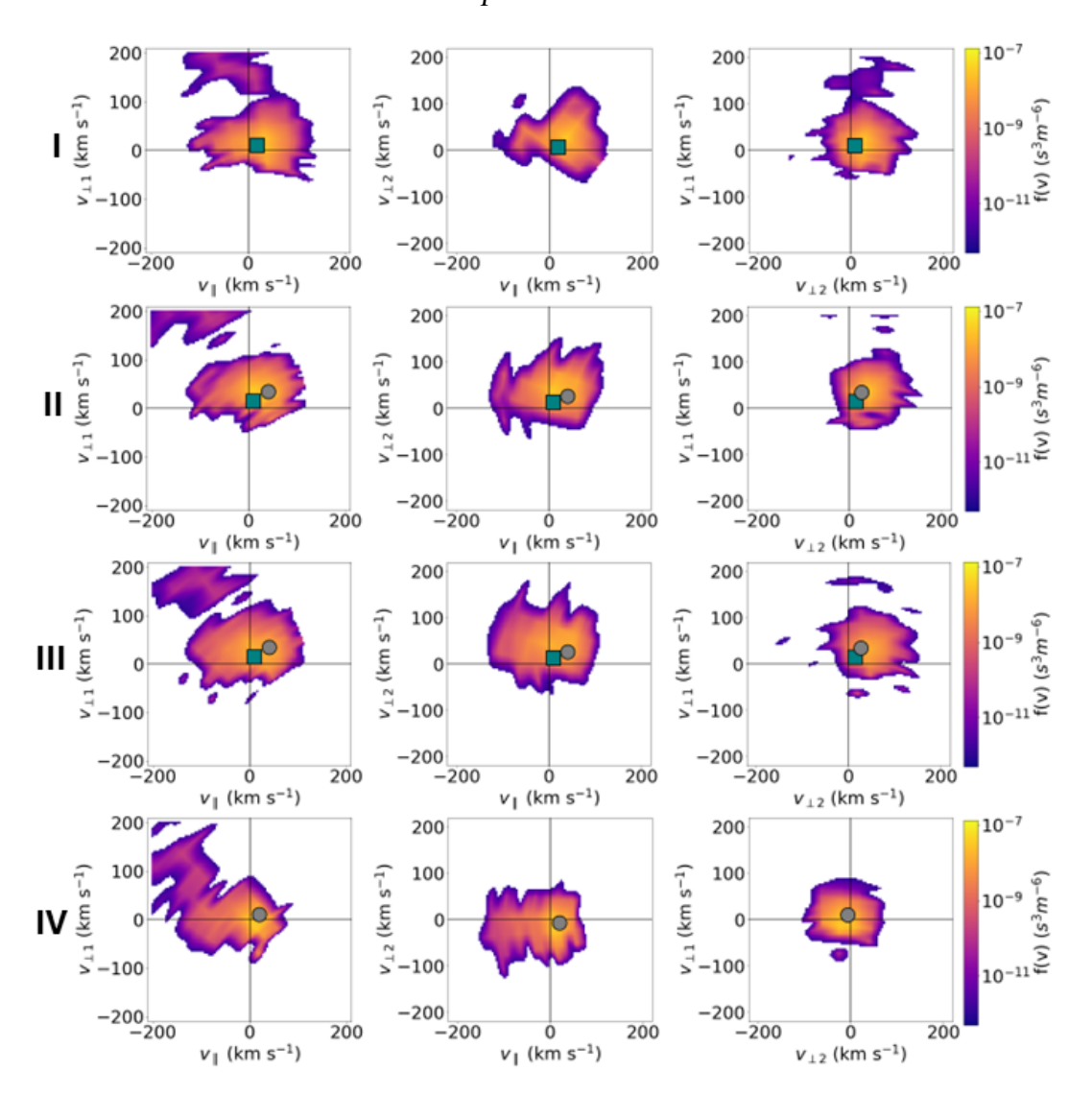


Figure 4.8: Selected PAS ion VDF measurements at different times during Event 4, presented in the NLRF using the field-aligned coordinate system. Distribution I is the VDF observed in Region A at 06:45:52 UT. Distributions II and III are the VDFs observed in Region B at 06:47:00 and 06:48:00, respectively. Distribution IV is the VDF observed in Region C at 06:49:48 UT. The left column shows the 2-D cut of the VDF in the $\mathbf{v}_{\parallel} - \mathbf{v}_{\perp 1}$ plane, the middle column shows the 2-D cut of the VDF in the $\mathbf{v}_{\parallel} - \mathbf{v}_{\perp 2}$ plane, and the right column shows the 2-D cut of the VDF in the $\mathbf{v}_{\perp} - \mathbf{v}_{\perp 2}$ plane.

1 and 2 are consistent with the observed VDFs, with Beam 1 having a field-aligned velocity component of $u_{1B,\parallel} = 9 \text{ km s}^{-1}$ and Beam 2 having a field-aligned velocity component of of $u_{2B,\parallel} = 40 \text{ km s}^{-1}$. In the $\mathbf{v}_{\perp 1} - \mathbf{v}_{\perp 2}$ plane, the observed VDF appears to be gyrotropic, although both it and the predicted velocities of Beams 1 and 2 are slightly offset from the origin.

In Region B, the relative field-aligned speed of Beams 1 and 2 is 31 km s⁻¹, which is comparable to their thermal velocity, both approximately ~ 30 km s⁻¹.

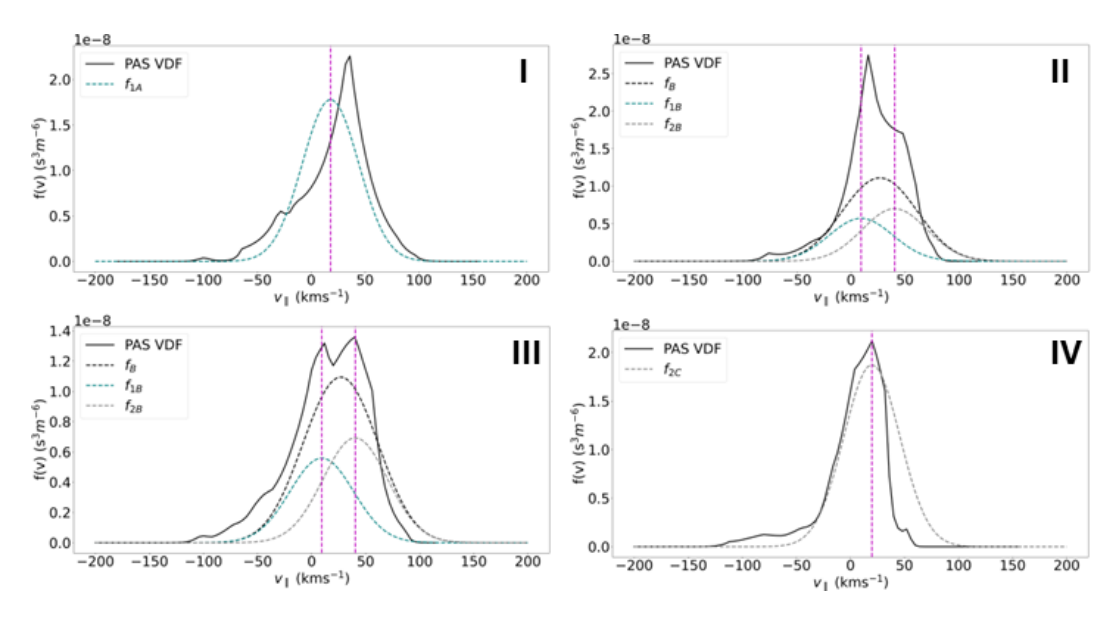


Figure 4.9: 1-D cuts through the reconstructed and observed VDFs shown in Figure 4.8. The solid black curves represent the observed VDF, while the dotted curves represent the reconstructed VDFs describing the reconnection inflow and outflow beam population. The vertical dashed purple lines mark the predicted field-aligned speed of the beams.

Consequently, the counterstreaming beams in the outflow region are not well-separated in velocity space (see Section 3.4), making them difficult to resolve in the observed VDFs, especially with the colour scale used in Figure 4.8. To better visualise the reconnection inflow and outflow beams in each region, I take identical cuts through the observed and reconstructed VDFs along the field-aligned direction. Figure 4.9 shows the comparison between the reduced VDFs, with the solid curve representing the observed VDF and the dotted curve representing the reconstructed VDF.

In distribution I, there is a distinct shoulder in the observed VDF to the left of the proton core population, which I interpret as a fast proton beam population propagating anti-parallel to the magnetic field line. The presence of this population of protons explains why the peak of the reconstructed VDF for Beam 1, f_{1A} , is displaced to the left of the peak of the observed VDF.

Distribution II and III show the proton distribution in Region B. Based on the framework of the model, a pair of counterstreaming reconnection outflow beams is expected to be observed in this region. Here, the reconstructed VDF is the sum of the individual distribution functions of Beams 1 and 2, $f_B = f_{1B} + f_{2B}$. The observed proton distribution in Region B is broader than in Region A and exhibits a double-peaked structure. I interpret this as the counterstreaming beam pair formed by the entry of Beams 1 and 2 into Region B from Regions A and C, respectively. This structure is more prominent in distribution III, which is the VDF measured towards the end of Region B, compared to distribution II, which is the VDF measured near

the beginning of Region B. In both distributions, the peaks of the observed VDF align closely with the predicted field-aligned speed of Beams 1 and 2 in Region B. The counterstreaming beams are resolved more clearly in the observed VDFs than the reconstructed VDFs, with the peaks of the reconstructed VDFs also being somewhat smaller than the peak of the observed VDFs. Finally, in distribution IV, the Maxwellian distribution f_{2C} used to model Beam 2 in Region 2 is a very good match to the observed VDF.

4.5.2 Event 1

Figure 4.10 shows the ion VDFs measured by PAS at various times during Event 1; these times are indicated by the vertical dashed black lines in Figure 4.6. The layout and symbols are identical to those in Figure 4.8. In general, the distribution functions observed in this event are broader than those of Event 4 as the plasma is warmer (see Table 4.6). Distribution I shows the VDF measured at 18:30:28 UT, when *Solar Orbiter* was in Region A. Here, the proton distribution is gyrotropic and consists of a broad proton core distribution around the origin with no clear signatures of a field-aligned proton beam population. The predicted velocity of Beam 1 is closely aligned with the proton core population.

As the spacecraft enters Region B, distribution II (18:35:56 UT) and III (18:37:44 UT) show an enhancement in the distribution function compared to Region A. Beam 1 has a predicted field-aligned velocity component of $u_{1B,\parallel}=87$ km s⁻¹, while $u_{2B,\parallel}=33$ km s⁻¹ for Beam 2. Both beams have negligible velocity components in the $\hat{\mathbf{v}}_{\perp 1}$ -direction, but have components in $\hat{\mathbf{v}}_{\perp 2}$ -direction of approximately -43 km s⁻¹ for Beam 1 and -28 km s⁻¹ for Beam 2. In the $\mathbf{v}_{\perp 1}$ - $\mathbf{v}_{\perp 2}$ plane, this non-zero perpendicular velocity component introduces an offset in the predicted velocities of Beam 1 and 2 along the $\hat{\mathbf{v}}_{\perp 2}$ -direction, even though the observed VDF is centred around the origin. The relative field-aligned speed of Beams 1 and 2 in Region B is 55 km s⁻¹. This is comparable to their thermal speeds of ~ 40 km s⁻¹, which again results in poorly-resolved counterstreaming beams in the outflow region.

Distribution IV (18:38:48 UT) and V (18:41:44 UT) show the VDFs measured after *Solar Orbiter* exits the outflow region and moves into Region C. Similar to Distribution I, the predicted velocity of Beam 2 falls within a broad, gyrotropic proton core population. However, unlike Distribution I, a shoulder in the distribution is observed along the field-aligned direction, which is consistent with a population of fast beam protons. Additionally, the tail of the observed distribution is now aligned in the $\hat{\mathbf{v}}_{\perp 1}$ -direction, rather than the $\hat{\mathbf{v}}_{\parallel}$ -direction.

Figure 4.11 shows the comparison between the 1-D cuts through the observed and reconstructed VDFs along the field-aligned direction. Distribution I shows that the Maxwellian distribution used to model Beam 1 in Region A, f_{1A} , is a good match to the observed VDF. Moreover, a separate population of fast, field-aligned proton beams is not distinguishable in the observed VDF.

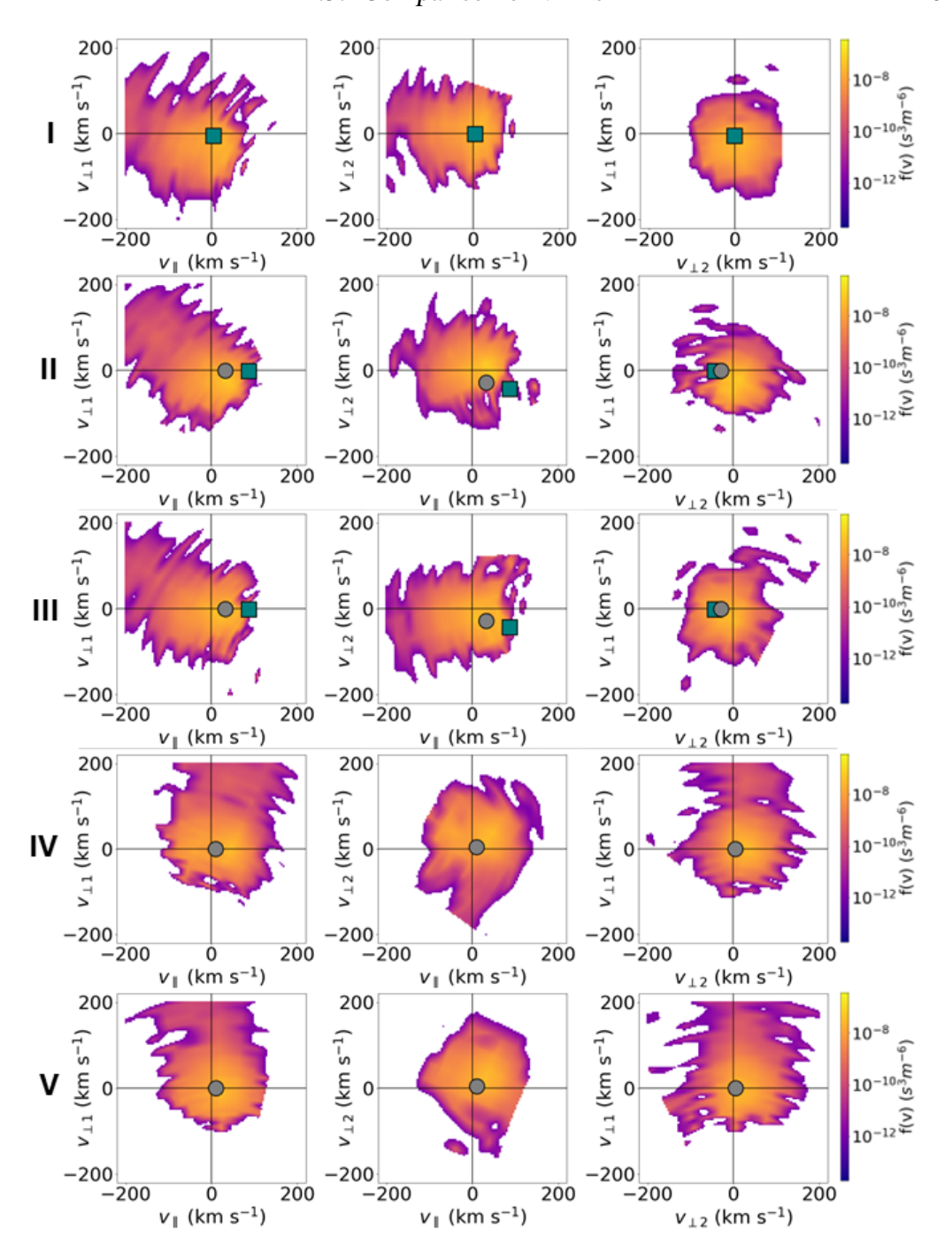


Figure 4.10: Selected PAS ion VDF measurements at different times during Event 1. The figure layout is identical to Figure 4.8. Distribution I is the VDF observed in Region A at 18:30:28 UT. Distributions II and III are the VDFs observed in Region B at 18:35:56 UT and 18:37:44 UT, respectively. Distribution IV and V are observed in Region C at 18:38:48 UT and 18:41:44 UT, respectively.

In distribution II, measured in the first half of Region B, a pair of counterstreaming beams in the outflow region is expected in both the observed and reconstructed VDF. However, the observed VDF is single-peaked and closely resembles

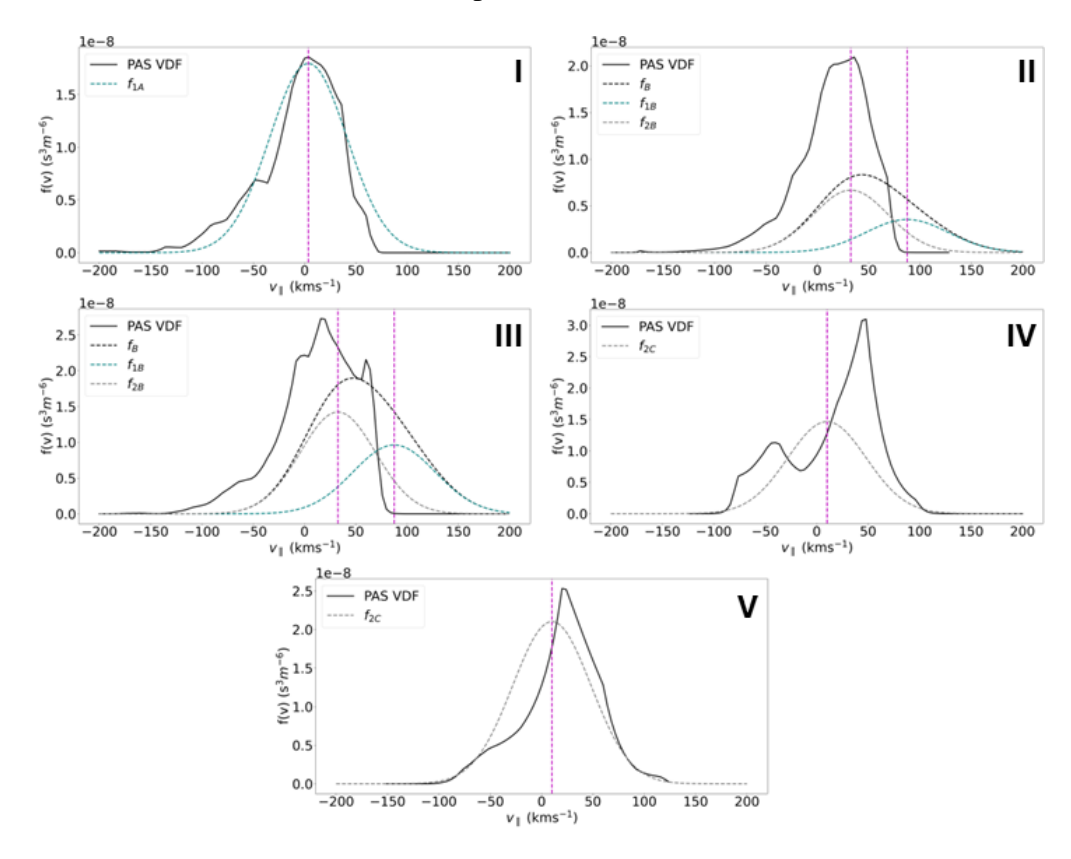


Figure 4.11: 1-D cuts through the reconstructed and observed VDFs shown in Figure 4.10. The figure layout is identical to Figure 4.9.

the observed VDF in Region A. Although the observed VDF is similar in width to the reconstructed VDF, it has a larger peak that is displaced to the left of the predicted values for $u_{1B,\parallel}$ and $u_{2B,\parallel}$.

In distribution III, measured in the second half of Region B, there is a significant change in the observed VDF. Compared to distributions I and II, the observed VDF becomes broader and develops a double-peaked structure consistent with a pair of counterstreaming beams. The position of the distribution peaks is displaced slightly to the left of the predicted values for $u_{1B,\parallel}$ and $u_{2B,\parallel}$, but the peak separation is comparable to the predicted relative field-aligned speed. Additionally, the observed VDF is similar in width to the reconstructed VDF. As is the case with Event 4, the counterstreaming beam signature is clearer in the observed VDF than the reconstructed VDF, and the peak of the observed VDF is also larger than the reconstructed VDF. The transition point between the regimes described by distribution II and III roughly coincides with the small jump in B_l at the midpoint of Region B (see Figure 4.6).

Contrary to the model assumptions, the presence of counterstreaming beams persists into Region C, as shown in distribution IV. Compared to distribution III, the height difference between the two peaks and the peak separation are both greater. This double-peaked structure is observed until around 18:40 UT, after which a

single-peaked VDF is observed in distribution V. Here, the Maxwellian distribution f_{2C} describing Beam 2 is a good approximation to the observed VDF. In addition to the core proton population, there is a small bump in the observed VDF around $v_{\parallel} \sim -50 \, \mathrm{km \, s^{-1}}$, which indicates the presence of a population of fast beam protons propagating anti-parallel to the magnetic field in this region. This accounts for the slight offset of the peak of f_{2C} to the left of the observed VDF.

4.6 Discussion

In the stress balance analysis, I determine two values, γ_1 and γ_2 , for the opening angle of the reconnection outflow region of all five events in the dataset, which range from 0.6° to 10.8° . I also estimate the width of the outflow region: Event 5 is the narrowest, with a width of $60 d_i$, while Event 2 is the thickest, with a width of $1002 d_i$ (see Table 4.5). These values for the outflow region opening angle and width are consistent with the observed properties of reconnection outflows in the solar wind (Gosling & Szabo, 2008; Mistry et al., 2015). The small opening angles justify the assumption that the bifurcated RCS pair IT and IB can be characterised by a common *lmn*-coordinate system.

Using these estimates for γ_1 , γ_2 , and the outflow region width, I then calculate the distance D between $Solar \ Orbiter$ and the neutral line. For Events 3, 4, and 5, the estimates for D derived from γ_1 are of the same order of magnitude as those derived from γ_2 , ranging from 2020 d_i to 6090 d_i . However, D_1 is much larger than D_2 in Events 1 and 2. For both events, the difference between D_1 and D_2 is similar: in Event 1, $D_1 = 19300 \ d_i$ and $D_2 = 5700 \ d_i$, while in Event 2, $D_1 = 22900 \ d_i$ and $D_2 = 5300 \ d_i$. The pronounced discrepancy between D_1 and D_2 for Events 1 and 2 is likely due to the larger difference between γ_1 and γ_2 compared to the other three events. Furthermore, the estimate for D (Equation 4.21) is very sensitive to changes in γ . Since γ is small for reconnection outflows, minor errors of a few degrees in its estimation can lead to large variations in D. Barring the two outlier values of D in Events 1 and 2 where $D \sim 20000 \ d_i$, the other estimates for the spacecraft distance to the neutral line are consistent with previous results (Mistry et al., 2015).

In the symmetric current sheet stress balance model, the proton beam population in Regions A and C is assumed to consist of a single isothermal inflow beam, while the beam population in Region B consists of a pair of isothermal counterstreaming beams. Although the observed proton distribution in the solar wind is characterised by the combination of a core population and a field-aligned fast beam population (Feldman et al., 1973; Marsch et al., 1982b), the proton population in Regions A and C is generally well-approximated by a single Maxwellian distribution defined by the proton bulk velocity, temperature, and density in these regions.

Out of the five reconnection events in the dataset, Event 4 is the one whose properties most closely match the predictions of the symmetric stress balance model. Throughout the entire duration where *Solar Orbiter* was in Region B, clear

signatures of counterstreaming outflow beams with similar intensity in the distribution function measurements are observed. The predicted velocities of the counterstreaming beams, as derived from the stress balance model, are in agreement with the observed velocity of the beams. The pitch angles of the reconnection inflow and outflow beams are also consistent with the reconnection geometry of the model (see Figure 3.2 and 3.3). Beam 1, the inflow beam from Region A, has a pitch angle of $\alpha_{1A} = 176^{\circ}$ in Region A and a pitch angle of $\alpha_{1B} = 154^{\circ}$ in Region B. This suggests that this beam is propagating roughly in the anti-parallel direction along the reconnected magnetic field line. Conversely, Beam 2, the inflow beam from Region C, has a pitch angle of $\alpha_{2C} = 0^{\circ}$ in Region C and a pitch angle of $\alpha_{2B} = 7^{\circ}$ in Region B. This suggests that Beam 2 propagates parallel to the field line in the opposite direction to Beam 1.

In earlier studies of the counterstreaming beam population in reconnection outflows, the relative field-aligned speed of the beams is expected to be the sum of the Alfvén speed, V_A , in the inflow regions. However, these studies consistently measure relative beam speeds that are smaller than this expected value (Gosling et al., 2005a; Lavraud et al., 2021). Similar behaviour is observed in Event 4; the relative field-aligned speed of the counterstreaming beams is 31 km s⁻¹, which is less than the sum of the Alfvén speed in Regions A and C, $V_{A,A} + V_{A,C} = 110 \text{ km s}^{-1}$. This discrepancy was previously attributed to electromagnetic ion beam instability limiting the relative beam speed to $\sim 1.5V_A$ (Goldstein et al., 2000). As discussed in Chapter 3, my results suggest that this discrepancy may instead be a natural consequence of stress balance at the bifurcated RCS. Additionally, the relative beam speed measured in this event is similar to the thermal velocity of the counterstreaming beams of $\sim 30 \text{ km s}^{-1}$. Consequently, the beams are not well-separated from each other in velocity space, a property I also observe in the model test case (see Section 3.5).

While the results for Event 4 demonstrate the symmetric current sheet stress balance model can explain some of the observed features of reconnection outflows in the solar wind, my other results suggest that the underlying assumption of a symmetric reconnection configuration does not always hold well. If the outflow region were symmetric, $\gamma_1 = \gamma_2$ would be expected. However, as noted above, I obtain different values for γ_1 and γ_2 for all five events (see Table 4.5). This difference in γ suggests that structure of the outflow region is asymmetric. I also observe asymmetries in the properties of the counterstreaming beams in Region B, particularly in the beam speed, which are not expected in the symmetric case. Based on the symmetry of the model, the counterstreaming beams are initially assumed to have equal densities. These results therefore call into question the validity of this assumption. Since the density enters the mass continuity condition to determine $u_{1B,n}^{IB}$ and $u_{2B,n}^{IB}$, which are then used to calculate the outflow region opening angle and beam temperature, this assumption has consequential effects on my predictions for these parameters.

Furthermore, the model predictions for the beam density and temperature affect the shape of the distribution function describing the counterstreaming beam population in Region B. This may explain the differences seen in Events 1 and 4 between the observed VDF and the VDF reconstructed from the results of the stress balance model.

Elaborating on the asymmetry between the counterstreaming beams in the outflow region, I now examine the 1-D VDFs for Event 1 in more detail (see Figure 4.9). Recall from Section 3.3, the assumption for symmetric current sheet bifurcation. Beam 1 (Beam 2) is required to catch up with the current sheet IB (IT) on the opposite side of Region B, but not pass through it and enter Region C (A). The key consequence of this assumption is that in the symmetric model, the counterstreaming beam population is expected to be present everywhere in Region B only. Although I observe this behaviour in Event 4, this is not the case for Event 1. In Event 1, the proton distributions in the first half of Region B are single-peaked and resemble the distribution functions for the inflow beam in Region A. A double-peaked distribution, consistent with a pair of counterstreaming beams, only develops in the second half of Region B and persists into Region C.

This has two implications on the behaviour of the beams in Region B. First, it suggests that Beam 1 is faster than expected and has sufficient speed to pass through the current sheet IB and enter Region C. In contrast, Beam 2 is slower than expected and has insufficient speed to catch up with current sheet IT. This is one interpretation of my results that is consistent with the observed evolution of the VDFs in Region B. Contrary to the expectations of the model, the results for Event 1 raise the possibility that the reconnection outflow region may be subdivided into two layers, each containing a distinct population of proton beams: one with a single beam and the other with a pair of counterstreaming beams. These layers may be separated by an additional current sheet, potentially corresponding to the small magnetic field discontinuity observed near the middle of Region B. This interpretation of the reconnection outflow region structure is consistent with a framework for multi-layer outflow structures proposed by Owen et al. (2021), as well as results showing reconnection can locally produce multiple proton beam populations in the solar wind (Lavraud et al., 2021; Phan et al., 2022; Duan et al., 2023). In order to properly describe the structure of these multi-layered reconnection outflows, I will need to adapt the stress balance models to account for reconnection configurations with multiple inflow or outflow beam populations.

The violation of the current sheet bifurcation condition implies Equation 3.25 no longer correctly defines the outflow region opening angle, which may be an additional contributing factor to the asymmetry in γ_1 and γ_2 . Moreover, this violation also invalidates the set of simplifying assumptions I use to derive the velocities of Beam 1 (Equations 3.27, 3.28, and 3.30) and Beam 2 (Equations 3.33–3.35) in Region B. As a result, the velocities of the counterstreaming beam, \mathbf{u}_{1B}^{IT} and \mathbf{u}_{2B}^{IB} ,

obtained from the symmetric stress balance model may no longer be accurate. This could explain why, with the exception of Event 4, the pitch angles of the counterstreaming beams for the other four events suggests oblique or quasi-perpendicular (Event 5) propagation relative to the magnetic field, rather than the expected field-aligned propagation. An alternative explanation for these unusual pitch angles is that the HT analysis (Khrabrov & Sonnerup, 1998; Paschmann & Sonnerup, 2008) has failed to properly identify the DRF at IT and IB. In an improperly defined DRF, the convection electric field is not fully transformed away (see Section 2.4.2), meaning the beam protons will still experience an $\mathbf{E} \times \mathbf{B}$ drift perpendicular to the magnetic field. The stress balance analysis would then have to be modified to factor in the effects of the residual electric field on the motion of the reconnection inflow and outflow beams. Further investigation is required to properly understand how changes to the HT analysis and the identification of the DRF affect the overall results of the stress balance analysis.

Finally, in the stress balance model (see Section 3.4), a 2-D reconnection structure is assumed where the B_m component of the magnetic field is neglected. For a symmetric magnetic field configuration, the B_l -component of the magnetic field is also assumed to reverse across the reconnection outflow region, with $B_l = 0$ inside it. However, my observations suggest that these assumptions do not hold in the solar wind, where the reconnection magnetic field typically has a strong B_m component. For all five reconnection events in the dataset, I find that B_m is of comparable magnitude to B_l and $B_l \neq 0$ in the outflow region. They have magnetic shear angles of $\sim 100^{\circ}$, which are smaller than what is assumed in the model. Notably, Event 5 has an even smaller shear angle of just 35°. Previous studies show that magnetic reconnection tends to occur across RCS with small to moderate shear angles $< 90^{\circ}$, similar to observations in the dataset (Gosling et al., 2007; Phan et al., 2010; Gosling & Phan, 2013). In future work, I will need to generalise the symmetric current sheet stress balance model to account for the effects of strong guide fields in the reconnection magnetic field, as well as asymmetries in the inflow and outflow beam population.

4.7 Conclusions

In this chapter, I apply my symmetric bifurcated current sheet stress balance model developed in Chapter 3 to observed cases of magnetic reconnection in the solar wind. Using in-situ magnetic field and solar wind proton data from *Solar Orbiter*, I identify 3163 potential reconnection outflows over a period spanning the entirety of 2023. Out of these events, I shortlist 5 events with symmetric magnetic field and inflow conditions that appear to closely satisfy the underlying assumptions of the model for further analysis.

I apply the stress balance model on the reconnection events in the dataset to first determine the opening angles of their outflow regions and the distance between Solar Orbiter and the neutral line. I obtain opening angles ranging from 0.2° to 10.8° and distances ranging from $2270 \ d_i$ to $6090 \ d_i$. My results for these two parameters are consistent with previous observations of reconnection outflows in the solar wind (Mistry et al., 2015). However, they also suggest that the outflow region is asymmetric, contrary to the model assumptions. I also calculate the velocity, density, and temperature of the reconnection inflow and outflow beams for all five events. I then perform a more detailed analysis of the 9 January 2023 and 9 July 2023 events, and use these parameters to reconstruct the VDF describing the beam population in the inflow and outflow regions. These reconstructed VDFs are compared with the observed proton VDFs from Solar Orbiter.

For the 9 July event, I observe a double-peaked structure in the observed proton distribution throughout the outflow region (Region B), consistent with a pair of counterstreaming proton beams (Gosling et al., 2005a; Lavraud et al., 2021). The velocities of the observed beams align very closely with the predicted velocities of the beams derived from the stress balance model. As the relative field-aligned speed of the beams are comparable to their thermal velocities, they are not well-separated in the VDFs and overlap with each other. The counterstreaming beam signature is more evident in the observed VDFs than the reconstructed VDFs. I observe similar overlap between the counterstreaming beam pair in the 9 January event.

The 9 January event is substantially more complex that the 9 July event and exhibits properties that are markedly different from the symmetric model. Instead of an outflow region characterised by a single population of counterstreaming proton beams, I observe an outflow region divided into two distinct halves. Counterstreaming beams are only visible in the proton distribution in the trailing half of Region B and persists into the trailing inflow region (Region C). In the leading half, the distribution is single-peaked and closely matches the VDFs measured in the leading inflow region (Region A). This suggests that the outflow region for this event is highly asymmetric and may not be adequately described by the symmetric current sheet stress balance model. The division of the outflow region into multiple layers, each containing a distinct population of proton beams, has been reported in previous studies using *Solar Orbiter* and *Parker Solar Probe* data (Lavraud et al., 2021; Phan et al., 2022; Duan et al., 2023). These observations are consistent with the theoretical framework for multi-layered reconnection outflow structures developed by Owen et al. (2021).

I conclude that as a proof-of-concept, the symmetric current sheet stress balance model can successfully reproduce some of the known properties of reconnection outflows in the solar wind, including current sheet bifurcation and counterstreaming outflow beams. However, the vast majority of reconnection outflows in the solar wind are asymmetric, as evidenced by the 9 January event. Further work needs to be done to generalise the symmetric stress balance model to account for asymmetries in the reconnection magnetic field and beam population.

Chapter 5

Magnetic reconnection as an erosion mechanism for magnetic switchbacks

5.1 Introduction

In Section 1.4, I present a general overview of the characteristics of magnetic switchbacks in the solar wind. Magnetic switchbacks are localised Alfvénic deflections of the heliospheric magnetic field (HMF) away from the Parker spiral, sometimes resulting in a full polarity reversal. They have previously been observed by *Helios* (Horbury et al., 2018), *Ulysses* (Balogh et al., 1999), and *ACE* (Owens et al., 2013) at heliocentric distances between 0.3 – 2.4 AU, both near the ecliptic plane and at high heliolatitudes. Recent observations from *Parker Solar Probe* (PSP) show that switchbacks are a prevalent feature of the near-Sun solar wind (Bale et al., 2019; Kasper et al., 2019), which are present for roughly 75% of the time during PSP Encounter 1 (Horbury et al., 2020b). They are convected over the observing spacecraft on timescales ranging from a few minutes to a few hours (Dudok de Wit et al., 2020) and have transverse scales comparable to solar granulation and supergranulation (Fargette et al., 2021).

At heliocentric distances of 1 AU and beyond, switchbacks are less frequently seen than in the inner heliosphere, suggesting that these structures evolve and eventually erode as they propagate away from the Sun (Tenerani et al., 2020, 2021). Magnetic reconnection is one possible mechanism that can enhance erosion of a switchback by removing magnetic flux from the polarity-reversed section of the magnetic field. Observations from *Helios* (Gosling et al., 2006a) and PSP (Froment et al., 2021) show that reconnection may occur at switchback boundaries.

I present examples of switchback boundary reconnection events observed by *Solar Orbiter* and use them to evaluate the effectiveness of magnetic reconnection as an erosion mechanism for switchbacks. In Section 5.2, I describe my data and analysis methods. In Section 5.3, I show observations of three instances of switchback reconnection. In Section 5.4, I present my interpretation of the switchback and reconnection geometry based on the observations, and estimate the remaining

lifetime of the switchbacks. In Section 5.5, I summarise my findings and discuss their implications for the global properties of switchbacks in the solar wind.

5.2 Data and methods

5.2.1 Instrumentation and event selection

I use publicly available magnetic field and ground-calculated proton moments (density, bulk velocity, and temperature) data from the MAG (Horbury et al., 2020a) and SWA-PAS (Owen et al., 2020) instruments onboard *Solar Orbiter* (Müller et al., 2020). In normal mode operation, MAG provides measurements at a cadence of 8 vectors/s (see Section 2.2.1), while SWA-PAS delivers proton moments data once every 4 seconds (see Section 2.3.1). In addition, I also use electron strahl pitch angle distribution (PAD) data at energies > 70 eV from SWA-EAS (Owen et al., 2020), when available, at a cadence of one measurement per 10 seconds.

For this case study, I sample a time interval during August 2021 for magnetic reconnection outflows in the solar wind, when the spacecraft was at a heliocentric distance of 0.6-0.7 AU. I exclude outflows with crossing durations less than 20 seconds to ensure that there are at least five proton measurements inside the outflow region. Out of the ten events that satisfy the selection criteria, three are associated with potential magnetic switchbacks.

5.2.2 Testing for rotational discontinuities

In the Gosling reconnection model (Gosling et al. 2005a, see Section 1.3.4), the reconnection current sheet (RCS) bifurcates and the outflow region is bound by a pair of standing Alfvénic rotational discontinuities (RDs). To test for RDs across the RCS, I use magnetic hodographs in conjunction with the Walén relation.

The MAG and SWA-PAS data are first transformed from the RTN coordinate system into the lmn coordinate system using the hybrid minimum variance analysis (MVAB) method (Gosling & Phan 2013, see Section 2.4.1). Magnetic hodographs illustrate the spatial and temporal evolution of $\bf B$ in 3D. They are plotted in pairs for the lm and ln-planes of the lmn-frame (Sonnerup & Scheible, 1998). For an RD across a current sheet, the temporal variation of $\bf B$ traces a semi-circular arc in the lm-plane hodograph and a vertical line at $B_n \neq 0$ in the ln-plane hodograph.

The Walén relation tests for the Alfvénicity of the RDs (Khrabrov & Sonnerup, 1998):

$$\mathbf{v_p} - \mathbf{V_{HT}} = \pm \mathbf{v_A} = \pm \frac{\mathbf{B}}{\sqrt{\mu_0 \rho}},\tag{5.1}$$

where V_{HT} is the deHoffmann-Teller (HT) frame velocity of the RD (de Hoffmann & Teller, 1950). In this chapter, I derive V_{HT} using the standard HT analysis procedure outlined in Section 2.4.2. However, the adaptive HT frame analysis method (Comişel et al., 2015; Marghitu et al., 2017; Schwartz et al., 2021) may be better suited for propagating structures and could provide better results. The sign in Equa-



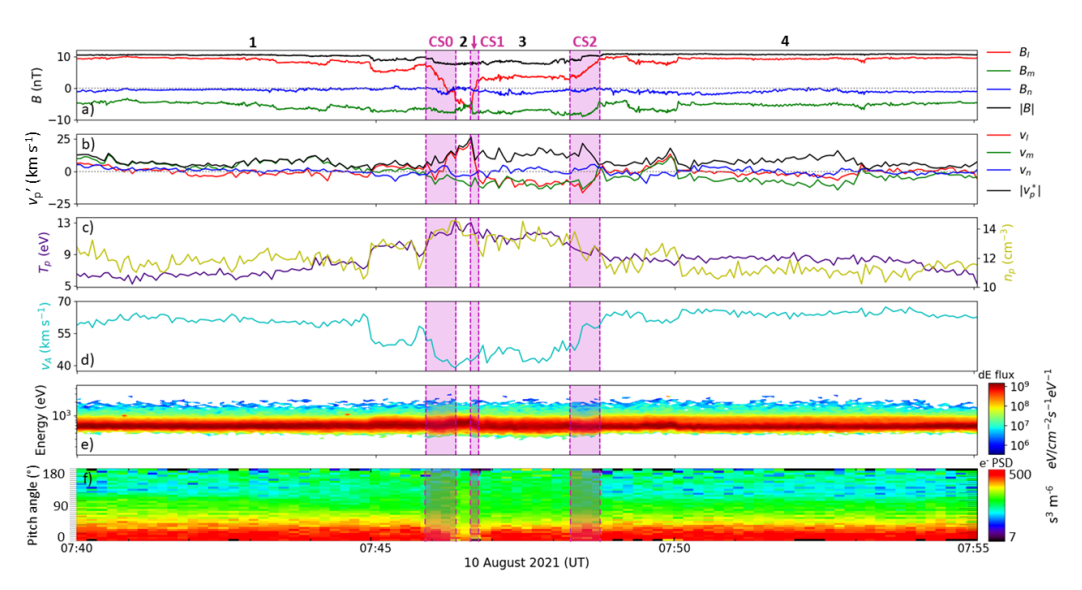


Figure 5.1: Combined magnetic field, proton, and electron strahl PAD time series data for Event 1 in the hybrid MVAB lmn-frame. a) Magnetic field vector with the magnetic field strength in black. b) Proton bulk velocity with the proton bulk speed in black. The average proton bulk velocity $\langle \mathbf{v_p} \rangle$ over this interval has been removed. In both panels, the l-component is in red, the m-component is in green, and the n-component is in blue. c) Proton temperature (left scale, purple) and number density (right scale, gold). d) Alfvén speed. e) 1D proton energy spectrogram. f) Electron strahl PAD for energies > 70 eV. The dashed lines mark the region boundaries identified in the text and numbered at the top of the figure.

tion 5.1 indicates whether the Alfvénic fluctuations in $\mathbf{v_p} - \mathbf{V_{HT}}$ and \mathbf{B} are correlated (positive) or anti-correlated (negative). I analyse component-by-component scatter plots of $\mathbf{v_p} - \mathbf{V_{HT}}$ against $\mathbf{v_A}$, known as Walén plots, and use the least-squares linear regression method to determine the line of best fit. The gradient of this line provides a means to quantify the strength of the Walén relation. From Equation 5.1, a gradient of ± 1 in the Walén plot is an indicator of an ideal Alfvénic RD. However, previous works suggest that gradients with magnitudes between 0.5 – 1 are sufficient to demonstrate the existence of an RD across a current sheet (Paschmann et al., 2005; Dong et al., 2017).

5.3 Results

5.3.1 Event 1 – 10 August 2021 07:45:50 - 07:48:45 UT

Figure 5.1 provides a general overview of the magnetic field and solar wind conditions observed between 07:40:00 and 07:55:00 UT on 10 August 2021, recorded at a heliocentric distance of 0.72 au. Panel a) shows the magnetic field **B** and b) shows the proton bulk velocity $\mathbf{v_p'}$ in the *lmn*-frame. In both panels, the *l*-component is in red, the *m*-component is in green, and the *n*-component is in blue. Panel c) shows the proton temperature T_p in purple and proton number density n_p in gold, d) shows

the Alfvén speed v_A , e) shows the 1D proton energy spectrogram, and f) shows the electron strahl PAD for energies $> 70 \,\text{eV}$. I remove the average proton bulk velocity $\langle \mathbf{v_p} \rangle$ across this interval from the data, such that $\mathbf{v_p'} = \mathbf{v_p} - \langle \mathbf{v_p} \rangle$.

Table 5.1: Event 1 *lmn*-frame basis vectors for CS0 and CS1 + CS2 expressed in RTN coordinates.

Current sheet	<i>lmn</i> -frame basis vectors (R, T, N)
CS0	$ \mathbf{\hat{l}} = (0.660, -0.216, 0.719) \mathbf{\hat{m}} = (0.016, -0.954, -0.300) \mathbf{\hat{n}} = (0.751, 0.210, -0.626) $
CS1 + CS2	$ \mathbf{\hat{l}} = (0.677, -0.343, 0.651) \mathbf{\hat{m}} = (0.086, 0.916, 0.393) \mathbf{\hat{n}} = (-0.731, -0.210, 0.649) $

In RTN coordinates, $\langle \mathbf{v_p} \rangle = (322.2, -5.6, -5.6)_{RTN} \, \mathrm{km \ s^{-1}}$ across this time interval and the predominant HMF polarity is in the anti-sunward (+R) direction. I divide this interval into several regions marked by the vertical dashed lines. Regions 1 $(07:40:00-07:45:50 \, \mathrm{UT})$ and 4 $(07:48:45-07:55:00 \, \mathrm{UT})$ correspond to the period of quiet HMF and steady, slow solar wind surrounding this event. The regions shaded in purple are centered around sharp discontinuities in the magnetic field that I identify as current sheets.

I derive the *lmn*-frames for the current sheets at the leading (CS0) and trailing edges (CS1, CS2) of this event using the hybrid MVAB method. As the trailing edge current sheets are bifurcated, I perform the MVAB analysis from the start of CS1 to the end of CS2. Table 1 shows the *lmn*-frame basis vectors for these current sheets. The angular differences between the corresponding basis vector pairs of both frames are small, ranging from 1.7° to 8.3°. Thus, the *lmn*-frames for the leading and trailing edges of this event are roughly aligned. As I am interested in the properties of the reconnection outflow, its properties are visualised in the *lmn*-frame of the trailing edge current sheet in Figs. 5.1a and 5.1b. I do the same for the overview plots of the other two events.

Across CS0 (07:45:50 – 07:46:20 UT), the polarity of the radial component of the HMF, B_R , flips from the anti-sunward direction to the sunward direction. In the *lmn*-frame of this event, this corresponds to a reversal in the B_l component of the magnetic field from +7 nT to -4 nT. Due to the relatively strong B_m component, the maximum magnetic shear angle across this current sheet is 77.2°. There is a 20% decrease in the average magnetic field strength $|\mathbf{B}|$, from 10 nT in Region 1 to 8 nT in CS0. v_l , the l-component of $\mathbf{v'_p}$, increases from 0 km s⁻¹ to +10 km s⁻¹, and the average proton bulk speed $|\mathbf{v'_p}|$ increases from 4 km s⁻¹ to 13 km s⁻¹. Here, T_p and n_p both reach a maximum of 13 eV and 14 cm⁻³, respectively.

Region 2 (07:46:20 – 07:46:35 UT) encompasses the polarity-reversed section

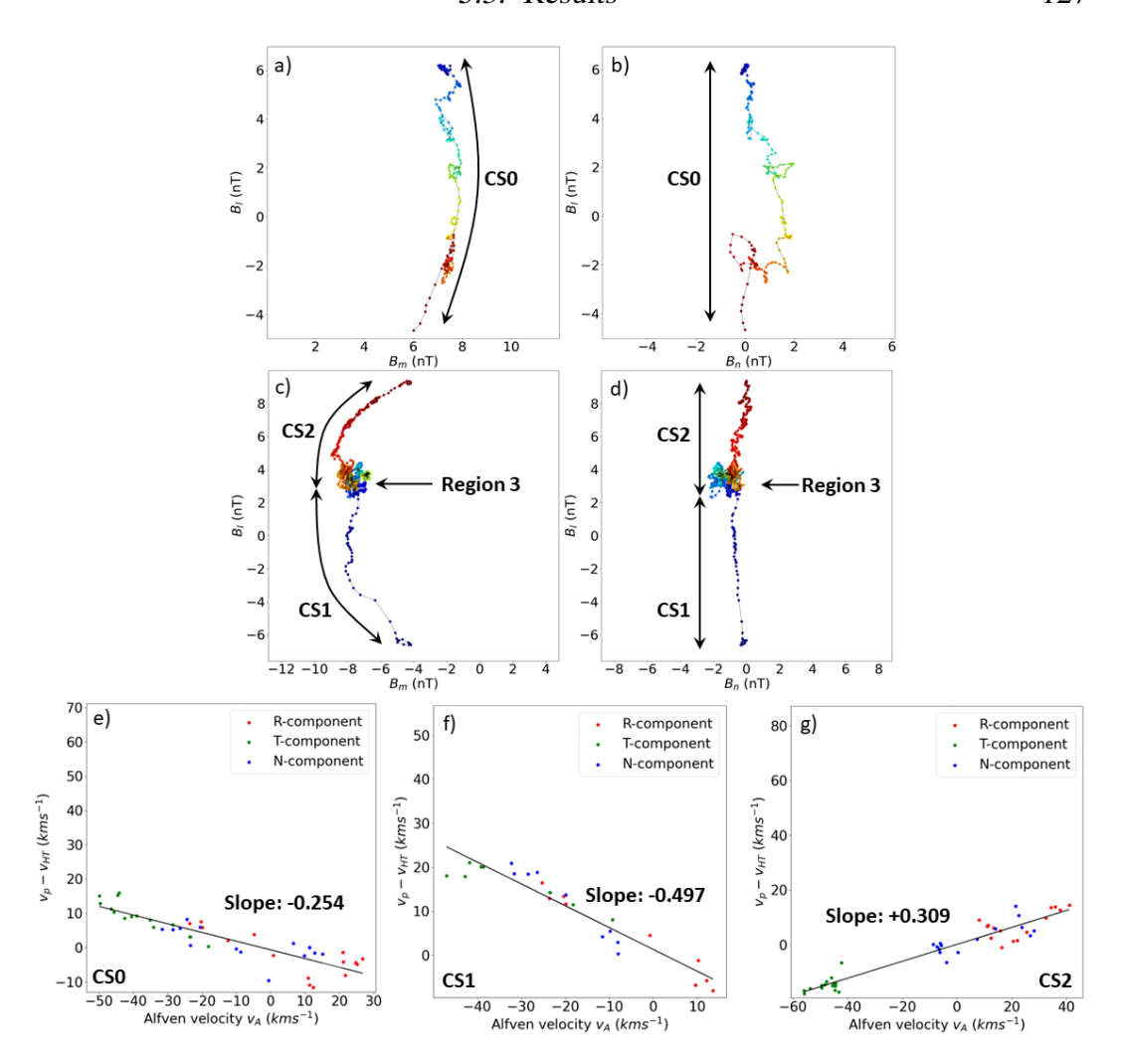


Figure 5.2: Magnetic hodographs and Walén plots for CS0 (07:45:50 − 07:46:20 UT), CS1 (07:46:35 − 07:46:43 UT), and CS2 (07:48:15 − 07:48:45 UT) in Event 1. Time progression in the hodographs is represented by the colour of the dots, with earlier times in blue and later times in red. The red, green, and blue dots in the Walén plots represent the *R*, *T*, and *N*-components of the Alfvén velocity **v**_A and the HT frame bulk plasma velocity **v**_P − **v**_{HT}. a) *lm*-plane hodograph for CS0. b) *ln*-plane hodograph for CS0. c) *lm*-plane hodograph for CS1 and CS2. d) *ln*-plane hodograph for CS1 and CS2. e) Walén plot for CS0. f) Walén plot for CS1. g) Walén plot for CS2.

of this event. Here, B_l decreases to -6 nT, v_l increases further to +24 km s⁻¹ and $|\mathbf{v_p'}|$ increases to +27 km s⁻¹. This is roughly 68% of the local v_A of 40 km s⁻¹. There is minimal change seen in $|\mathbf{B}|$, T_p , and n_p in this region compared to CS0. The electron strahl PAD peaks in the field-aligned direction (0°) both in the background HMF and in the regions containing polarity-reversed magnetic flux (CS0 and Region 2).

Across CS1 (07:46:35 – 07:46:43 UT) and CS2 (07:48:15 – 07:48:45 UT), the HMF polarity reverts back towards the anti-sunward direction observed in Region 1. B_l increases from -6 nT to +3 nT across CS1 and then increases again from

+3 nT to +9 nT across CS2. In Region 3 (07:46:43 – 07:48:15 UT), B_l remains roughly constant at +4 nT; this is intermediate between its value in Region 2 and the background HMF in Regions 1 and 4. The total magnetic shear angle across CS1, CS2, and Region 3 is 117°. There is a slight decrease in $|\mathbf{v}_p'|$ from 25 km s⁻¹ to an average of 15 km s⁻¹. v_l sharply decreases across CS1 and is negative in Region 3, with an average value of -10km s⁻¹. There are also gradual decreases in T_p from 12.5 eV to 9 eV, and in n_p from 14 cm⁻³ to 12 cm⁻³. Moreover, a brief strahl dropout across CS1 and the latter part of Region 2 is observed, accompanied by a sustained broadening of the strahl PAD in CS1 and Region 3. As both features are also present in the raw electron counts data, they are unlikely to be aliasing effects caused by the rapid rotation of the magnetic field.

Using the methods described in Section 5.2.2, Figure 5.2 shows the magnetic hodographs and Walén plots for CS0, CS1, and CS2. Panels a) and b) show the hodographs for CS0 in its associated lmn-frame, panels c) and d) show the hodographs for CS1 and CS2 combined in their associated lmn-frame, and panels e) – g) show the Walén plots for CS0, CS1, and CS2. For the Walén plots, **B** is re-sampled onto $\mathbf{v_p}$ as MAG has higher time resolution than PAS. I also include all data points 15 seconds before and after the current sheet crossing in the analysis. This ensures that a representative number of data points are included in the Walén plots, even for short-duration current sheets containing only a single proton measurement inside the current sheet. The choice of 15 seconds is deliberate, to prevent data points from CS1 contaminating the analysis for CS0 and vice-versa. For consistency, I apply the same method and the same timeframe of 15 seconds to all three events.

In the lm-plane hodographs (Figures 5.2a, 5.2c), **B** across all three current sheets traces an arc consistent with the measured magnetic shear angle. In the ln-plane hodograph for CS0 (Figure 5.2b), $B_n \simeq 0$ nT at the start and end of the interval, but deflects out to $B_n \simeq +2$ nT in the middle. For CS1 and CS2 (Figure 5.2d), **B** has a small B_n component of -1.0 nT and traces a quasi-vertical line in the ln-plane. In Figures 5.2c and 5.2d, the rotation of **B** is split into two arcs that individually correspond to CS1 and CS2. They are separated by an interval where the orientation of **B** does not change significantly, corresponding to Region 3. The magnitudes of the gradient of the line of best fit of the Walén plots for CS0 (-0.254), CS1 (-0.497), and CS2 (+0.309) fall below the range 0.5 – 1 expected for an Alfvénic structure.

5.3.2 Event 2 - 30 August 2021 10:19:05 - 10:21:28 UT

Figure 5.3 shows Event 2 observed between 10:15:00 and 10:25:00 UT on 30 August 2021 at a heliocentric distance of 0.61 au. The figure layout is the same as in Figure 5.1, except for the absence of electron strahl PAD data. In lieu of the strahl PAD, panel f) instead shows the signed magnitude of the alpha-proton velocity difference vector $v_{\alpha p} = |\mathbf{v}_{\alpha} - \mathbf{v}_{\mathbf{p}}| \cdot \mathrm{sgn}(v_{\alpha,R} - v_{p,R})$, which I use as an alternative method of checking for folded field configurations (see Section 1.4.1, Fedorov et al.

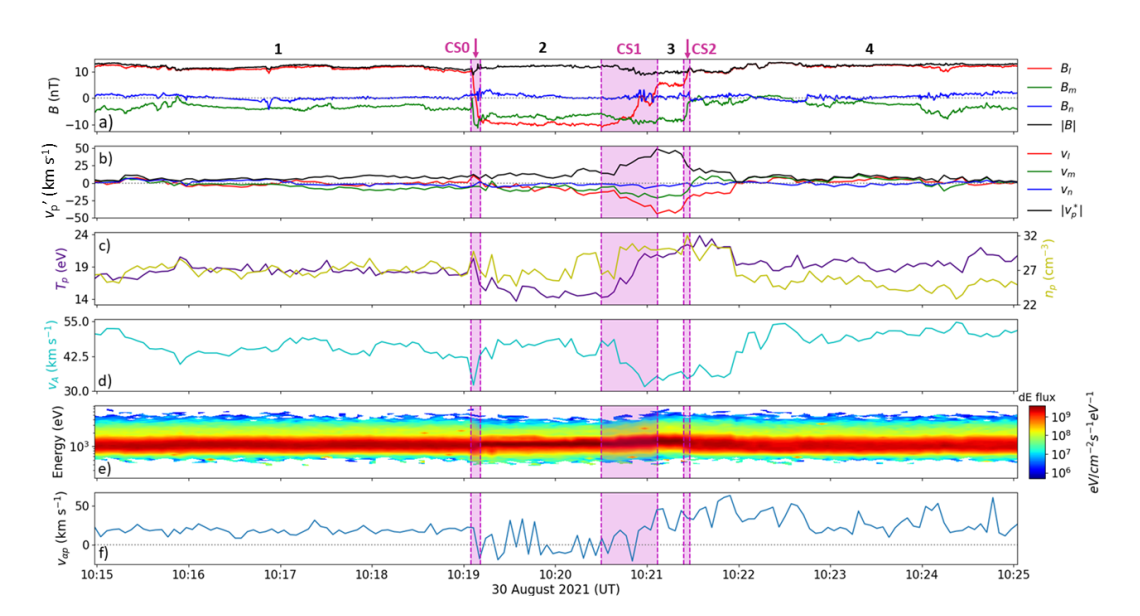


Figure 5.3: Combined magnetic field and proton time series data for Event 2 in the hybrid MVAB *lmn*-frame. The figure layout is the same as in Figure 5.1 except for the absence of electron strahl PAD data, which are unavailable for this interval. Panel f) instead shows the signed magnitude of the alpha-proton velocity difference vector, $v_{\alpha p}$.

Table 5.2: Event 2 *lmn*-frame basis vectors for CS0 and CS1 + CS2 expressed in RTN coordinates.

Current sheet	<i>lmn</i> -frame basis vectors (R, T, N)
CS0	$ \mathbf{\hat{l}} = (0.971, -0.220, -0.093) \mathbf{\hat{m}} = (-0.185, -0.939, 0.287) \mathbf{\hat{n}} = (-0.151, -0.261, -0.953) $
CS1 + CS2	$ \mathbf{\hat{l}} = (-0.835, 0.550, -0.020) \mathbf{\hat{m}} = (-0.452, -0.665, 0.594) \mathbf{\hat{n}} = (0.313, 0.505, 0.804) $

2021). This data is obtained using the techniques described in De Marco et al. (2023). For this interval, $\langle \mathbf{v_p} \rangle = (438.8, -14.6, -2.3)_{RTN} \, \mathrm{km \, s^{-1}}$ and the predominant HMF polarity before (Region 1, 10:15:00 – 10:19:05 UT) and after (Region 4, 10:21:28 – 10:25:00 UT) this event is in the sunward direction. I again identify three regions of strong magnetic gradients and label them CS0, CS1, and CS2. Table 5.2 shows the *lmn*-frame basis vectors for these current sheets. The angular differences between the basis vectors of the *lmn*-frames for CS0 and CS1 + CS2 are 21.6° for $\hat{\mathbf{l}}$, 28.4° for $\hat{\mathbf{m}}$, and 18.9° for $\hat{\mathbf{n}}$.

 B_R flips from its sunward orientation in Region 1 to an anti-sunward orientation in Region 2 (10:19:11 – 10:20:30 UT) across CS0 (10:19:05 – 10:19:11 UT). In the *lmn*-frame, this is visible as a reversal in B_l from +10 nT to -9 nT; the maximum

magnetic shear angle across this current sheet is 113° . There are no major changes in $|\mathbf{B}|$, v_l , $|\mathbf{v'_p}|$, and n_p in this region from their values in the background HMF in Region 1, although T_p decreases from 19 eV to 14 eV.

Region 2 corresponds to the polarity-reversed section of this event. Both B_l and $|\mathbf{B}|$ remain approximately constant at -10 nT and 12 nT, respectively. Here, v_l decreases gradually over Region 2 from $0\,\mathrm{km\,s^{-1}}$ to $-14\,\mathrm{km\,s^{-1}}$, while there is a very slight increase in $|\mathbf{v_p'}|$ from $7\,\mathrm{km\,s^{-1}}$ to $14\,\mathrm{km\,s^{-1}}$. This is around 30% of the average local $v_A \sim 45\,\mathrm{km\,s^{-1}}$. T_p remains roughly constant at an average of $14\,\mathrm{eV}$, while n_p fluctuates about an average value of $25\,\mathrm{cm^{-3}}$.

Across CS1 (10:20:30 – 10:21:07 UT) and CS2 (10:21:24 – 10:21:28 UT), B_l reverses from -10 nT to +10 nT in two steps, dwelling at +5 nT in Region 3 (10:21:07 – 10:21:24 UT). The total magnetic shear across CS1 and CS2 is 134° and $|\mathbf{B}|$ decreases from 12.5 nT to 10 nT. Across CS1, v_l continues decreasing at a faster rate than in Region 2, reaching a minimum value of -45 km s⁻¹ in Region 3. $|\mathbf{v}_p'|$ peaks at 50 km s⁻¹, a value ~ 43% greater than the local $v_A \sim 35$ km s⁻¹. T_p increases from 14 eV to 25 eV, while n_p also increases from 25 cm⁻³ to 30 cm⁻³.

Table 5.3: Event 3 *lmn*-frame basis vectors for CS0 and CS1 + CS2 expressed in RTN coordinates.

Current sheet	<i>lmn</i> -frame basis vectors (R, T, N)
CS0	$ \mathbf{\hat{l}} = (-0.970, -0.240, 0.037) \mathbf{\hat{m}} = (-0.235, 0.889, -0.394) \mathbf{\hat{n}} = (0.061, -0.391, -0.918) $
CS1 + CS2	$ \hat{\mathbf{l}} = (-0.977, 0.177, 0.120) \hat{\mathbf{m}} = (-0.115, -0.908, 0.403) \hat{\mathbf{n}} = (0.180, 0.308, 0.907) $

Figure 5.4 shows the hodographs and Walén plots for Event 2, the format of this figure is the same as in Fig. 5.2. The arc traced by **B** in the *lmn*-frame for CS0, CS1, and CS2 is consistent with the measured magnetic shear. Across the trailing edge current sheets, the largest rotation in **B** occurs over CS1. In the *ln*-plane, **B** traces an approximately vertical line and has a B_n component of +0.5 nT. Around 10:21:00, there are fluctuations in B_n of ± 2.5 nT inside CS1. The Walén plot gradients of +0.077 for CS0 and -0.437 for CS1 are below the range expected for an Alfvénic RD. Conversely, the Walén plot gradient of +0.973 for CS2 indicates that the discontinuity in **B** across this structure is Alfvénic.

5.3.3 Event 3 - 30 August 2021 10:03:46 - 10:12:15 UT

Event 3 (see Figure 5.5) is observed between 10:00:00 UT to 10:15:00 UT on 30 August when *Solar Orbiter* was at a heliocentric distance of 0.61 au. This event has a duration of around eight minutes, four times greater than that of Events 1

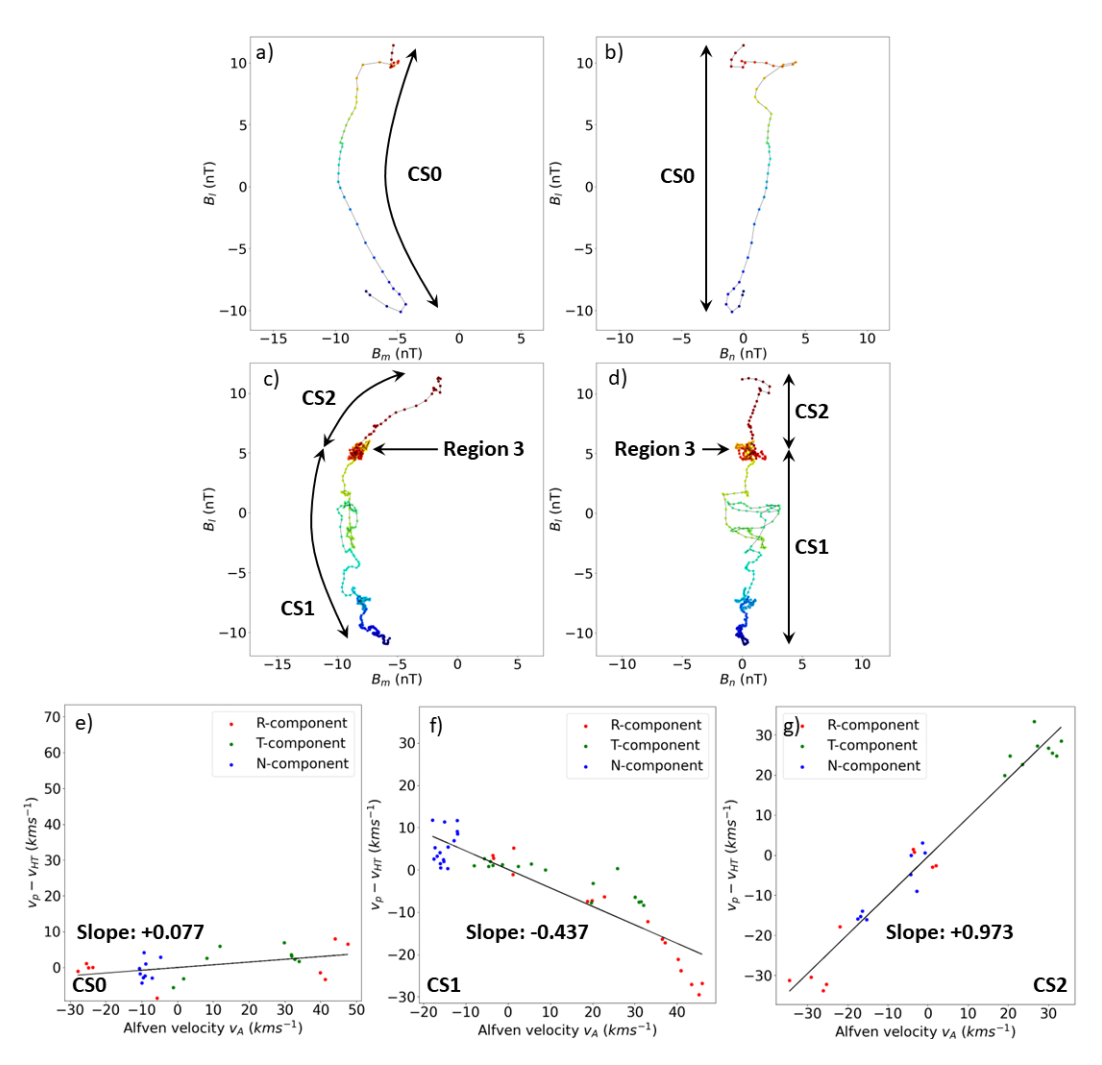


Figure 5.4: Magnetic hodographs and Walén plots for CS0 (10:19:05 – 10:19:11 UT), CS1 (10:20:50 – 10:21:07 UT), and CS2 (10:21:24 – 10:21:28 UT) in Event 2. The figure layout is the same as in Figure 5.2.

and 2. Event 3 occurs in close temporal proximity to Event 2, thus $\langle \mathbf{v_p} \rangle$ and the background HMF polarity for both events are similar. Table 5.3 shows the *lmn*-frame basis vectors for CS0 and CS1 + CS2. The angular differences between the basis vectors of these *lmn*-frames are 24.6° for $\hat{\mathbf{l}}$, 20.2° for $\hat{\mathbf{m}}$, and 13.9° for $\hat{\mathbf{n}}$.

In Region 2, B_R (10:03:46 – 10:11:05 UT) is in the anti-sunward direction, opposite to the polarity of the background HMF in Regions 1 (10:00:00 – 10:03:35 UT) and 4 (10:12:15 – 10:15:00 UT). This polarity reversal occurs across CS0 (10:03:35 – 10:03:46 UT), where B_l reverses from +8 nT to -4 nT with a magnetic shear angle of 61°. Here, $|\mathbf{B}|$, v_l , and $|\mathbf{v}'_{\mathbf{p}}|$ do not deviate noticeably from their values in Region 1. T_p decreases from 17 eV to 14 eV, while there is a slight increase in n_p from 23.5 cm⁻³ to 25.5 cm⁻³.

From 10:03:46 - 10:05:20, B_l remains roughly constant at -5 nT and decreases further to -10 nT from 10:05:55 UT onwards. $|\mathbf{B}|$ is roughly constant at 12 nT

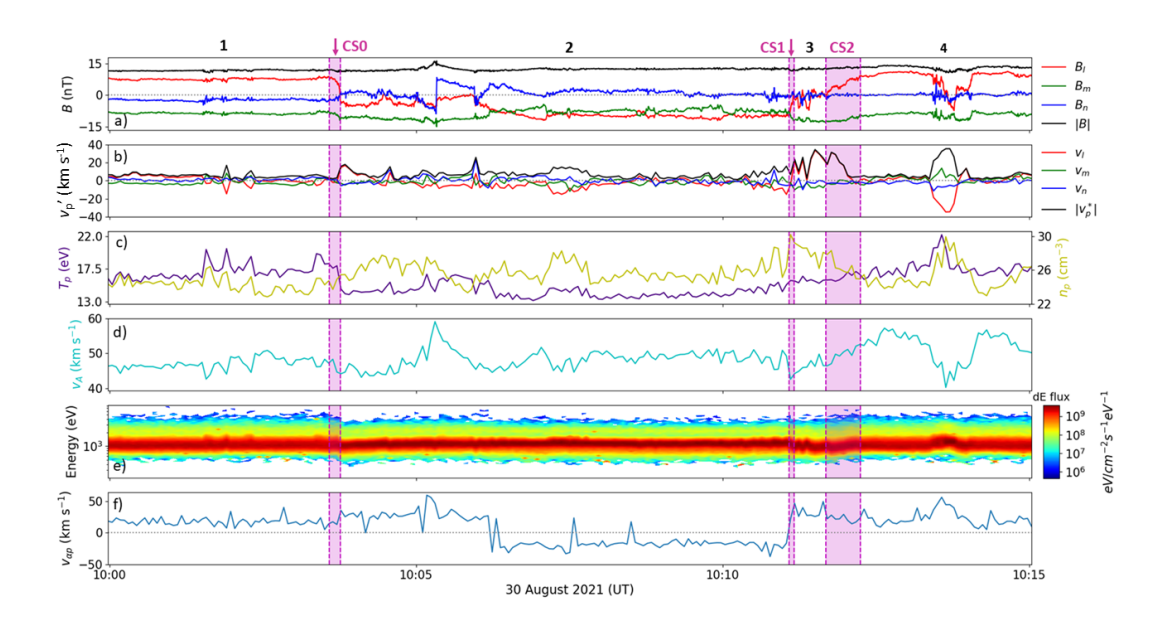


Figure 5.5: Combined magnetic field and proton time series data for Event 3 in the hybrid MVAB *lmn*-frame. The figure layout is the same as Figure 5.3.

throughout most of Region 2 and is similar in magnitude to $|\mathbf{B}|$ in the background HMF. There is an increase in $|\mathbf{B}|$ between 10:05:20 and 10:05:55 UT that coincides with near-zero B_l and a large deflection in B_n , suggesting that this event contains some internal substructure that is not evident in the other two events. There is no significant change in v_l or $|\mathbf{v}'_{\mathbf{p}}|$ in Region 2. The value of T_p for the full duration of Region 2 is roughly constant at 13 eV, while n_p increases gradually from 25.5 cm⁻³ to 30 cm⁻³.

Across CS1 (10:11:05 – 10:11:10 UT), B_l increases from -10 nT to -2 nT and then reverses from -1 nT to +9 nT across CS2 (10:11:41 – 10:12:15 UT). In contrast to Events 1 and 2, the magnetic field does not linger at a constant orientation in Region 3 (10:11:10 – 10:11:41 UT), but instead, it shows large fluctuations. The total magnetic shear across these two current sheets is 95°. v_l increases from -15 km s⁻¹ to +20 km s⁻¹, accompanied by a smaller increase in $|\mathbf{v'_p}|$ from 10 km s⁻¹ to 24 km s⁻¹. The peak $|\mathbf{v'_p}|$ of 35 km s⁻¹ is observed in Region 3 and is roughly 75% of the average local $v_A \sim 46$ km s⁻¹ in this region. There is a small increase in T_p from 14 eV to 17 eV, whereas n_p decreases from a maximum of 30 cm⁻³ to 24 cm⁻³.

Figure 5.6 shows the hodographs and Walén plots for Event 3. Although it is not as distinct as Event 1, there is still an arc in the lm-plane hodographs and a quasi-vertical line in the ln-plane hodographs for all three current sheets. Across CS1 and CS2, the rotation in $\bf B$ is no longer clearly separated by a period during which the field orientation remains roughly constant. This is caused by the magnetic field fluctuations in Region 3 causing $\bf B$ to 'double back' on itself in both hodographs.

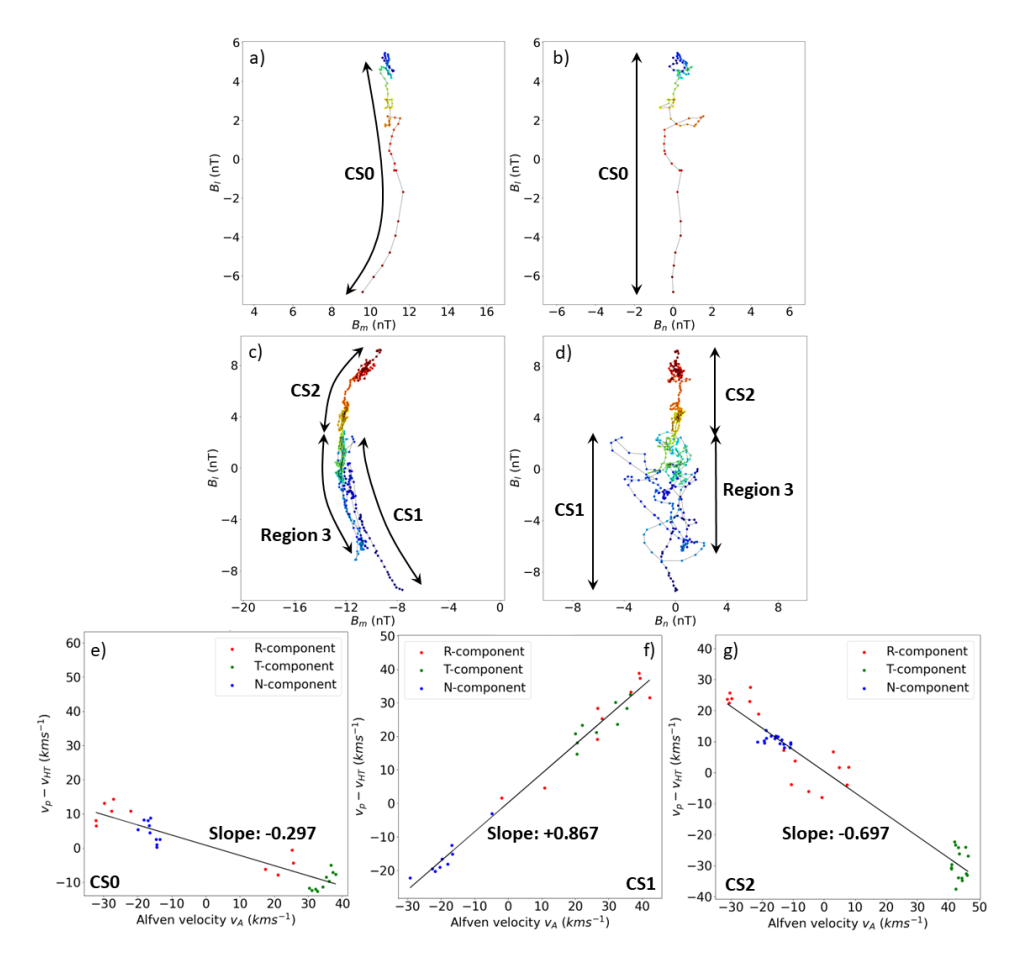


Figure 5.6: Magnetic hodographs and Walén plots for CS0 (10:03:35 – 10:03:46 UT), CS1 (10:11:05 – 10:11:10 UT), and CS2 (10:11:41 – 10:12:15 UT) in Event 3. The figure layout is the same as in Figure 5.2.

According to the ln-plane hodograph, **B** has a smaller B_n -component of -0.1 nT than Events 1 and 2. The Walén plot gradient of -0.297 for CS0 is below the range expected for an Alfvénic RD, whereas the gradients of +0.867 for CS1 and -0.697 for CS2 indicates that Alfvénic RDs are present across these two current sheets.

5.4 Discussion

5.4.1 Evidence for reconnection at switchback boundaries

My overall findings suggest that the three observed events are magnetic switchbacks undergoing magnetic reconnection at their trailing edge boundaries. Based on the magnetic field observed in all three events, there is a polarity reversal in B_R , first at CS0 in each case and returning across CS1 and CS2 combined, consistent with magnetic switchbacks. For Event 1, the electron strahl PAD data supports this interpretation. As expected, the strahl pitch angle remains constant at 0° both in the background HMF and in Region 2, the polarity-reversed section of the switchback. For Events 2 and 3, I used $v_{\alpha p}$ to confirm if these events are magnetic switchbacks

(Fedorov et al., 2021) as the electron strahl PAD data are unavailable. $v_{\alpha p}$ is positive in Regions 1, 3, and 4, where there are no polarity reversals in B_R . Conversely, $v_{\alpha p}$ is negative in Region 2 for both events; $v_{\alpha p} \sim -10\,\mathrm{km\,s^{-1}}$ for Event 2 and $v_{\alpha p} \sim -20\,\mathrm{km\,s^{-1}}$ for Event 3. This is in line with the expectation that $v_{\alpha p} > 0$ in the background solar wind and $v_{\alpha p} < 0$ inside the reversed section of a folded field configuration (Marsch et al. 1982a; Reisenfeld et al. 2001, see Section 1.4.1).

An anti-correlation between the fluctuations in **B** and $\mathbf{v'_p}$ in CS0 and Region 2 of Event 1 is consistent with an Alfvénic structure. However, the $|\mathbf{v'_p}|$ enhancement of $27 \,\mathrm{km \, s^{-1}}$ inside Region 2 is 68% of the local Alfvén speed of $40 \,\mathrm{km \, s^{-1}}$. This is less than the enhancements observed at switchbacks in the near-Sun solar wind, which are often roughly equivalent to the Alfvén speed (Horbury et al., 2018; Kasper et al., 2019; Horbury et al., 2020b). Combined with the decrease in $|\mathbf{B}|$, accompanying increase in n_p , and the Walén plot for CS0 (Figure 5.2e), these properties suggest that this event also has a non-Alfvénic component (Kasper et al., 2019; Krasnoselskikh et al., 2020). Conversely, neither Event 2 nor Event 3 show similar correlations or any obvious change in $\mathbf{v'_p}$. These velocity enhancements (if they do indeed exist) are considerably less than the local Alfvén speed. This property is also noted in reference to previously observed examples of reconnecting switchbacks (Froment et al., 2021).

The trailing edge boundary of all three switchbacks exhibit large increases in $|\mathbf{v}_p'|$. The regions of accelerated flow at the trailing edge of the switchbacks are bound by a pair of current sheets CS1 and CS2 in each case, across which the fluctuations in \mathbf{B} and \mathbf{v}_p' are anti-correlated on one side and correlated on the other. This bifurcation of the RCS at the trailing edge of the switchbacks and the presence of an accelerated outflow jet are consistent with the Gosling reconnection model (Gosling et al., 2005a). By contrast, the leading edge boundary of all three switchbacks show no signatures of current sheet bifurcation and, instead, they are comprised of a single current sheet CS0. Furthermore, with the exception of Event 1, no accelerated flows are observed across CS0 for the three events. This suggests that in each case, reconnection occurs only at the trailing edge boundary of the switchbacks, while the leading edge boundary of the switchback is non-reconnecting.

In the case of Event 1 (Figure 5.1), the \mathbf{v}_p' enhancement in the polarity-reversed section of the switchback (Region 2) is oriented in the $+\hat{\mathbf{l}}$ direction, whereas the \mathbf{v}_p' enhancement in the trailing edge boundary reconnection outflow region (Region 3) is oriented in the $-\hat{\mathbf{l}}$ direction, suggesting that these two features are distinct from each other. The cause of the strahl dropout and broadening of the strahl PAD across CS1 is unknown but is not an instrumental effect, as a drop in the raw electron counts was also clearly detected by SWA-EAS at this time.

The hodographs show that five out of the six RCS have clear signatures associated with RDs, but the magnitudes of the line of best fit gradients for half of the Walén plots fall below the 0.5–1 range that is typically expected for an Alfvénic

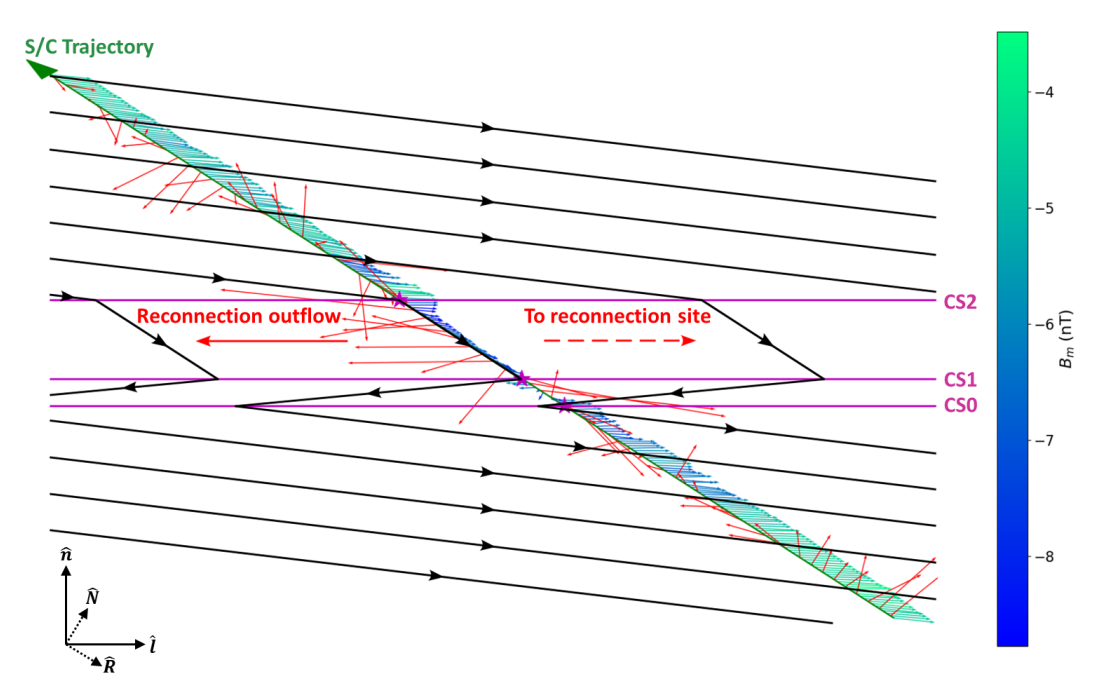


Figure 5.7: Feather plot of the **B** (blue/light green) and $\mathbf{v'_p}$ vectors measured in Event 1 in the ln-plane with the spacecraft trajectory marked by the dark green arrow. The B_m component of **B** is represented by the colour bar on the right. Overlaid on top is a possible interpretation of the magnetic field configuration of the switchback, shown here by the black arrows. The purple lines mark the assumed configuration of the current sheets CS0, CS1, and CS2. The purple stars show the locations where *Solar Orbiter* crosses the current sheets.

structure. This suggests that the reconnection outflow is sub-Alfvénic – a result that is not uncommon for reconnection in astrophysical plasmas (Haggerty et al., 2018). Any modification of the Walén relation (Equation 5.1) by factoring in a pressure anisotropy term (Paschmann & Sonnerup, 2008) makes no appreciable difference to the results of this analysis. Other reconnection models (Petschek, 1964) and observational studies (He et al., 2018; Phan et al., 2020) suggest that the reconnection outflow region boundaries can be composed of a combination of Alfvénic RDs and slow mode shocks. Shocks are not accounted for in the Walén relation and may reduce the outflow velocity to sub-Alfvénic speeds (Teh et al., 2009; Feng et al., 2017). These may reduce the observed $\mathbf{v'_p}$ to 34–64% of the predicted v_A (Phan et al., 2013, 2020), which is more consistent with the Walén plots. However, a detailed analysis of different reconnection models lies beyond the scope of this work.

5.4.2 Switchback and reconnection geometry

Figure 5.7 shows a feather plot of the magnetic field and proton velocity measurements recorded during Event 1. The measured **B** is shown by the blue-and-light green arrows and the measured $\mathbf{v'_p}$ is shown by the solid red arrows. The colours of the **B** arrows represent the strength of the B_m component of the magnetic field. I overlay a possible and consistent interpretation of the magnetic field configura-

tion of the switchback on top, shown by the solid black arrows. As measurements are limited to those along the trajectory of *Solar Orbiter* through this structure, the configuration shown here is one of many possible configurations that are considered to be consistent with the observations. On large scales, the switchback is assumed to be rigidly frozen into the bulk solar wind flow as it is convected across the spacecraft with a constant velocity of $\langle \mathbf{v_p} \rangle = (322.2, -5.6, -5.6)_{RTN} \, \mathrm{km \, s^{-1}}$. Under this assumption, I map the measurement time stamps, t, to spatial coordinates $\mathbf{r} = -(t - t_0) \langle \mathbf{v_p} \rangle$, where t_0 is an arbitrary reference time, defined here at 07:40:00 UT.

The dark green arrow represents the trajectory of *Solar Orbiter* through Event 1, from the bottom right to the top left of the figure. The locations where *Solar Orbiter* crosses CS0, CS1, and CS2 are marked with purple stars. In this assumed configuration, the spacecraft starts in the region of quiet anti-sunward (+R) HMF immediately preceding the switchback. As the spacecraft crosses the leading edge boundary of the switchback (CS0), the polarity of the HMF reverses towards a sunward orientation and $|\mathbf{B}|$ decreases relative to the ambient HMF. As for $\mathbf{v_p'}$, its value gradually increases and is directed in the $+\hat{\mathbf{l}}$ direction.

The trailing edge boundary of the switchback, formed by the current sheets CS1 and CS2, together form a Gosling-type bifurcated RCS (Gosling et al., 2005a) that bounds the reconnection outflow region. In order for the reconnection geometry to be consistent with the observed outflow, the RCS must extend back along the solid purple lines towards a reconnection site located off-page, in the $+\hat{\mathbf{l}}$ direction of the spacecraft trajectory. Inside the outflow region, \mathbf{B} is roughly parallel with the spacecraft trajectory. Unlike at the leading edge of the switchback, $\mathbf{v}_{\mathbf{p}}'$ is directed in the -l direction in this region. After crossing CS2, Solar Orbiter exits the switchback and re-enters the surrounding solar wind, where conditions are similar to those observed immediately before the switchback encounter.

In the proposed scenario, magnetic reconnection occurs between oppositely directed field lines at the trailing edge boundary of the switchback. Within the overall geometry of the switchback, this topology may produce a magnetic flux rope on one side of the reconnection site and newly reconnected open field lines on the other, as illustrated in Figure 5.8. This scenario has many similarities to that proposed by Fedorov et al. (2021) to explain the formation of magnetic flux ropes at switchback-like structures observed near 1 AU.

Flux rope crossings present distinct signatures in time series measurements of the magnetic field vector and strahl PAD. Upon entry into the flux rope, the magnitude of the component of the magnetic field aligned with its central axis, and hence the total magnetic field strength, increases relative to the background solar wind. This enhancement is greatest near the centre of the flux rope. Additionally, one or both components of the magnetic field perpendicular to the flux rope axis may exhibit smooth, bipolar variation with a sign change (Eastwood et al., 2021;

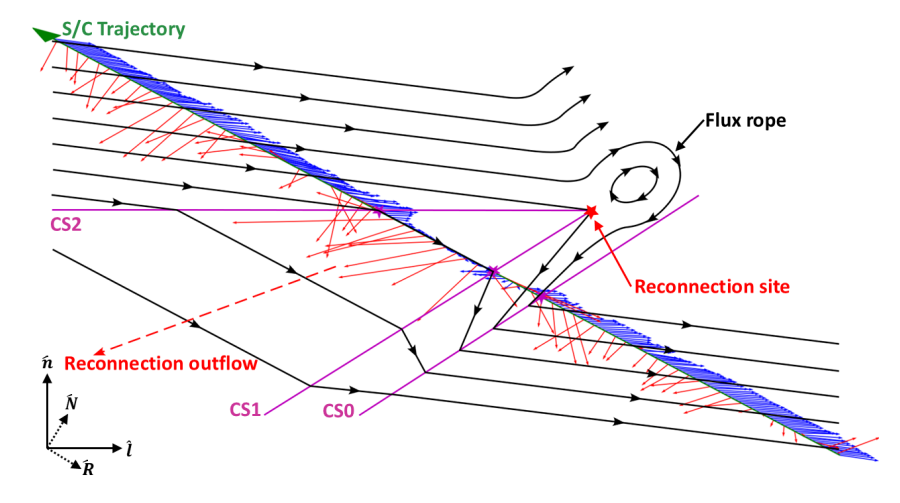


Figure 5.8: Diagram showing possible mechanism by which switchback boundary reconnection can generate a flux rope embedded within a switchback. For visualisation purposes, the figure is not to scale and has been compressed along the **Î**-axis to show the switchback structure on both sides of the reconnection site. Arrow colours are defined as in Figure 5.7.

Choi et al., 2025). In flux ropes formed by switchback boundary reconnection, a transition from a uni-directional to bi-directional strahl may also be observed, indicating a closed magnetic field topology (Fedorov et al., 2021).

However, no signatures associated with flux rope crossings are observed in any of the three events presented here. For Event 1, the strahl PAD in the outflow region is uni-directional and parallel to the magnetic field, suggesting that *Solar Orbiter* sampled magnetic flux associated with the open, newly reconnected field lines rather than a flux rope. These field lines are highly kinked and magnetic tension causes them to recoil away from the reconnection site and straighten out, unwinding the switchback in the process. In general, observation of a flux rope is contingent on the spacecraft trajectory passing through the correct region of the switchback, which likely does not occur in these cases. By contrast, Fedorov et al. (2021) report a fortuitous encounter in which *Solar Orbiter* passed through both sides of a switchback reconnection site, allowing observations of both a flux rope and reconnection outflow.

5.4.3 Estimating the timescales for switchback erosion

I estimate the remaining lifetime, τ , of the three switchbacks discussed in this paper as they are being eroded by magnetic reconnection, assuming reconnection is the sole erosion mechanism and proceeds uniformly at the observed rate. This parameter depends on the magnetic flux ϕ_{SB} remaining in the polarity-reversed portion of the switchback, which is yet to be reconnected, as well as the total rate of magnetic flux transport, $2\dot{\phi}_{in}$, into the reconnection site from both sides of the reconnection region. As illustrated in Figure 5.7, the proposed switchback geometry suggests that direct measurements of the magnetic field and plasma in the outflow region are only

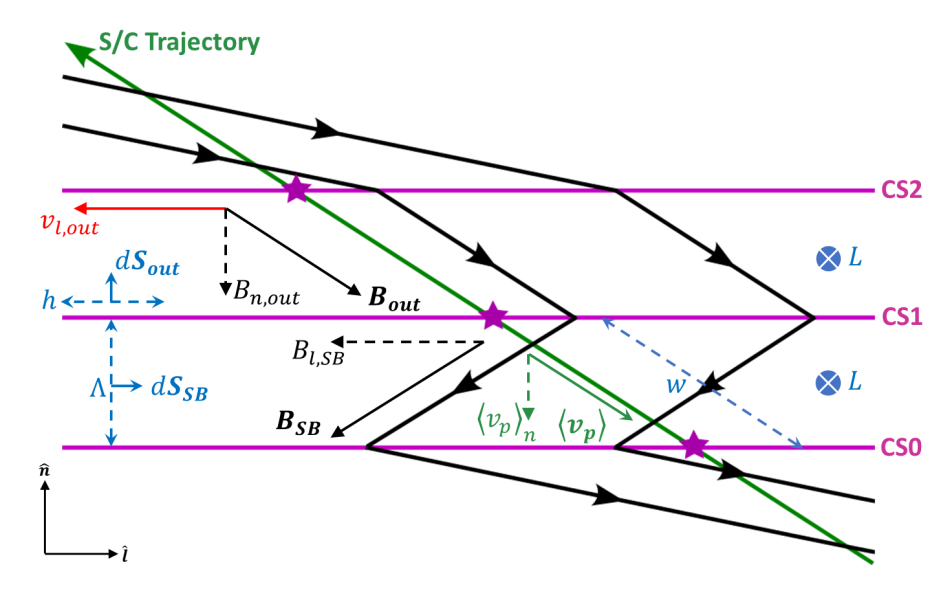


Figure 5.9: Simplified diagram of the switchback and reconnection geometry in Event 1, with quantities relevant to the calculation of τ .

available on one side of the reconnection site. These measurements allow the rate of magnetic flux transport, $\dot{\phi}_{out}$, to be quantified on that side. Under the conservation of magnetic flux, $2\dot{\phi}_{in} = 2\dot{\phi}_{out}$, this leads to:

$$\tau = \frac{\phi_{SB}}{\dot{\phi}_{in}} = \frac{\phi_{SB}}{\dot{\phi}_{out}}.\tag{5.2}$$

Figure 5.9 shows a simplified diagram of the assumed switchback and reconnection geometry depicted in Figure 5.7. I first consider the amount of magnetic flux ϕ_{out} transported by the reconnection outflow $\mathbf{v_{out}}$ in time dt. The general expression for magnetic flux through a surface composed of infinitesimal surface elements $d\mathbf{S}$ is given by $\phi = \int \mathbf{B} \cdot \mathbf{dS}$. In this 2D configuration, a surface element $d\mathbf{S_{out}} = hL\hat{\mathbf{n}}$ is defined, where $h = v_{l,out}dt$ is the distance the reconnected field lines are convected by the outflow in time t, and L is the out-of-plane extent of the switchback. Hence,

$$\phi_{out} = \int \mathbf{B_{out}} \cdot \mathbf{dS_{out}} \approx B_{n,out} v_{l,out} L dt, \qquad (5.3)$$

where $B_{n,out}$ is the average B_n -component of the magnetic field in the outflow region. This is equivalent to

$$\dot{\phi}_{out} \approx B_{n,out} v_{l,out} L.$$
 (5.4)

The distance w travelled by *Solar Orbiter* in the polarity-reversed section of the switchback (Region 2) is trajectory-dependent and hence, is an unreliable measure for the switchback width. I instead use $\Lambda = \langle \mathbf{v_p} \rangle_n dt_{SB}$, the perpendicular distance between CS0 and CS1, to estimate the width of the polarity-reversed section of

the switchback. Here, dt_{SB} is the crossing duration of Region 2. Applying similar reasoning to the derivation of ϕ_{out} above, ϕ_{SB} is given by:

$$\phi_{SB} = \int \mathbf{B_{SB}} \cdot \mathbf{dS_{SB}} \approx B_{l,SB} \Lambda L. \tag{5.5}$$

Here, the surface element $d\mathbf{S_{SB}} = \Lambda L\hat{\mathbf{l}}$ is oriented along the *l*-direction, as $B_{l,SB}$ is the component of $\mathbf{B_{SB}}$ that reconnects. Finally, I substitute Eqs. 5.4 and 5.5 into Eq. 5.2 to obtain the time remaining until complete erosion of the switchback:

$$\tau = \frac{B_{l,SB}\Lambda}{B_{n,out}\nu_{l,out}}.$$
(5.6)

Additionally, I estimate the remaining convection distance D until the complete erosion of the switchback as $D \simeq |\langle \mathbf{v_p} \rangle| \tau$.

Table 5.4 shows the estimated τ and D for the three events discussed in this paper. From Eq. 5.6, the value of τ depends linearly on switchback width Λ , which determines the amount of magnetic flux remaining in the polarity-reversed section of the switchback; it is also inversely proportional to $v_{l,out}$, which indicates the rate at which reconnected flux is transported away from the reconnection site. Since Event 1 has the smallest width of $\Lambda = 3570 \,\mathrm{km}$ and the largest absolute $B_{n,out}$ of 1.0 nT, it has the shortest τ of 40 minutes despite having the slowest absolute $v_{l,out}$ of 7.2 km s⁻¹. Given the small Λ and short τ compared to the other two events, this suggests that Event 1 may be a switchback that has almost been completely eroded by reconnection. Conversely, Event 3 is the widest with $\Lambda = 31700 \, \mathrm{km}$ and the smallest $B_{n,out}$ of 0.1 nT, a factor of ten smaller than $B_{n,out}$ for Event 1. As a result, it has the longest $\tau = 2005$ minutes out of the three events. Event 2 is roughly three times wider than Event 1 with $\Lambda = 10100 \,\mathrm{km}$ and has $B_{l,SB} = 9.7 \,\mathrm{nT}$ twice as large as Event 1, but has the greatest $v_{l,out} = 28.3 \,\mathrm{km}\,\mathrm{s}^{-1}$. Its $\tau = 126 \,\mathrm{minutes}$ is thrice as long as for Event 1. The range for D values travelled by these three switchbacks before they fully erode goes from 0.005 au (Event 1) to 0.4 au (Event 3).

5.4.4 Implications on switchback formation and evolution in the heliosphere

A key assumption made in the calculations for τ and D (detailed in Section 5.4.3) is that reconnection proceeds uniformly at the observed rate. Because no information is available about the time history of these switchbacks as they evolve from their place of origin to their place of detection, it is not known when or where the onset of reconnection occurs. Therefore, neither τ nor D should be taken as the actual time or distance between reconnection onset and complete erosion of the switchback.

However, τ and D are both small compared to the characteristic timescales and distances of the solar wind expansion, which suggests that reconnection is a fast and efficient mechanism through which switchbacks can be eroded. To high-

Table 5.4: Estimates for the remaining lifetime, τ , of the three switchbacks discussed in this paper, and the convection distance, D, travelled by the switchbacks before they fully erode away. Λ : switchback width, B_{SB} : magnetic field strength in the switchback, B_{out} : magnetic field strength in the outflow region, v_{out} : exhaust outflow bulk speed, $\langle v_{SW} \rangle$: average solar wind speed.

Event	A (km)	$B_{l,SB}$ (nT)	$B_{n,out}$ (nT)	Event Λ (km) $B_{l,SB}$ (nT) $B_{n,out}$ (nT) $\nu_{l,out}$ (km s ⁻¹) $ \langle \mathbf{v_p} \rangle $ (km s ⁻¹) τ (min) D (au)	$ \langle \mathbf{v_p} \rangle (\mathrm{km \ s^{-1}})$	τ (min)	D (au)
Event 1	3570	-4.8	-1.0	-7.2	322	40	0.005
Event 2	10100	7.6-	0.5	-28.3	439	126	0.02
Event 3	31700	-7.5	-0.1	15.4	443	2005	0.4

light this point, let us assume that the onset of reconnection occurs at heliocentric distances similar to PSP perihelion 1 (\sim 0.2 au), during which PSP made its observations of prominent switchbacks and switchback patches (Bale et al., 2019; Kasper et al., 2019; Horbury et al., 2020b). If the reconnection rate remains constant during transport in the solar wind, Λ for the observed switchbacks at these distances would be 0.1 – 0.5 solar radii. This is significantly larger than what was observed by PSP and has two possible implications.

The first is that the switchbacks are formed near the Sun and propagate stably into interplanetary space, before encountering conditions enabling the onset of reconnection and thus the rapid erosion of the switchback. This scenario would explain the rarity of observations of reconnection at switchback boundaries, as the observing spacecraft would need to serendipitously encounter the switchback at almost the same time as reconnection onset. It would also explain why fewer switchbacks are observed at 0.6-0.7 au by *Solar Orbiter* compared to PSP at heliocentric distances < 0.2 au. Furthermore, Tenerani et al. (2020) have demonstrated that large switchbacks formed in the corona can only survive out to ~ 0.2 au if the background solar wind conditions are sufficiently calm, before the parametric decay instability causes them to decay.

The second plausible explanation is that the switchbacks are formed in situ in the solar wind at a time much closer to the moment of their detection. This is supported by new results from Macneil et al. (2020) and Pecora et al. (2022) that suggest the occurrence rate of magnetic switchbacks increases with heliocentric distance. There is the possibility that two (or more) populations of switchbacks exist: those that form in the Sun's corona and those that form in the solar wind (Tenerani et al., 2021).

5.5 Conclusions

Using *Solar Orbiter* data from 10 August and 30 August 2021, I identified three magnetic switchbacks at heliocentric distances between 0.6 - 0.7 au. The trailing edge boundaries of all three events show signatures of jetting and current sheet bifurcation that are consistent with the Gosling reconnection model (Gosling et al., 2005a).

I propose a possible configuration of the switchback observed on 10 August and reconnection geometry based on measurements of the switchback. In this scenario, reconnection at the trailing edge boundary of the switchback results in the formation of a magnetic flux rope on one side of the reconnection site and kinked field lines on the other. Magnetic tension causes the reconnected field lines to recoil away from the reconnection site, resulting in the unwinding of the switchback. In this chapter, I only find cases in which magnetic reconnection occurs at the trailing edge boundary of switchbacks. However, in principle, this process may also occur at the leading edge boundary of switchbacks or at the leading and trailing edge

boundaries simultaneously. Although magnetic tension acts naturally to straighten field line kinks in non-reconnecting switchbacks as well, my observation-driven scenario suggests that reconnection can increase the rate at which these structures unwind.

My estimates of the remaining lifetime of the switchbacks suggest that they erode within a few minutes to a few hours after being observed by $Solar\ Orbiter$. During this time, the switchbacks are carried a further 0.005-0.4 au by the surrounding solar wind flow. If typical, these results could explain why switchbacks are rarely seen at 1 au and has implications on how these structures form and evolve in the heliosphere. The short τ and small D relative to the characteristic timescales and distances of the solar wind expansion show that reconnection is an efficient process for switchback erosion. This suggests that the onset of reconnection must occur during transport in the solar wind in these examples and supports theories of in-situ switchback formation in the solar wind.

There are some caveats to my results and interpretation. The use of single-spacecraft measurements limits knowledge of the magnetic field and solar wind conditions inside the switchback to what is observed along the spacecraft's trajectory. Furthermore, no information is available about the time history of the switchbacks. Consequently, it is not known when the onset of reconnection occurs at the switchback boundaries, nor whether this process creates a flux rope embedded within the switchback. Therefore, the interpretation presented here must be understood as one possible scenario that is considered in the context of the measured knowledge of the field and plasma geometry.

In order to further develop the ideas presented here, multi-spacecraft observations will be needed. Radial line-up opportunities between *Solar Orbiter* and other spacecraft such as PSP will allow us to track the temporal evolution of individual switchbacks with heliocentric distance and to identify the conditions required for reconnection to occur at their boundaries. Repeating my analysis on PSP events (Froment et al., 2021) and comparing the results with the ones discussed here would also be an interesting idea to explore in future studies.

My model predicts that reconnection will convert a portion of the switchback into a magnetic flux rope disconnected from the Sun. Such a structure will appear as a reversal in the HMF polarity but can be distinguished from a switchback in the strahl PAD data. Simultaneous multi-point measurements of the switchback, reconnection outflow region, and flux rope by constellation-type missions such as *Cluster* (Escoubet et al., 1997), *MMS* (Burch et al., 2016), and the upcoming *HelioSwarm* (Klein et al., 2019; Broeren et al., 2021; Matthaeus et al., 2022) will allow verification of the validity of the model. These types of measurements can also better constrain the 3D geometry of these structures and isolate spatial variations from temporal variations.

Chapter 6

Conclusions and future work

In this thesis, I use a combination of mathematical modelling methods and in-situ observations from the *Solar Orbiter* mission to study the properties of magnetic reconnection in the solar wind, focusing on three important aspects of reconnection. First, I examine the structure of reconnection outflows in the solar wind, placing particular emphasis on the bifurcated reconnection current sheet. Second, I analyse the proton populations observed in the reconnection outflow region and how it relates to the outflow region structure. Third, I investigate the role reconnection plays in the erosion of magnetic switchbacks, which are structures that are ubiquitous in the near-Sun solar wind.

In Chapter 3, I extend existing current sheet stress balance models describing reconnection in the Earth's magnetotail (Owen & Cowley, 1987a,b) to develop a novel mathematical framework to describe the structure of reconnection outflows in the solar wind. I show that unlike in the magnetotail, the forces due to magnetic and thermal pressure gradients contribute to the stress balance and must be accounted for in the analysis. I then set up a simple model of a 2-D, steady-state, symmetric reconnection outflow bound by a bifurcated RCS, with a pair of identical inflow proton beams incident upon it from opposite sides. As the two inflow beams pass through the bifurcated RCS into the outflow region, they form a pair of counterstreaming proton beams within the outflow region. This reconnection configuration is characteristic of those observed in the solar wind (Gosling et al., 2005a). Using the current sheet stress balance conditions, I derive a set of equations for various parameters describing this reconnection configuration, such as the opening angle of the outflow region, as well as the velocity, density, and temperature of the counterstreaming beam pair in the outflow region. After initialising the model with typical magnetic field and plasma conditions in the solar wind, I obtain values for the outflow region opening angle and bulk outflow speed that are consistent with observations of reconnection outflows in the solar wind (Enžl et al., 2014; Mistry et al., 2015). By reconstructing the velocity distribution function in the outflow region, I show that counterstreaming beams are difficult to clearly resolve in the solar wind because their relative speeds are comparable their thermal speeds. Previous 144

studies (Gosling et al., 2005a; Lavraud et al., 2021) of this phenomenon found that the observed relative speeds were consistently smaller than expected and attributed this to the electromagnetic ion beam instability (Goldstein et al., 2000). My results suggest that this discrepancy may more likely be a natural consequence of stress balance at the current sheet, as the inflow beams slow down and heat up as they enter the outflow region.

In Chapter 4, I apply my symmetric current sheet stress balance models to Solar Orbiter observations of reconnection outflows in the solar wind. Out of 3163 potential reconnection outflows identified in 2023, I shortlist five events with symmetric magnetic field and inflow conditions most compatible with the model assumptions for further analysis. For these events, I find outflow region opening angles ranging from 0.2° to 10.8°, consistent with results from earlier studies (Mistry et al., 2015). I then reconstruct the VDF of the proton beam population in the reconnection inflow and outflow regions, and compare them with the observed VDFs from the PAS instrument onboard Solar Orbiter. Here, I highlight the results from two events: one on 9 January 2023 and the other on 9 July 2023. For the 9 July event, the symmetric stress balance model successfully describes the structure and beam population of the reconnection outflow region. A clear counterstreaming beam signature is observed throughout the outflow region, and the observed beam velocities are a good match to the predicted velocities derived from the model. By contrast, the structure of the 9 January event is more complex and deviates significantly from that predicted by the symmetric stress balance model. The outflow region is divided into two halves, each characterised by a different beam population. In the leading half, the proton population is characterised by a a single outflow beam with properties similar to the inflow beam from the leading inflow region. However, in the trailing half, the proton population is characterised by a pair of counterstreaming beams which persists into the trailing inflow region. This suggests that this event has an outflow region with an asymmetric, multi-layered structure, consistent with the framework described by Owen et al. (2021). In this picture, the outflow region is divided into multiple layers, each containing a distinct population of proton beams that may be separated by additional current sheets. Several examples of this type of multi-layered reconnection outflow have been reported in other studies using Solar Orbiter and Parker Solar Probe data (Lavraud et al., 2021; Phan et al., 2022; Duan et al., 2023).

My analysis of the symmetric current sheet stress balance model in Chapter 3 is limited to ensuring consistency with previous results and observations of reconnection outflows in the solar wind. The first step in generalising this model would be to introduce asymmetric inflow conditions and magnetic field geometries, while retaining the bifurcated RCS structure. Since the majority of reconnection outflows in the solar wind are characterised by a bifurcated RCS (Gosling et al., 2006a; Gosling & Szabo, 2008; Mistry et al., 2015; Phan et al., 2020), an asymmetric current sheet

145

stress balance model provides the framework for describing the structure and proton beam population for a wider range of reconnection events in the solar wind. Another useful experiment would be to determine the range of inflow conditions for which a solution to the stress balance model exists for a given magnetic field geometry. Reconnection can occur in the range where a solution exists, but is suppressed in the range where no solution exists (Owen & Cowley, 1987b). The results of this analysis could then be compared with existing studies which use the magnetic shear angle and plasma β difference across the RCS as indicators of whether reconnection is allowed or suppressed (Swisdak et al., 2003, 2010; Phan et al., 2010).

Going beyond the bifurcated RCS case, I can also further extend the current sheet stress balance models to describe multi-layered reconnection outflows. This will require relaxing the requirement that the reconnection inflow beam just catch up with current sheet on the opposite side of the outflow region and not exit the outflow region (see Section 3.3). Taking the 9 January event discussed in Section 4.5.2 as an example, the interpretation of this event suggests that one of the inflow beams has sufficient speed to pass through the outflow region entirely, while the other is too slow to reach the opposite side of the outflow region. Based on the VDF measurements, this reconnection outflow can be divided into five layers, potentially separated by up to four current sheets (Owen et al., 2021). The stress balance model for this multi-layered reconnection configuration would be significantly more complicated than the bifurcated RCS case, as it requires evaluating the stress balance conditions for a coupled system of four or more current sheets while ensuring self-consistency in the results. This would build upon previous work by Heyn et al. (1985); Owen & Cowley (1987b); Owen et al. (2021) that sets up the theoretical framework for describing the structure of reconnection outflows with multiple layers or inflow beams.

Most existing observations of counterstreaming proton beams in reconnection outflows are associated with reconnection at ICMEs (Gosling et al., 2005a). This is because ICMEs are characterised by stronger magnetic fields and cooler plasma, leading to a higher Alfvén speed and lower proton beam thermal speed compared to elsewhere in the solar wind. Since the relative speed of the counterstreaming beams is related to the Alfvén speed, these conditions make it easier to observe well-separated counterstreaming beams in ICMEs. A follow-up study focusing mainly on the properties of the counterstreaming beam population could involve searching specifically for reconnection events associated with ICMEs. This would involve going through my catalogue of 3163 potential reconnection events in 2023, but instead employing selection criteria aimed at looking for reconnection outflows embedded within solar wind flows with properties associated with ICMEs. These properties may include strong magnetic fields, cool plasma, and bi-directional electron strahl (Gosling, 1990; Neugebauer & Goldstein, 1997). Using the automated reconnection identification algorithm developed by Fargette et al. (2023), I could also expand my

146

search to other periods where Solar Orbiter data is available.

Finally, in Chapter 5, I evaluate the viability of magnetic reconnection as an erosion mechanism for magnetic switchbacks in the solar wind. I identify three examples of magnetic switchbacks in the solar wind with magnetic field and plasma data from Solar Orbiter between 10 August 2021 and 30 August 2021. During this interval, the spacecraft was at a heliocentric distance of 0.6–0.7 AU from the Sun. Using hodographs and Walén analysis methods, I test for rotational discontinuities and reconnection outflows at the switchback boundaries. For all three switchbacks, I find evidence of magnetic reconnection at their trailing edge boundaries. I postulate that reconnection can accelerate the erosion of switchbacks through the removal of polarity-reversed magnetic flux from the switchback interior. The timing analysis of this process show that complete erosion of the switchback occurs over timescales ranging from a few minutes to a few hours, suggesting that reconnection is a fast and efficient mechanism for eroding individual switchbacks. During this time, the switchbacks are convected a further 0.005-0.4 AU from their point of detection by the background solar wind flow, implying complete erosion occurs before they reach 1 AU. This could explain the relative lack of switchback observations near Earth compared to near the Sun.

Although I have demonstrated that reconnection can rapidly remove individual switchbacks, questions still remain about the overall importance of magnetic reconnection to the evolution and erosion of switchbacks in the inner heliosphere. Including the three events discussed in this thesis, there have only been eight examples of switchback boundary reconnection reported thus far: five using *Solar Orbiter* data (Fedorov et al., 2021; Lavraud et al., 2021; Suen et al., 2023), and three using PSP data (Froment et al., 2021). A logical follow-up to the case study presented here would be to conduct a large-scale survey of reconnecting switchbacks in the solar wind, using *Solar Orbiter* or PSP data from the past few years.

Automated methods of identifying switchback based on identifiers such as the deflection angle of the magnetic field (Dudok de Wit et al., 2020) and velocity enhancements (Horbury et al., 2020b) already exist, and could be used to create a catalogue of switchbacks analogous to the one for reconnection outflows created in Chapter 4. By comparing the two catalogues, I could determine the proportion of reconnection events that occur at switchback boundaries, as well as the occurrence rate of switchback boundary reconnection and how this rate varies with heliocentric distance. Combining the estimates of the occurrence rate of switchback boundary reconnection and the timing analysis for switchback erosion could then allow inference of how reconnection governs the overall evolution and decay of switchbacks. As switchbacks carry energy from the Sun's corona into the heliosphere (Rivera et al., 2024), understanding how they decay and thus, transfer their stored energy into their surroundings, has implications for the solar wind heating and acceleration problem.

References

- Acuña, M. H. 2002, Review of Scientific Instruments, 73, 3717, doi: 10.1063/1.1510570
- Aellig, M. R., Lazarus, A. J., & Steinberg, J. T. 2001, Geophysical Research Letters, 28, 2767, doi: 10.1029/2000GL012771
- Agapitov, O. V., Drake, J. F., Swisdak, M., et al. 2022, The Astrophysical Journal, 925, 213, doi: 10.3847/1538-4357/ac4016
- Antiochos, S. K., DeVore, C. R., & Klimchuk, J. A. 1999, The Astrophysical Journal, 510, 485, doi: 10.1086/306563
- Babcock, H. W. 1961, The Astrophysical Journal, 133, 572, doi: 10.1086/147060
- Bale, S. D., Badman, S. T., Bonnell, J. W., et al. 2019, Nature, 576, 237, doi: 10. 1038/s41586-019-1818-7
- Bale, S. D., Horbury, T. S., Velli, M., et al. 2021, The Astrophysical Journal, 923, 174, doi: 10.3847/1538-4357/ac2d8c
- Balogh, A., Forsyth, R. J., Lucek, E. A., Horbury, T. S., & Smith, E. J. 1999, Geophysical Research Letters, 26, 631, doi: https://doi.org/10.1029/1999GL900061
- Barlow, R. 1989, Statistics: a guide to the use of statistical methods in the physical sciences / Roger Barlow, The Manchester physics series (Chichester: Wiley)
- Baumjohann, W., & Treumann, R. A. 2022, Basic Space Plasma Physics, third edition. edn. (New Jersey: World Scientific)
- Bethe, H. A. 1939, Physical Review, 55, 434, doi: 10.1103/PhysRev.55.434
- Biermann, L. 1952, in Liege International Astrophysical Colloquia, Vol. 4, Liege International Astrophysical Colloquia, ed. P. Swings, 251–262
- Boyd, T. J. M., & Sanderson, J. J. 2003, The Physics of Plasmas (Cambridge University Press)

- Broeren, T., Klein, K. G., TenBarge, J. M., et al. 2021, Frontiers in Astronomy and Space Sciences, 8, 144, doi: 10.3389/fspas.2021.727076
- Burch, J. L., Moore, T. E., Torbert, R. B., & Giles, B. L. 2016, Space Science Reviews, 199, 5, doi: 10.1007/s11214-015-0164-9
- Carlson, C. W., Curtis, D. W., Paschmann, G., & Michael, W. 1982, Advances in Space Research, 2, 67, doi: 10.1016/0273-1177 (82) 90151-X
- Chen, F. F. 2015, Introduction to Plasma Physics and Controlled Fusion (Springer Cham)
- Choi, K.-E., Agapitov, O. V., Lee, D.-Y., et al. 2025, The Astrophysical Journal, 988, 49, doi: 10.3847/1538-4357/ade4be
- Comişel, H., Narita, Y., & Motschmann, U. 2015, Annales Geophysicae, 33, 345, doi: 10.5194/angeo-33-345-2015
- Cowley, S. W. H., & Shull, Jr., P. 1983, Planetary and Space Science, 31, 235, doi: 10.1016/0032-0633(83)90058-2
- Cowley, S. W. H., & Southwood, D. J. 1980, Geophysical Research Letters, 7, 833, doi: 10.1029/GL007i010p00833
- Cranmer, S. R. 2009, Living Reviews in Solar Physics, 6, 3, doi: 10.12942/ lrsp-2009-3
- D'Amicis, R., Bruno, R., Panasenco, O., et al. 2021, Astronomy & Astrophysics, 656, A21, doi: 10.1051/0004-6361/202140938
- de Hoffmann, F., & Teller, E. 1950, Physical Review, 80, 692, doi: 10.1103/ PhysRev.80.692
- De Marco, R., Bruno, R., Jagarlamudi, V. K., et al. 2023, Astronomy & Astrophysics, 669, A108, doi: 10.1051/0004-6361/202243719
- Denton, R. E., Sonnerup, B. U. Ö., Russell, C. T., et al. 2018, Journal of Geophysical Research (Space Physics), 123, 2274, doi: 10.1002/2017JA024619
- Dong, X.-C., Dunlop, M. W., Trattner, K. J., et al. 2017, Geophysical Research Letters, 44, 5951, doi: 10.1002/2017GL073411
- Drake, J. F., Agapitov, O., Swisdak, M., et al. 2021, Astronomy & Astrophysics, 650, A2, doi: 10.1051/0004-6361/202039432
- Duan, D., He, J., Zhu, X., et al. 2023, The Astrophysical Journal Letters, 952, L11, doi: 10.3847/2041-8213/acd553

- Dudok de Wit, T., Krasnoselskikh, V. V., Bale, S. D., et al. 2020, Astrophysical Journals, 246, 39, doi: 10.3847/1538-4365/ab5853
- Eastwood, J. P., Stawarz, J. E., Phan, T. D., et al. 2021, Astronomy & Astrophysics, 656, A27, doi: 10.1051/0004-6361/202140949
- Enžl, J., Přech, L., Šafránková, J., & Němeček, Z. 2014, Astrophysical Journal, 796, 21, doi: 10.1088/0004-637x/796/1/21
- Eriksson, S., Swisdak, M., Weygand, J. M., et al. 2022, Astrophysical Journal, 933, 181, doi: 10.3847/1538-4357/ac73f6
- Escoubet, C. P., Schmidt, R., & Goldstein, M. L. 1997, Space Science Reviews, 79, 11, doi: 10.1023/A:1004923124586
- European Space Agency. 2021, Solar Orbiter Archive, https://soar.esac.esa.int/soar/
- Fargette, N., Lavraud, B., Rouillard, A. P., et al. 2022, Astronomy and Astrophysics, 663, A109, doi: 10.1051/0004-6361/202243537
- —. 2021, The Astrophysical Journal, 919, 96, doi: 10.3847/1538-4357/ac1112
- —. 2023, Astronomy & Astrophysics, 674, A98, doi: 10.1051/0004-6361/202346043
- Fedorov, A. 2020, SWA-PAS L2 Data User Guide, Tech. Rep. V02, Institut de Recherche en Astrophysique et Planétologie (IRAP), Toulouse, France
- —. 2022, PAS Data Tutorial, PowerPoint Presentation, Solar Orbiter In-situ Working Group Meeting
- Fedorov, A., Louarn, P., Owen, C. J., et al. 2021, Astronomy & Astrophysics, 656, A40, doi: 10.1051/0004-6361/202141246
- Feldman, W. C., Asbridge, J. R., Bame, S. J., & Montgomery, M. D. 1973, Journal of Geophysical Research, 78, 2017, doi: 10.1029/JA078i013p02017
- Feng, H., Li, Q., Wang, J., & Zhao, G. 2017, Solar Physics, 292, 53, doi: 10. 1007/s11207-017-1083-6
- Fisk, L. A., & Kasper, J. C. 2020, The Astrophysical Journal Letters, 894, L4, doi: 10.3847/2041-8213/ab8acd
- Fox, N. J., Velli, M. C., Bale, S. D., et al. 2016, Space Science Reviews, 204, 7, doi: 10.1007/s11214-015-0211-6

- Froment, C., Krasnoselskikh, V., Dudok de Wit, T., et al. 2021, Astronomy & Astrophysics, 650, A5, doi: 10.1051/0004-6361/202039806
- García Marirrodriga, C., Pacros, A., Strandmoe, S., et al. 2021, Astronomy & Astrophysics, 646, A121, doi: 10.1051/0004-6361/202038519
- Goldstein, B. E., Neugebauer, M., Zhang, L. D., & Gary, S. P. 2000, Geophysical Research Letters, 27, 53, doi: 10.1029/1999GL003637
- Gopalswamy, N. 2003, Advances in Space Research, 31, 869, doi: 10.1016/ S0273-1177(02)00888-8
- Gosling, J. T. 1990, Geophysical Monograph Series, 58, 343, doi: 10.1029/GM058p0343
- —. 2012, Space Science Reviews, 172, 187, doi: 10.1007/s11214-011-9747-2
- Gosling, J. T., Eriksson, S., & Schwenn, R. 2006a, Journal of Geophysical Research (Space Physics), 111, A10102, doi: 10.1029/2006JA011863
- Gosling, J. T., McComas, D. J., Skoug, R. M., & Smith, C. W. 2006b, Geophysical Research Letters, 33, L17102, doi: 10.1029/2006GL027188
- Gosling, J. T., & Phan, T. D. 2013, Astrophysical Journal, 763, L39, doi: 10. 1088/2041-8205/763/2/139
- Gosling, J. T., Phan, T. D., Lin, R. P., & Szabo, A. 2007, Geophysical Research Letters, 34, L15110, doi: 10.1029/2007GL030706
- Gosling, J. T., & Pizzo, V. J. 1999, Space Science Reviews, 89, 21, doi: 10.1023/ A:1005291711900
- Gosling, J. T., Skoug, R. M., McComas, D. J., & Smith, C. W. 2005a, Journal of Geophysical Research: Space Physics, 110, doi: 10.1029/2004JA010809
- —. 2005b, Geophysical Research Letters, 32, L05105, doi: 10.1029/ 2005GL022406
- Gosling, J. T., & Szabo, A. 2008, Journal of Geophysical Research (Space Physics), 113, A10103, doi: 10.1029/2008JA013473
- Haggerty, C. C., Shay, M. A., Chasapis, A., et al. 2018, PhPl, 25, 102120, doi: 10. 1063/1.5050530
- Hagyard, M. J., Smith, Jr., J. B., Teuber, D., & West, E. A. 1984, Solar Physics, 91, 115, doi: 10.1007/BF00213618

- Hale, G. E. 1908, The Astrophysical Journal, 28, 315, doi: 10.1086/141602
- Hale, G. E., Ellerman, F., Nicholson, S. B., & Joy, A. H. 1919, The Astrophysical Journal, 49, 153, doi: 10.1086/142452
- He, J., Zhu, X., Chen, Y., et al. 2018, Astrophysical Journal, 856, 148, doi: 10. 3847/1538-4357/aab3cd
- Heyn, M. F., Biernat, H. K., Semenov, V. S., & Kubyshkin, I. V. 1985, Journal of Geophysical Research, 90, 1781, doi: 10.1029/JA090iA02p01781
- Horbury, T. S., Matteini, L., & Stansby, D. 2018, Monthly Notices of the Royal Astronomical Society, 478, 1980, doi: 10.1093/mnras/sty953
- Horbury, T. S., O'Brien, H., Carrasco Blazquez, I., et al. 2020a, Astronomy & Astrophysics, 642, A9, doi: 10.1051/0004-6361/201937257
- Horbury, T. S., Woolley, T., Laker, R., et al. 2020b, Astrophysical Journals, 246, 45, doi: 10.3847/1538-4365/ab5b15
- Hudson, P. D. 1970, Planetary and Space Science, 18, 1611, doi: 10.1016/0032-0633(70)90036-X
- Hughes, W. J. 1995, The Magnetopause, Magnetotail, and Magnetic Reconnection, ed. M. G. Kivelson & C. T. Russell (Cambridge University Press), 227–287
- Kasper, J. C., Stevens, M. L., Korreck, K. E., et al. 2012, The Astrophysical Journal, 745, 162, doi: 10.1088/0004-637X/745/2/162
- Kasper, J. C., Bale, S. D., Belcher, J. W., et al. 2019, Nature, 576, 228, doi: 10. 1038/s41586-019-1813-z
- Khrabrov, A. V., & Sonnerup, B. U. Ö. 1998, ISSI Scientific Reports Series, 1, 221
- Klein, K. G., Alexandrova, O., Bookbinder, J., et al. 2019, arXiv e-prints, arXiv:1903.05740
- Klimchuk, J. A. 2006, Solar Physics, 234, 41, doi: 10.1007/s11207-006-0055-z
- Knetter, T., Neubauer, F. M., Horbury, T., & Balogh, A. 2004, Journal of Geophysical Research (Space Physics), 109, A06102, doi: 10.1029/2003JA010099
- Krasnoselskikh, V., Larosa, A., Agapitov, O., et al. 2020, Astrophysical Journal, 893, 93, doi: 10.3847/1538-4357/ab7f2d
- Laker, R., Horbury, T. S., Matteini, L., et al. 2022, Monthly Notices of the Royal Astronomical Society, 517, 1001, doi: 10.1093/mnras/stac2477

- Larosa, A., Krasnoselskikh, V., Dudok de Wit, T., et al. 2021, Astronomy & Astrophysics, 650, A3, doi: 10.1051/0004-6361/202039442
- Lavraud, B., Kieokaew, R., Fargette, N., et al. 2021, Astronomy & Astrophysics, 656, A37, doi: 10.1051/0004-6361/202141149
- Leighton, R. B. 1969, The Astrophysical Journal, 156, 1, doi: 10.1086/149943
- Lewis, G., Anekallu, C., Raines, J., & Fedorov, A. 2023, SWA Data Product Definition Document Version J, Tech. rep., University College London Mullard Space Science Laboratory
- Macneil, A. R., Owens, M. J., Wicks, R. T., et al. 2020, Monthly Notices of the Royal Astronomical Society, 494, 3642, doi: 10.1093/mnras/staa951
- Maksimovic, M., Bale, S. D., Chust, T., et al. 2020, Astronomy & Astrophysics, 642, A12, doi: 10.1051/0004-6361/201936214
- Marghitu, O., Comişel, H., & Scholer, M. 2017, Geophysical Research Letters, 44, 6500, doi: 10.1002/2017GL073241
- Marsch, E., Rosenbauer, H., Schwenn, R., Muehlhaeuser, K. H., & Neubauer, F. M. 1982a, Journal of Geophysical Research, 87, 35, doi: 10.1029/ JA087iA01p00035
- Marsch, E., Schwenn, R., Rosenbauer, H., et al. 1982b, Journal of Geophysical Research, 87, 52, doi: 10.1029/JA087iA01p00052
- Matteini, L., Horbury, T. S., Neugebauer, M., & Goldstein, B. E. 2014, Geophysical Research Letters, 41, 259, doi: 10.1002/2013GL058482
- Matthaeus, W. H., Adhikari, S., Bandyopadhyay, R., et al. 2022, arXiv e-prints, arXiv:2211.12676
- McComas, D. J., Elliott, H. A., Schwadron, N. A., et al. 2003, Geophysical Research Letters, 30, 1517, doi: 10.1029/2003GL017136
- McComas, D. J., Gosling, J. T., Hammond, C. M., et al. 1994, Geophysical Research Letters, 21, 1751, doi: https://doi.org/10.1029/94GL01077
- Meyer-Vernet, N. 2007, Basics of the Solar Wind (Cambridge University Press), doi: 10.1017/CBO9780511535765
- Mikic, Z., Barnes, D. C., & Schnack, D. D. 1988, The Astrophysical Journal, 328, 830, doi: 10.1086/166341
- Mistry, R., Eastwood, J. P., Phan, T. D., & Hietala, H. 2015, Geophysical Research Letters, 42, 10,513, doi: 10.1002/2015GL066820

- Mozer, F. S., Agapitov, O. V., Bale, S. D., et al. 2020, The Astrophysical Journal Supplement Series, 246, 68, doi: 10.3847/1538-4365/ab7196
- Müller, D., Marsden, R. G., St. Cyr, O. C., Gilbert, H. R., & Solar Orbiter Team. 2013, Solar Physics, 285, 25, doi: 10.1007/s11207-012-0085-7
- Müller, D., St. Cyr, O. C., Zouganelis, I., et al. 2020, Astronomy & Astrophysics, 642, A1, doi: 10.1051/0004-6361/202038467
- Ness, N. F. 1970, Space Science Reviews, 11, 459, doi: 10.1007/BF00183028
- Neugebauer, M., & Goldstein, R. 1997, Geophysical Monograph Series, 99, 245, doi: 10.1029/GM099p0245
- Neugebauer, M., & Snyder, C. W. 1962, Science, 138, 1095, doi: 10.1126/science.138.3545.1095.a
- Nicolaou, G., Wicks, R. T., Rae, I. J., & Kataria, D. O. 2020, Space Weather, 18, e2020SW002559, doi: 10.1029/2020SW002559
- Owen, C. J., & Cowley, S. W. H. 1987a, Planetary and Space Science, 35, 451, doi: 10.1016/0032-0633(87)90102-4
- —. 1987b, Planetary and Space Science, 35, 467, doi: 10.1016/0032-0633(87)90103-6
- Owen, C. J., & Mist, R. T. 2001, Geophysical Research Letters, 28, 2771, doi: 10. 1029/2001GL013032
- Owen, C. J., Bruno, R., Livi, S., et al. 2020, Astronomy & Astrophysics, 642, A16
- Owen, C. J., Foster, A. C., Bruno, R., et al. 2021, Astronomy & Astrophysics, 656, L8, doi: 10.1051/0004-6361/202140944
- Owens, M. J., Crooker, N. U., & Lockwood, M. 2013, Journal of Geophysical Research (Space Physics), 118, 1868, doi: 10.1002/jgra.50259
- Owens, M. J., & Forsyth, R. J. 2013, Living Reviews in Solar Physics, 10, 5, doi: 10.12942/lrsp-2013-5
- Parker, E. 1988, Astrophysical Journal, 330, 474, doi: 10.1086/166485
- Parker, E. N. 1957, Journal of Geophysical Research, 62, 509, doi: 10.1029/ JZ062i004p00509
- —. 1958, The Astrophysical Journal, 128, 664, doi: 10.1086/146579

- —. 1959, Journal of Geophysical Research, 64, 1675, doi: 10.1029/ JZ064i011p01675
- —. 1960, The Astrophysical Journal, 132, 821, doi: 10.1086/146985
- —. 1965, Space Science Reviews, 4, 666, doi: 10.1007/BF00216273
- Paschmann, G., & Sonnerup, B. U. O. 2008, ISSI Scientific Reports Series, 8, 65
- Paschmann, G., Papamastorakis, I., Sckopke, N., et al. 1979, Nature, 282, 243, doi: 10.1038/282243a0
- Paschmann, G., Haaland, S., Sonnerup, B. U. Ö., et al. 2005, Annales Geophysicae, 23, 1481, doi: 10.5194/angeo-23-1481-2005
- Pecora, F., Matthaeus, W. H., Primavera, L., et al. 2022, The Astrophysical Journal Letters, 929, L10, doi: 10.3847/2041-8213/ac62d4
- Petschek, H. E. 1964, in NASA Special Publication, Vol. 50 (NASA), 425
- Phan, T. D., Paschmann, G., Gosling, J. T., et al. 2013, Geophysical Research Letters, 40, 11, doi: 10.1029/2012GL054528
- Phan, T. D., Gosling, J. T., Paschmann, G., et al. 2010, Astrophysical Journal Letters, 719, L199, doi: 10.1088/2041-8205/719/2/L199
- Phan, T. D., Bale, S. D., Eastwood, J. P., et al. 2020, Astrophysical Journals, 246, 34, doi: 10.3847/1538-4365/ab55ee
- Phan, T. D., Lavraud, B., Halekas, J. S., et al. 2021, Astronomy & Astrophysics, 650, A13, doi: 10.1051/0004-6361/202039863
- Phan, T. D., Verniero, J. L., Larson, D., et al. 2022, Geophysical Research Letters, 49, e96986, doi: 10.1029/2021GL09698610.1002/essoar. 10508706.1
- Phan, T. D., Drake, J. F., Larson, D., et al. 2024, The Astrophysical Journal Letters, 971, L42, doi: 10.3847/2041-8213/ad6841
- Priest, E., & Forbes, T. 2007, Magnetic Reconnection (Cambridge University Press)
- Priest, E. R. 1978, Solar Physics, 58, 57, doi: 10.1007/BF00152555
- —. 1995, The Sun and Its Magnetohydrodynamics, ed. M. G. Kivelson & C. T. Russell (Cambridge University Press), 58–90
- Reisenfeld, D. B., Gary, S. P., Gosling, J. T., et al. 2001, Journal of Geophysical Research, 106, 5693, doi: 10.1029/2000JA000317

- Rivera, Y. J., Badman, S. T., Stevens, M. L., et al. 2024, Science, 385, 962, doi: 10. 1126/science.adk6953
- Schrijver, C. J., Title, A. M., Harvey, K. L., et al. 1998, Nature, 394, 152, doi: 10. 1038/28108
- Schwadron, N. A., & McComas, D. J. 2021, Astrophysical Journal, 909, 95, doi: 10.3847/1538-4357/abd4e6
- Schwartz, S. J., Ergun, R., Kucharek, H., et al. 2021, Journal of Geophysical Research (Space Physics), 126, e29295, doi: 10.1029/2021JA029295
- Solanki, S. K. 2003, The Astronomy & Astrophysics Review, 11, 153, doi: 10. 1007/s00159-003-0018-4
- Somov, B. V., Kosugi, T., Hudson, H. S., Sakao, T., & Masuda, S. 2002, The Astrophysical Journal, 579, 863, doi: 10.1086/342842
- Sonnerup, B. U. O., & Cahill, L. J., J. 1967, Journal of Geophysical Research, 72, 171, doi: https://doi.org/10.1029/JZ072i001p00171
- Sonnerup, B. U. Ö., & Scheible, M. 1998, ISSI Scientific Reports Series, 1, 185
- Sonnerup, B. U. O., Paschmann, G., Papamastorakis, I., et al. 1981, Journal of Geophysical Research, 86, 10049, doi: 10.1029/JA086iA12p10049
- Squire, J., Chandran, B. D. G., & Meyrand, R. 2020, The Astrophysical Journal Letters, 891, L2, doi: 10.3847/2041-8213/ab74e1
- Squire, J., Johnston, Z., Mallet, A., & Meyrand, R. 2022, Physics of Plasmas, 29, 112903, doi: 10.1063/5.0099924
- Steinberg, J. T., Lazarus, A. J., Ogilvie, K. W., Lepping, R., & Byrnes, J. 1996, Geophysical Research Letters, 23, 1183, doi: 10.1029/96GL00628
- Steinvall, K., Khotyaintsev, Y. V., Cozzani, G., et al. 2021, Astronomy & Astrophysics, 656, A9, doi: 10.1051/0004-6361/202140855
- Suen, G. H. H., Owen, C. J., Verscharen, D., et al. 2023, Astronomy & Astrophysics, 675, A128, doi: 10.1051/0004-6361/202345922
- Sweet, P. A. 1958, in IAU Symposium, Vol. 6, Electromagnetic Phenomena in Cosmical Physics, ed. B. Lehnert, 123
- Swisdak, M., Opher, M., Drake, J. F., & Alouani Bibi, F. 2010, The Astrophysical Journal, 710, 1769, doi: 10.1088/0004-637X/710/2/1769

- Swisdak, M., Rogers, B. N., Drake, J. F., & Shay, M. A. 2003, Journal of Geophysical Research (Space Physics), 108, 1218, doi: 10.1029/2002JA009726
- Teh, W. L., Sonnerup, B. U. Ö., Hu, Q., & Farrugia, C. J. 2009, Annales Geophysicae, 27, 807, doi: 10.5194/angeo-27-807-2009
- Telloni, D., Zank, G. P., Stangalini, M., et al. 2022, The Astrophysical Journal Letters, 936, L25, doi: 10.3847/2041-8213/ac8104
- Tenerani, A., Sioulas, N., Matteini, L., et al. 2021, The Astrophysical Journal Letters, 919, L31, doi: 10.3847/2041-8213/ac2606
- Tenerani, A., Velli, M., Matteini, L., et al. 2020, Astrophysical Journals, 246, 32, doi: 10.3847/1538-4365/ab53e1
- Tilquin, H., Eastwood, J. P., & Phan, T. D. 2020, Astrophysical Journal, 895, 68, doi: 10.3847/1538-4357/ab8812
- Van Doorsselaere, T., Srivastava, A. K., Antolin, P., et al. 2020, Space Science Reviews, 216, 140, doi: 10.1007/s11214-020-00770-y
- Verscharen, D., Klein, K. G., & Maruca, B. A. 2019, Living Reviews in Solar Physics, 16, 5, doi: 10.1007/s41116-019-0021-0
- Wang, R., Vasko, I. Y., Phan, T. D., & Mozer, F. S. 2024, Journal of Geophysical Research (Space Physics), 129, e2023JA032215, doi: 10.1029/2023JA032215
- Wilcox, J. M., & Ness, N. F. 1965, Journal of Geophysical Research, 70, 5793, doi: 10.1029/JZ070i023p05793
- Wyper, P. F., DeVore, C. R., Antiochos, S. K., et al. 2022, The Astrophysical Journal Letters, 941, L29, doi: 10.3847/2041-8213/aca8ae
- Yamauchi, Y., Suess, S. T., Steinberg, J. T., & Sakurai, T. 2004, Journal of Geophysical Research (Space Physics), 109, A03104, doi: 10.1029/2003JA010274
- Zhou, Z., Wei, F., Feng, X., et al. 2018, Astrophysical Journal, 863, 84, doi: 10. 3847/1538-4357/aad098
- Zouganelis, I., De Groof, A., Walsh, A. P., et al. 2020, Astronomy & Astrophysics, 642, A3, doi: 10.1051/0004-6361/202038445